Femtosecond Optical Pulse Shaping and Multiple-Pulse Femtosecond Spectroscopy

by

Marc Michael Wefers
B. Sc. Chemical Physics, University of Toronto 1991

Submitted to the Department of Chemistry in partial fulfillment of the requirements for the degree of

DOCTOR OF PHILOSOPHY

at the

MASSACHUSETTS INSTITUTE OF TECHNOLOGY

September 1996

Signature of Author _____
Department of Chemistry
July 23, 1996

Certified by _____
Keith A. Nelson
Thesis Supervisor

Accepted by _____
Dietmar Seyferth
Chairman, Departmental Committee on Graduate Studies

This doctoral thesis has been examined by a committee of the Department of Chemistry as follows:

Professor Robert W. Field _____
Chairman

Professor Keith A. Nelson _____
Thesis Supervisor

Professor Robert G. Griffin _____

Femtosecond Optical Pulse Shaping and Multiple-Pulse Femtosecond Spectroscopy

Marc M. Wefers

Submitted to the Department of Chemistry on July 23, 1996 in partial fulfillment of the requirements for the degree Doctor of Philosophy in Chemistry

Abstract

Femtosecond pulse shaping methods are developed in which a single ultrashort optical pulse is transformed into a shaped ultrafast optical waveform with a specified time-dependent profile, such as a multiple-pulse sequence. The technique involves the spectral filtering of spatially-separated frequency components using a spatially varying mask. Liquid crystal (LC) spatial light modulators (SLM) are used as computer-controlled masks allowing high-fidelity programmable waveform-generation. For the case of two SLMs used together, independent specification of temporal amplitude and temporal phase profiles is possible. Amplification and control over time-dependent polarization profiles is also demonstrated. In conjunction with experimental efforts, a methodology for user-specified waveform generation and a theoretical analysis of spatial effects accompanying temporal shaping are also performed.

The chemical motivation behind femtosecond pulse shaping is the development of capabilities for more versatile and detailed optical manipulation over molecular and material systems. Experiments are demonstrated in which excitation with shaped multiple-pulse waveforms permit control over multiple electronic coherences (in atomic potassium vapor) and lattice vibrational trajectories (in crystalline quartz) along one and two dimensions, the latter case including motions of ions in crystals along elliptical, circular, and other two-dimensional trajectories. Combined temporal and spatial shaping of ultrafast optical waveforms is also demonstrated. This is essential for the manipulation of propagating material responses, and some possibilities are presented.

Results suggest that large-amplitude lattice displacements can be produced in solid-state systems through shaped waveform excitation that circumvents sample damage. To this end, a derivation of the impulse responses of non-dispersive optic phonons and dispersive phonon-polaritons with anharmonic potentials is presented. This is important since large-amplitude lattice displacements will sample anharmonic regions of the lattice potential energy surface. The results show that anharmonic contributions to the response can be observed and isolated, if optical grating excitation is used and diffraction from material responses at spatial harmonics of the grating is detected.

Thesis Supervisor: Dr. Keith A. Nelson
Title: Professor of Chemistry

Personal Thanks:

Life at MIT has been fun and intense. It is hard to separate long nights of anguish in the laboratory from the goofy humor and curiosity of those with whom I work and play. This eclectic group has made the last couple of years a pleasure and I will sorely miss them.

First and foremost, I want to thank my advisor Keith Nelson. His eternal enthusiasm in life and science amaze me. Be it optic phonons behaving like children on swings, polaritons propagating toward their destruction, or Latin dancing, Karaoke, and the midnight sun in St. Petersberg, Keith's attitudes are infectious and inspirational. Keith, I hope you will remain a good friend and mentor.

A large portion of my research was conducted together with my endeared colleague Hitoshi Kawashima, who visited our lab from Japan. His theoretical abilities, hard work, and quirky smile were essential and greatly appreciated. I am particularly amazed that he survived two years in the U.S. on only coffee and donuts! Andy Cook helped me through my initial experiences with lasers and provided crucial computer code for the early pulse shaping experiments. I particularly enjoyed my scientific discussions with John Fourkas who was with us for only a short time, but was a great sounding board and an even better friend. Many thanks also to Dutch and Yang, who manage to restrain me during my many feuds with our lab's Macs.

From afar, Prof. Martin Moskovits at the University of Toronto was always full of encouragement. Eight summers ago he gave me my first opportunity to do scientific research and I owe much of the confidence I have gained since that time to him. From the beginning of my scientific studies to the end, I want to thank Professors Phil Bucksbaum, Kent Wilson, Andrew Weiner, Dwayne Miller, and Paul Corkum for their patience and support as I muddled through my future career plans. I also should mention the financial support of the Natural Science and Engineering Research Council of Canada who provided me with a 1967 Centennial Graduate Studies Fellowship from 1991 to 1995.

The many friends I have found at MIT will form my strongest memories of this place. From the early days of alcohol-induced antics during Friday morning Quantum Mechanics lectures to the Caustic Rebels

ice hockey success and present-day Thursday poker nights, hard work always went hand and hand with lots of fun. Chris M, Ted, David, John O, Cherie, Andy, Alex, Jen, John G, Sean, Tom, Mike, Lenny, Chris T, Henrik, and more recent troublemakers Bob, Greg, Tim, Richard, Dave, Steve, Doug, thanks for all those inspired and often required philosophical debates at the Muddy and elsewhere. To all the people past and present in the Nelson group, Anil, Lisa, Andy, Gary, Matt, Weining, Laura, John, Yang, Alex, Jun, Yasuo, Hitoshi, Dora, Dutch, Pat, Randy, Jiang-Ping, Tanya, Toshi, Kerry, Tim, Greg, Richard, it was an honor to share with all of you the ups and downs of life in the basement of Building 2. The stories and names (and I am sure I have missed a few) are many but all are special.

Finally, I want to thank my family. Their love and support is unshakable. Mom, Dad, Tom, Darcy, and Straun, you all mean so much to me, especially when you try to say femtosecond spectroscopy. Of course, I cannot imagine the last couple of years or anticipate the future without my soon-to-be bride. Sophie, I dedicate my thesis to you.

Table of Contents

Chapter 1: Introduction

1.1 MULTIPLE-PULSE FEMTOSECOND SPECTROSCOPY

The development of femtosecond lasers and spectroscopy during the 1980s permitted a revolution in our ability to observe natural events on previously inaccessible time scales. The elementary motions of nature including lattice vibrations in crystalline solids, intermolecular motions ("collisions") in liquids, and molecular vibrations were first observed directly in the time domain. Collective and molecular rearrangements which involve these motions, including phase transitions, liquid-state structural relaxation, and chemical reactions were also examined in detail. Femtosecond spectroscopy has since broadened into wide-ranging areas in chemistry, physics, biology, and materials science.

While femtosecond spectroscopy seeks direct optical *observation of* ultrafast processes with the aim of understanding them, a related but distinct effort seeks optical *control over* ultrafast processes with the dual aims of improved understanding and production of new states of matter, either transient or long-lived, including some with possible practical applications. Can ultrashort pulse sequences be used to induce ultrafast switching between different crystalline phases or domain orientations? Can phase-controlled waveforms be used to control chemical reaction pathways? Can irradiation of a sample by a complex series of pulses produce a simpler response, more amenable to interpretation and understanding, than irradiation by a single pulse? These questions illustrate the objectives of *multiple-pulse femtosecond spectroscopy*. These objectives are not novel in their own right: photolithography, optical data storage,

and photon echo measurements are among the many examples of optically induced rearrangements and multiple-pulse excitation. What is dramatically different from earlier efforts is the degree of control which can be exerted over the irradiation field itself, on the fastest accessible time scales. Through *femtosecond pulse shaping*, it is now possible to generate sequences of many femtosecond pulses, each one of which has a specified amplitude, time of arrival, and optical phase. In general, complex waveforms with specified amplitude and phase profiles can be generated. This opens up extraordinary possibilities for manipulation of behavior of materials and isolated molecules with the objectives mentioned above.

Another crucial development, partly preceding and partly in parallel with those introduced above, has been in the theoretical effort to guide experimentation in coherent waveform spectroscopy and optical control [1-5]. Many of the central control objectives, especially those involving chemical reactivity, were first formulated theoretically. Some of the first theoretical schemes involving femtosecond pulses dealt with two-pulse "pump-dump" sequences [1] in which absorption of the first pulse initiates wavepacket propagation on a bound excited electronic potential energy surface (PES) and the second pulse, which could be phase-related as well as optimally timed, projects the wavepacket back down to a reactive part of the ground-state PES (or up to a reactive part of a higher-energy PES).

Theoretical treatments have since greatly evolved. One approach has been the use of optimal control theory [2] determine the 'optimal' excitation waveform to bring a system into a prescribed quantum state. This method is based on a calculus of variations to minimize deviation between the specified and observe response. Problems including incomplete information about the Hamiltonian and robustness of the

solution have been treated. Recently a procedure has been formulated for determination of the optical field that produces a transient state that, to first order, shows the best possible overlap with a specified objective state [3]. This procedure gives the globally optimal solution within linear response (i.e. the weak-field limit) and permits the focus of attention to be placed not on waveform design but on whether the objective is in principle even possible.

Theoretical and experimental developments in optical control based on time-domain femtosecond pulse shaping have taken place in parallel with complementary efforts employing multiple narrowband (cw and quasi-cw) waveforms. Considerable theoretical effort has been devoted toward the exploitation of interferences between single-photon and multiple-photon quantum pathways to control molecular reactivity [4]. These efforts provided guidance for experimental demonstrations of optical control over photoionization yields [6] and the trajectories of photoexcited electrons in semiconductors [7].

Similarly, most if not all of the "quantum control" experiments in the time domain reported to date have been in the nature of demonstrations of principle. As such, many have involved rather simple waveforms, i.e. two phase-related pulses, chirped pulses, or several pulses without optical phase control. Control has been demonstrated in this fashion over atomic and molecular electronic coherences [8,9], molecular wavepacket dynamics [9,10], and collective vibrational and electronic responses in ionic crystals [11] and multiple quantum wells [12-13]. Several experiments involving more extensive control over the ultrashort optical field have also been reported. In one, involving the pulse shaping methods described herein, phase-controlled waveforms were generated and used to manipulate the

Kepler orbits of highly excited atomic Rydberg states [14]. In others, involving relatively simpler "chirping" (i.e. time-ordering of the frequency components) of a single pulse, enhanced electronic population transfer was demonstrated [15], and the wavepacket dynamics of excited-state motion of molecules in gases and solutions were controlled [16-17]. Very recently, phase-controlled chirping of femtosecond pulses has been used to influence unimolecular photodissociation yields in gas-phase molecules [18] by enhancing overlap with the dissociative potential after controlled wavepacket propagation on an intermediate potential.

The first spectroscopic application of femtosecond pulse-shaping involved multiple-pulse excitation of coherent lattice vibrations through impulsive stimulated Raman scattering (ISRS) [19-20]. In ISRS, an ultrashort excitation pulse is used to exert a sudden ("impulse") force on those Raman-active vibrational modes whose vibrational periods are longer than the pulse duration. This sudden driving force results in coherent time-dependent vibrational oscillations. Figure 1a shows time-dependent coherent scattering intensity from the molecular crystal α-perylene following excitation with a pair of nonresonant 70-fs pulses in a grating geometry. The large signal at t=0 corresponds to the nonresonant electronic response that arises only when the excitation and probe pulses are temporally overlapped in the sample. In this sample, several low-frequency lattice vibrational modes are excited coherently and their oscillations go in and out of phase following excitation, producing a characteristic "beating" pattern observed in the signal following the nonresonant electronic response at t=0. An excitation pulse sequence, shown in Fig. 1b, whose inter-pulse separation is timed to match the vibrational period of a selected vibrational mode, has also been used.

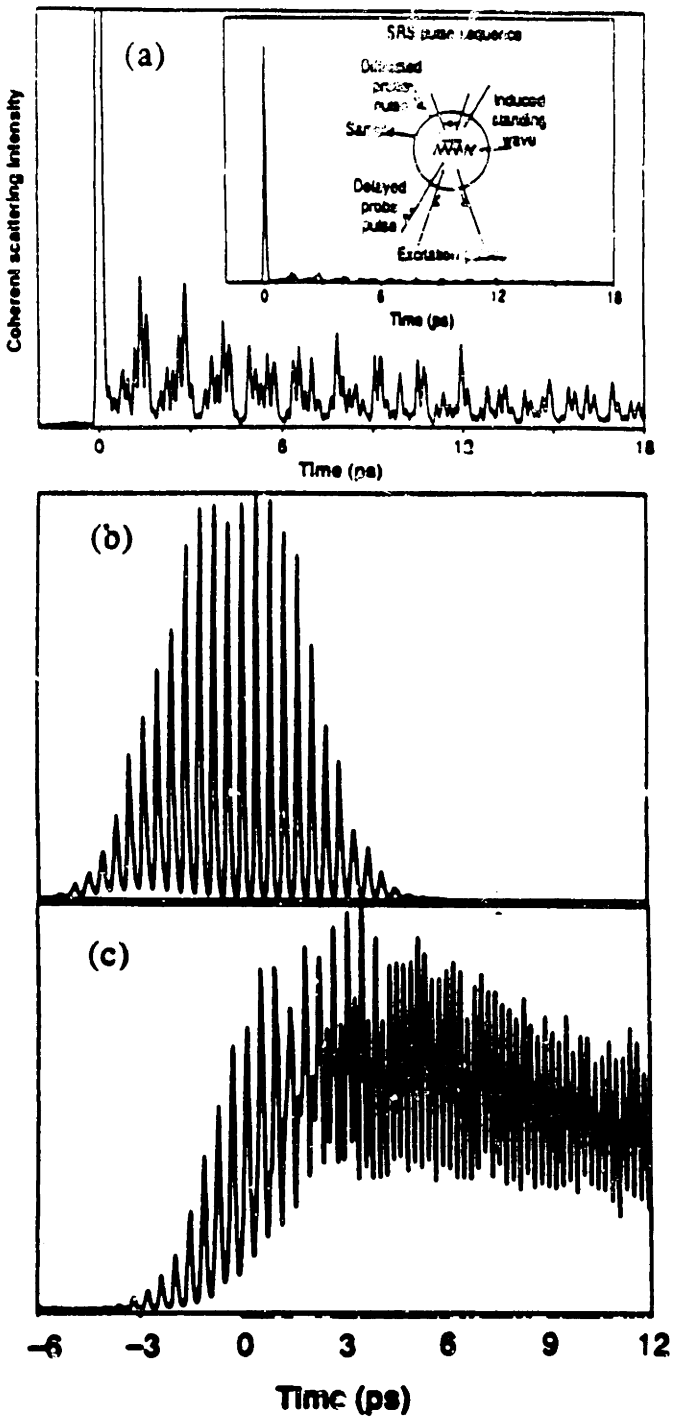

Figure 1: a) ISRS data from α-perylene crystal driven by single femtosecond pulses. The inset shows the relative signal intensities of the electronic "spike" and the vibrational response; b) Cross-correlation of a sequence of femtosecond pulses with a repetition rate of 2.39 THz (419 fsec between pulses). c) ISRS data from α-perylene driven by the pulse train shown in b). Selective amplification of an 80-cm^{-1} phonon mode is achieved.

Figure 1c shows the results of multiple-pulse excitation.. The signal in Fig. 1c shows an instantaneous nonresonant electronic response to each pulse in the excitation pulse sequence, as well as a response associated with a single coherently excited vibrational mode. This vibrational response builds up during the excitation pulse sequence and persists long after the end of the pulse sequence. Use of a properly timed multiple-pulse excitation sequence permits selective amplification of one lattice vibrational mode and discrimination against the other modes.

The results of a similar experiment on the ferroelectric crystal $LiTaO_3$ are shown in Fig. 2 [21]. In this noncentrosymmetric crystal, the polar lattice vibrational mode is both Raman and infrared active. The coherent oscillating dipole produced by the vibrating ions couples to electromagnetic radiation, and the mode that is excited is a coupled lattice vibrational/electromagnetic mode called a phonon-polariton mode. This coupled excitation, whose wavelength and orientation (i.e. wavevector) are determined by the interference pattern formed by the crossed excitation beams, propagates through the crystal at the speed of far-infrared radiation. The possibility of further amplification of this sort of propagating excitation is discussed herein. In the present case, multiple-pulse excitation permitted lattice vibrational characterization at low temperatures despite photorefractive effects, arising from two-photon absorption, which restricted the peak single-pulse intensity to levels too low to yield reproducible signals in ISRS experiments with just one excitation pulse. Multiple-pulse excitation circumvents sample damage through reduced intensity of any one pulse below the photorefractive damage threshold, and provides amplification of the coherent vibrational response sufficient to yield a detectable signal level [21].

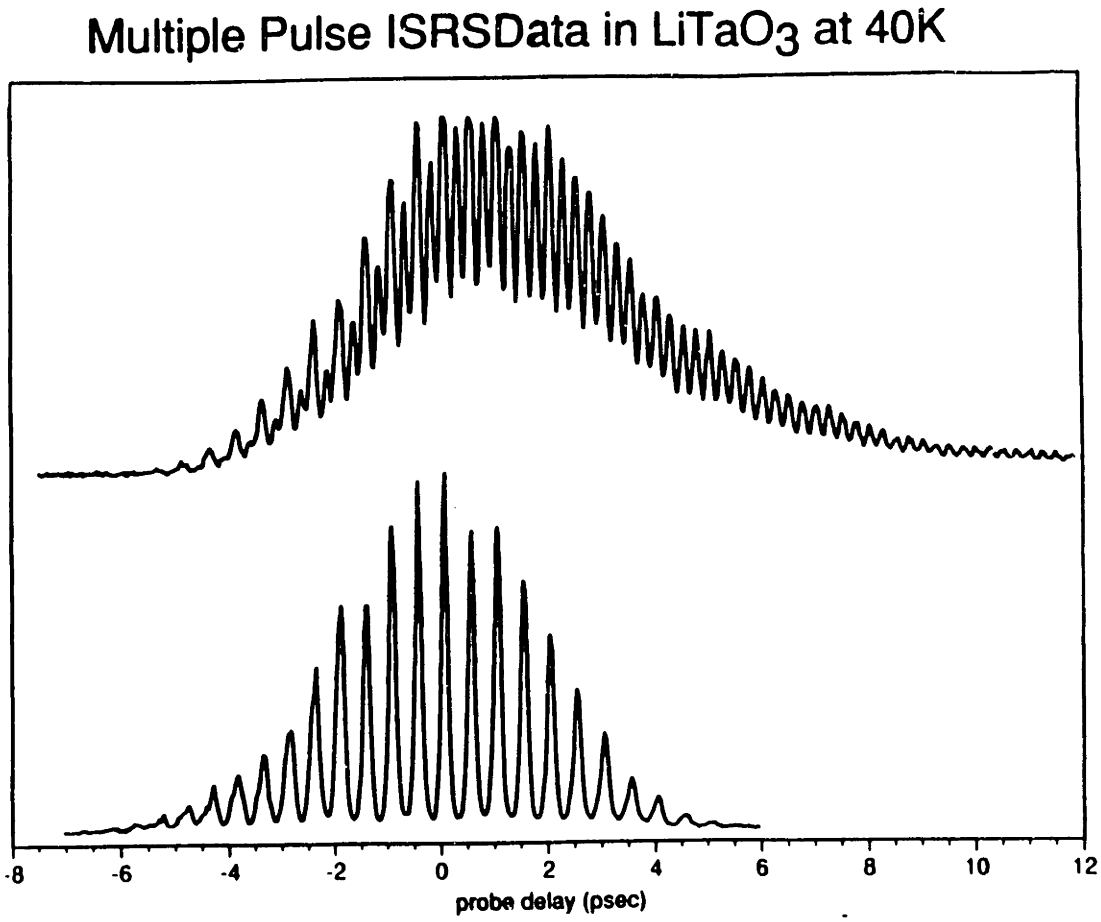

Figure 2: The upper trace shows ISRS data from $LiTaO_3$ at 40K driven by a pulse train whose cross-correlation is shown in the lower trace. The time separation between the pulses is chosen to be 507 fsec to resonantly amplifies the phonon-polariton of 66-cm^{-1} at a wavevector of 2320 cm^{-1}.

Both of these examples illustrate how a tailored excitation waveform can be used to induce a selected material response while suppressing other responses. In solid-state systems, large-amplitude lattice displacements generated by ISRS with shaped waveforms might induce or assist chemical reactions or solid-state rearrangements. Recent suggestions and computational simulations affirm this possibility for ferroelectric domain switching in particular [22-24].

These experiments motivated the continuing efforts toward femtosecond pulse shaping and multiple-pulse femtosecond spectroscopy described in this thesis. Crucial to further progress are technological efforts to generate tailored optical excitation fields in a manner compatible with an automated ultrafast spectroscopy system. Such advances in femtosecond pulse shaping are the subject of chapter 2, and represent a sizable part of this work. We describe the generation of programmable ultrafast optical waveforms which have temporal features as short as the duration of an input femtosecond pulse (typically 70 fsec) and a temporal range of about fifty times this duration, but otherwise can be specified with arbitrary temporal amplitude and temporal phase profiles. This set-up describes the current state of the art in this field. Chapter 3 continues the discussion on femtosecond pulse shaping, providing a theoretical discussion of the spatial effects that necessarily accompany temporal pulse shaping.

In chapter 4 results are described in which phase-related multiple-pulse sequences generated by our pulse shaping apparatus are used to control coherences of a three-level electronic system in potassium vapor in an automated fashion. These results, in conjunction with the non-resonant multiple-pulse experiments on α-perylene and lithium tantalate, foreshadow experiments in which phase-related multiple-pulse sequences

are used to control both electronic and vibrational coherences. In chapter 5, an experiment on crystalline quartz is described which further expands optical control possibilities by demonstrating control over multi-dimensional vibrational motion using multiple excitation pulses with differing polarizations.

Pulse shaping methods can also be expanded to include simultaneous temporal and spatial shaping of optical excitation waveforms. These developments, which are described in chapter 6, indicate new possibilities for manipulation of propagating excitations which can be irradiated by different, independently specified time-dependent waveforms as they move through different regions of a sample.

Finally in chapter 7, in anticipation of the larger amplitude lattice-displacements produced by shaped optical excitation waveforms, the impulse responses for dispersive (polariton) and non-dispersive (optic phonon) lattice modes in an anharmonic potential are calculated. Isolation of the anharmonic contribution to the response by excitation at one wavevector and observation at higher harmonics of that wavevector is analytically described. Characterization of lattice anharmonicities could provide guidance for the generation of interesting effects such as non-linear lattice responses and soliton formation.

CHAPTER 1: REFERENCES

1. D. J. Tannor, S. A. Rice, *Adv. Chem. Phys.* **70**, 441 (1988)
2. D. Neuhauser, H. Rabitz, *Acc. Chem. Res.* **26**, 496 (1993)
3. J. L. Krause, R. M. Whitnell, K. R. Wilson, Y. J. Yan, S. Mukamel, *J. Chem. Phys.* **99**, 6562 (1993)
4. M. Shapiro, P. Brumer, *Int. Rev. Phys. Chem.* **13**, 187 (1994)
5. W. S. Warren, H. Rabitz, M. Dahleh, *Science* **259**, 1581 (1993)
6. C. Chen, Y. Y. Yin, D. S. Elliot, *Phys. Rev. Lett.* **64**, 507 (1990)
7. E. Dupont, P. B. Corkum, H. C. Liu, M. Buchanan, Z. R. Wasilewski, *Phys. Rev. Lett.* **74**, 3596 (1995)
8. J. T. Fourkas, W. L. Wilson, G. Wackerle, A. E. Frost, M. D. Fayer, *J. Opt. Soc. Am. B.* **6**, 1905 (1989)
9. N. F. Scherer, A. J. Ruggiero, M. Du, G. R. Fleming, *J. Chem. Phys.* **93**, 856 (1990)
10. J. L. Herek, A. Materny, A. H. Zewail, *Chem. Phys. Lett.* **15**, 228 (1994)
11. W. Kutt, T. Pfeifer, T. Dekorsy, H. Kurz, pg 418-419 in *Ultrafast Phenomena VIII,* J.-L. Matin, A. Migus, G. A. Mourou, A. H. Zewail, Eds. (Springer-Verlag, Berlin, 1993)
12. P. C. M. Planken, I. Brener, M. C. Nuss, M. S. C. Luo, S. L. Chuang, *Phys. Rev. B.* **48**, 4903 (1993)
13. I. Brener, P. C. M. Planken, M. C. Nuss, L. Pfeiffer, D. E. Leaird, A. M. Weiner, *Appl. Phys. Lett.* **63**, 2213 (1993)
14. P. H. Bucksbaum, D. W. Schumacher, D. Pinkos, J. H. Hoogenraad, J. L. Krause, K. R. Wilson, pg 260-262 in *Ultrafast Phenomena IX,* G. A. Mourou, A. H. Zewail, P. F. Barbara, W. H. Knox, Eds. (Springer-Verlag, Berlin, 1994)
15. J. S. Melinger, S. R. Gandhi, A. Hariharan, D. Goswami, W. S. Warren, *J. Chem. Phys.* **101**, 6439 (1994)
16. B. Kohler, V. V. Vakolev, J. Che, J. L. Krause, K. R. Wilson, *Phys. Rev. Lett.* **74**, 3360 (1995)
17. C. J. Bardeen, Q. Wang, C. V. Shank, *Phys. Rev. Lett.* **75**, 3410 (1995)
18. C. J. Bardeen, J. Che, P. Cong, B. Kohler, M. Messina, K. R. Wilson, V. V. Yakovlev, in preparation.
19. A. M. Weiner, D. E. Leaird, G. P. Wiederrecht, K. A. Nelson, *Science* **247**, 1317 (1990)
20. A. M. Weiner, D. E. Leaird, G. P. Wiederrecht, K. A. Nelson, *J. Opt. Soc. Am. B.* **5**, 1264 (1991)

21. G. P. Wiederrecht, T. P. Dougherty, L. Dhar, K. A. Nelson, D. E. Leaird, A. M. Weiner, *Phys. Rev. B.* **51**, 916 (1995)

22. S. Fahy, R. Merlin *Phys. Rev. Lett.* **73**, 1122 (1994)

23. K. A. Nelson, 'Coherent Control: Optics, Molecules, and Materials', pp.47-49 in *Ultrafast Phemonena IX*, G. A. Mourou, A. H. Zewail, P. F. Barbara, W. H. Knox, Eds. (Springer-Verlag, Berlin, 1994)

24. L. Dhar, B. Burfeint, K. A. Nelson, C. M. Foster, *Ferroelectrics* **164**, 1 (1995)

Chapter 2:
Programmable Femtosecond Pulse Shaping Using Liquid Crystal Spatial Light Modulators

The majority of work in this chapter is published in:

1. M. M. Wefers, K. A. Nelson, Opt. Lett. ***18****, 2032 (1993)*

2. M. M. Wefers, K. A. Nelson, Opt. Lett. ***20****, 1047 (1995)*

3. M. M. Wefers, K. A. Nelson, J. Opt. Soc. Am. B. ***12****, 1343 (1995)*

2.1. INTRODUCTION

Femtosecond optical pulses have produced a revolution in spectroscopy as well as many exciting possibilities in optical communications. Recently there has been growing interest in the generation of shaped femtosecond waveforms for a variety of applications. As described in the previous chapter, there is a substantial amount of literature on the application of ultrafast optical to 'mode selective chemistry', which expands the context of spectroscopy to emphasize detailed optical control over chemical events [1-8]. Applications to high speed optical communication [9], all-optical switching [10], and soliton propagation in fibers [11] have also been demonstrated. Clearly the ability to synthesize specified optical waveforms offers considerable possibilities throughout the field of ultrafast optics.

Though some pulse shaping techniques have been developed that modulate waveforms directly in the time domain [12,13], and some emerging techniques involving holography have been reported [14-16], the majority of femtosecond pulse shaping efforts have involved the linear

filtering of spatially dispersed frequency components [17-20] as pioneered by Weiner, Heritage, and co- workers at Bellcore. Typically, optical frequency components are spatially dispersed within a simple lens and grating apparatus (figure 1). The dispersed frequency components are focused onto a spatially varying 'mask'. The mask attenuates (or retards) some components and allows other components to pass unaffected. The filtered frequency components are recombined, producing the shaped wave form. The mask patterns were originally etched onto glass substrates using microlithography techniques [20]. This provides excellent spatial resolution, but since the patterns are permanently etched there is no possibility for flexible, on-the-spot generation of new waveforms. A major advance was the use of a liquid crystal (LC) spatial light modulator (SLM) as a mask [21,22] as demonstrated by Weiner and co-workers. The pixels of the LC SLM can be individually addressed, so the mask becomes programmable and can be used to iteratively improved a specified waveform or can be changed to produce a new waveform. The liquid crystal mask demonstrated originally was used to variably retard the dispersed frequency components, i.e. as a 'phase' mask. This was used to generate waveforms with linear, quadratic, and cubic spectral phase sweeps as well as a temporal odd pulse and various types of pulse trains [21,22].

We have reported the use of two liquid crystal SLMs to manipulate both spectral phase and amplitude using only commercial components [23,24]. Subject to the available bandwidth of the input pulse and the spatial resolution of the mask, this allows for the production of arbitrarily shaped temporal wave forms. Waveforms as long as 2.9 psec with features as short as 70 fsec, including a variety of pulse trains with specified intensity and/or phase profiles, could be generated. Numerical algorithms

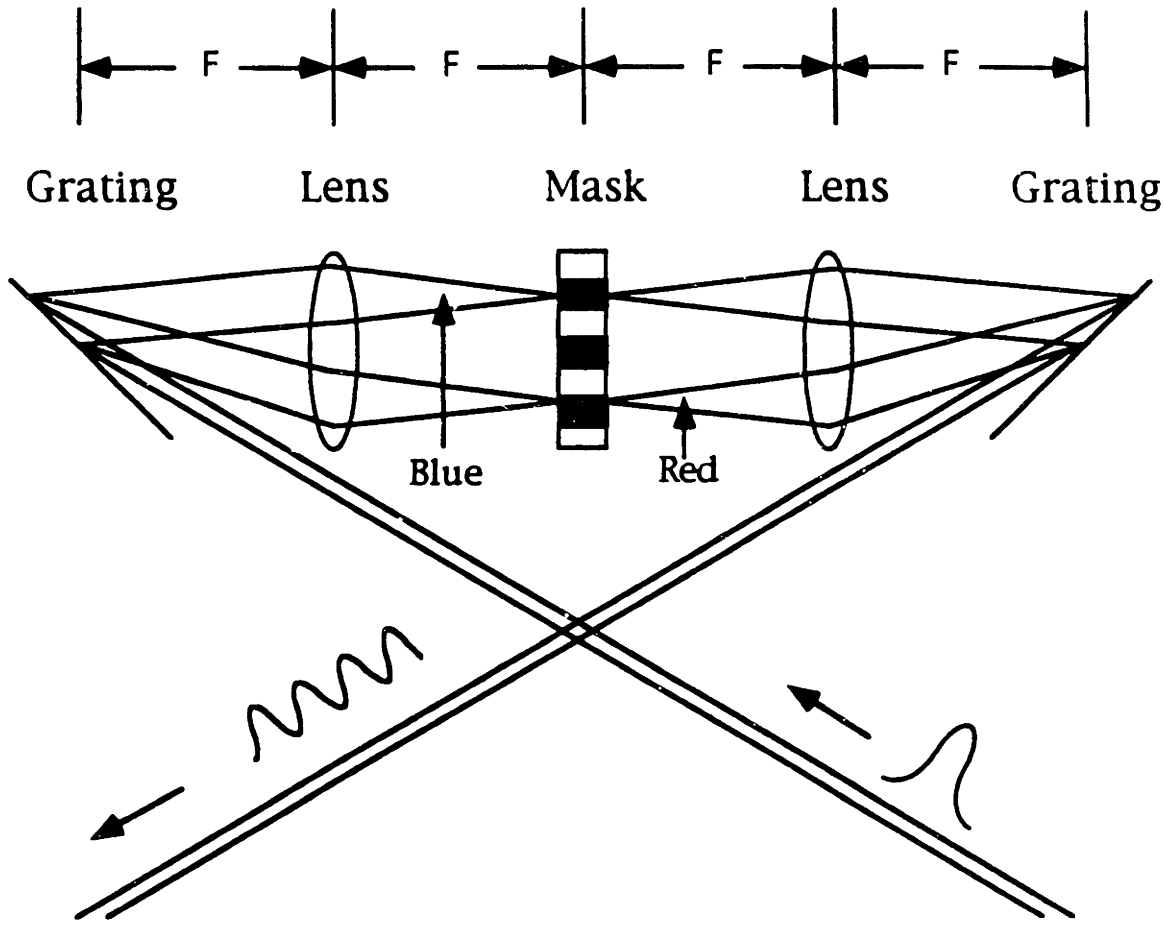

Figure 1. The '4f' pulse shaping apparatus. A grating angularly disperses an ultrashort pulse, and a lens collimates and focuses the laterally dispersed frequency components onto different regions of a spatially varying mask. The mask attenuates or retards selected frequency components. A subsequent lens and grating recombine the spectrally filtered light, producing a shaped waveform in the time domain.

were written to take into account the specific characteristics and limitations of the optical system, so that the user need only specify the desired waveform and not the detailed mask pattern. Recently we have improved the fidelity of waveforms requiring two LC SLMs by increasing the number of pixels and reducing the size of inter-pixel gaps in the individual LC SLMs and by combining two improved masks into a single device with improved alignment [25]. With these improvements waveforms such as phase-related multiple-pulse sequences have been used to demonstrate automated multi-dimensional optical spectroscopy [26] which is discussed in chapter 4. Examples of shaped femtosecond waveforms produced by these methods are shown in figure 2.

The possibility of using a programmable acousto-optic modulator (AOM) in place of the LC SLM has also been reported [27]. In principle such a device can produce a continuous mask filter without inter-pixel gaps. A single AOM device should enable manipulation of both spectral amplitude and phase.

In this chapter, femtosecond pulse shaping with liquid crystal spatial light modulators is reviewed. In the sections 2 through 6, theoretical considerations are addressed. We rigorously analyze the pulse shaping operations including the effects of the gaps between adjacent pixels of the LC SLM, the discrete nature of the mask, and diffraction off one or two masks. The emphasis is to set up a formalism that clearly describes the experimental impact of different pulse shaping set-ups. Since two LC masks are required to manipulate both spectral amplitude and phase, a particular concern is whether the two masks should be used within a single telescope (4-f arrangement) or whether the frequency components should

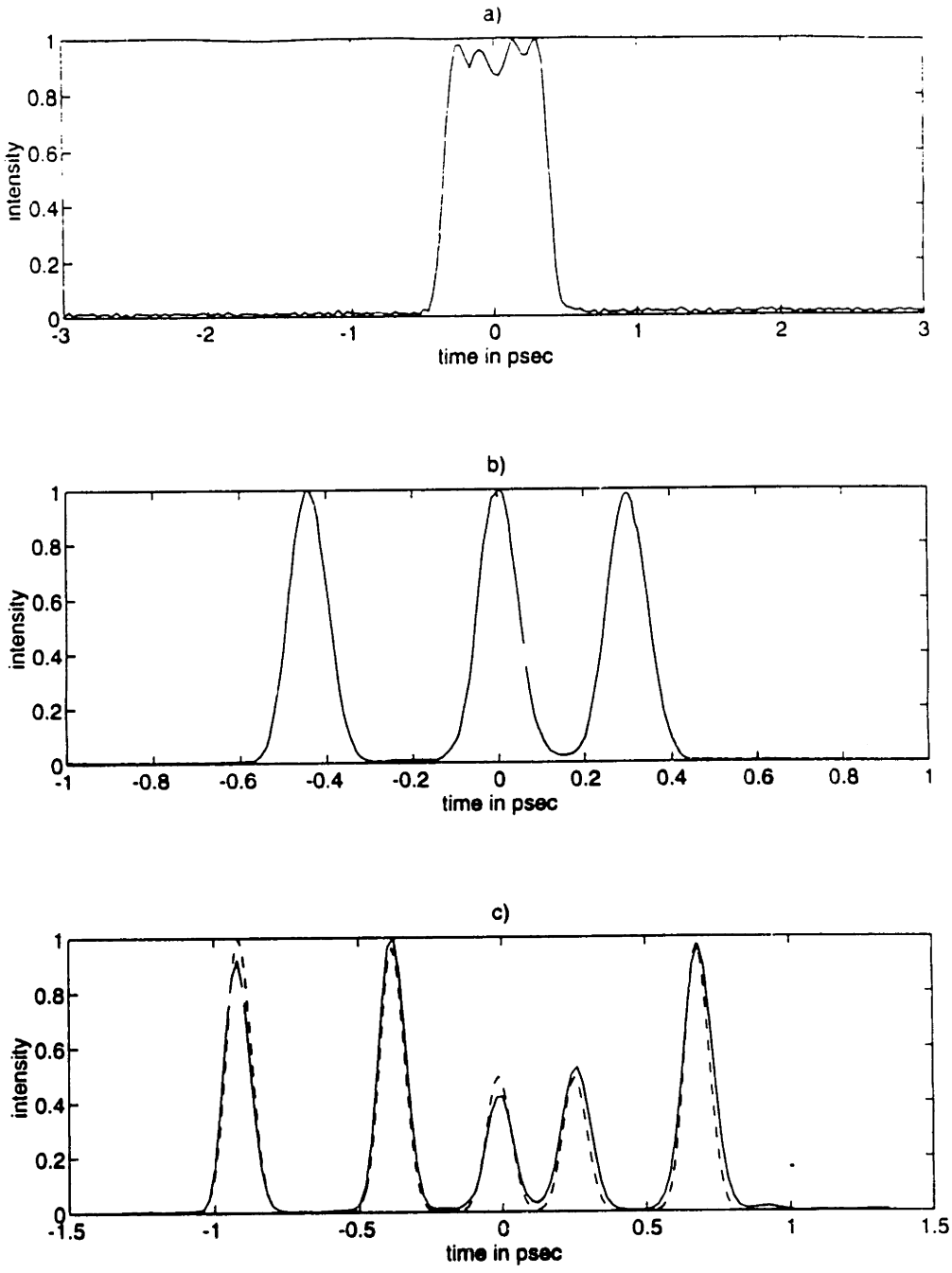

Figure 2. Examples of shaped ultrafast waveforms generated from a 70-fsec input pulse with our improved pulse shaping apparatus and measured by cross-correlation with an unshaped reference pulse. (A) 800-fsec optical square pulse. Structure on the top of the square pulse follows from the limited bandwidth of the input pulse. (B) Phase-related equal-amplitude three pulse sequence. (C) Phase-related five pulse sequence. The desired waveform for (C) is given by the dashed curve. In all cases manipulation of both spectral amplitude and spectral phase is required to produce the desired waveforms.

be dispersed and filtered twice within two telescopes (8-f arrangement) as in figure 3. Our goal is to evaluate effects that limit the fidelity of the shaped waveform, and to determine methods that optimally compensate for these effects in such a way that a user need only specify a desired temporal waveform and not formulate detailed mask patterns. In sections 7 through 11, practical considerations are addressed and our results with various experimental arrangements are illustrated. These results indicate that versatile generation of high-fidelity waveforms is now possible enabling new spectroscopic applications.

In section 2, the filters produced by a series of one or two LC masks and polarization optics in various arrangements are presented. It will be shown how two LC filters can be combined to provide independent control over optical retardation and attenuation.

In section 3, the temporal response resulting from a discrete filter within the grating and lens apparatus is derived. It is shown that the temporal resolution of the shaped waveform is limited by the bandwidth available in the input pulse and that the spatial resolution of the mask limits the temporal range of the shaped waveform. Furthermore the discreteness of the masks produces replica waveforms outside this temporal range. All of these results were previously reported by the Bellcore researchers [20,22]. However, we also explicitly include the contribution from inter-pixel gaps and perform the derivation in a discrete formalism. The gap contribution reproduces the input pulse at zero time with an amplitude proportional to the gap size. This feature can interfere with time-coincident parts of the desired waveform, leading to significant waveform distortion. The discrete formalism describes the output waveform in terms

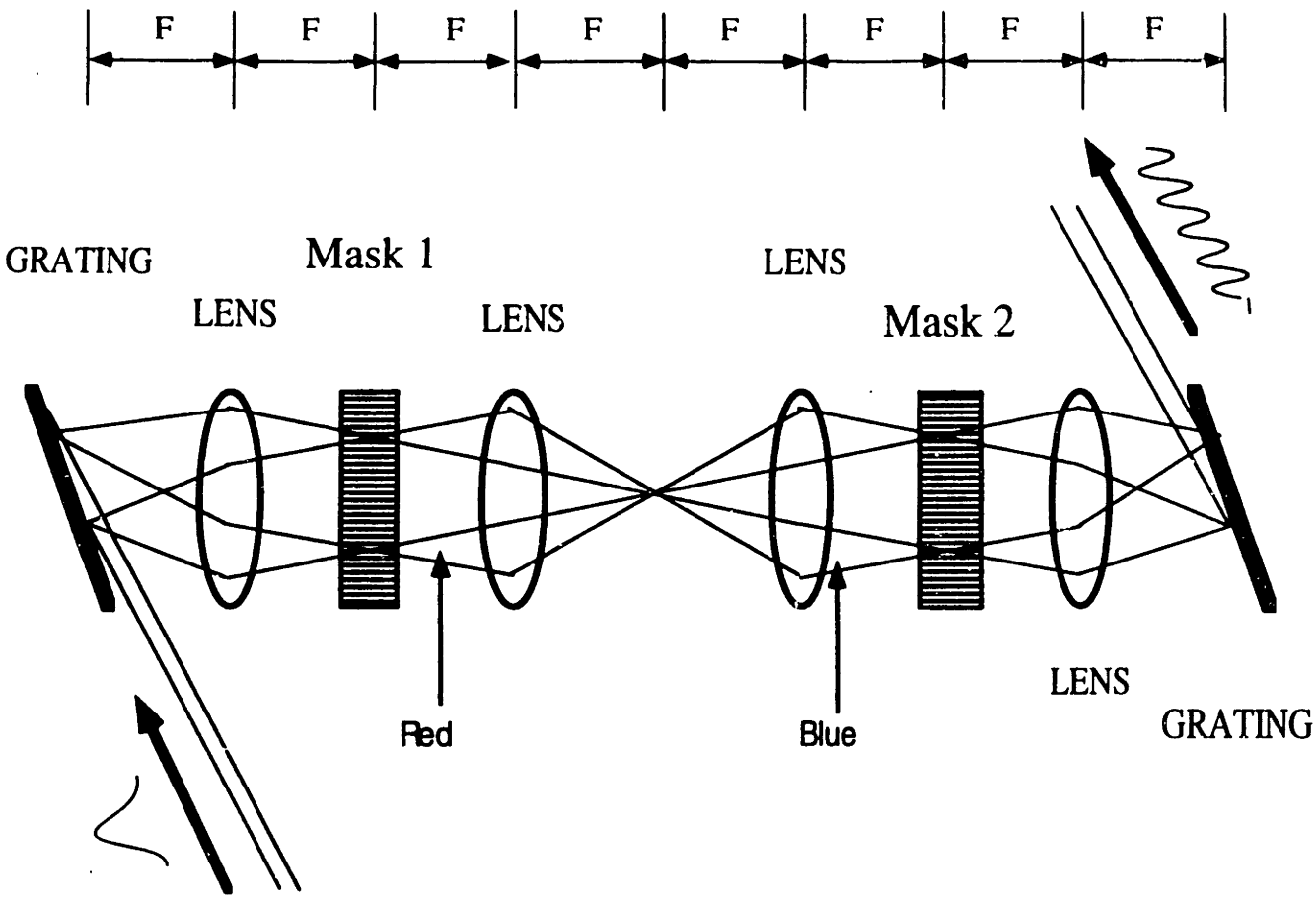

Figure 3. The '8f' pulse shaping apparatus. In this case two 1:1 telescopes are placed between parallel gratings so that angularly dispersed frequency components are focused and filtered twice.

of the spectral filters of the individual pixels, and can be easily extended to the modeling of waveforms generated using two masks. The discrete formalism is also employed in section 6 in determination of the appropriate mask patterns for user-specified waveforms. In section 3 we also reproduce an earlier calculation [31] by the Bellcore researchers which solves for the gaussian spatial mode of the output waveform after spectral filtering by a single mask. The mask pattern diffracts the input pulse into different spatial modes, each with a different temporal profile. It is assumed that an aperture will retain only the gaussian spatial mode of the output beam. In this case the output waveform includes a broad gaussian temporal modulation that helps to remove the replica features produced by discrete Fourier sampling.

In section 4 an expression for the space-time profile of a waveform shaped through filtering of spatially separated frequency components is derived. One fascinating result is that the output waveform shaped by a single mask undergoes a time-dependent transverse spatial shift (25,28). Rather than shaping the waveform along its propagation axis (**z**-axis), it is shaped along an axis in the **x**-**z** plane. The slope of this time dependent shift depends inversely on the angular dispersion produced by the grating. This result is valid even for continuous masks without gaps and therefore applies to pulse shaping with acousto-optic modulators (AOMs) as well as LC SLMs. If the is mask displaced from the focal plane of the lens pair, the output waveform acquires a small divergence that also depends linearly on time. This effect is explored more generally in chapter 4.

In section 5, the space-time profiles for waveforms shaped by two masks in a 4-f or 8-f arrangement are presented using the methods of section 4. These results describe the cases in which the combined spectral

filter for the two masks can be approximated by the product of the individual masks. Under this assumption, two LC SLMs can be considered as a single mask capable of independently filtering both amplitude and phase. It is shown that for an optimally aligned 8-f arrangement the combined spectral filter is given exactly by the product of the two individual LC SLMs. In general the separation of two masks and their displacement from the focal plane(s) of the lens pair(s) produce variations in spectral path length as light is diffracted by the individual masks. This modifies the effective spectral filter produced by the pair of LC SLMs. It is shown that for the temporal profile of the gaussian spatial mode of a waveform shaped by a pair of LC SLMs which filter orthogonal light polarizations these effects can be eliminated. The temporal profiles for the gaussian spatial mode of the output waveform for 4-f and 8-f arrangements are also presented.

In section 6, a practical method is presented to determine the appropriate mask patterns for user-specified waveforms. Simulations illustrate that for most circumstances one can consider two LC SLMs as equivalent to a single mask capable of an arbitrary spectral filter. Under such circumstances it is shown that one can easily generate user-specified waveforms. Alternatively an iterative algorithm is presented that can determine appropriate mask patterns for spatially separated masks even with significant misalignment (such as lack of pixel registration).

In section 7, we review our initial experimental results using one LC SLM in a 4-f set-up for phase-only filtering and two LC SLMs in an 8-f set-up for the first demonstration of programmable phase and amplitude filtering [23]. In section 8, the generation of high-fidelity programmable waveforms with an improved pulse shaping set-up is described. This set-up

provides the current state of the art for ultrafast optical pulse shaping. In section 9 it is shown that pulse shaping using LC SLMs can be used to generate waveforms with shaped time-dependent polarization profiles. In section 10, we briefly describe amplification of these shaped waveforms in a regenerative amplifier. Finally, in section 11 we discuss characterization of shaped waveforms and prospects for their iterative improvement.

Throughout the chapter the following mathematical conventions will be used. Fourier transform pairs and discrete Fourier transform pairs (for a sequence of length N) will be described respectively as follows:

$$F(k,\omega) = (2\pi)^{-1} \iint f(x,t) e^{i(kx-\omega t)} dx dt \tag{1}$$

$$f(x,t) = (2\pi)^{-1} \iint F(k,\omega) e^{-i(kx-\omega t)} dk d\omega \tag{2}$$

$$A_n = \frac{1}{\sqrt{N}} \sum_{j=0}^{N-1} B_j \exp(i2\pi jn/N) \quad \Leftrightarrow \quad B_j = \frac{1}{\sqrt{N}} \sum_{n=0}^{N-1} A_n \exp(-i2\pi jn/N) \tag{3}$$

where $F(k,\omega)$ is the Fourier transform of $f(x,t)$ and A_n is the discrete Fourier transform of B_n. Convolution of two functions $f(x)$ and $g(x)$ to give $h(x)$ will be defined as:

$$h(x) = f(x) \otimes g(x) = \int_{-\infty}^{\infty} dx' f(x - x') g(x') \tag{4}$$

The **z**-axis will be the propagation direction for the beam. The **x**-axis will define the orientation of the mask pattern and the direction along which the

optical frequency components are dispersed by the gratings. The y-axis will be along the height of the individual pixels of the mask. The temporal profile e(t) of waveforms will be described independent of their optical carrier frequency ϖ. so for example the unshaped pulse $e_{in}(x,t)$ entering the pulse shaping apparatus will be described as:

$$e_{in}(x,t) = f(x)e_{in}(t)\exp(i\varpi t) \qquad (5)$$

where $e_{in}(t)$ is the temporal envelope and f(x) is the spatial profile.

2.2. LIQUID CRYSTAL FILTER

The LC SLM consists of a thin (5-20 μm) nematic liquid crystal layer sandwiched between two silica substrates. The two substrates are coated with indium tin oxide (ITO) which is optically transparent but electrically conductive. One substrate acts as a ground plate while the second is patterned with a linear array of N evenly spaced, equal sized electrodes which define the pixels of the SLM. The LCs are rod-like molecules that have a variable birefringence. They tend to align themselves with an applied electric field, so that their birefringence is voltage dependent and can be controlled independently at each pixel. The regions of LC between the patterned electrodes cannot be controlled and are referred to as 'gaps'. In these 'gap' regions the LCs behave, ignoring fringing fields, as though there is zero applied voltage so that the filter for the gap regions is assumed to be constant across the array.

We will define the axis along the SLM array as the x-axis, the axis across the LC thickness will be the z-axis (light propagation direction), and the axis along the individual pixels will be the y-axis. The LC SLM can be

fabricated with the long axes of the LCs aligned along any axis in the **x-y** plane. This LC alignment axis will be defined as the **c**-axis. As a voltage is applied across the individual pixels the LCs tilt from the **c**-axis toward the **z**-axis in the **c-z** plane. For light propagating along the **z**-axis this produces a variable index of refraction for the polarization component along the **c**-axis and a constant index of refraction for the polarization component orthogonal to the **c**-axis. The difference in retardance $\Delta\phi$ for these orthogonal polarizations is given by:

$$\Delta\phi = \omega\Delta n(V)l/c \tag{6}$$

where $\Delta n(V)$ is the voltage-dependent birefringence, V is the applied voltage, ω is the angular frequency of the light, c is the speed of light in a vacuum, and l is the LC layer thickness.

For light polarized along the **c**-axis, the LC SLM acts as a variable phase retarder or 'phase' mask, producing a filter B_n for pixel 'n' given by:

$$B_n = \exp\left(i\Delta\phi(V_n)\right) \quad \text{(phase mask)} \tag{7}$$

Typically LC SLMs used as phase masks have the LCs aligned (at zero applied voltage) along the **y**-axis (**c=y**). Weiner and co-workers at Bellcore showed that if instead the LCs are aligned along the **x**-axis (which is along the array), then the LCs near the pixel edges are affected by adjacent fields and are not properly controlled [22].

If the alignment of the LCs (**c**-axis) is at 45 degrees from the polarization of the incident light, then the LC filter is a polarization

rotater. For incoming light polarized along the **x**-axis and the **c**-axis given by **x+y**, the filter for pixel 'n' is given by:

$$B_n = \exp\left(i\,\Delta\phi(V_n)/2\right)\left[\hat{\mathbf{x}}\cos\left(\Delta\phi(V_n)/2\right) + i\hat{\mathbf{y}}\sin\left(\Delta\phi(V_n)/2\right)\right] \quad (8)$$

If a polarizer that is crossed (**y**-axis) or parallel (**x**-axis) to the incident polarization is placed after the LC SLM, the resultant filter can attenuate incident light producing an 'amplitude' mask. So for crossed polarizers, the filter for pixel 'n' is:

$$B_n = \exp\left(i\Delta\phi(V_n)\right)\exp\left(i\,\Delta\phi(V_n)/2\right)\sin\left(\Delta\phi(V_n)/2\right) \text{ (amplitude mask)} \quad (9)$$

Equation 9 shows that an amplitude mask also imparts an attenuation-dependent phase retardance. Weiner and co-workers showed that by configuring a single LC SLM as an amplitude mask, measurement of the voltage-dependent attenuation allows one to calibrate a given LC SLM and determine $\Delta\phi(V)$.

To produce a filter capable of independent control of retardance and attenuation, two LC SLMs are required. In our original demonstration [], two LC SLMs with LCs aligned along the **y**-axis were used and each was placed within a separate telescope in an 8-f lens and grating pulse shaping apparatus (figure 3). The highly dispersive gratings preferentially diffracted **x**-polarized light, so half-waveplates and polarizers were used to configure the first LC SLM as a 'phase' mask and the second LC SLM as an 'amplitude' mask, producing an arbitrary spectral filter. Note that the

phase mask needs to correct for the retardance imparted by the amplitude mask.

For two LC SLMs combined into a single device and placed in a '4-f' arrangement there is no room for intermediate polarization optics between the two masks. This practical problem arises since each mask should be as close as possible to the (single) focal plane and because sandwiching of a polarizer between two masks in a single structure could result in considerable heating and phase distortion due to absorption of light of the unwanted polarization. To produce an arbitrary filter in this case, the alignment of the LCs in the two masks could differ by 45 degrees. The first mask would have LCs aligned along the **y**-axis, again acting like a phase mask, while the second mask would have LCs aligned at 45 degrees from the **y**-axis so that when followed by a polarizer along the **x**-axis, it acts like an amplitude mask. For this arrangement the incident light must be **y**-polarized.

The filter for both of these '4-f' and '8-f' set-ups would be given by:

$$B_n = \exp\left(i\Delta\phi^{(1)}\right)\exp\left(i\,\Delta\phi^{(2)}/2\right)\sin\left(\Delta\phi^{(2)}/2\right) \qquad (10)$$

where the superscripts denote the first or second mask and the pixel-dependent voltage for the retardances $\Delta\phi^{(i)}\left(V_n^{(i)}\right)$ has been implicitly included.

Alternatively, an arbitrary filter could be produced by combining two LC SLMs whose LCs differ in alignment by 90 degrees. This would produce independent retardances for orthogonal polarizations. If the LCs for the two masks were respectively aligned at -45 degrees and +45 degrees

from the x-axis, the incident light were polarized along the x-axis, and the two LC SLMs were followed by a polarizer aligned along the x-axis, the filter in this case for pixel 'n' is given by:

$$B_n = \exp\left(i\left(\Delta\phi^{(1)} + \Delta\phi^{(2)}\right)/2\right)\cos\left(\left(\Delta\phi^{(1)} - \Delta\phi^{(2)}\right)/2\right) \quad (11)$$

where the dependence on the voltage for pixel 'n' is again implicitly included. In this case neither mask acts alone as a phase or amplitude mask, but the two in combination are capable of independent attenuation and retardance. Furthermore, since the respective LC SLMs act on orthogonal polarizations, light filtered by one mask is unaffected by the second mask. In section 5 we show that this eliminates multiple-diffraction effects of the two masks.

2.3. TEMPORAL RESPONSE FROM PULSE SHAPING

2.3.1 Grating and lens apparatus

To filter dispersed frequency components using spatially varying masks, one needs to image the focused spectrum of the ultrashort pulse onto the masks. For a single mask, this is most easily accomplished by a pair of gratings and lenses configured in a '4f' arrangement where f is the focal length (shown in figure 1). This set-up has been studied in detail by Martinez as a way to produce positive group velocity dispersion (GVD) (29-30). The first grating angularly disperses the frequency components of the ultrashort incident pulse. The grating is placed in the back focal plane of a subsequent lens, so that the lens collimates the spatially separated frequency components and focuses the individual frequency components onto the spatially varying mask placed in the front focal plane of the lens.

The mask is in the back focal plane of a second lens (so that the lens pair form a telescope around the mask) which collimates the individual frequency components and bends them toward a second antiparallel grating which is in the front focal plane of the second lens. The second lens and grating thus recombine the spectrally filtered pulse yielding a 'shaped' pulse in the time domain.

A second mask can either be placed immediately behind the first mask or in the focal plane of a second lens pair. In the latter case the two gratings and four lenses form an '8f' arrangement as shown in figure 3. In the former case, the second mask is displaced from the focal plane of the telescope and so the spectrum it filters is not perfectly in focus. We will study the impact of this in section 5. In the latter case the spectrum is imaged and filtered twice and the gratings are placed parallel rather than anti-parallel.

For a mask consisting of a linear array of evenly spaced pixels it is important that each pixel sample a frequency range of the same magnitude so that linear sampling is maintained. First order diffraction off a grating is given by:

$$\lambda = d(\sin\theta_i + \sin\theta_d) \tag{12}$$

where λ is wavelength, d is the spacing between grating lines, and θ_i and θ_d are angles of incidence and diffraction respectively. The first lens directs the diffracted frequency components from the first grating along parallel paths toward the first mask. The lateral displacement x of a given wavelength component λ from the center wavelength component λ_0 immediately after the lens is given by:

$$x = f \times \tan[\theta_d(\lambda) - \theta_d(\lambda_0)] \tag{13}$$

Expanding x as a power series in angular frequency ω gives:

$$x = f\left[\left.\frac{\partial\theta_d}{\partial\omega}\right|_{\omega=\varpi}(\omega-\varpi) + \frac{1}{2}\left.\frac{\partial^2\theta_d}{\partial\omega^2}\right|_{\omega=\varpi}(\omega-\varpi)^2 + \ldots\right] \tag{14}$$

where

$$\left.\frac{\partial\theta_d}{\partial\omega}\right|_{\omega=\varpi} = \frac{-2\pi c}{\varpi^2 d\cos\theta_d(\varpi)}, \tag{15}$$

c is the speed of light, and ϖ is the central carrier frequency of the input pulse.

Usually the expansion is terminated after the linear term, so that the frequency components are laterally dispersed linearly across the masks. However for very broad bandwidth pulses, this assumption may break down. Subtle second-order dispersion effects have noticed experimentally by Weiner and co-workers [20]. In general the ratio of the second order term to the first order term is:

$$\frac{\text{2nd Order Term}}{\text{1st Order Term}} = -\frac{(\omega-\varpi)}{\varpi}\left[1 + \frac{\lambda\tan\theta_d}{2d\cos\theta_d}\right] \tag{16}$$

For a central wavelength at 800 nm, with the mask accommodating the spectrum of a 60 fs pulse, the second order term is about 5 percent of the first order term at the edges of the mask. For pulse durations of less than 20 fsec it may be necessary to design the mask such that its pixels become

physically smaller near its edges so to account for the quadratic term of the angular dispersion from the grating. For the remainder of this analysis we will assume that the frequency components are linearly dispersed across the mask, according to:

$$x(\omega) = \frac{-2\pi cf}{\varpi^2 d \cos\theta_d(\varpi)}(\omega - \varpi) \equiv \alpha(\omega - \varpi) \tag{17}$$

Equation 17 describes the transverse position of the spatial center of frequency component ω. For the '4f' and '8f' arrangements, these central positions remain constant throughout each telescope. However the spatial profile of each individual frequency component is focused by the first lens onto the mask and then recollimated by the second lens so that the spatial width of each component changes within each telescope.

Note that for a properly aligned set up, there is no path length variation (no group velocity dispersion (GVD)) for the different frequency components since the refraction in the achromatic lenses compensates for the path length variation arising from the angular dispersion. Therefore in the absence of a mask, a pulse will emerge unaltered by the apparatus. However, positive and negative GVD can be introduced by moving the last grating away from the front focal plane of the last lens. It is clear from ray optics that this will introduce a quadratic variation in optical path length $P(\omega)$ which is equivalent to GVD:

$$P(\omega) = P(\varpi)\left[1 - a(\omega - \varpi)^2\right] \tag{18}$$

where

$$a = \frac{1}{2}\left(\left.\frac{\partial\theta_d}{\partial\omega}\right|_{\omega=\varpi}\right)^2 = \frac{2\pi^2 c^2}{\varpi^4 d^2 \cos^2\theta_d(\varpi)} \qquad (19)$$

This can be used to compensate for GVD arising from different optical elements including the liquid crystal mask which are contained in the grating and lens set-up. This strategy is used routinely in ultrafast optics for GVD compensation and pulse compression [29-30].

2.3.2 Fourier transform of the mask pattern and the 'shaped' waveform

Ignoring spatial (diffraction) effects, the mask pattern m(x) filters the dispersed input spectrum $E_{in}(\Omega)$ as follows:

$$E_{out}(x,\omega) = g(x)E_{in}(\Omega)m(\alpha\Omega) \qquad (20)$$

where $E_{in}(\omega)$ is the fourier transform of $e_{in}(t)$, g(x) is the spatial profile of the input pulse, and $\Omega = \omega - \varpi$. The mask can manipulate the amplitude profile of $E_{in}(\Omega)$ through attenuation and the phase profile of $E_{in}(\Omega)$ through retardation (varying optical path length) of selected frequency components. The mask filter cannot introduce any new frequency components, so temporal features in the shaped waveform are limited by the bandwidth available in the input pulse. Unless one is willing to throw away energy from the center of the pulse spectrum, this implies that the features of the shaped waveform cannot be shorter than the bandwidth limited input pulse. It is assumed that the lateral dispersion of the lenses and gratings is such that the mask can accommodate the entire bandwidth of the input pulse. The shaped waveform in the time domain is given (ignoring spatial effects) by the inverse fourier transform of equation 9, whose envelope is given by the convolution of the input pulse envelope

$e_{in}(t)$ with the inverse fourier transform of $m(\alpha\Omega)$ Even taking into account spatial effects, it is clear that the fourier transform of the mask pattern will be directly related to the shaped waveform.

The mask filter m(x) is given by:

$$m(x) = \partial(x - x_0) \otimes \sum_{n=-N/2}^{N/2-1} \left[\begin{array}{l} \left(B_n \partial(x - nw)\right) \otimes \mathrm{squ}\left(\frac{x}{rw}\right) \quad + \\ \left(B_g \partial(x - (n+1/2)w)\right) \otimes \mathrm{squ}\left(\frac{x}{(1-r)w}\right) \end{array} \right] \tag{21}$$

where w is the distance between the centers of pixels (which includes the gap spacing), x_0 is the displacement of the center of the middle pixel (n=0) of the mask from the $\omega = \varpi$ central frequency component, r is the pixel width divided by the pixel width plus gap width, N is the total number of pixels on the mask, B_n is the filter for pixel n, B_g is the filter for the gaps, and $\partial(x)$ denotes the Dirac delta function. Note that B_i are necessarily less than or equal to one. The square function squ(x) is defined as:

$$\mathrm{squ}(x) = \left\{1 \text{ for } |x| \le \tfrac{1}{2}, \quad 0 \text{ for } |x| > \tfrac{1}{2}\right\} \tag{22}$$

To simplify the calculation of M(k), the fourier transform of m(x), we assume that the pattern defined by the N pixels of the SLM repeats infinitely for $x \to \pm\infty$. Though the mask has a finite width, this simplification is justified if the dispersed frequency spectrum fits on the actual width of the array. This is because there will be no contributions to the shaped waveform from regions of the masks on which no frequency

components are incident. Even if the spectrum of the input pulse does not completely fit on the mask, the equations still obtain as long a spectrally windowed input pulse is substituted for the original input pulse.

With this assumption, M(k) is given by the fourier transform of a modified equation 10 in which the sum is extended to $\pm\infty$ and the N length pattern for B_n is repeated infinitely. The result is

$$M(k) = \exp(ikx_0)\left[\begin{array}{l} \dfrac{\sin(rkw)}{\pi k}\left(\sum_{n=-\infty}^{\infty} A_{rem(n,N)}\,\partial\left(k - n\dfrac{2\pi}{Nw}\right)\right) + \\ B_g\,\dfrac{\sin[(1-r)kw]}{\pi k}\left(\sum_{n=-\infty}^{\infty}(-1)^n\,\partial\left(k - n\dfrac{2\pi}{w}\right)\right) \end{array}\right] \qquad (23)$$

where rem(n,N) gives the remainder of n/N and A_n is the discrete fourier transform of the N length sequence B_j.

Each dispersed frequency component incident on the mask has a finite spot size associated with it. This 'blurs' the discrete features of the mask and gives rise to diffraction. To exploit the spatial resolution of the mask, the incident frequency components should be focused to a spot size comparable to or less than the pixel width. If the spot size is too small, replica waveforms arising from discrete fourier sampling will be unavoidable. If the spot size is too big the 'blurring' of the mask will give rise to substantial diffraction effects.

To study this effect we reproduce a derivation by Thurston and co-workers at Bellcore [31], in which the shaped waveform is expanded into transverse gaussian-hermite spatial modes. The assumptions in this derivation are that the spatial profile of the input pulse is gaussian, that the mask is exactly in the focal plane of the lens pair, and (most importantly)

that only the gaussian transverse spatial mode of the shaped waveform is retained. Light that is diffracted off the mask into higher order spatial modes is assumed to be removed by the spatial filtering of a subsequent aperture. We will drop this assumption and study more carefully the light diffracted out of the gaussian spatial mode in section 4.

The amplitude $A(\omega, x, y)$ of the field as a function of angular frequency and position in the masking plane can be expressed as:

$$A(\omega, x, y) = E_{in}(\Omega) m(x) u_{00}(x - \alpha\Omega, y) \tag{24}$$

where $u_{00}(x, y)$ is the spatial profile of a transverse spatial gaussian mode with spot size w_0 in the focal plane of the lens pair:

$$u_{00}(x, y) = \left(2/\pi w_0^2\right)^{\frac{1}{2}} \exp\left(-\left(x^2 + y^2\right)/w_0^2\right) \tag{25}$$

$A(\omega, x, y)$ is now expanded in transverse hermite-gaussian modes $u_{mn}(x, y)$.

$$A(\omega, x, y) = \sum_{m,n} A_{mn}(\omega) u_{mn}(x - \alpha\Omega, y) \tag{26}$$

If only the gaussian spatial mode is retained after the mask, the spectral content of the shaped waveform will be given by $A_{00}(\omega)$. Solving for $A_{00}(\omega)$ using the orthogonality of the gaussian-hermite modes gives:

$$A_{00}(\omega) = \left(2/\pi w_0^2\right)^{\frac{1}{2}} E(\Omega) \int_{-\infty}^{\infty} m(x) \exp\left(-2(x - \alpha\Omega)^2/w_0^2\right) dx \tag{27}$$

The inverse fourier transform of $A_{00}(\omega)$ thus gives the temporal profile of the shaped output waveform:

$$e_{out}(x,y,t) = u_{00}(x,y)\exp(i\varpi t)\left[e_{in}(t) \otimes \left(M(-t/\alpha) \times g(t)\right)\right] \quad (28)$$

where M(k) is given by equation 23 and g(t) is defined as:

$$g(t) = \exp\left(-w_0^2 t^2 / 8\alpha^2\right) \quad (29)$$

Thus the effective temporal response of the mask filter, taking into account diffraction, involves a gaussian envelope that further modulates equation 23.

Combining the results of equations 23, 28 and 29 gives the following result for the profile of the temporal profile of the gaussian spatial mode $e_{out}^{00}(t)$ of the shaped waveform:

$$e_{out}^{00}(t) = \sum_{-\infty}^{\infty} C_n e_{in}(t + \tau n) \quad (30)$$

where

$$C_n = \frac{N}{\pi n}\exp\left(i\frac{2\pi x_0 n}{Nw}\right)\exp\left[-\left(\frac{\pi w_0 n}{Nw}\right)^2 / 2\right]$$
$$\times\left\{A_{rem(n,N)}\sin\left(\frac{r\pi n}{N}\right) + \partial_{0,rem(n,N)}B_g(-1)^{n/N}\sin\left(\frac{(1-r)\pi n}{N}\right)\right\} \quad (31)$$

$\tau = 2\pi\alpha/Nw$, and ∂_{nk} is the Kroenecker delta function.

The spectral bandwidth of the incident pulse is assumed to fit on the mask, so τ is necessarily smaller than the incident pulse width of the input light. The shaped waveform is thus given by the superposition of evenly spaced input pulses with varying complex amplitudes. This formalism easily lends itself to computation (especially for the case of two masks) since the coefficients C_n are determined discretely and they (along with the input pulse) completely determine the shaped waveform.

2.3.3 Features of the shaped waveform

2.3.3 a. Single ideal mask

The implications of the derivation in the previous section will now be described. It is instructive to begin with the ideal case in which we have a single mask with negligible gaps (r=1) which is aligned with the center of the dispersed frequency spectrum (x_0=0). For this case we have:

$$C_n = A_{rem(n,N)} \frac{\sin(\pi n/N)}{(\pi n/N)} \exp\left(-\left(\frac{\pi w_0 n}{wN}\right)^2 \Big/ 2\right) \qquad (32)$$

Because τ is smaller than the input pulse width, adjacent pulses in equation 30 can interfere, and so equation 30 can describe an arbitrary temporal waveform as long as its temporal features are no shorter than the input pulse. However only the middle N coefficients of C_n are uniquely specified by the mask pattern, so the shaped pulse is only controlled for a time interval defined by:

$$-N\tau / 2 = -\alpha\pi / w \leq t < N\tau / 2 = \alpha\pi / w \qquad (33)$$

Outside this time window (whose width is related to the smallest feature of the mask), replica waveforms are produced. The entire waveform is also modulated by the sinc function in equation 32. These features follow directly from the sampling theorem for fourier transforms [32]. If the spot size for the dispersed frequency components is infinitesimal, the replica waveforms would persist unavoidably for a significant duration under the sinc envelope. Instead the finite spot size for each frequency component blurs the discrete features of the mask, and this modulates the shaped waveform with the gaussian envelope in equation 32. The fast rolloff of the gaussian envelope can remove the replica waveforms. This means that the spatial extent of the incident frequency components smooths out the discrete features of the mask. The time window for the sinc envelope is related to α / w (total frequency per pixel) while the gaussian envelope is related to w_0 / w (the ratio of spot size to pixel width). For removal of the replicas, the temporal length of the shaped waveform must not only fit within the time window specified by the sinc envelope, but also be short enough that its replica waveforms are far enough in the tails of the gaussian envelope. Note that field amplitude removed by the gaussian envelope corresponds to light that is diffracted into higher order spatial modes. The results described by equations 30, 32 and 33 have been previously derived in a slightly different formalism by Weiner and co-workers [20,22].

Even though 'arbitrary' waveforms can be produced by superposition (and interference) of the N evenly spaced pulses (with complex amplitudes given by C_n) according to equation 30, it is sometimes

easier to consider pattern sequences with lengths different than the number of pixels N on the mask (including those with p>N since the mask accommodates the spectral bandwidth of the input pulse). If p is the number of features in the designed sequence, then the output waveform will be the superposition of p evenly spaced input pulses (with complex amplitudes) within the time window given by equation 33. In designing the shaped waveform the time window can be discretized arbitrarily. All the results from equation 23 onward still hold for N=p.

For p small enough that the pulses do not interfere, a pulse train is produced with a frequency given by $wp/2\pi\alpha$. For pulse trains with irregular timings or frequencies that are non integral values of $w/2\pi\alpha$, p must be large enough to discretize the desired time points, and the amplitudes of unwanted pulses specified to be zero. The p-length pattern B_n should be applied to the mask as follows: if the center pixel of the mask is pixel 0, then pixels 0, 1, 2, ... correspond to B_0, B_1, B_2, ... and pixels -1, -2, -3, correspond to B_{p-1}, B_{p-2}, B_{p-3}, ...with the pattern repeating for p<N.

2.2.3.b. Effects of gaps

With an ideal mask, the effects of discrete sampling and diffraction from pixel edges must still be accounted for as described above. The impact of the gaps between adjacent pixels on a real mask will now be discussed. Recalling equation 31, we see that the first term corresponding to the active pixels is similar to equation 32 except that the sinc envelope is broadened and lessened in amplitude. This is to be expected, since the mask still samples new angular frequency components every w / α but each pixel only modulates a fraction rw / α of the light at each angular frequency. Since the sinc envelope is broadened the replica waveforms are

somewhat more apparent. The second term in equation 31 is the contribution of the gaps to the mask's temporal response. Since the filter in each gap is assumed to be the same, the gaps simply reproduce the single input pulse at time zero with a reduced complex amplitude given by $(1-r)B_g$. This input pulse is also reproduced as replica waveforms every $\pm 2\pi\alpha/w$ outside the pulse shaping time window. If the spot size for the dispersed frequency components is comparable to the pixel spacing then these replicas should be largely removed by the fast rolloff of the gaussian envelope resulting from diffraction. Thus the zero-time coefficient C_0 for equation 30 is modified to include the contribution of the gaps:

$$C_0 = rA_0 + (1-r)B_g \tag{34}$$

Note that both A_0 and B_g are in general complex and so the two terms may interfere. For small r this effect can be compensated by choosing A_0 appropriately.

2.3.3.c. Centering of the dispersed spectrum on the mask

The effect of a lateral shift x_0 in the position of the mask relative to the center of the dispersed spectrum will now be considered. One expects that a shift in a frequency filter gives rise to a temporal phase sweep. The first part of equation 31 describes such a phase sweep. This effect needs to be accounted for if one wants to produce waveforms or pulsetrains with well defined and pre-specified phase relationships. It also might be advantageous to use this effect to produce phase relationships between pulses which could not be produced with only a phase mask. In any case, it is crucial to know the relative lateral alignment of the mask array to the dispersed spectrum. In practice this can be done by monitoring the power

spectrum of the shaped pulse as various pixels are used to attenuate the spectrum.

2.3.3.d. Phase and amplitude modulation

For a mask filter that manipulates both spectral phase and amplitude, desired waveforms (subject to the available time window and temporal resolution) can be generated simply by choosing a mask pattern whose inverse discrete fourier transform compensates for the sinc and gaussian envelopes and for the gap contribution at t=0 to give the desired coefficients C_n. Note that only the relative values of C_n can be specified since the mask can only attenuate (and not create) spectral components.

2.2.3.e. Summary and illustration

The features discussed in this section are summarized in figure 4, assuming a mask with seventy 100-μm pixels separated by 15-μm gaps, a 75-fsec input pulse, and a spot size at the mask of 85 μm. For purposes of illustration, we have assumed that the single mask is capable of independent phase and amplitude modulation. Figure 4a shows a desired waveform consisting of four equal-amplitude phased-locked pulses. The dashed curve shows the time window available for arbitrary pulse shaping. Figure 4b shows the modifications in the output which result due to the effects of discrete frequency sampling and finite gaps between the pixels. Discrete sampling results in replica waveforms outside the temporal range that is under arbitrary control. The dashed curve shows the sinc envelope which modulates the pulse amplitudes, also as a result of discrete frequency sampling. Pulses associated with the gap contribution are also apparent at times -4 psec, 0, and 4 psec. Figure 4c indicates additional modifications to the waveform associated with diffraction effects of the mask. Diffraction effects result in modulation of the waveform shown in figure 4b with a

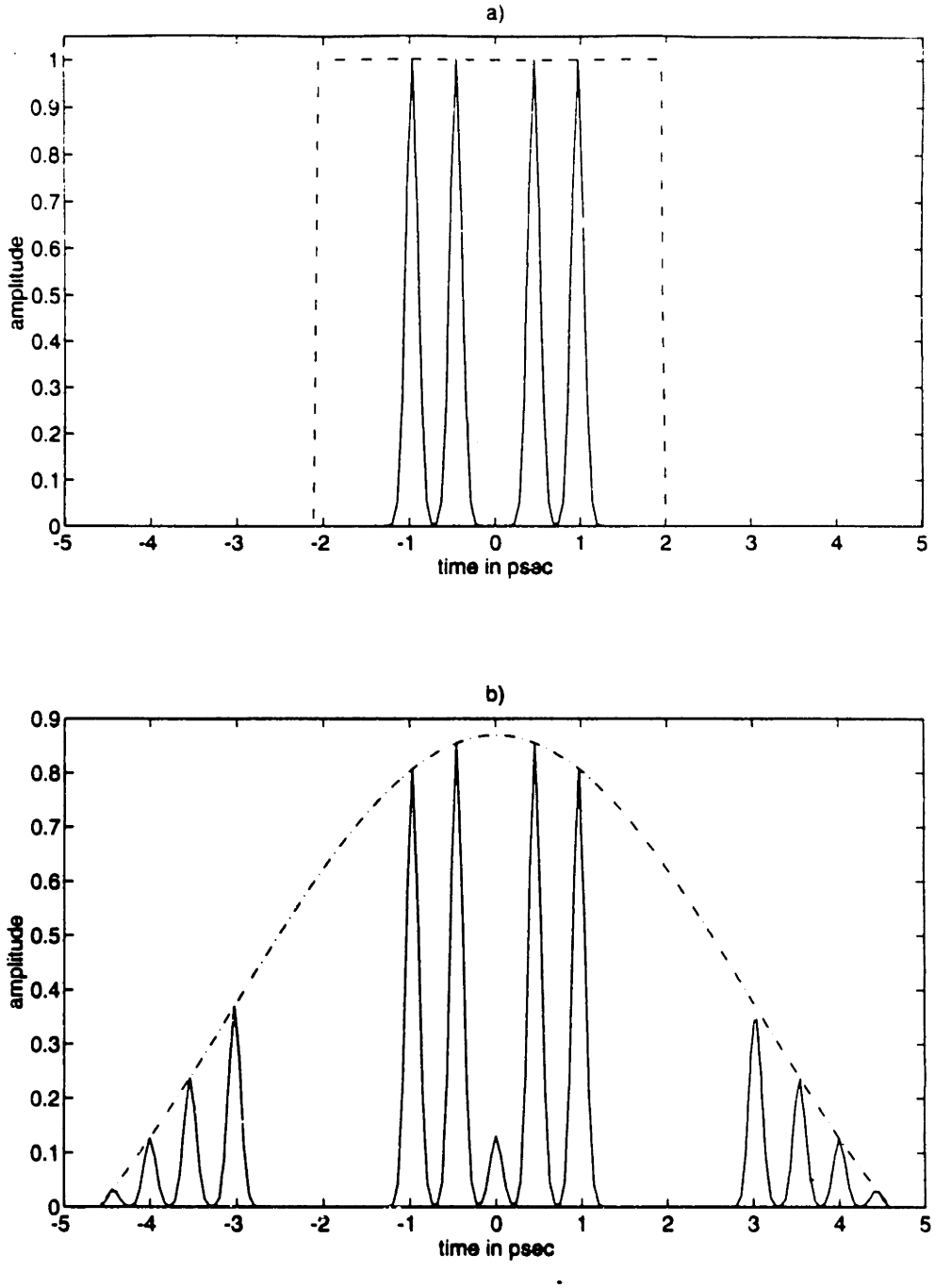

Figure 4ab. An illustration of the effects of pulse shaping using a discrete frequency filter with gaps. See text for details. Figure 4a shows a desired shaped waveform. The dashed curve gives the time window associated with the spatial resolution of the mask. Figure 4b shows the effects of discrete fourier sampling and gaps between pixels on the desired waveform, if these effects are not compensated for in the design of the mask pattern. Replica waveforms appear, and the waveform is modulated by a sinc envelope function (dashed curve). Additional features associated with the gaps appear in the center of the desired waveform and the replicas.

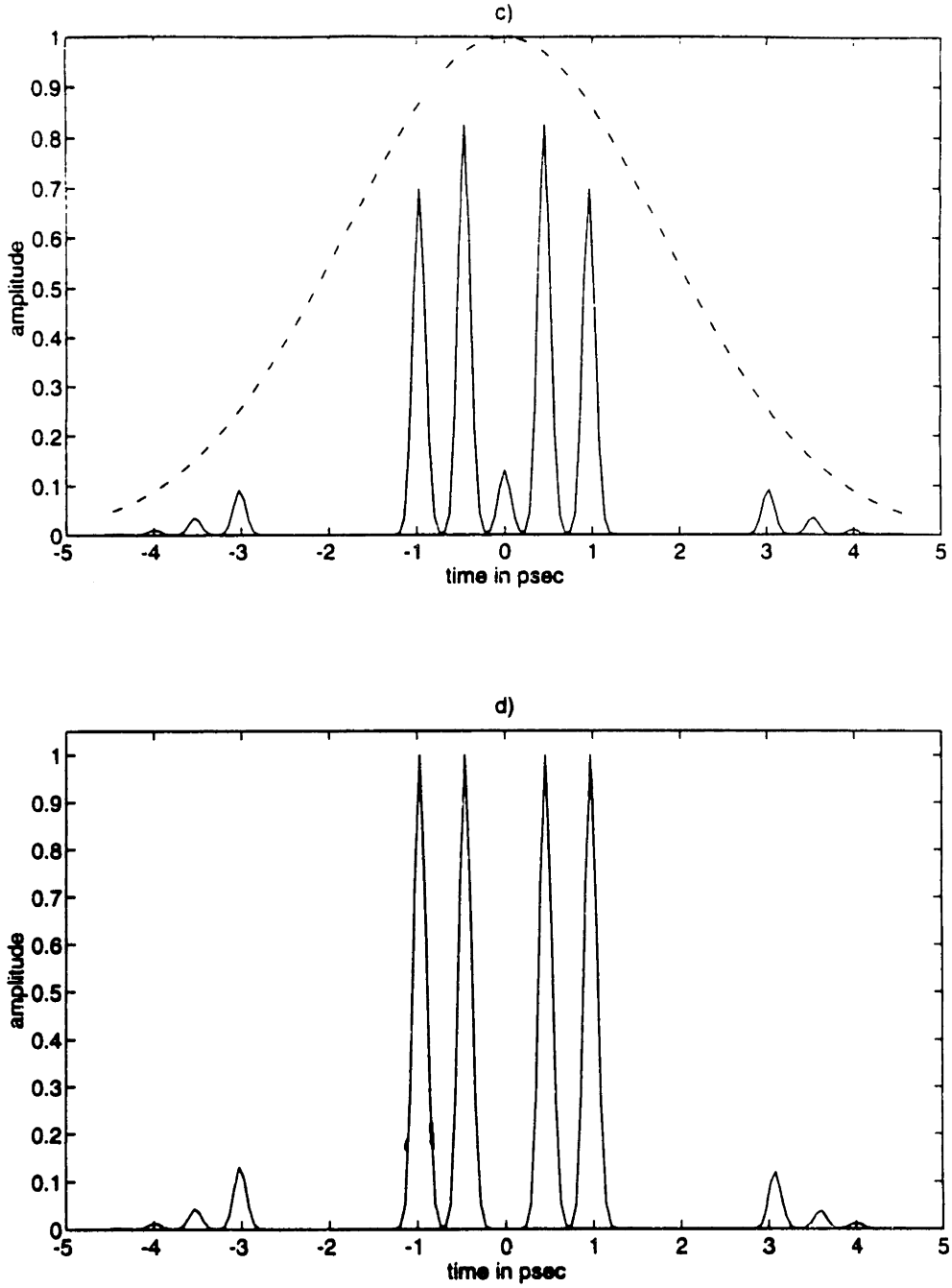

Figure 4cd. An illustration of the effects of pulse shaping using a discrete frequency filter with gaps. See text for details. Figure 4c includes the effects of diffraction, which yields a gaussian temporal modulation (dashed curve) of the waveform. Figure 4c shows the waveform produced by simply using the discrete fourier transform of the desired waveform as the frequency filter. Figure 4d shows the output waveform produced by the mask when the effects described above are compensated for according to the prescription in section 4.

gaussian temporal envelope (dashed curve in figure 4c). The gaussian and sinc temporal envelopes lead to substantial reduction of the replica waveforms. In summary, use of the discrete Fourier transform of the desired waveform as the frequency filter yields the output given in Fig. 4c. Better results can be obtained by modifying the mask to compensate for the effects of discrete sampling, gaps, and diffraction. Figure 4d shows the best approximation to the desired waveform which can be generated by a mask with the assumed characteristics, through use of an appropriately modified pattern. A prescription for appropriate pattern design will be described in section 6. Note that the figure plots amplitude and not intensity, so that the total energy in the replica pulses is very small.

Currently available masks have smaller (2-3 μm) gaps and more pixels. The reduction in gap size results in comparable reduction in the amplitude of the unwanted feature at t = 0 and its replicas. This may appear to essentially eliminate such features, but if the desired waveform includes a feature at t = 0 then the interference effects may still be significant and should be accounted for in the design of the mask pattern. An increase in pixel number results in a comparable relative increase in the temporal range which can be controlled. If a desired waveform extends over the same fraction of the range as that illustrated in Fig. 4, the replica amplitudes will be the same.

2.4. DIFFRACTION OF THE SPATIAL PROFILE OF THE SHAPED WAVEFORM

2.4.1 General Considerations

The derivation by Thurston and coworkers reproduced in section 3.2 shows that the spatial extent of the frequency components incident on the

mask filter will affect the temporal profile of the shaped waveform. As the spot size of the incident frequency components becomes larger, more light is diffracted out of the gaussian spatial mode and the gaussian envelope modifying the temporal profile of the shaped waveform becomes narrower. In this section we derive the complete space-time profile of the shaped waveform. We will see that light diffracted into higher order spatial modes still adds coherently to the shaped waveform and cannot be simply removed by spatial filtering with an aperture. In particular, it will be shown that filtering of spatially separated frequency components within the grating and lens apparatus shapes the waveform not along the propagation **z**-axis (temporal profile) but along an axis in the **x-z** plane. This implies that there is a transverse spatial shift that varies linearly along the temporal profile of the shaped waveform. The variation in the space-time profile as the mask is displaced from the focal plane will also be derived.

These theoretical results explain some peculiar experimental observations both in our laboratory and that of the Bellcore researchers. In the Bellcore experiments, waveforms whose intensity profiles were supposed to be symmetric were observed to be asymmetric. The asymmetry varied depending on the size of an aperture used to spatially filter the shaped waveform and on the position of the mask relative to the focal plane [20]. In our own lab, we have made similar observations. We have also noticed that this asymmetry appears to vary directly with the position of the doubling crystal used to measure the shaped waveforms by non-collinear cross-correlation with an unshaped reference pulse. This observation is consistent with the hypothesis that the shaped waveform has

a space-time dependence which affects its overlap and phase-matching with the reference pulse in the doubling crystal.

The derivation will combine the earlier result for the fourier transform of a discrete mask pattern (equation 23) with the formalism of Danailov and Christov [33]. The electric field will be expressed both in time and frequency domains and also in position and wavevector domains to be distinguished by the notational conventions $e(x,t)$, $E(x,\omega)$, $\bar{e}(k,t)$, and $\bar{E}(k,\omega)$. The following three properties will also be used: 1) From fourier optics it is known that the transverse spatial profile in the front focal plane $e(x, z = f)$ of a lens of focal length f, situated at position z=0, is related through a fourier transform to the transverse spatial profile in the back focal plane of a lens $e(x, z = -f)$. In particular:

$$e(x, z = -f) = f(x) \rightarrow e(x, z = f) = F(2\pi x / \lambda f) \tag{35}$$

where f(x) and F(k) are a fourier transform pair and λ is the wavelength of the light. This property will be used repeatedly to determine the spatial characteristics of the spectrally filtered pulse. 2) Under the paraxial approximation, if $\bar{E}(k, z = 0)$ is the fourier transform of the spatial transverse profile of the field at z=0, its profile in wavevector space at z=z0 is given by:

$$\bar{E}(k, z = z_0) = \bar{E}(k, z = 0) \exp\left(-i \frac{z_0 \lambda}{4\pi} k^2 \right) \tag{36}$$

3) As derived by Martinez [30] (under the assumption of linear dispersion), the transfer function for a grating is given by:

$$E(x,\omega)_{grating} = b_1 E_{in}(\delta x,\omega)\exp(i\gamma\Omega x) \tag{37}$$

where $\delta = \cos(\theta_i)/\cos(\theta_d)$, $\gamma = 2\pi/\varpi d\cos(\theta_d)$, $\Omega = \omega - \varpi$, θ_i and θ_d are the angles of incidence and diffraction respectively, and d is the grating line spacing.

The multipliers b_i are multiplicative constants that take into account reflection and absorptive losses, and also normalize the waveform energy for the different mathematical operations.

2.4.2 Space-time profile of a waveform shaped using a single mask

Figure 1 illustrates the single mask in the 4-f pulse shaping apparatus. Let the mask be displaced from the focal plane by a distance z_0. The input waveform is assumed to be separable in time and space with a collimated gaussian spatial profile of spot size a:

$$e_{in}(x,t) = e_{in}(t)\exp(i\varpi t)\exp\left(-x^2/a^2\right) \tag{38}$$

Applying equation 37, immediately after the first grating one has:

$$E_1(x,\omega) = b_1 E_{in}(\Omega)\exp\left(-\frac{\delta^2}{a^2}x^2 + i\gamma\Omega x\right) \tag{39}$$

where $E_{in}(\omega)$ is the temporal fourier transform of the input pulse envelope $e_{in}(t)$. The spatial profile of the beam in the focal plane of the lens pair is given by the spatial fourier transform of equation 39 according to equation 35. To propagate the beam so as to account for a displacement of the mask

position from the focal plane, an expression for the field amplitude in wavevector space is needed so one can apply equation 36. The field amplitude at the focal plane in wavevector space is given by the double fourier transform of equation 39 and the substitution $x = k\lambda f/2\pi$ giving:

$$\bar{E}_2(k,\omega) = b_2 E_{in}(\Omega)\exp\left(-\left(\frac{\delta\lambda f}{2\pi a}\right)^2 k^2 - i\frac{\lambda\gamma f}{2\pi}\Omega k\right) \qquad (40)$$

Equation 40 will now be used to propagate the field a distance z_0 to the displaced mask. In position space the mask profile is multiplied by the field amplitude so in wavevector space the mask profile is convolved with the field amplitude according to the product theorem for fourier transforms. The field amplitude is then propagated a distance $-z_0$ back into the focal plane of the lens pair. After the mask and in the focal plane one has:

$$\bar{E}_3(k,\omega) = b_3\left(\bar{E}_2(k,\omega)\exp\left(-i\frac{z_0\lambda}{4\pi}k^2\right)\otimes M(k)\right)\exp\left(+i\frac{z_0\lambda}{4\pi}k^2\right) \qquad (41)$$

Recall that the fourier transform of the mask pattern (equation 23) can be expressed as:

$$M(k) = \sum_{n=-\infty}^{\infty} c_n \delta\left(k - n\frac{2\pi}{Nw}\right) \qquad (42)$$

with

$$c_n = \frac{N}{\pi n}\exp\left(i\frac{2\pi x_0 n}{L}\right)\left\{\begin{array}{l} A_{rem(n,N)}\sin\left(\frac{r\pi n}{N}\right) \\ +\partial_{0,rem(n,N)}B_g(-1)^{n/N}\sin\left(\frac{(1-r)\pi n}{N}\right)\end{array}\right\} \qquad (43)$$

Carrying out the convolution in equation 41 gives:

$$\bar{E}_3(k,\omega) = b_3 E_{in}(\Omega)\sum_{n=-\infty}^{\infty}\left(\begin{array}{l} c_n\exp\left[-\left(\left(\frac{\delta\lambda f}{2\pi a}\right)^2 + i\frac{z_0\lambda}{4\pi}\right)\left(k - n\frac{2\pi}{Nw}\right)^2\right] \\ \times\exp\left[-i\Omega\frac{\gamma\lambda f}{2\pi}\left(k - n\frac{2\pi}{Nw}\right)\right] \\ \times\exp\left(i\frac{z_0\lambda}{4\pi}k^2\right)\end{array}\right) \qquad (44)$$

The spatial profile of the electric field immediately before the second grating is determined by inverse spatial fourier transformation of equation 44 followed by a spatial fourier transformation according to equation 35:

$$E_4(x,\omega) = b_4 E_{in}(\Omega)\sum_{n=-\infty}^{\infty}\left(\begin{array}{l} c_n\exp\left[-\left(\frac{\delta^2}{a^2} + i\pi\frac{z_0}{\lambda f^2}\right)\left(x - n\frac{\lambda f}{Nw}\right)^2\right] \\ \times\exp\left[-i\Omega\gamma\left(x - n\frac{\lambda f}{Nw}\right)\right] \\ \times\exp\left(i\pi\frac{z_0}{\lambda f^2}k^2\right)\end{array}\right) \qquad (45)$$

The inverse transfer function of equation 37 is used to describe the action of the second grating (which is anti-parallel to the first grating), so that the output electric field amplitude after the pulse shaping apparatus is given by:

$$E_{out}(x,\omega) = b_5 E_4(x/\delta,\omega)\exp(i\gamma\Omega x/\delta) \tag{46}$$

Taking the inverse temporal fourier transform of equation 46 gives the shaped output waveform:

$$e_{out}(x,t) = b_6 \exp(i\varpi t)\sum_{n=-\infty}^{\infty}\left\{\begin{array}{l} c_n \exp\left(-i\pi\frac{z_0\lambda}{w^2}\left(\frac{n}{N}\right)^2\right)e_{in}(t+n\tau) \\ \times\exp\left(-\frac{(x-n\chi)^2}{a^2}\right)\exp\left(i2\pi\frac{z_0}{\delta f w}\left(\frac{n}{N}\right)x\right)\end{array}\right\} \tag{47}$$

where $\tau = \gamma\lambda f/Nw$ (which is the same as the previous definition in section 2.2), and $\chi = \delta\lambda f/Nw$.

Calculation of the temporal profile for the gaussian spatial mode (with spotsize a) $e_{out}^{00}(t)$ of the shaped waveform from equation 47 gives the following result:

$$e_{out}^{00}(t) = \sum_{n=-\infty}^{\infty} c_n e_{in}(t+n\tau)\exp\left\{-\frac{n^2}{2}\left(\frac{\chi}{a}\right)^2\left(1+\left(\frac{\pi\lambda a^2 z_0}{\chi^2 w^2 N^2}\right)^2\right)\right\} \tag{48}$$

The gaussian envelope modulating the shaped waveform in equation 48 is identical to that calculated section 2.2, except that the dependence of the spot size on the position of the mask relative to the focal plane is made explicit.

For the case of $z_0 = 0$, which means that the mask is exactly in the focal plane of the lens pair, the space-time profile in equation 47 simplifies to give:

$$e_{out}(x,t) = \exp(i\varpi t) \sum_{n=-\infty}^{\infty} c_n e_{in}(t + n\tau) \exp\left(-\frac{(x - n\chi)^2}{a^2} \right) \qquad (49)$$

This is a very significant result since it shows that even for a perfectly aligned spectral filtering set-up, the output waveform is both temporally *and* spatially shaped, and this spatial shaping cannot be simply removed by spatial filtering with an aperture. Equation 49 shows that the shaped waveform is a superposition of equally spaced input pulses as discussed earlier, but it also shows that each input pulse that is displaced in time is *also transversely displaced*, and the greater the displacement in time the greater the displacement in space. In particular replica waveforms, arising from the discrete sampling of the mask filter, are always present in the shaped waveform but are displaced away from the central gaussian spatial spot. An aperture can remove the distant replicas but pulses within the apertured light are still displaced spatially from one another.

Figure 5 shows the space-time electric field amplitude for a simulation of a shaped waveform designed to consist of three evenly spaced pulses of equal intensities. The simulation assumes an available time window of 10 psec. Since the three pulses occupy about 6 psec of this,

replica pulses outside the time window are apparent. The striking feature of the waveform is the transverse displacement of the different pulses. In principle there are additional replica pulses (of reduced intensity) that would continue to be further displaced transversely as they are further displaced from the temporal origin of the unshaped pulse. Clearly the contributions of these different pulses to the gaussian spatial transverse mode of the shaped waveform are reduced as they are displaced in time. Thus the removal of replicas effectively consists of diffracting them away from the central portion of the desired waveform. Nonetheless even the three pulses comprising the desired waveform have a time-dependent transverse displacement. Note that the plots are of field amplitude and not field intensity so there is still relatively little energy in the replica pulses.

The slope of the this time-dependent lateral shift is given by:

$$\partial x/\partial t = -\chi/\tau = -cd\cos(\theta_i)/\lambda \qquad (50)$$

which for typical parameters (d=1800 lines/mm gratings, λ=800 nm) is about 0.15 mm/psec. Equation 50 shows that this slope depends only on the angular dispersion produced by the grating. However the impact of this lateral shift is measured relative to the spot size of the unshaped incident pulse. Spatially large input pulses produce a very tightly focussed spectrum on the mask, minimizing diffraction, so that less light is diffracted away from the gaussian spatial mode. For example, if in figure 5 the spotsize of the individual pulses is made larger, the time-dependent transverse shift is less emphasized.

To determine the maximum transverse displacement $\overline{\chi}$ in the desired part of the shaped waveform recall that the shaped waveform is

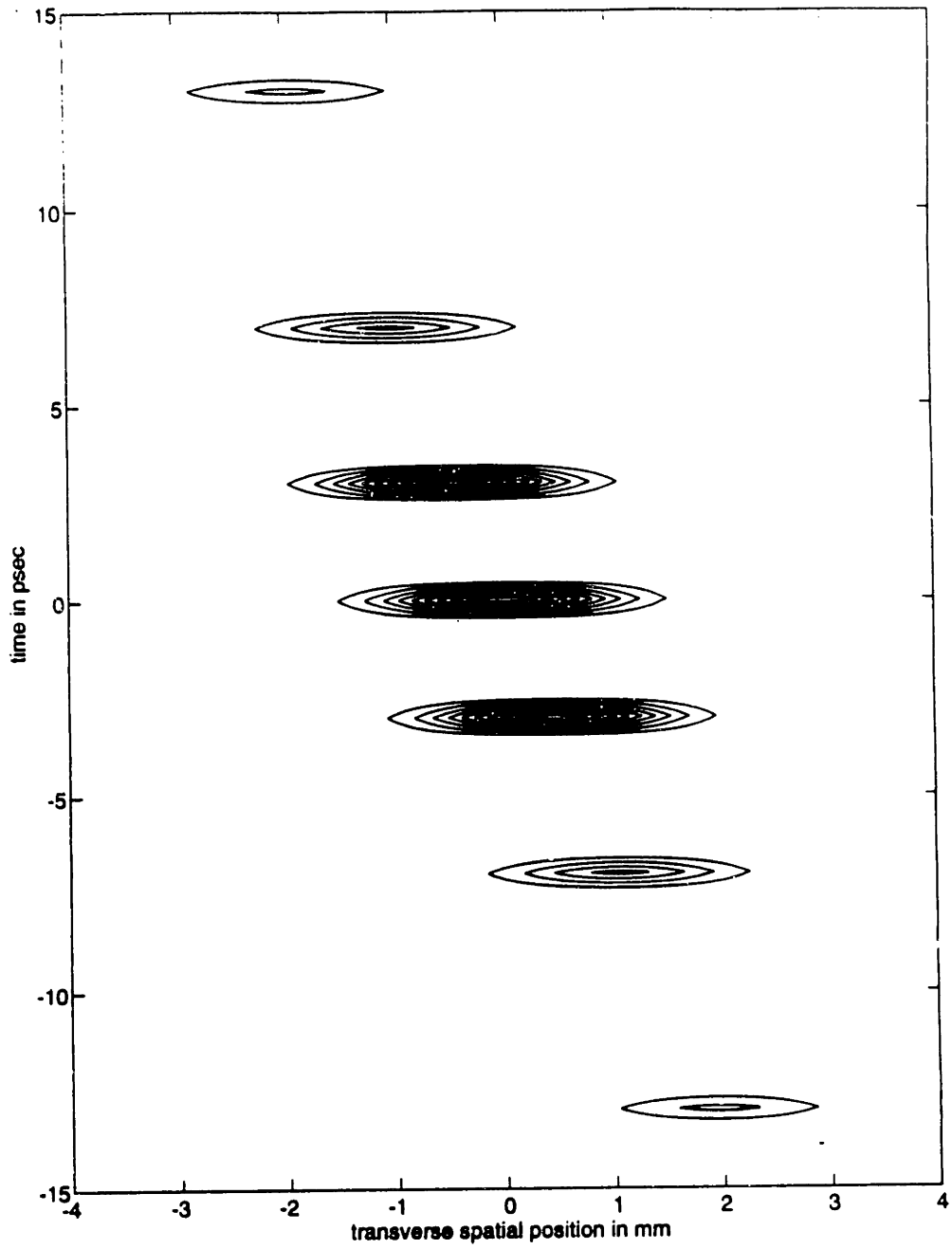

Figure 5. A contour plot of the spatio-temporal amplitude profile of a shaped waveform. The desired waveform consists of three evenly spaced pulses with equal intensities. Since the desired waveform uses more than half of the 10-psec time window given by the spatial resolution of the mask, weak replica pulses outside this time window are apparent. Diffraction from the mask linearly shifts the spatial positions of the different pulses as a function of time. This is a general feature of the shaping of ultrafast waveforms through filtering of spatially dispersed frequency components.

only controlled within the time window given by $-N\tau/2 \le t \le N\tau/2$, so that the transverse displacement in this time window is given by:

$$\bar{\chi} = N\tau|\partial x/\partial t| = \delta\lambda f/w \tag{51}$$

For typical experimental parameters (λ=800nm, w=100μm, and f=20cm) $\bar{\chi} = 1.6mm$, which is not negligible for comparable spot sizes. Replicas are tranversely shifted by a magnitude exceeding $\bar{\chi}/2$.

If the mask is displaced from the focal plane, the wavefronts of the incident frequency components have some curvature. Equation 47 shows that this results in a linear spatial phase sweep across the individual pulses whose superposition produces the shaped waveform and that there is a small phase modification to the coefficients c_n. This spatial phase sweep $\exp\left(i2\pi\frac{z_0}{\delta f w}\frac{n}{N}x\right)$ is equivalent to a shift in transverse wavevector space of $2\pi\frac{z_0}{\delta f w}\frac{n}{N}$ and implies that the propagation direction of the shaped waveform slightly changes along its temporal profile. Thus for a mask filter displaced from the focal plane the time-dependent transverse shift is accompanied by a time-dependent shift in propagation direction. In figure 5, this would be illustrated by a slight tilt in the phase fronts of the different pulses. The slope of this tilt would increase in absolute magnitude as pulses are displaced further from t=0. As shown by equation 48, this implies that more light is diffracted away from the gaussian spatial mode.

An estimate of the magnitude of this 'temporal divergence' ρ can be determined by comparing the difference $\Delta\bar{k}_x$ between the shift in transverse wavevector at opposite ends of the pulse shaping time window

(n=-N/2 and n=+N/2) to the magnitude of the propagation wavevector $\bar{k}_z = 2\pi/\lambda$:

$$\tan(\rho) = \frac{\Delta\bar{k}_x}{\bar{k}_z} = \frac{z_0\lambda}{\delta f w} \tag{52}$$

For typical parameters and z_0=5mm, equation 52 gives ρ=200 μrad. This is the angular difference in propagation direction between the opposite temporal ends of a shaped waveform that fills the pulse shaping time window. Replica pulses outside this time window have an angular divergence whose magnitude exceeds $\rho/2$. For large propagation distances this effect may become significant.

2.5. PULSE SHAPING WITH TWO MASKS

2.5.1 General Considerations

It is clear that generation of arbitrary temporal waveforms requires a spectral filter that can manipulate both amplitude and phase independently, so two LC SLMs need to be incorporated into the pulse shaping set-up. What needs to be determined is under what circumstances can the combined spectral filter associated with two LC SLMs simply be given by their product. In this case the two LC SLMs can be treated as a single mask with independent control over spectral attenuation and spectral retardation. Clearly if there were no spatial separation between the two masks the combined filter is given by their product and one can apply the LC filters described in section 1. However for separated masks diffraction effects will manifest themselves as the light field propagates between the masks.

In our initial demonstration of pulseshaping using two LC SLMs [23], the SLMs were placed within separate telescopes of an 8-f arrangement as in figure 3. An aperture was placed between the second and third lens (where the separated frequency components are recombined) with the assumption that this would retain only gaussian spatial mode of light shaped by the first mask. Under such an assumption the combined frequency filter is not given by the product of the two masks because the gaussian envelope given by equation 29 modulates the temporal response of the individual masks.

Alternatively the two SLMs could be placed back to back in a single telescope of a 4-f arrangement (figure 1). However the physical size of the SLM devices including the windows makes it impossible for both masks to be inside the focus of the lens pair. One mask will necessarily by displaced from the focal plane and the spatial profile of light diffracted off the first mask will change as it propagates through the space between masks.

In this section we will give the electric field space-time amplitude profiles for waveforms shaped by two LC SLMs in both the 4-f and 8-f arrangements. The temporal profile for the gaussian spatial mode of the shaped waveform will also be given. Derivation of these results follows along exactly the same path as the calculation in section 4, and will not be presented here. The dependence on the position of the masks relative to the focal plane(s) will be described explicitly. The equations which follow can be used to model the tolerances of different pulse shaping arrangements. Some simulations are shown in section 6.

It is also important to distinguish the case in which the orientations of the LCs in the two separate SLMs differ by 90 degrees and there are no intermediate polarization optics to couple them. In this case the two LC

SLMs operate on orthogonal polarizations and the output waveform is given by the superposition of two waveforms with orthogonal polarizations, each shaped by a single phase mask. A subsequent polarizer can be used so that the two masks combine to produce a filter that independently manipulates spectral amplitude and spectral phase (equation 11 in section 1). The individual masks will still be affected by displacements from the focal plane (as described in section 4). However, there will be no multiple diffraction by the two masks. In particular, light diffracted by one mask out of the gaussian spatial mode cannot be diffracted back into the gaussian spatial mode by the second mask. This is not the case for a pair of masks coupled to the same polarization, which will generate a temporal profile that will manifest path-length variation associated with multiple diffraction.

It will be shown that properly aligned masks in an 8-f arrangement produce a shaped waveform whose space-time profile is given exactly by a spectral filter that is the product of the two separate masks. The same is true for the temporal profile of the gaussian spatial mode of a waveform shaped by properly aligned masks (with some finite separation) that manipulate orthogonal polarizations. In all cases, the time-dependent transverse spatial shift described in section 4 for a single mask is still present.

2.5.2 Two masks in an '8-f' arrangement

For two separated masks that filter non-orthogonal polarizations within the '8-f' grating and lens apparatus (figure 3), with the masks displaced by distances $z_0^{(1)}$ and $z_0^{(2)}$ away from the respective focal planes of the two telescopes, the field amplitude of the shaped waveform is:

$$e_{out}(x,t) = \exp(i\varpi t) \sum_{n=-\infty}^{\infty} \left\{ \begin{array}{l} e_{in}(t+\tau n) \\ \times \exp\left(-\dfrac{(x-n\chi)^2}{a^2} \right) \\ \times \exp\left(-i\pi \dfrac{z_0^{(1)}\lambda}{w^2} \left(\dfrac{n}{N} \right)^2 \right) \exp\left(-i2\pi \dfrac{z_0^{(1)}}{\delta f w} \left(\dfrac{n}{N} \right) x \right) \\ \times \displaystyle\sum_{n'=-\infty}^{\infty} \left\{ \begin{array}{l} c_{n'+n}^{(1)} c_{n'}^{(2)} \exp\left(i\pi \dfrac{\lambda\left(z_0^{(1)} - z_0^{(2)} \right)}{w^2} \left(\dfrac{n'}{N} \right)^2 \right) \\ \times \exp\left(-i2\pi \dfrac{\left(z_0^{(1)} - z_0^{(2)} \right)}{\delta f w} \left(\dfrac{n'}{N} \right) x \right) \end{array} \right\} \end{array} \right\} \tag{53}$$

where the superscripts denote the first or second mask respectively, and the other parameters are as defined in section 4.

Under the condition $z_0^{(1)} = z_0^{(2)} = z_0$, equation 53 simplifies to give:

$$e_{out}(x,t) = \exp(i\varpi t) \sum_{n=-\infty}^{\infty} \left\{ \begin{array}{l} e_{in}(t+\tau n) \exp\left(-\dfrac{(x-n\chi)^2}{a^2} \right) \exp\left(-i2\pi \dfrac{z_0^{(1)}}{\delta f w} \left(\dfrac{n}{N} \right) x \right) \\ \times \exp\left(-i\pi \dfrac{z_0^{(1)}\lambda}{w^2} \left(\dfrac{n}{N} \right)^2 \right) \displaystyle\sum_{n'=-\infty}^{\infty} c_{n'+n}^{(1)} c_{n'}^{(2)} \end{array} \right\} \tag{54}$$

These results are derived assuming that there is no aperture between the second and third lenses (unlike in our initial experiments), so light

diffracted by the first mask into higher order modes is retained. Equation 54 shows that the shaped waveform has properties identical to those produced by a single mask (equation 47) except $c_n = \sum_{n'=-\infty}^{\infty} c^{(1)}_{n'+n} c^{(2)}_{n'}$. This describes exactly a single mask whose spectral filter is given by the product of the two separated masks (with the second mask inverted as a result of the telescope). Even though the first mask diffracts the incident pulse into higher order spatial modes, the frequency filter for the spatially separated masks is given exactly by their product. This result obtains because in the case of $z_0^{(1)} = z_0^{(2)} = z_0$ the spatial profile immediately after the first mask is exactly imaged onto the second mask except for the inversion $x \rightarrow -x$ which can be accounted for by also inverting the mask pattern.

The temporal envelope for the gaussian spatial mode associated with the space-time profile given by equation 53 is:

$$e^{00}_{out}(t) = \sum_{\substack{n=-\infty \\ n'=-\infty}}^{\infty} \left\{ \begin{array}{l} c^{(1)}_n c^{(2)}_{n'} e_{in}\left(t + (n-n')\tau\right) \\ \times \exp\left(i\pi \dfrac{\lambda\left(z_0^{(1)} - z_0^{(2)}\right)}{w^2} \dfrac{nn'}{N^2} \right) \\ \times \exp\left\{ -\dfrac{\chi^2}{2a^2} \left((n-n')^2 + \left(\dfrac{\pi\lambda a^2}{\chi^2 w^2} \right)^2 \left(\dfrac{z_0^{(1)} n - z_0^{(2)} n'}{N} \right)^2 \right) \right\} \end{array} \right\} \qquad (55)$$

Again under the condition $z_0^{(1)} = z_0^{(2)} = z_0$, equation 55 simplifies to give a result identical to the single mask result in equation 48, with $c_n = \sum_{n'=-\infty}^{\infty} c_{n'+n}^{(1)} c_{n'}^{(2)}$.

2.5.3 Two masks in a '4-f' arrangement.

For two masks that filter non-orthogonal polarizations, situated back to back within a '4-f' grating and lens apparatus (figure 1), the space-time electric field profile is given by:

$$e_{out}(x,t) = \exp(i\varpi t) \sum_{n=-\infty}^{\infty} \left\{ \begin{array}{l} e_{in}(t+\tau n) \\ \times \exp\left(-\dfrac{(x-n\chi)^2}{a^2} \right) \\ \times \exp\left(-i\pi \dfrac{z_0 \lambda}{w^2} \left(\dfrac{n}{N} \right)^2 \right) \exp\left(i2\pi \dfrac{z_0}{\delta f w} \dfrac{n}{N} x \right) \\ \times \sum\limits_{n'=-\infty}^{\infty} \left\{ \begin{array}{l} c_{n-n'}^{(1)} c_{n'}^{(2)} \exp\left(-i\pi \dfrac{\lambda \bar{z}}{w^2} \left(\dfrac{n'}{N} \right)^2 \right) \\ \exp\left(i\pi \dfrac{2\bar{z}}{\delta f w} \dfrac{n}{N} x \right) \end{array} \right\} \end{array} \right\} \qquad (56)$$

where the first mask is displaced from the focal plane by a distance of z_0 and the second mask is placed a fixed distance $\bar{z}$ in front of the first. This expression has terms similar to those of equation 53. However for practical considerations (in particular due to the finite size of the SLM devices) this expression usually requires $\bar{z} \neq 0$, meaning that there is a minimum separation between the two masks which therefore cannot both

be in the focal plane. The temporal envelope for the gaussian spatial mode of the waveform described by equation 56 is given by:

$$e_{out}^{00}(t) = \sum_{\substack{n=-\infty \\ n'=-\infty}}^{\infty} \left\{ \begin{array}{l} c_n^{(1)} c_{n'}^{(2)} e_{in}\left(t + (n+n')\tau\right) \exp\left(i\pi \dfrac{\lambda \bar{z}}{w^2} \dfrac{nn'}{N^2} \right) \\ \times \exp\left\{ -\dfrac{\chi^2}{2a^2} \left((n+n')^2 + \left(\dfrac{\pi \lambda a^2}{\chi^2 w^2} \right)^2 \left(\dfrac{z_0(n+n') + \bar{z}n'}{N} \right)^2 \right) \right\} \end{array} \right\} \tag{57}$$

With the first mask in the focal plane (z_0=0), equation 56 only partially simplifies to give:

$$e_{out}(x,t) = \exp(i\varpi t) \sum_{n=-\infty}^{\infty} \left\{ \begin{array}{l} e_{in}(t + \tau n) \exp\left(-\dfrac{(x - n\chi)^2}{a^2} \right) \\ \times \displaystyle\sum_{n'=-\infty}^{\infty} \left\{ \begin{array}{l} c_{n-n'}^{(1)} c_{n'}^{(2)} \exp\left(-i\pi \dfrac{\lambda \bar{z}}{w^2} \left(\dfrac{n'}{N} \right)^2 \right) \\ \times \exp\left(i2\pi \dfrac{\bar{z}}{\alpha f w} \dfrac{n'}{N} x \right) \end{array} \right\} \end{array} \right\} \tag{58}$$

A neater expression does not result for the symmetric case of $z_0 = -\bar{z}/2$. For small separations the spatial periods in the second sum are small compared to typical spot sizes so the spatial variation from this sum should be negligible and we can replace x in this term with $n\chi$ giving the following expression:

$$e_{out}(x,t) = \exp(i\varpi t) \sum_{n=-\infty}^{\infty} \left\{ e_{in}(t+\tau n) \exp\left(-\frac{(x-n\chi)^2}{a^2}\right) \times \sum_{n'=-\infty}^{\infty} \left\{ c^{(1)}_{n-n'} c^{(2)}_{n'} \exp\left(-i\pi \frac{\lambda \bar{z}}{w^2}\left(\frac{n'}{N}\right)^2\right) \right\} \times \exp\left(i2\pi \frac{\lambda \bar{z}}{w^2}\frac{nn'}{N^2}\right) \right\} \tag{59}$$

Equations 56-59 shows that the combined spectral filter in this case is not given exactly by the product of the individual masks but includes terms that account for path-length variations as diffracted light propagates between the two masks. The parameter $\bar{z}\lambda/w^2$ is indicative of the magnitude of this effect measuring the degree to which the spatial profile of each frequency component changes between the two masks. If this parameter is small then the combined spectral filter of the two masks is given approximately by the product of the individual mask filters. Otherwise, the appropriate mask patterns for a desired waveform must be determined by numerically inverting equation 57. Such a method is described in section 6.

2.5.4 Two masks that filter orthogonal polarizations

Here we consider the case described in section 1, consisting of two masks with LCs aligned along axes at 45 degrees and -45 degrees in the **x**-**y** plane, followed by a polarizer aligned along the **x**-axis. The incoming polarization is also aligned along the **x**-axis and can be decomposed into components of equal amplitude polarized at ±45 degrees. Each mask will

appear uniform for one polarization and will provide a variable retardance across its array for the other polarization. Because the orthogonal polarizations only see one mask pattern there is no multiple diffraction. After the polarizer following the pair of masks, the field is given by the sum of the two orthogonal fields.

The space-time profile of the shaped waveform produced using two masks in a '4-f' arrangement is given by the sum of two expressions describing the field produced by a single mask (equation 47) with parameters $z_0^{(i)}$ and $c_n^{(i)}$, where i denotes the first or second mask:

$$e_{out}(x,t) = \exp(i\varpi t) \sum_{n=-\infty}^{\infty} \left\{ e_{in}(t + n\tau) \exp\left(-\frac{(x - n\chi)^2}{a^2} \right) \times \left(c_n^{(1)} \exp\left(-i\pi \frac{z_0^{(1)}\lambda}{w^2} \left(\frac{n}{N} \right)^2 \right) \exp\left(i2\pi \frac{z_0^{(1)}}{\delta f w} \left(\frac{n}{N} \right) x \right) \right. \right.$$
$$\left. \left. + c_n^{(2)} \exp\left(-i\pi \frac{z_0^{(2)}\lambda}{w^2} \left(\frac{n}{N} \right)^2 \right) \exp\left(i2\pi \frac{z_0^{(2)}}{\delta f w} \left(\frac{n}{N} \right) x \right) \right) \right\} \tag{60}$$

The coefficients $c_n^{(i)}$ are those produced by a phase-only filter in expression (43) and in the case of an '8-f' apparatus $c_n^{(2)}$ must be replaced with $c_{-n}^{(2)}$ to account for the spatial inversion by the second telescope.

The temporal envelope for the gaussian spatial mode of the shaped waveform described by equation 60 is given by:

$$e_{out}^{00}(t) = \sum_{n=-\infty}^{\infty} e_{in}(t + n\tau) \exp\left(-\frac{n^2\chi^2}{2a^2} \right) \left\{ \begin{array}{l} c_n^{(1)} \exp\left\{ -\frac{n^2}{2}\left(\frac{\chi}{a}\right)^2 \left(\frac{\pi\lambda a^2 z_0^{(1)}}{\chi^2 w^2 N^2} \right)^2 \right\} \\ + c_n^{(2)} \exp\left\{ -\frac{n^2}{2}\left(\frac{\chi}{a}\right)^2 \left(\frac{\pi\lambda a^2 z_0^{(2)}}{\chi^2 w^2 N^2} \right)^2 \right\} \end{array} \right\} \quad (61)$$

Equation 60 and 61 shows that the combined frequency filter for two masks which filter orthogonal polarizations and have some finite separation is not in general given by the product of the individual mask filters.

If the respective displacements of the two masks from the focal plane are equal and opposite $z_0^{(2)} = -z_0^{(1)} = \bar{z}/2$, equation 61 simplifies to give:

$$e_{out}^{00}(t) = \sum_{n=-\infty}^{\infty} \left(\frac{c_n^{(1)} + c_n^{(2)}}{2} \right) e_{in}(t + n\tau) \exp\left(-\frac{n^2\chi^2}{2a^2} \left(1 + \left(\frac{\pi\lambda a^2 \bar{z}}{2\chi^2 w^2 N^2} \right)^2 \right) \right) \quad (62)$$

Equation 62 is identical to equation 48 which describes the temporal envelope for the gaussian spatial mode of a shaped waveform produced by a single mask, except that $c_n = \left(c_n^{(1)} + c_n^{(2)}\right)/2$, and $z_0 = \bar{z}/2$. This shows that with respect to the gaussian spatial mode of the shaped waveform, two masks that filter orthogonal polarizations and have some finite separation between them can be positioned so that the combined spectral filter for the two masks is given by the product of the individual mask filters.

2.6 SPECIFYING TEMPORAL PROFILES

2.6.1 Single mask with independent phase and amplitude control

In this section, we present a systematic prescription to generate specified temporal profiles for shaped waveforms. Ideally one would have a single mask with infinite spatial resolution, no gaps, and the capability to independently filter both spectral amplitude and spectral phase. Thus if the desired waveform were h(t) (implicitly including the optical carrier frequency), the appropriate mask filter m(x) would be given by:

$$m(x) = H(-x/\alpha)/E_{in}(x/\alpha - \varpi) \tag{63}$$

where H(ω) is given by the temporal fourier transform of h(t). Since the mask can only filter existing frequency components the absolute value of m(x) is always less than or equal to one, and so equation 63 shows that the desired waveform has temporal features and a carrier frequency limited by the bandwidth available in the input pulse. Otherwise the desired waveform can be arbitrary.

Even with such an ideal mask, since we are filtering spatially separated frequency components, the diffraction results described in section 4 still obtain. Thus the waveform produced by the mask filter m(x) in equation 63 is given by:

$$e(x,t) = h(t)f(x - t\delta/\gamma) \tag{64}$$

where f(x) is the spatial profile of the input pulse. The temporal profile of the gaussian spatial mode of e(x,t) in equation 64 is modified by a gaussian temporal envelope as described in sections 2.2 and 3.2. For the remainder

of this section we will assume that it is this temporal envelope of the gaussian spatial mode $e_{out}^{00}(t)$ of the shaped waveform that is to be specified.

In the more realistic case of an impixellated mask with N discrete pixels such as an LC SLM, the output waveform shaped by the pulse shaping apparatus (as derived in section 2.2) is given by:

$$e_{out}^{00}(t) = \sum_{-\infty}^{\infty} C_n e_{in}(t + \tau n) \tag{65}$$

where the coefficients C_n are given by equation 31 and are only independently specified by the N pixel filters B_n for $-N/2 \leq n < N/2$. Other values of n correspond to replicas. Within this time window arbitrary waveforms can be be produced for the appropriate values of the coefficients C_n, though the temporal resolution of the desired waveform is still limited by the bandwidth of the input pulse. In appendix A, the appropriate values for C_n are determined for an arbitrary waveform.

To determine the appropriate mask pattern B_n which produces the desired values C_n, one must recall equation 31. Rather than B_n being specified by the inverse discrete fourier transform of C_n, it should be given by the inverse discrete fourier transform of C_n after compensation for the gap contribution, the sinc envelope resulting from discrete sampling, and the gaussian envelope resulting from diffraction by the mask. If the mask filter B_n is capable of both amplitude and phase manipultion then this is trivial. B_n should be given by the inverse discrete fourier transform of A_n, where A_n is given by:

$$A_n = \frac{\eta C_n - \partial_{0,n} B_g (1-r)}{\frac{\sin(r\pi n)}{r\pi} \exp\left(-\left(\frac{\pi w_0 n}{wN}\right)^2 / 2\right)} \qquad (66)$$

for the desired values of C_n for $-N/2 \le n < N/2$, and for η determined self-consistently so as to normalize the desired waveform such that $|B_n| \le 1$. Note that the subscripts n are labelled such that the filter B_0 corresponds to the pixel on the mask on which the central carrier frequency ϖ is incident. For r=1 (no gaps or negligible gaps) equation 66 simplifies and A_n needs only to be scaled for the gaussian and sinc envelopes.

The above prescription was used to determine the correct mask pattern to compensate for gaps and pixellation in the generation of figure 4d (as described in section 3.3e). Recall that the desired waveform consisted of four equal-amplitude phase-locked pulses spanning 2 psec and was generated with a hypothetical mask consisting of 70 100-μm pixels and 15-μm gaps. Within the 4-psec time window the desired waveform is easily produced. However outside this time window low-amplitude replica pulses are necessarily produced as well.

The replicas become larger as the temporal extent of the desired waveform occupies more of the time window $-N\tau/2 \le t < N\tau/2$. Both the desired waveform and the replicas are modulated by the sinc and gaussian envelopes. The sinc envelope modulates the temporal profile of the output waveform across its entire transverse spatial profile. As derived in section 4, the output waveform undergoes a time-dependent transverse spatial shift along its temporal profile as a result of diffraction. The gaussian envelope reflects the fact that this transverse spatial shift removes light amplitude away from the central gaussian spatial mode. To reduce

the amplitude of replica pulses, the spot size of the frequency components incident on the mask can be made larger, thus narrowing the gaussian envelope. This is equivalent to making the spot size of the input pulse smaller, thus increasing the relative magnitude of the transverse spatial displacements. Thus the replica amplitudes in the temporal profile of the gaussian spatial mode of the output waveform can be made very small by narrowing the gaussian envelope, but the absolute energy (across the entire transverse spatial profile) is only modulated by the sinc envelope.

In practice, if one generates waveforms that occupy only a third of the available time window, the largest replica will have an amplitude about one fifth of the desired waveform's amplitude and within the central gaussain spatial mode (with $w_0=w$) the amplitude of the largest replica is about one twelfth of the desired waveform's amplitude.

2.6.2 Two Mask Filtering and Iterative Improvement of the Shaped Waveform

A single LC filter cannot independently control retardation and attenuation, but as shown in section 2, when two LC filters are combined the product of their filters can provide independent control. In the case of two LC SLMs with some finite separation, the combined filter is not necessarily given by the product of the individual masks because the propagation of light diffracted by the first mask pattern will result in a modified spatial profile incident on the second mask. In section 5, the exact space-time profiles of light shaped by two spatially-separated masks were calculated. Determination of the apppropriate mask patterns $B_n^{(i)}$ for a specified waveform given by the coefficients C_n would require the inversion of equations 55, 57, 61. In general this would have to be done

numerically. However the temporal modifications resulting for the separation of the two LC SLMs and some misalignment with respect to their displacements from the focal plane(s) are in general small. In practice, it is best to assume that the two LC SLMs do approximate a single device capable of independent control over spectral amplitude and spectral phase. In section 5 it was shown that this is exactly true for two properly positioned masks in an '8-f' arrangement and also true for the temporal profile of the gaussian spatial mode of a waveform shaped by two orthogonal LC SLMs with some finite separation in a 4-f arrangement.

To generate user-specified waveforms one implements the prescription in the previous section to determine the mask filter for a single mask B_n for the desired coefficients C_n. The appropriate filters for the individual masks $B_n^{(i)}$ are then determined according to section one so that their product equals the hypothetical single mask pattern B_n.

Figure 6 illustrates a simulation of the temporal amplitude of the gaussian spatial profile of a waveform shaped by two LC SLMs (with 128 95-μm pixels and 5-μm inter-pixel gaps) that filter orthogonal polarizations in a 4-f apparatus. The desired waveform consists of three pairs of equal amplitude pulses with the relative amplitudes of the three pulse pairs given by the ratio 2:4:3. The six pulses each have the same optical phase. The spot size of individual frequency components in the focal plane is specified as 80 μm. The masks are separated by 5 mm and the first mask is displaced from the focal plane by +1 cm. Figure 6a gives the amplitude of the shaped waveform for a mask without any compensation ($A_n=C_n$). The gap term at t=0 and the modulation of the pulse amplitudes is clearly evident. Figure 6b shows the amplitude of the shaped waveform using equation 66 to determine A_n. The spotsize w_o

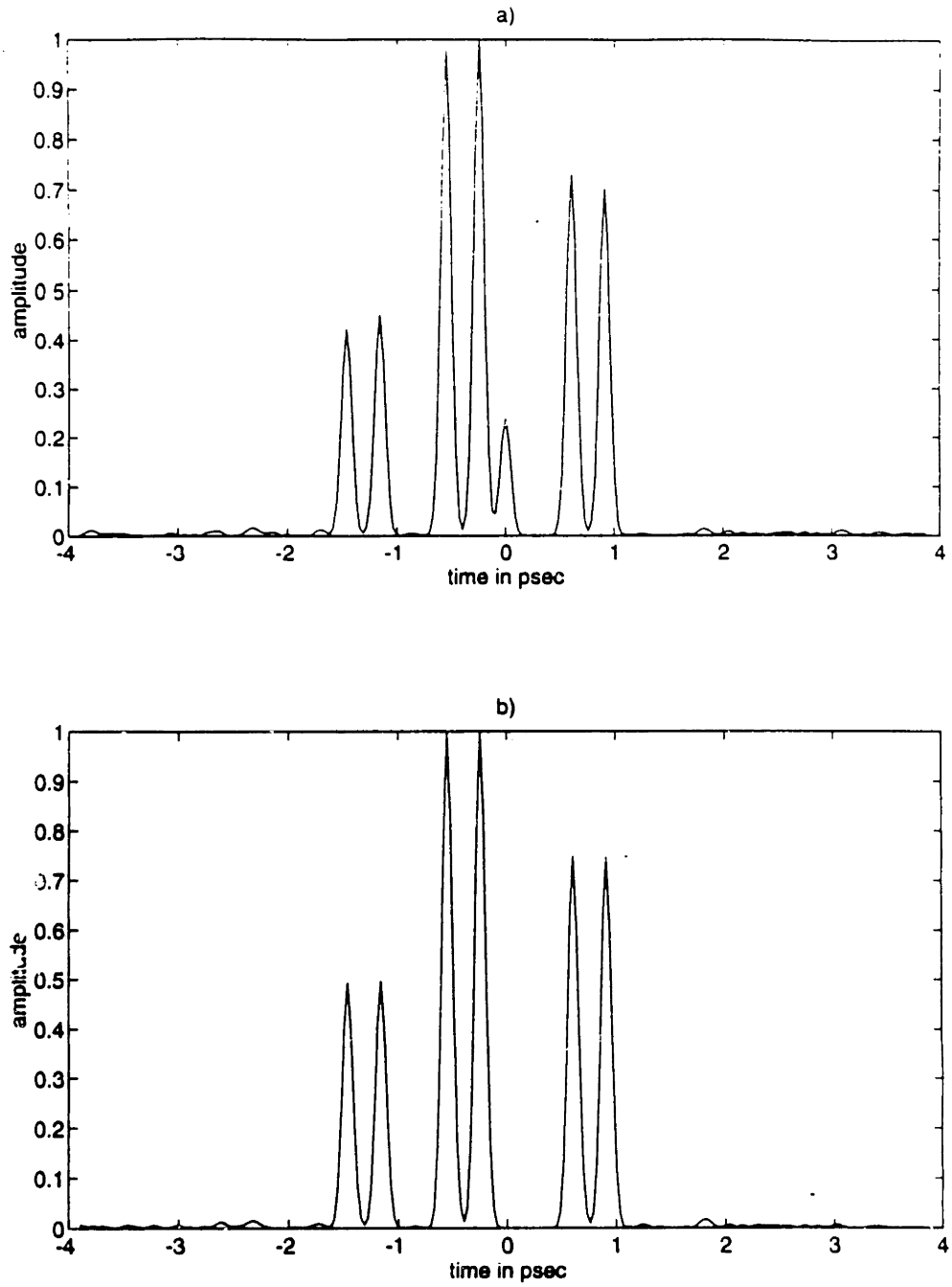

Figure 6. Simulations of the time-dependent amplitude profile of the gaussian spatial mode of a waveform shaped using two LC SLMs that filter orthogonal polarizations in a 4-f apparatus. The masks are displaced by 1 cm and 1.5 cm from the focal plane. The desired waveform consists of three equal-amplitude pulse pairs with relative amplitude 2:4:3. Figure 6a gives the output waveform for a mask pattern derived by discrete sampling of the fourier transform of the desired waveform, without compensation for impixellation, finite gap effects, and diffraction. Figure 6b gives the output waveform for a mask pattern determined according to equation 66.

used in the gaussian envelope (equation 29) is that of an individual frequency component incident on the first mask. Figure 6b shows that the desired wavefom can be produced with excellent fidelity. The somewhat noisy baseline results from the finite separation between the two masks and the displacement of the combined device from the focal plane. However the mask separation and displacement from the focal plane are relatively large compared to the placements that can be acheived experimentally. Therefore the assumption that the two LC SLMs can combine to produce an arbitrary spectral mask filter given by the product of their individual mask patterns seems well within experimental tolerances.

An exception to this is the gap contribution at t=0 for LC SLMs that do not filter orthogonal polarizations and thus produce multiple diffraction. Because the effective pixel width of the gaps is very small, diffraction by these features is manifested for shorter propagation distances as predicted by the size of the parameter $\bar{z}\lambda/w^2$ (as discussed in section 5.3) where w is replaced by the gap width.

Figure 7 shows a simulation of the temporal amplitude of a waveform shaped by two LC SLMs configured as a phase and amplitude masks (masks that filter non-orthogonal polarizations) in a 4-f arrangement. Unless otherwise stated, the parameters for the simulation, such as the desired waveform, are the same as in figure 6. The two mask filters are specified such that their product is given by the inverse discrete fourier transform of C_n, and so the gap and envelope contributions to the output waveform are not being explicitly compensated for. The two masks are positioned symmetrically about the focal plane with a separation of 0-mm, 3-mm, and 3-cm, for figures 7a, 7b, and 7c respectively. While the baseline noise increases with mask separation, the gap term at t=0 actually

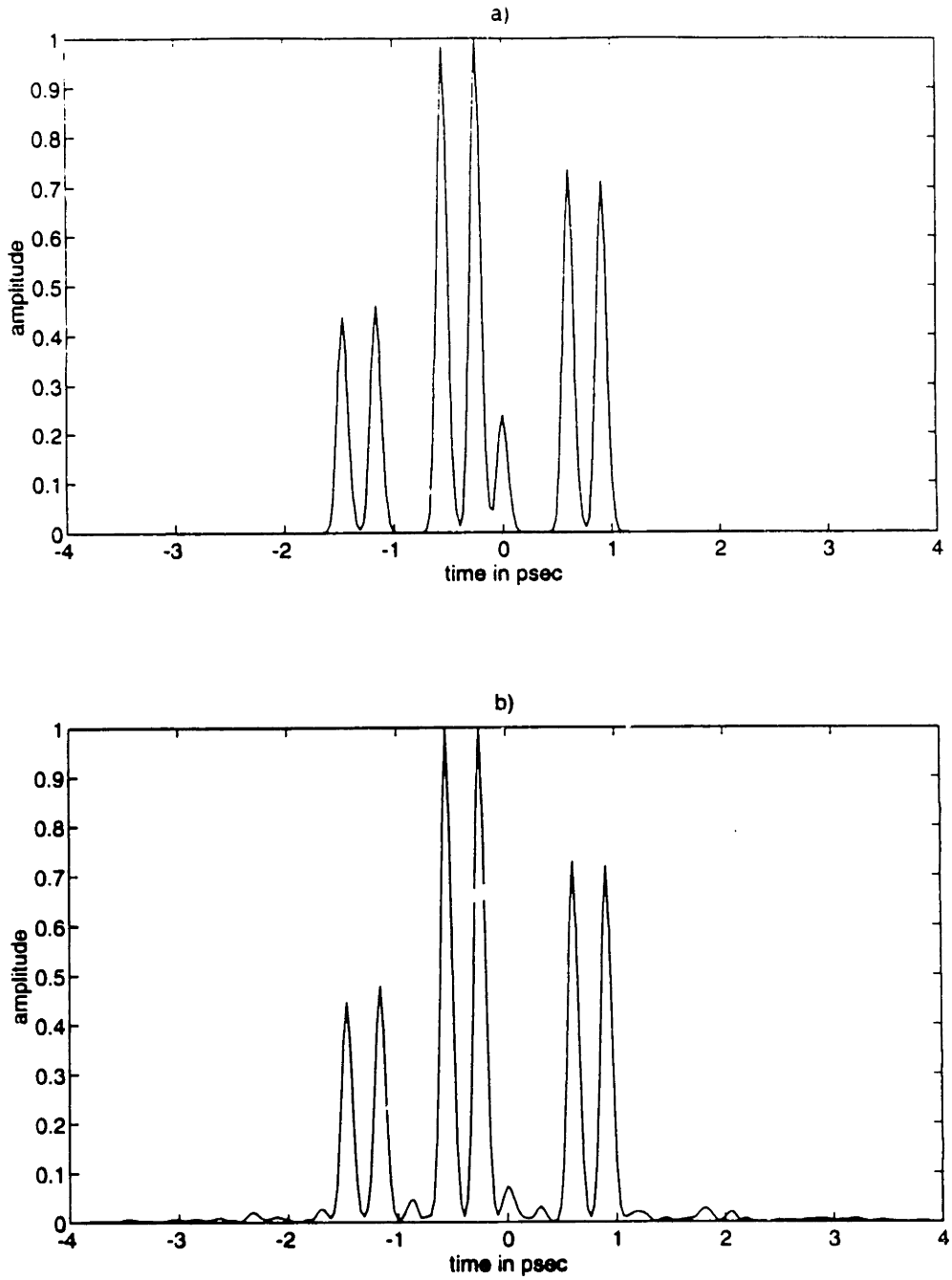

Figure 7ab: Description on next page.

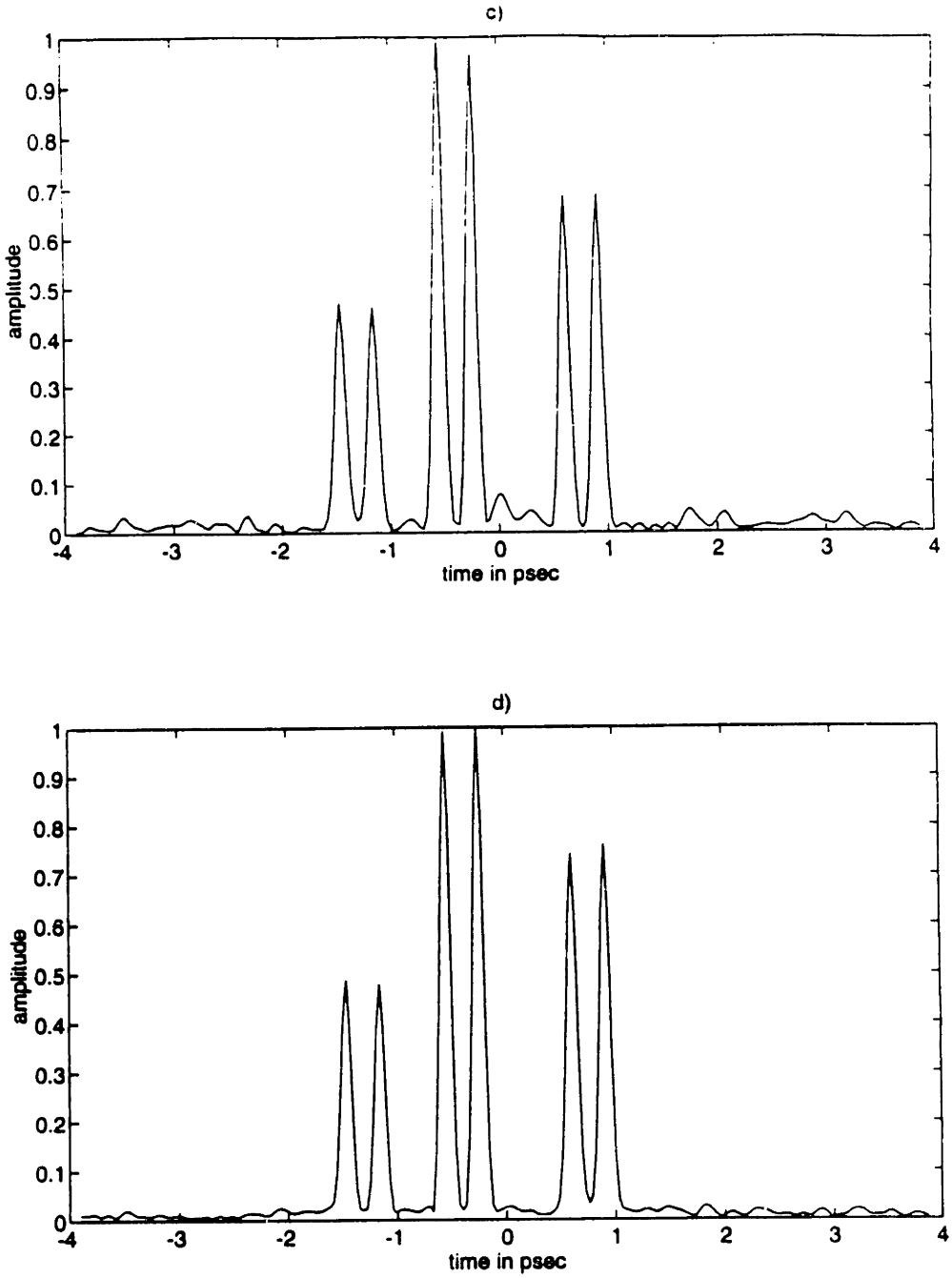

Figure 7a-d. Simulation of the time-dependent amplitude profile of the gaussian spatial mode of a waveform shaped using two LC SLMs that filter non-orthogonal polarizations in a 4-f apparatus and that are positioned symmetrically about the focal plane. The masks are separated respectively by 0 mm, 3 mm, 3 cm, and 3 cm, in figures 7a-d. The desired waveform is the same as in figure 6. The mask pattern for figures 7a-c are determined by discrete sampling of the fourier transform of the desired waveform. In figure 7d the mask pattern was determined by using the iterative algorithm described by equation 67.

disappears with increasing mask separation. This occurs because the frequency components incident on the gaps of the first mask do not reach the gaps of the second mask as effectively when the mask separation is large.

Implementation of the prescription in section 6.1 would not correctly compensate for the gap contribution in this case. Nonetheless the waveforms in figures 7a-7c are close to the desired waveform. This suggests that the filter given by $A_n=C_n$ is a reasonable initial guess which if needed, can be followed by iterative imporvement of the fidelity of the generated waveform. This is the starting point we have used in in generating a numerical algorithm to derive the appropriate mask patterns for a desired waveform that is not produced with sufficient accuracy by the previous prescription.

For the 'jth' guess $A_n^{(j)}$, the mask filters $B_n^{(1)}$, $B_n^{(2)}$ for the two LC SLMs are determined such that their product is given by the inverse discrete fourier transform of $A_n^{(j)}$. The coefficients $C_n^{(j)}$ for the output waveform given by equation 65 are then determined according to equations 55, 57, or 61, depending on the experimental arrangement. To improve the guess for $A_n^{(j)}$, the values for $C_n^{(j)}$ are compared to the desired coefficients C_n, and the next guess $A_n^{(j+1)}$ is determined according to:

$$A_n^{(j+1)} = A_n^{(j)} + \frac{C_n - C_n^{(j)}}{p} \qquad (67)$$

The initial guess is usually given by $A_n^{(0)} = C_n$ and the parameter p is typically 4. We have found that this algorithm usually converges within about 20 iterations and can compensate for some systematic misalignment.

Figure 7d shows a simulation of the temporal amplitude of the gaussian spatial mode with the filters for the two LC SLMs determined according to this algorithm and with the two masks separated by 3cm as in figure 7c. The waveform noise in the baseline is both smoothed and reduced in intensity in comparison to the waveform in figure 7c.

A more dramatic example of the implementation of this algorithm is given by the simulation illustrated in figure 8. In this case the registration of the two masks is off by 30-μm. Clearly the assumption that the two combined LC SLMS are equivalent to a single mask capable of an arbitrary filter is no longer valid in this case. The desired waveform is identical to that of figures 6 and 7. The two LC SLMs are configured to filter orthogonal polarizations and are situated symmetrically about the focal plane of a 4-f pulse shaping apparatus with a separation of 3-mm. Figure 8a shows the temporal profile of the gaussian spatial mode of the waveform shaped with mask filters determined according to $A_n=C_n$. The lack of registration considerably degrades the fidelity of this waveform. Figure 8b shows the waveform produced after 20 iterations of the algorithm described by equation 67. The resulting waveform reproduces the desired one with excellent fidelity.

2.6.3 Single Phase Mask

There has been a significant amount of work by Weiner and coworkers on shaped waveforms using prefabricated masks that manipulate only the spectral phase [34,19]. In these works the pixel widths can be varied but usually involve only binary filters. For example, pulse trains of varying repetition rates have been produced by binary valued phase-only filters made from etched silica substrates in which different repetition rates

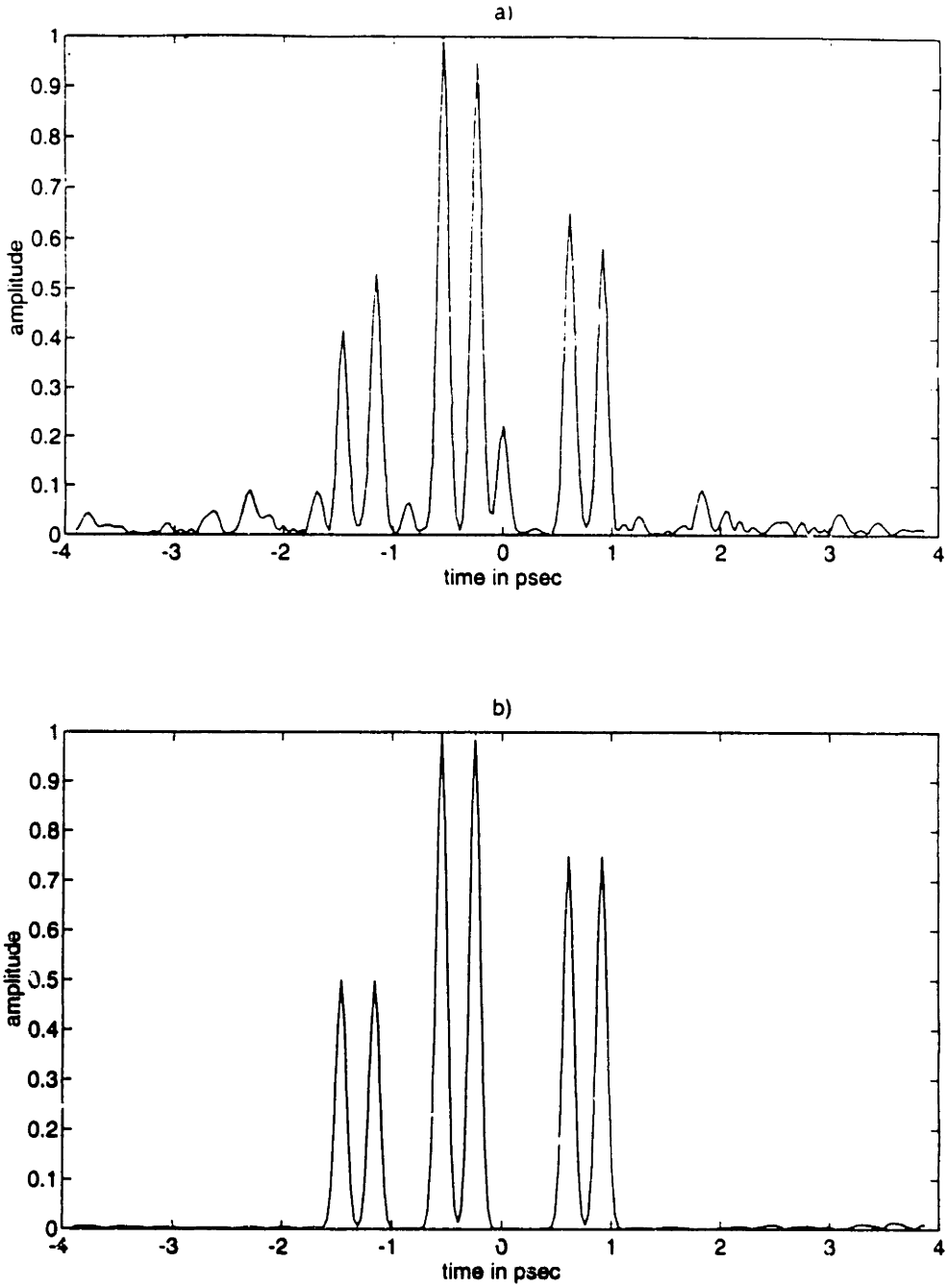

Figure 8. Simulation of the time-dependent amplitude profile of the gaussian spatial mode of a waveform shaped using two LC SLMs with a separation of 3 mm that filter orthogonal polarizations in a 4-f apparatus. The two masks are positioned symmetrically about the focal plane but are laterally translated from one another by 30 μm (i.e. they are no longer in register). The desired waveform is the same as in figures 6 and 7. The mask pattern for figure 8a was determined by discrete sampling of the fourier transform of the desired waveform and assuming that the masks were equivalent to a single device capable of manipulating both spectral phase and amplitude. The mask pattern for figure 8b was determined according to equation 67. This illustrates that iterative improvement of the output waveform can correct for the lack of registration between the two masks.

correspond to different pixel widths. In contrast, a single LC SLM has fixed pixel widths but is capable of gray-scale retardation.

A variety of shaped pulses can be produced with a single liquid crystal mask configured as a phase mask. The shaped waveform is still given by equations 43, 47, and 48, except now A_n is no longer arbitrary, since its discrete fourier transform must be given by:

$$B_n = \exp(i\varphi_n) \text{ where } 0 \leq \varphi_n \leq 2\pi \tag{68}$$

General spectral phase manipulation such as linear, quadratic, and cubic phase sweeps will produce the desired output waveform along with the superposition (and possible interference) of the gap contribution. As the phase manipulation begins to produce temporally extended or displaced pulses, replica wave forms will also contribute to the output wave form. For very large phase sweeps (ones that produce waveforms outside the available time window), the sampling of the discrete pixels will be insufficient and the replica waveforms will interfere with the desired wave form. Because the frequency filter is no longer arbitrary, temporal amplitude and phase for the shaped waveform cannot both be specified. For many applications, pulse trains without specified phase relationships may be useful (7). For this reason we tried to produce optical waveforms with specified temporal intensity profiles but arbitrary temporal phase profiles from a single phase mask.

In this case we must find the spectral phase filter $\exp(i\varphi_n)$ whose inverse discrete fourier transform has a square modulus that approximates the desired intensity of the pulse sequence:

$$I_n^{desired} \approx |A_n|^2 = \left| \frac{1}{p} \sum_{k=-N/2}^{N/2-1} \exp(i\varphi_k) \exp(i2\pi nk/p) \right|^2 \qquad (68)$$

Note that since only the amplitude of A_n is specified, we do not control the interferences between the superposition of input pulses. Thus we will only try to specify waveforms that consist of temporally separated input pulses. To do this the pattern length p (which specifies the number of pulses that are evenly spaced in the time window) must be small enough that the pulses are separated from each other or that the amplitudes of pulses that would interfere are specified to be zero. As p increases it becomes increasingly difficult to find a phase-only filter in which many of the elements of A_n are zero, since we lose the degree of freedom associated with letting the temporal phases of those elements vary.

To produce a series of evenly spaced pulses, for example, we can specify a mask such that:

$$I_n = |A_n|^2 = |\text{inverse discrete fourier transform of } B_n|^2 = \text{constant} \qquad (69)$$

The pixel width and hence the size of the time window is fixed but the number (equal to the length of the filter pattern) of evenly spaced pulses within the time window is integrally varied. The repetition rates F of the generated pulse trains are given by:

$$F = n \frac{w}{2\pi\alpha} \qquad (67)$$

where n is integral and gives the length of the pattern sequence. Thus generation of pulse trains with various repetition rates is possible with a phase-only mask. Clearly if n is too small, there are too few pulses in the train, and if n is too large the pulses in the train begin to interfere with each other. Changing the angle of the gratings or changing the focal lengths of the lenses in the apparatus will both change α and so will also change the available frequencies for the pulse trains, but these adjustments are not made routinely.

The gap contribution will still contribute to the pulse at t=0. This interference can be controlled by adjusting the overall phase of the shaped waveform to add a constant retardation across the spectrum. More complicated pulse trains in which the intensities of different pulses are changed and some pulses eliminated can be made. Again the task is to find some sequence whose length discretizes the time window appropriately and whose phase-only filter satisfies equation 65.

We have used simulated annealing algorithms [35] and simple inverse fourier transform algorithms to determine the phases φ_n that best satisfy equation 65 for a variety of waveforms. These were used to generate the mask filters for the phase-only waveforms which included pulse trains with variably repetition rates from 1.10 THz to 3.95 THz with 0.22 THz intervals. The overall intensity envelope of the pulse train could also be manipulated, and flat-topped and 'descending' pulse trains were also produced. Experimental measurements of these waveforms will be shown in the next section.

2.7. INITIAL PULSE SHAPING EXPERIMENTS

Our original pulse shaping experiments employed LC SLMs purchased commercially from Meadowlark Optics. The SLM pixel array is 2-mm high by 8-mm across with seventy 100-micron pixels and 15-micron gaps between adjacent pixels. The liquid crystals are driven by a 2 kHz bipolar square wave varying between 0 and 10 volts. The long axis of the liquid crystals are initially aligned along the **y**-axis and twist in the **y-z** plane toward the **z**-axis with an applied voltage. As before our convention is that the pixel array is aligned along the **x**-axis and that light propagates along the **z**-axis through the thickness of the LC layer. Therefore for light polarized along the **y**-axis (usually perpendicular to the table), the SLMs act as phase masks.

The first test was to reproduce results from Weiner and co-workers in which a single LC phase mask was used to impart simple patterns such as linear, quadratic, and cubic spectral phase sweeps, as well as binary patterns [21,22]. A 4-F grating compressor as illustrate previously in figure 1 was employed with the addition of two half-wave-plates that sandwiched the modulator. The first wave-plate rotated the **x**-polarized light which is preferentially diffracted by the gratings to **y**-polarized light so that the mask could manipulate spectral phase. This rotation is then reversed by the second waveplate thereby optimizing the throughput of the apparatus. Gratings with 1800 lines/mm and 12-cm lenses were used. In subsequent experiments employing two SLMs in an 8-F set-up, 1200 lines/mm gratings were used, in both cases the mask aperture could accommodate the bandwidth of the 70-fsec input pulse and the pulse width was not broadened when traversing the apparatus with a uniform mask pattern. The input pulse was derived from Ti:Sapphire mode-locked

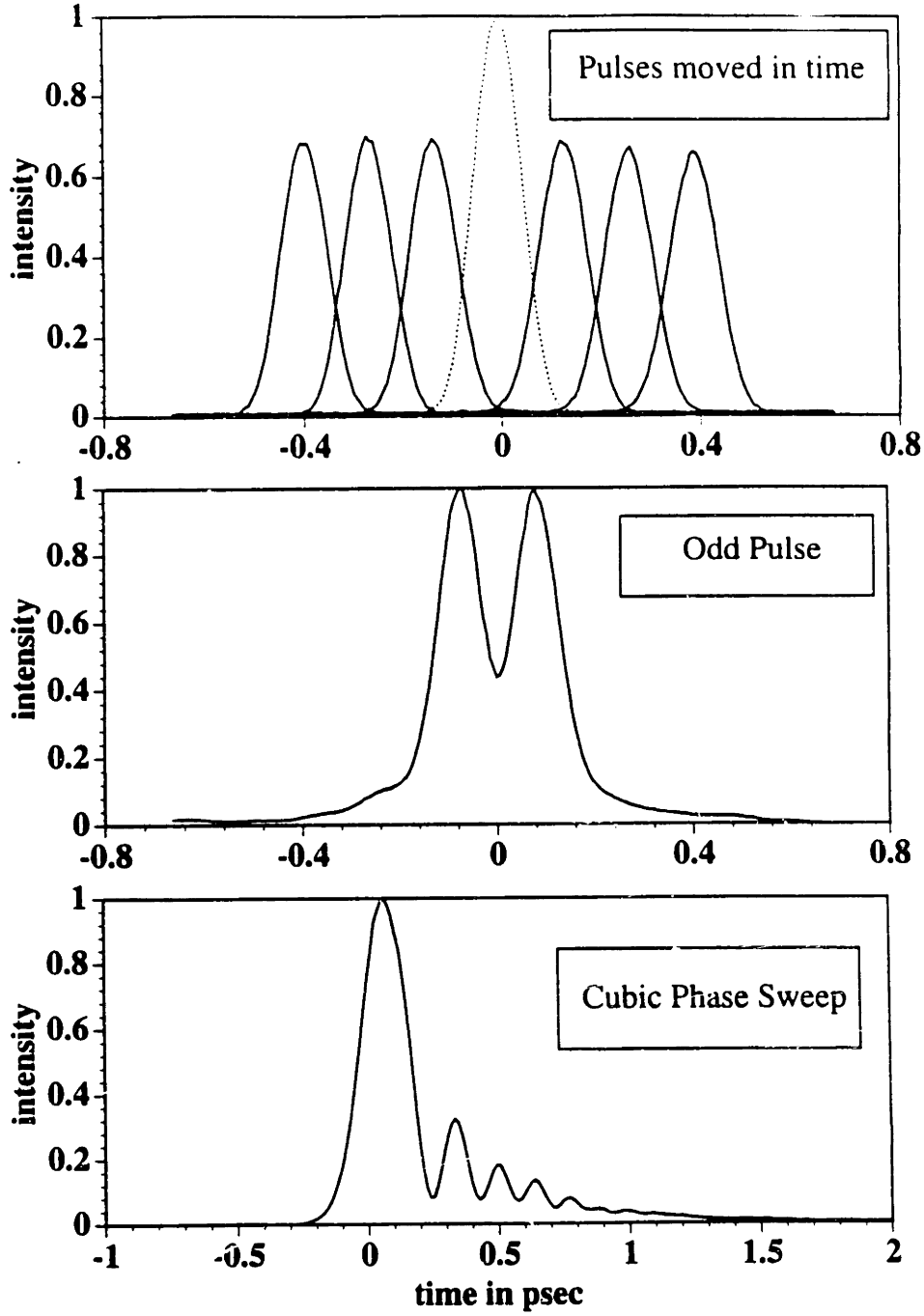

Figure 9: Cross-correlation measurements of waveforms shaped using a single mask for phase modulation.

oscillator operating at 800-nm and 76 MHz with 1 W of average power. In this and subsequent sections, the intensity profile of the shaped waveform are generally characterized by standard cross-correlation techniques which is described in Section 11.

Figure 9 show experimental cross-correlation measurements of shaped waveforms for some simple mask patterns. Figure 9a shows temporally shifted pulses resulting from linear spectral phase of different magnitudes. Temporal shifted pulses have less intensity than the unshaped pulse as a result of diffractive losses from the gaps between the pixels. Figure 9b shows the an 'odd or zero-amplitude' pulse in which half the spectrum undergoes a pi phase shift. Because of the finite-duration of the probe pulse performing the cross-correlation, the observed signal at t=0 is non-zero though the actual intensity of the odd-pulse should be zero at t=0. Figure 9c shows the characteristic cross-correlation measurement of a pulse following a cubic spectral phase sweep. Such manipulation can be useful in ultrafast pulse recompression.

To show that a single phase mask can also generate more complicated waveforms, the algorithms previously described in section 6 were used to generate pulse trains with specified intensity profiles. Figure 10 show three pulse trains with varying repetition rates which were generated using phase-only filters. Pulse trains with repetition rates from 1.10 to 4.39 THz in 0.22 THz intervals were easily produced. Figure 11 show additional pulse trains in which the phase filter has been modified to generate flat-topped and descending sequences of pulses. In these case replica pulses are visible (though with small intensity) near +/- 4 psec.

These results show that very complicated waveforms can be produced using a single phase mask. Nonetheless, many features of the

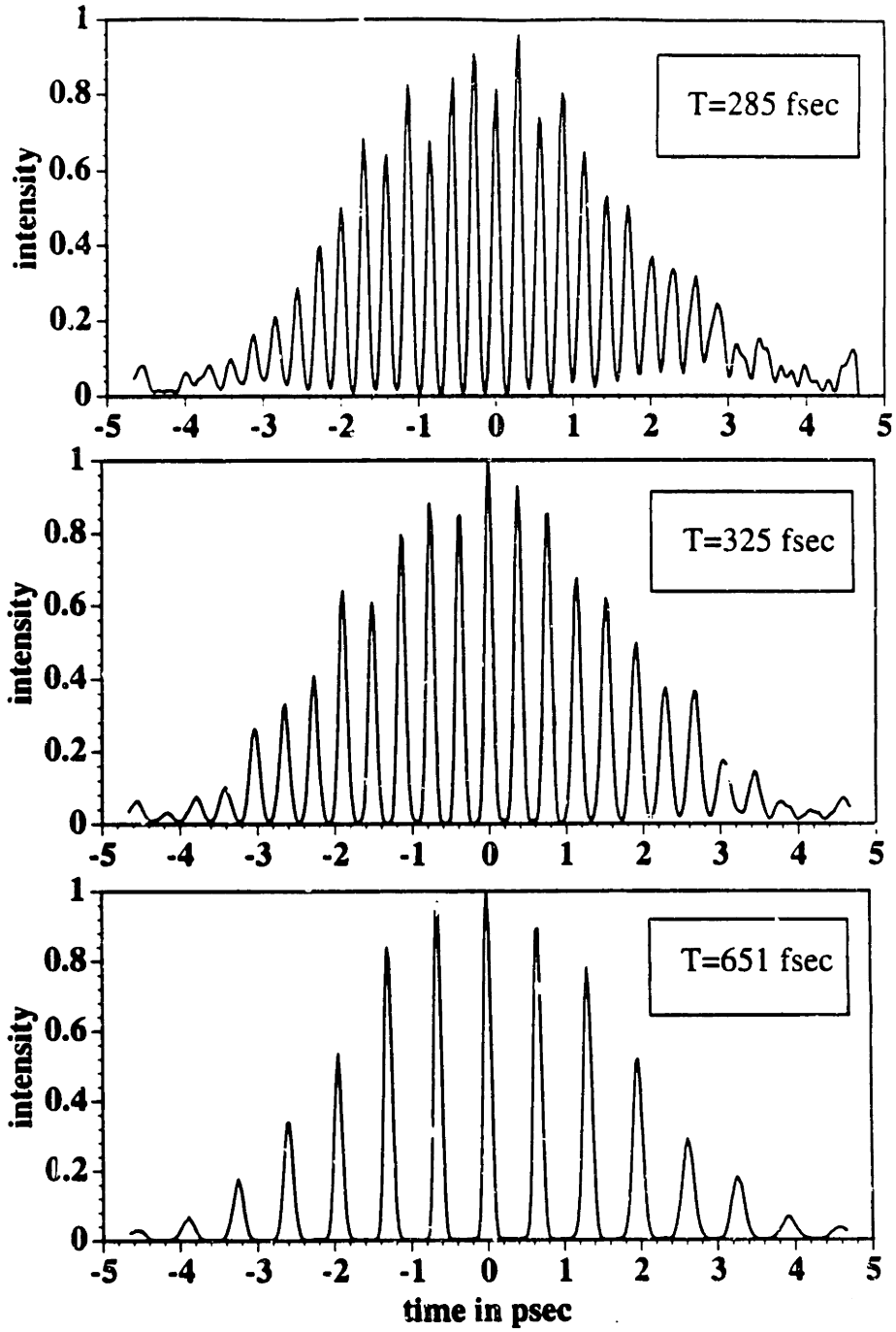

Figure 10: Cross-correlation measurements of multiple-pulse waveforms shaped using a single mask for phase modulation. The repetition rate of the pulse train can be varied by the phase-only spectral filter. The number in the insets give the repetition period.

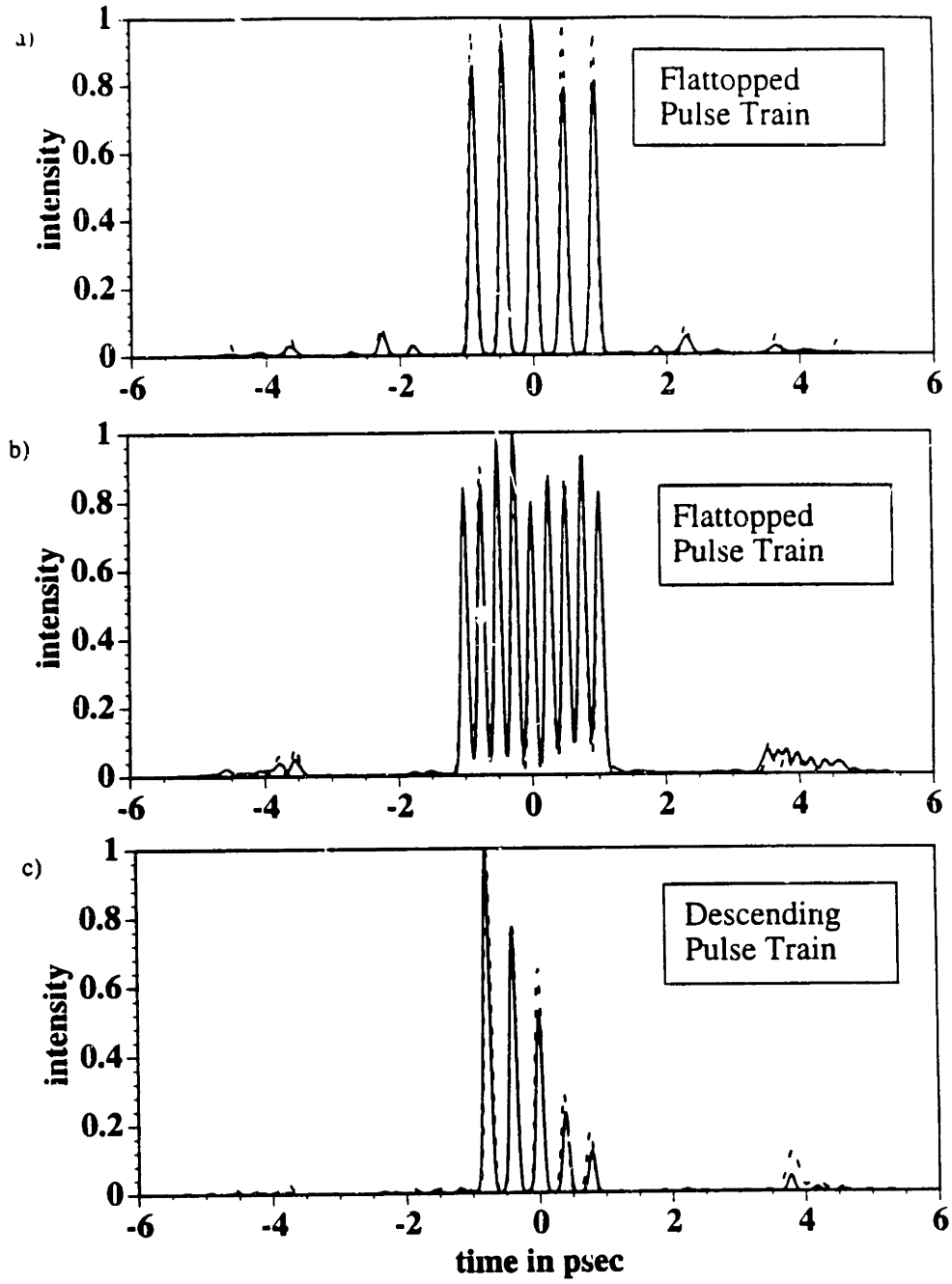

Figure 11: Cross-correlation measurements of multiple-pulse waveforms shaped using a single mask for phase modulation. The envelope function for the pulse trains can be modified by a properly chosen spectral phase filter.

waveforms are not specified. For the case of the pulse trains, the optical phase relationship between subsequent pulses is fixed but unspecified. This parameter must be allowed to vary to generate the desired temporal intensity profile given a fixed spectral amplitude profile. If the independent filtering of both spectral amplitude and spectral phase is possible, arbitrary temporal profiles can be specified subject to bandwidth limitations and the spatial resolution of the mask as discussed in section 3.

As discussed in section 2, independent filtering of both spectral amplitude and phase is possible if two LC SLMs are employed. Our initial set-up with two masks is shown in figure 12. Half-waveplates and polarizers were used to configure the first mask as an amplitude mask for the incoming **x**-polarized light and the second mask as a phase mask. As described in section 2, the amplitude mask is accompanied by a variable phase retardance that must be compensated by the second phase mask. The polarizers nearest to the two gratings are actually redundant and were placed to guarantee good polarization purity.

Figure 13 show experimentally generated waveforms with shaped temporal amplitude and phase profiles. Figure 13a shows a 550-fsec optical square pulse and figure 13b shows a temporally-displaced 350-fsec optical square pulse. Figure 13c shows a three-pulse sequence in which the timing and optical phase relationships have been specified. None of these waveforms could be produced using either a single phase or amplitude mask. The dashed curve in all three cases indicate the anticipated waveform assuming optimal alignment and calibration. The time window for this set-up is only 2.9 psec since 1200 lines/mm gratings were used. (For the phase-only filtering results using 1800 lines/mm gratings, the time

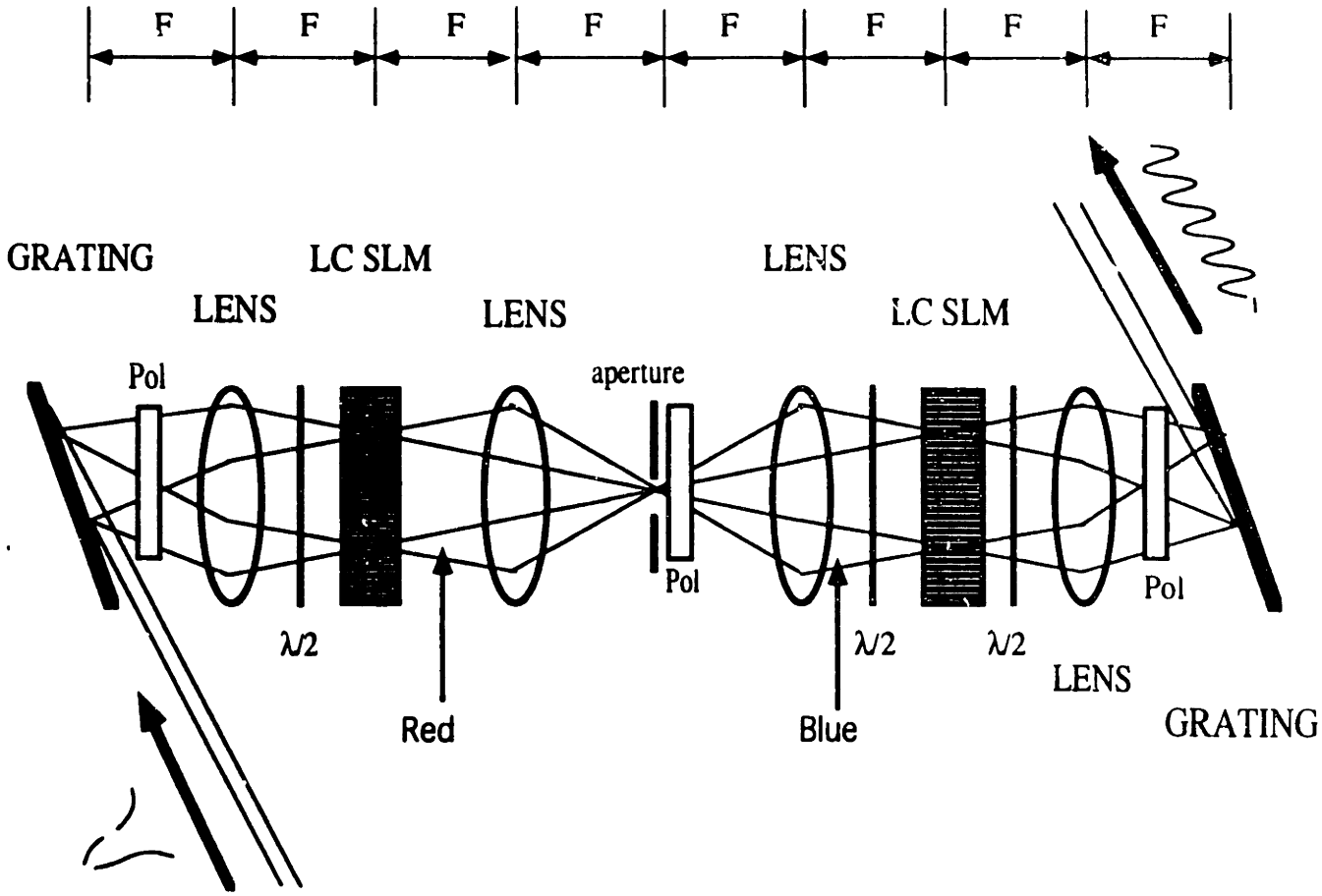

Figure 12. The '8f' pulse shaping apparatus. In this case two 1:1 telescopes are placed between parallel gratings so that angularly dispersed frequency components are focused and filtered twice. A combination of polarizers (Pol) and wave plates is used so that the first LC SLM attenuates the frequency profile and the second LC SLM manipulates the relative phase of the frequency profile.

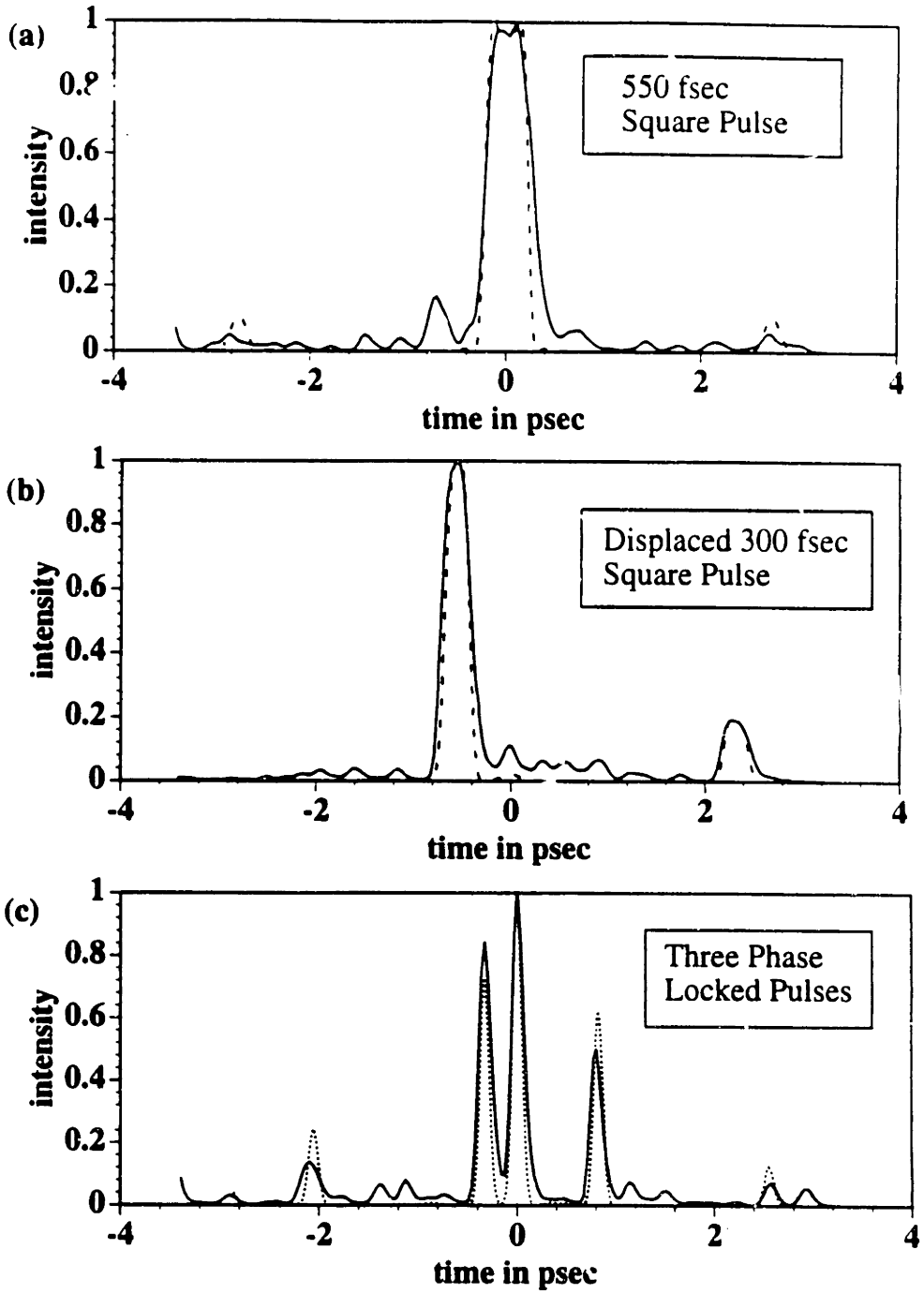

Figure 13: Shaped waveforms produced by two LC SLMs for manipulation of both spectral phase and spectral amplitude. The theoretical fit (dashed curve), which assumes exact calibration and alignment, is also shown. a) 550-fs optical square pulse. b) 350-fs optical square pulse displaced in time. c) Phase-related three-pulse sequence.

window was about 4 psec). In each case replica waveforms can be seen outside this time window.

The results clearly show the desired waveforms and indicate that simultaneous control over the temporal amplitude *and* temporal phase profile of shaped waveforms is possible using LC SLMs. However the results are far from optimal. The number of pixels on the mask could be increased and the gap size reduced. Complications also arise since the two masks need to be exactly in register with each other as well as being properly positioned in the focal planes of the two telescopes. Furthermore the various polarization optics need to be correctly aligned with the long axes of the LCs on the respective masks.

2.8. HIGH FIDELITY PROGRAMMABLE PULSE SHAPING

2.8.1 Generation of high-fidelity waveforms

The dominant factors that limit the range of specified optical waveforms are limitations in temporal resolution according to the available spectral bandwidth of the input pulse (which also restricts the optical carrier frequency of any waveform feature), limitations in temporal range according to the spatial resolution of the mask, and temporally varying transverse spatial profiles resulting from diffraction off the discrete mask pixels. These effects are present even for the ideal case of a single mask capable of arbitrary spectral filtering. Assuming that one is only concerned with the gaussian transverse spatial mode of the shaped waveform, only the temporal envelopes resulting from discrete sampling and diffraction into the gaussian mode and a small correction for the gap contribution at t=0 need to be compensated for as described in section 6.1. For appropriate arrangements, replica waveforms arising from the discrete

sampling are diffracted away from the gaussian transverse spatial mode and so do not contribute significantly.

In practice, even for cases with two masks it is best to consider only these factors as illustrated by the simulations in section 6. The LC device described in section 8 only have inter-pixel gaps of 2-3 microns with approximately 100-micron pixel widths, so the gap contributions become very small. For small gaps it is sometimes best to ignore the gaps altogether when determining the appropriate mask filters, especially for the case of two spatially separated masks that filter non-orthogonal polarizations in a 4-f arrangement (as discussed in section 6.2).

More critical practical concerns are accurate alignment and calibration of the two LC SLMs. As shown in figure 8b, inappropriate registration between the two masks seriously degrades the fidelity of the anticipated waveform. Significant degradation can also occur if the polarization of the incident light and the relative orientations of the LCs in the two SLMs are not matched properly. This reduces the possible extinction of the dual LC filter, and makes it difficult to produce the desired attenuation and retardance for the combined filter. Relative displacement of the LC SLMs should also be optimized though this is less critical.

In our initial pulse shaping attempts using two LC SLMs (section 7), the masks were placed in an 8-f arrangement and a series of polarization optics were used within the grating and lens apparatus to configure the first mask as a phase mask and the second mask as an amplitude mask. Such a set-up should in principle produce high-fidelity shaped waveforms, but in practice proper alignment is very difficult. The two masks must be aligned such that their pixels are in register and the lenses must be aligned properly

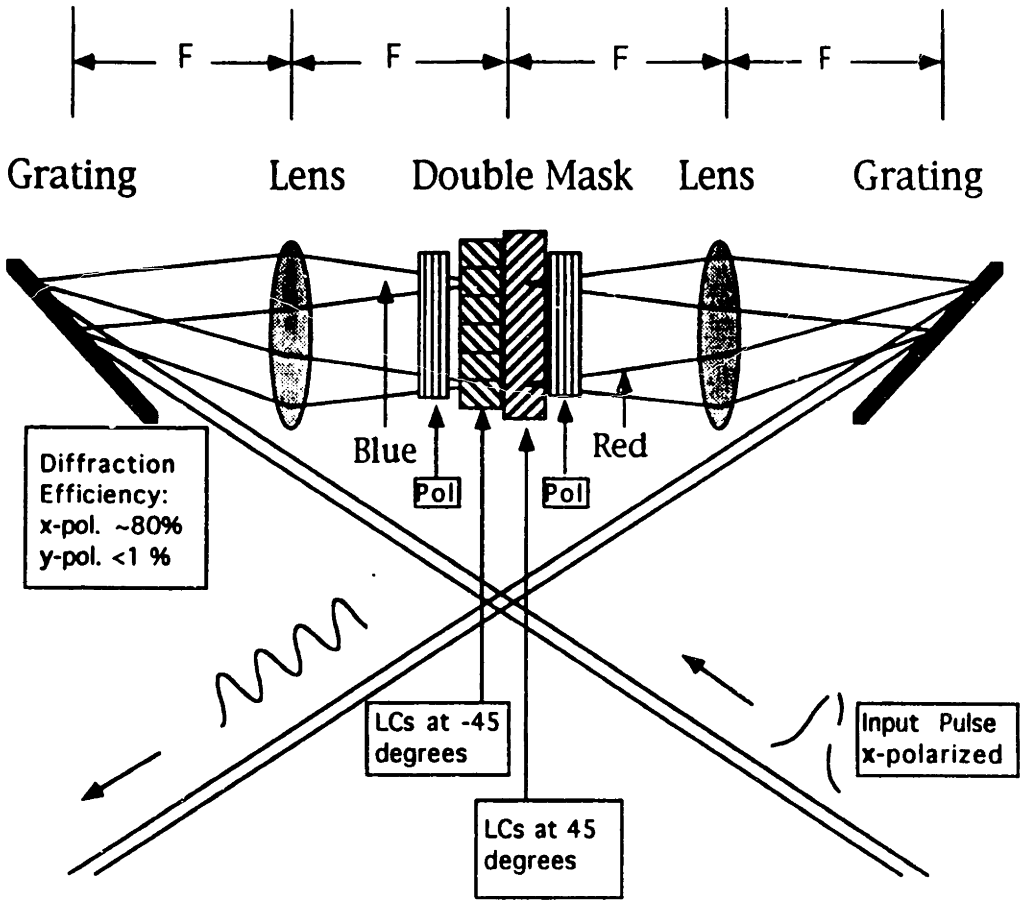

Figure 14: Schematic illustration of the new pulse shaping apparatus. The mask consists of two LC SLMs separated by 2.2 mm, with LCs aligned at +/-45 degrees from the mask (x) axis. The SLMs are sandwiched between two polarizers (Pol's) aligned along the x-axis. The input pulse has a duration of 75 fsec at 800 nm.

parallel to the LCs. The two SLMs are separated by 2.2 mm, but simulations in section 6.2 show that the small separation between the two masks is negligible especially since the two masks filter orthogonal polarizations.

The individual LC SLMs contain 128 97-μm pixels with 3-μm inter-pixel gaps. The larger number of pixels increases the effective resolution of the spectral filter, expanding (to about 6.5 psec) the temporal range over which the shaped waveform can be controlled and reducing the relative amplitude of replicas arising from discrete Fouler sampling. The reduced gap size leads to proportionally reduced transmission of unfiltered light.

The resulting device is effectively equivalent to a single mask capable of independent control over both attenuation and retardance and with gap contributions that are small enough to be neglected. Since the registration and angular orientation of the two masks are optimized (along with the attached polarizers) during fabrication, the user need only position the device within the focal plane of the grating compressor. In addition, either SLM in the combined unit will independently attenuate light so that the two masks can be calibrated within the pulse shaping apparatus. Calibration of the device is described in Appendix B.

2.8.3 Experimental Results

Figure 15 shows cross-correlation measurements of five-pulse sequences generated by the apparatus. The timings, amplitudes, and optical phase relationships between pulses have been specified. The fidelity is far superior to the results of the previous section. The long-time scan in figure 15c also shows that replica waveforms at long times are no longer detectable. Figure 16 show examples of optical square pulses of various

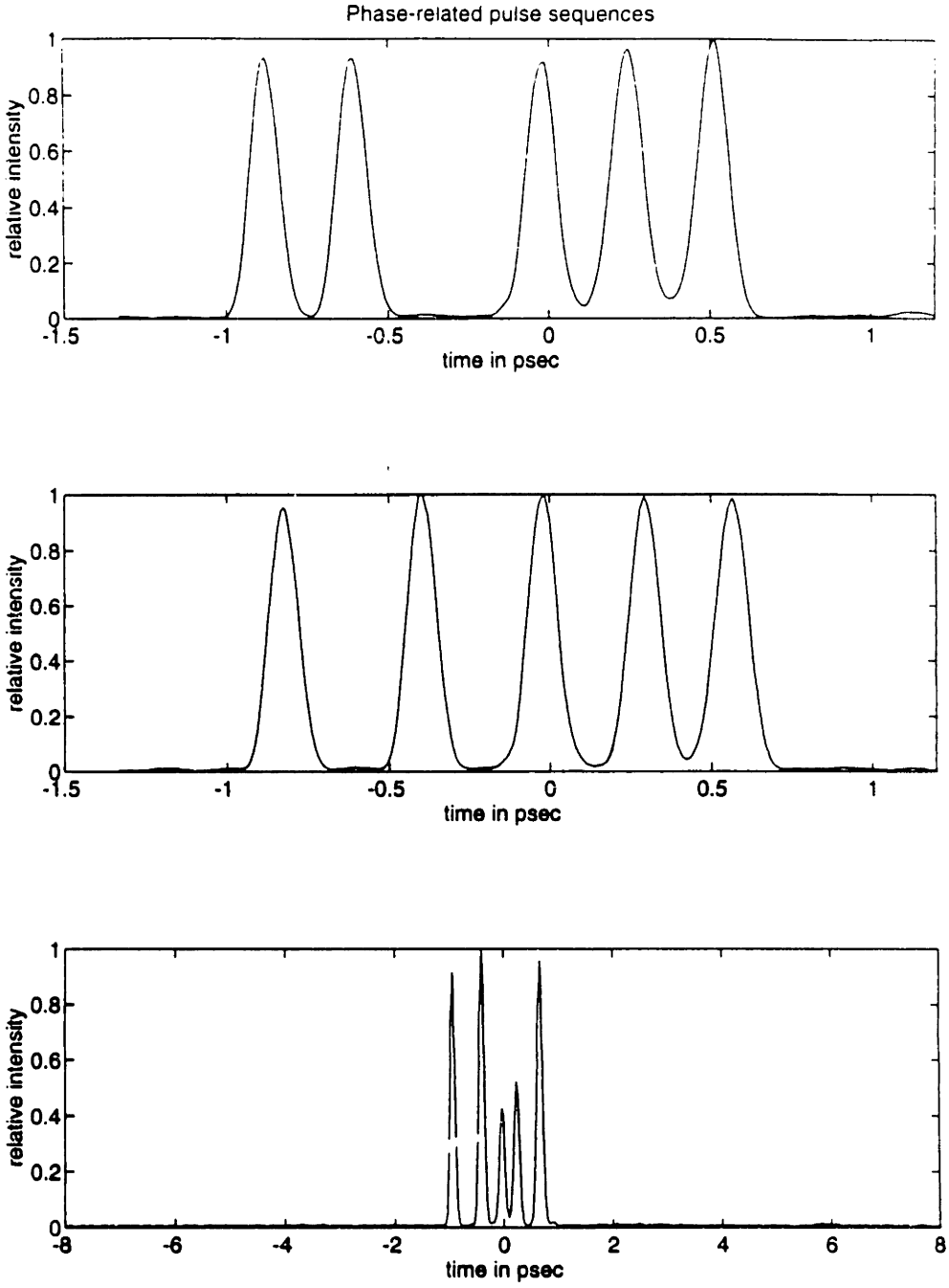

Figure 15: Cross-correlation measurements of shaped waveforms produced by the new pulse shaping apparatus. Five-pulse sequences with specified timings, amplitudes, and optical phase relationships. The last plot shows that, unlike previous efforts, replica waveforms at long times are very weak.

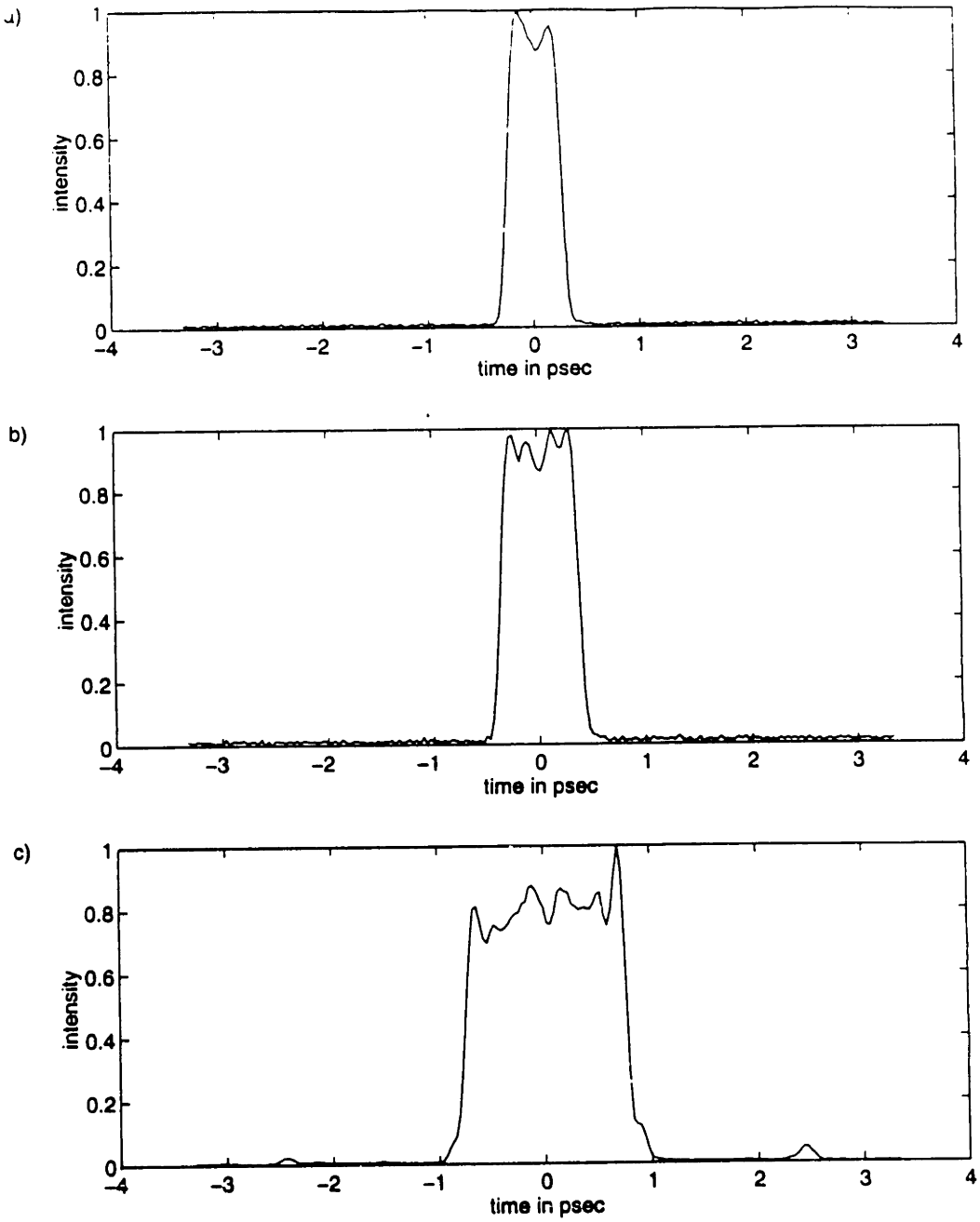

Figure 16: Cross-correlation measurements of shaped waveforms produced by the new pulse shaping apparatus. Optical square pulses of varying durations. Some intensity structure on the top of the square pulse is a necessary consequence of limited bandwidth.

durations. Some structure on the top of the square pulse is a necessary consequence of the limited bandwidth in the input pulse.

Pulse sequences in which the pulses themselves have been shaped are also possible. Figure 17 shows three pulse sequences in which in addition to specifying the timing, amplitude, and phase relationships between pulses, the individual pulses have been 'chirped' to varying degrees. Chirping of a pulse means that optically carrier frequency under its intensity envelope varies from blue to red or red to blue at a specified rate. For the cases illustrated in figure 17, each pulse contains identical bandwidth so that the more a pulse is chirped the longer its duration.

Figure 18 again shows multiple-pulse waveforms in which the timing, amplitude, and phase-relationship between pulses have been specified. These waveforms consist of eight and ten pulses respectively and were used to test the fidelity of the pulse shaping apparatus. As the desired waveform becomes more complex, imperfections in alignment and calibration will more clearly manifest themselves. The dashed curves in the figure show the desired intensity profiles and it can be seen that at about ten features the experimentally generated results begin to differ from the desired results. Nonetheless these results show profound improvements in the fidelity, complexity, and versatility of the waveforms that can be produced. While it is unclear what the waveforms in figure 18 might be applied to, we emphasize that they were produced through a simple computer-controlled interface in which the user simply specifies a desired pulse sequence.

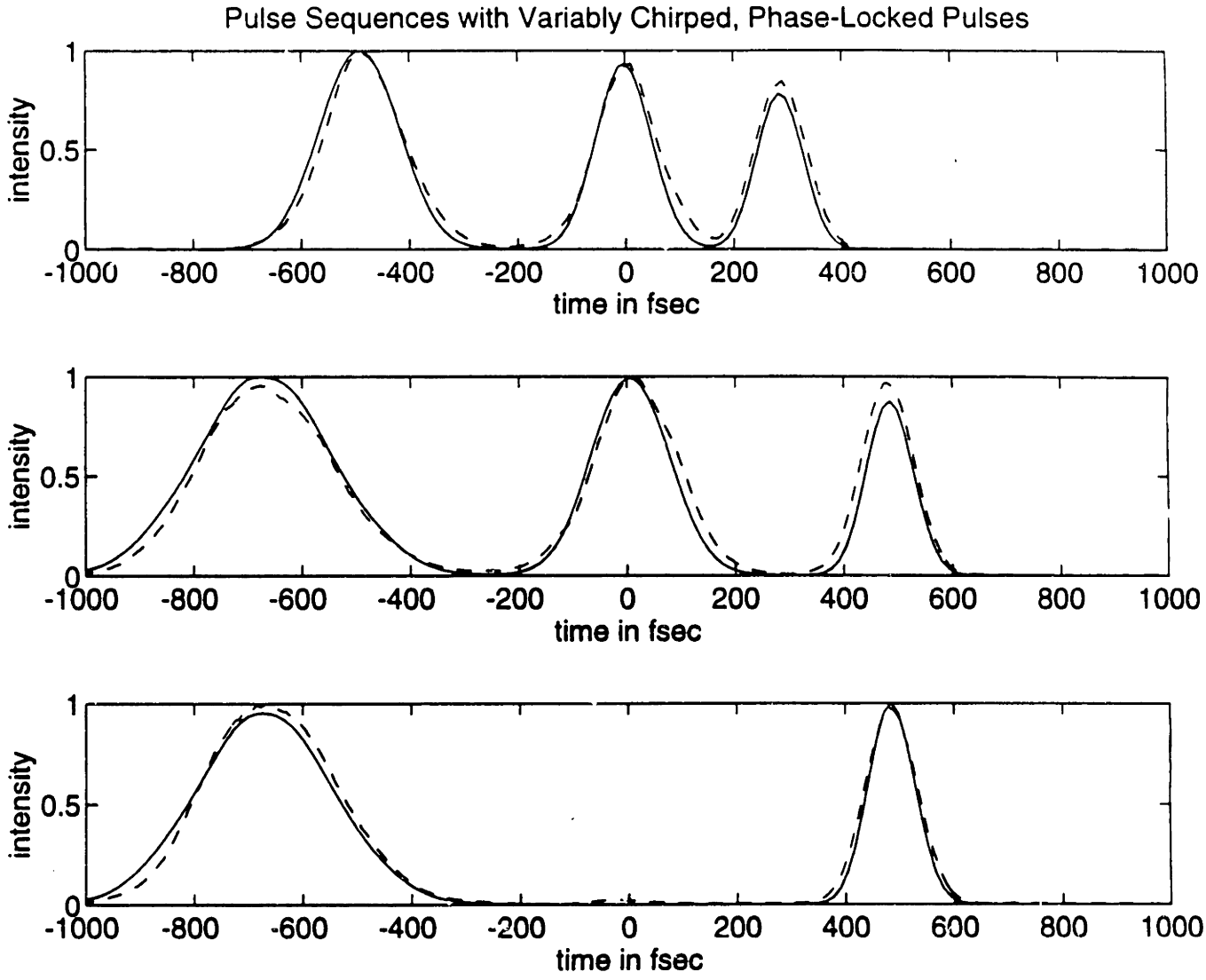

Figure 17: Cross-correlation measurements of shaped waveforms produced by the new pulse shaping apparatus. Multiple-pulse waveforms in which the profile of the individual pulses has also been modified. In this case, some pulses are temporally broadened by 'chirping', producing an instantaneous carrier frequency that varies linearly with time through the duration of the pulse. The dashed curve gives the desired intensity profile.

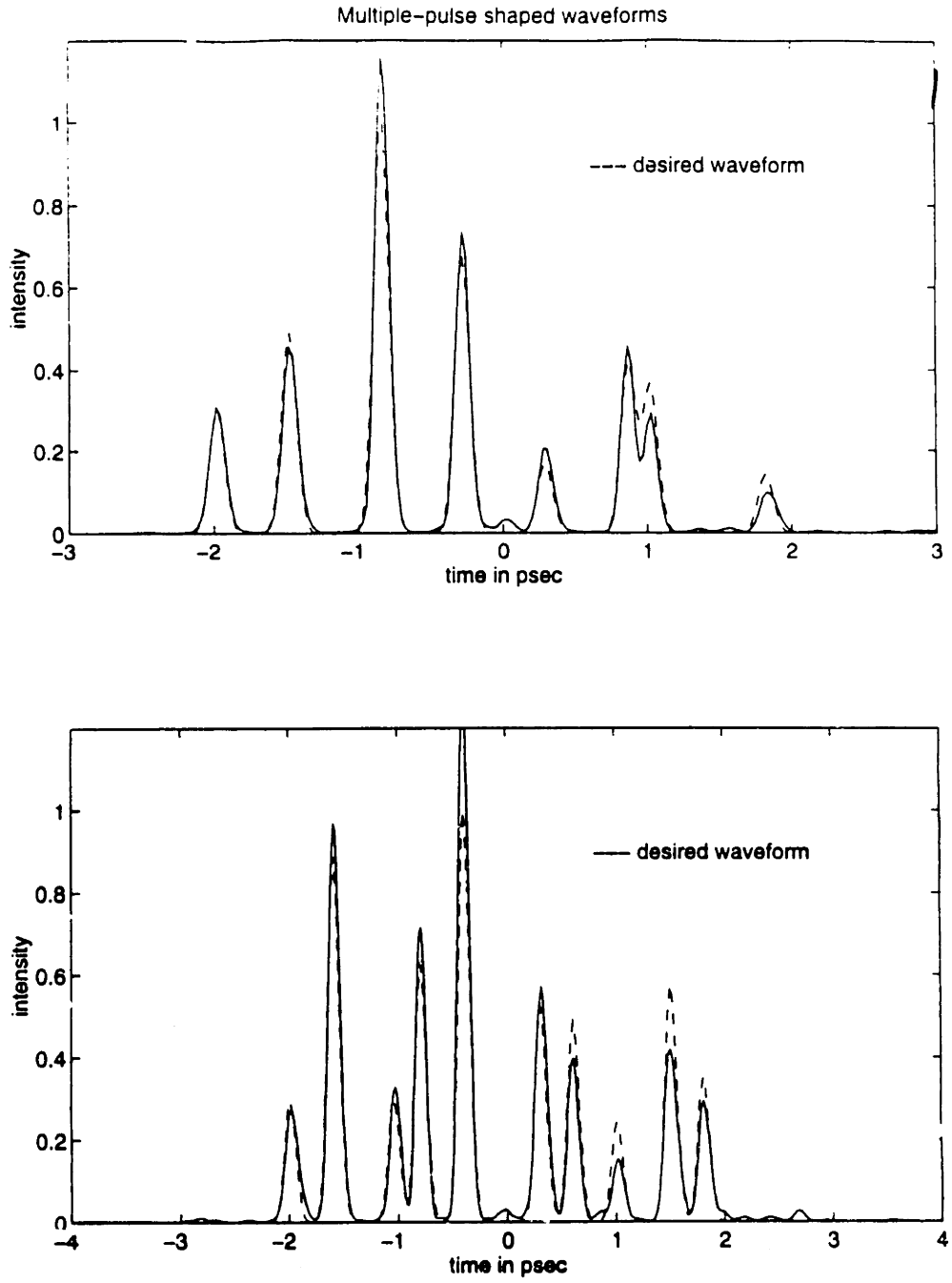

Figure 18: Cross-correlation measurements of shaped waveforms produced by the new pulse shaping apparatus. Multiple-pulse sequences consisting of eight and ten pulses. The timings, amplitudes, and phase relationships have been specified. The dashed curve gives the desired intensity profile.

2.9. SHAPING OF TIME-DEPENDENT POLARIZATION PROFILES

In this section, we show that spectral filtering by the LC masks can also produce waveforms with specified time-dependent polarization profiles. Though we have emphasized that two LC SLMs are required to produce an arbitrary desired waveform, an arbitrary optical waveform actual involves specification of the temporal amplitude and temporal phase profiles for not a single polarization but two orthogonal polarizations. This in turn requires independent control over spectral attenuation and retardance for these two polarizations. We will show that this is actually possible if four LC SLMs are employed. This could also be done if an input pulse is split into two pulses which are shaped by two separate pulse shapers as described in the previous section and the two resulting waveforms, one of which has had its polarization rotated 90 degrees using a subsequent waveplate, are recombined with interferometric accuracy. However such an apparatus would clearly be quite cumbersome.

Shaping of the polarization profile is possible because the LC masks themselves do not attenuate light, rather they produce a tunable birefringence which is used to rotate the polarization of light. It is the polarizers that follow the LC masks that attenuate light. For example, if **x**-polarized light incident on the dual-mask device described in the previous section, the filter B_n for pixel 'n' is given by:

$$B_n = \left(\exp\left(i\Delta\phi^{(1)}\right)(\mathbf{x}+\mathbf{y}) + \exp\left(i\Delta\phi^{(2)}\right)(\mathbf{x}-\mathbf{y})\right)/2 \qquad (72)$$

where $\Delta\phi^{(i)}$ is the voltage-dependent birefringence of the 'ith' LC SLM in terms of retardance. Proper specification of the two birefringences results in a filter capable of independent control over the amplitude and phase for

either the outgoing **x**-polarized light or **y**-polarized light, but not both. The subsequent polarizer is used to retain only the desired polarization. If that polarizer is removed, light is spectrally shaped along two orthogonal polarizations yielding a time-dependent polarization profile. Again since the spectral filter can only be specified for one of the polarizations, the time-dependent polarization profile is not arbitrary. Figure 19a shows the cross-correlation measurement of a phase-related pulse pair generated with the dual-mask device. If the same mask pattern is used, but **y**-polarized light is retained rather than **x**-polarized light, the shaped waveform is given by figure 19b. We can call this the 'conjugate' waveform for light polarized orthogonal to our desired waveform, its profile is fixed by specification of the **x**-polarized waveform. The circles in figure 19 give the theoretical waveforms based on equation 72.

To control the temporal profiles of both polarizations, four LC SLMs can used. For example, if the current device containing the two polarizers and two LC SLMs (as described in the previous section) were followed by two more LC SLMs with their LCs respectively aligned at 45 and 90 degrees to the **x**-axis, the filter B_n for pixel 'n' would be given by:

$$B_n = \cos\left(\left(\Delta\phi^{(1)} - \Delta\phi^{(2)}\right)/2\right)\exp\left(i\left(\Delta\phi^{(1)} + \Delta\phi^{(2)}\right)/2\right) \times\left[\mathbf{x}\cos\left(\Delta\phi^{(3)}/2\right) + \mathbf{y}\sin\left(\Delta\phi^{(3)}/2\right)\exp\left(i\Delta\phi^{(4)}\right)\right] \tag{73}$$

which provides an independent arbitrary filter for both polarizations. Note that the diffraction efficiency of the gratings, which is usually polarization-sensitive, also needs to be considered.

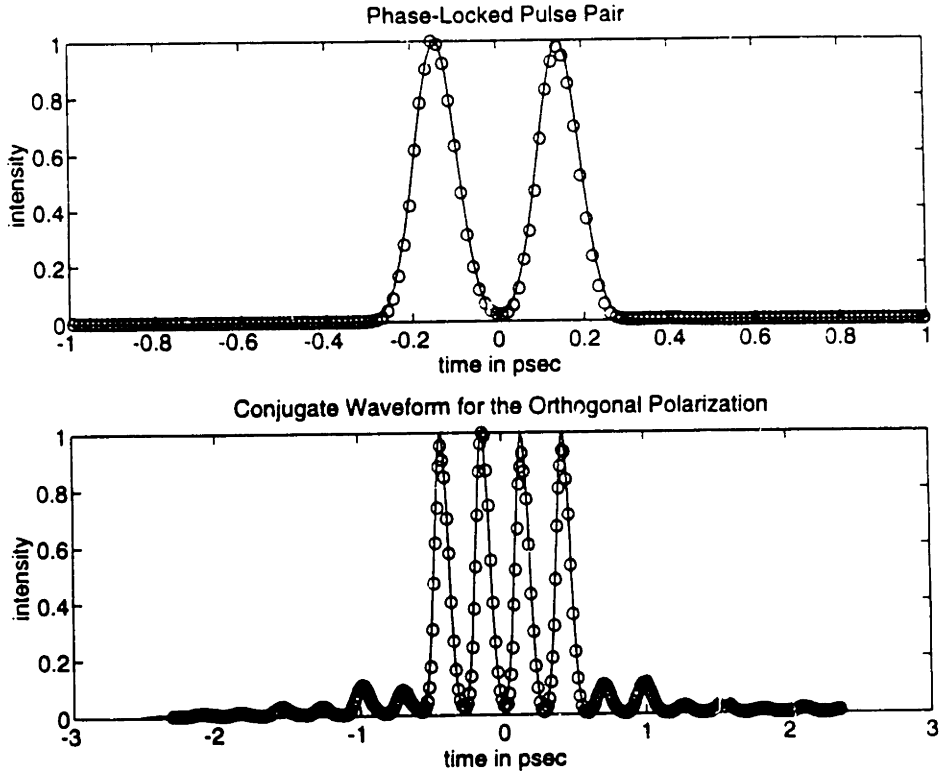

Figure 19: Cross-correlation measurements of a phase-related two-pulse sequence and the 'conjugate' waveform produced at the orthogonal polarization. The circles give the anticipated results based on the theoretical spectral filters.

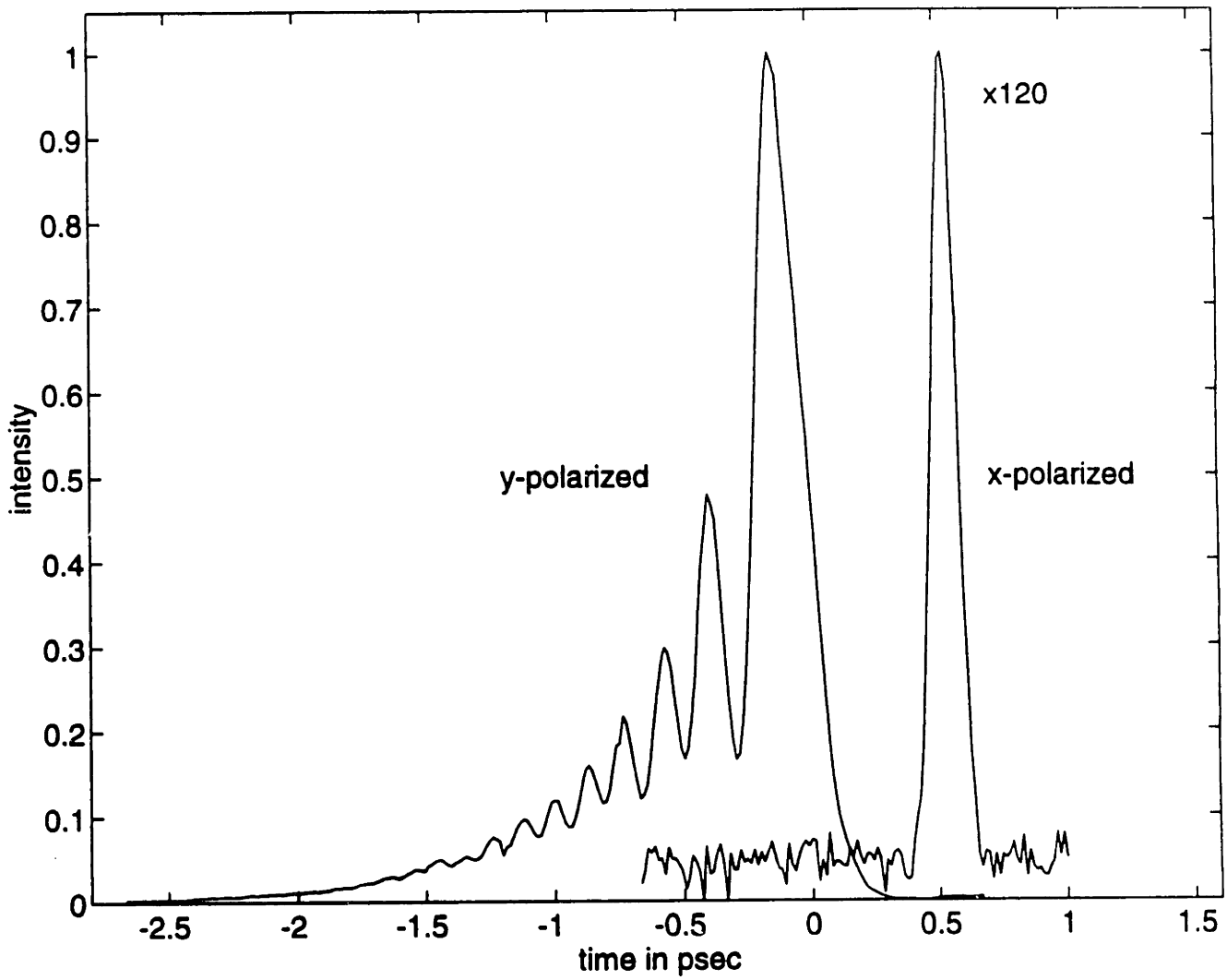

Figure 20: Cross-correlation measurements of the orthogonal (x and y) polarizations of a waveform produced by the pulse shaping apparatus. The specified waveform consists of an x-polarized pulse with a cubic spectral phase sweep and a y-polarized pulse with a linear spectral phase sweep.

In the current arrangement, the composite LC SLM device can produce an arbitrary spectral phase filter for orthogonal polarizations. To demonstrate the generation of waveforms with controlled polarization profiles, the first and second LC SLMs were respectively patterned with a linear and cubic spectral phase sweep. The second polarizer was replaced with a waveplate that rotates the polarization by 45 degrees so that light with a linear spectral phase sweep remains othogonally polarized to light with a cubic spectral phase sweep upon being diffracted by the second grating (which has a polarization-dependent diffraction efficiency). The intensity profiles for orthogonal polarizations of the shaped waveform are shown in figure 20. As expected, the linear phase sweep displaces the input pulse from t=0 and the cubic phase sweep produces a 'ringing' of the input pulse toward negative times. As desired, the two waveforms have orthogonal polarizations. The poor diffraction efficiency of the 1800 line/mm grating for the y-polarized 800-nm light is reflected in the reduced amplitude of the temporally displaced pulse. Less dispersive gratings would make the diffraction efficiency of the grating more comparable for the two orthogonal polarizations. Note that the optical phase relationship between the two waveforms is specified and the waveforms would interfere coherently if they overlapped temporally.

2.10. AMPLIFICATION OF SHAPED WAVEFORMS

The throughput of the pulse shaping device depends on four factors: 1) diffraction efficiency of the gratings (typically 80-90% each) 2) throughput of the polarizers when the mask is set for maximum transmission attenuation (typically 80-85% for the pair) 3) attenuation of the spectral components to yield the desired waveform 4) diffraction light

into higher order spatial modes by the mask pattern. In the absence of any shaping factors 1 and 2 results in a throughput of about 60%. Factors 3 and 4 depend on the specific form of the desired waveform. For example, the spectral filter for an arbitrary N-pulse sequences can attenuate the total spectral energy by as much as $(N-1)^2/N^2$. Also as discussed in section 3 and 4, the longer the temporal extent of the desired waveform, the more light is lost due to diffraction by the mask into higher order spatial modes.

Given these considerations, it might be worthwhile to amplify the shaped waveform in a regenerative amplifier in which case the output energy is relatively insensitive to the energy of the input seed waveform. Amplification of sub-femtosecond pulses usually involves chirped pulse amplification (CPA) [36]. In CPA, a mode-locked seed pulse is temporally stretched to many thousands times its bandwidth-limited pulse duration by passing the pulse through an optical network of gratings and lenses (called a stretcher) in which variation in the accumulated optical path lengths of the different frequency components results in a large quadratic spectral phase sweep and hence a temporally lengthened pulse duration. Because the seed pulse duration into the regen is long, the peak intensity remains small during amplification and damage is avoided. After optimizing the gain from regen, the amplified pulse is passed through a second network of gratings and lenses (called a compressor) which reverses the quadratic phase sweep of the first network, yielding an amplified and temporally compressed pulse. There has been interest in using pulse shaping methods to help compensate for higher order spectral phase distortions introduced by the amplifier and misalignment of the stretcher and compressor [21] which left uncompensated lengthen the amplified pulse duration. Each step of the CPA process manipulates frequency components in the same way as

our pulse shaper and the output remains coherent. Therefore the spectral filtering imparted by a pulse shaper onto a seed pulse should be retained during amplification. Furthermore the seed pulse can be precompensated to account for effects such as gain narrowing in the amplifier [37]. One concern however, is that the seed pulse have sufficient bandwidth after shaping so that it can still be stretched to a long enough duration to avoid peak intensity damage during amplification.

Figure 21 show some preliminary attempts at amplification of shaped input waveforms. Figure 21a shows the cross-correlation of an unamplified 800-fsec square pulse (dotted) along with the auto-correlation of the experimental amplified square pulse (dashed) and the anticipated autocorrelation based on the unamplified waveform (solid). Figure 21b shows the cross-correlations of an unampified (solid) and amplified (dashed) phase-locked equal intensity three-pulse sequences. The broadening of the individual pulses in the amplified waveform is similar to that of an unshaped pulse and reflects a partially misaligned stretcher and compressor and not some inherent limitation. Measurement of the amplified spectrum does show however, that for our amplifier the output spectrum is slightly red-shifted which will effect the carrier frequency and associated phase-relationships between pulses.

An important consideration in time-resolved spectroscopy experiments is that by amplifying a shaped seed waveform, and amplified unshaped reference pulse cannot be split off from the amplified output. It is for this reason that an auto-correlation of the amplified square pulse in figure 21a was measured rather than a cross-correlation. Though figure 21b appears to be a cross-correlation measurement, it is also an autocorrelation measurement of the amplified waveform, since again it is

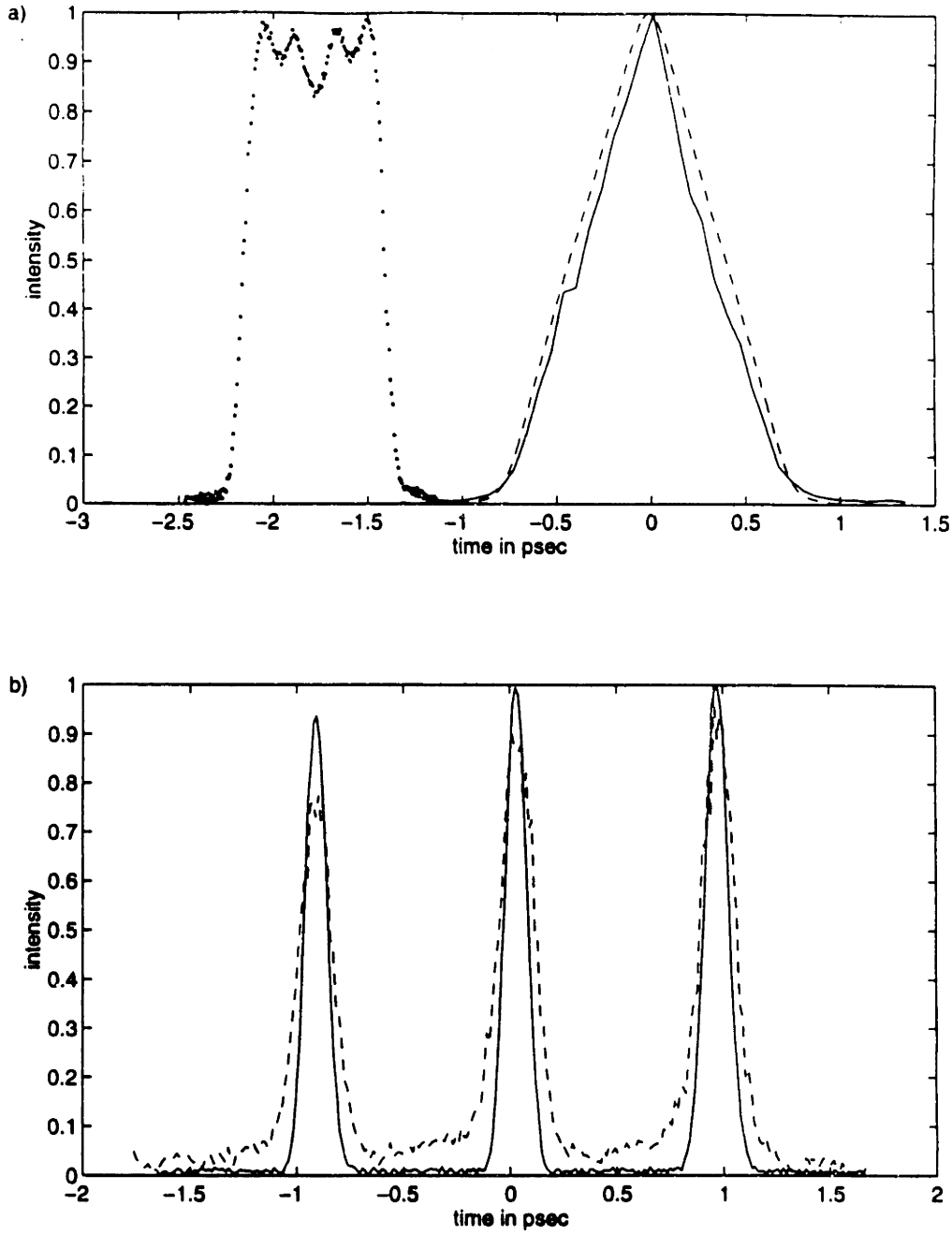

Figure 21: Autocorrelation a) and cross-correlation b) of amplified and unamplified waveforms. Figure 21a shows the cross-correlation of an unamplified 800-fsec square pulse (dotted) along with the auto-correlation of the experimental amplified square pulse (dashed) and the anticipated autocorrelation based on the unamplified waveform (solid). Figure 21b shows the cross-correlations of an unampified (solid) and amplified (dashed) phase-locked equal intensity three-pulse sequences.

impossible to split off an unshaped but amplified reference pulse. In this case, the unamplified three-pulse sequence was recombined with a temporally displaced unshaped unamplified reference pulse using a beam splitter and a delay line. The resulting waveform was a actually a four-pulse sequence with the fourth pulse delayed by many hundreds of psec. Though this fourth pulse could be produced by the pulse shaping apparatus, the spatial resolution of the mask would not be sufficient to displaced the fourth pulse to such a large extent. This recombined waveform can then be amplified. Figure 21b is thus a portion of the autocorrelation measurement in which the fourth pulse of one arm overlaps with the three pulse-sequence of the second arm yielding something equivalent to a cross-correlation measurement. Such a method could also be used in spectroscopy experiments as long as the dynamics of interest completely relax during the time between the shaped waveform and the additional reference pulse. Otherwise the pulse shaper must be used after amplification despite its losses.

2.11 CHARACTERIZATION OF SHAPED WAVEFORMS

Both the shaped and unshaped waveforms described in this thesis have temporal features that are much shorter than response times of the fastest detectors. Characterization must be performed by correlation techniques with similarly short optical field. A standard technique in ultrafast science is cross-correlation by second harmonic generation [38]. The non-collinear version of this technique was employed throughout this section to characterize shaped waveforms. The technique is illustrated in figure 22, two optical fields with intensities $I_1(t)$ and $I_2(t)$ are focused non-collinearly onto the same spot on a second harmonic crystal. A delay

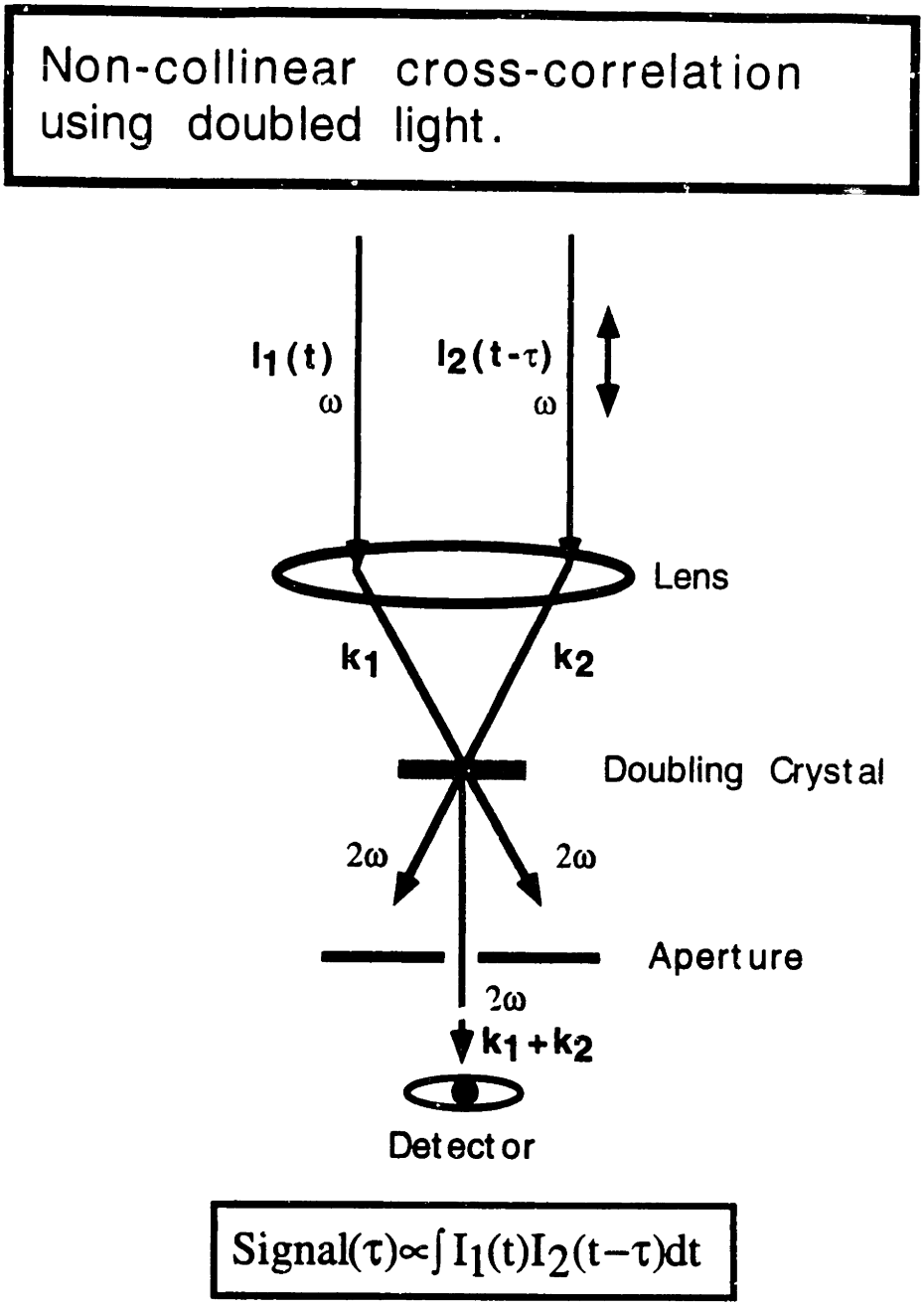

Figure 22: Schematic of cross-correlation method used to characterize shaped waveforms. Details are in the text.

line is used to introduce a controllable temporal separations between the two fields. Doubled light will emerge from either arm independent of the delay between the two fields. However, when the two fields temporally overlap in the crystal, doubled light will also emerge along the direction that bisects the two arms, this light intensity is called the cross-correlation signal and is proportional to:

$$Signal(\tau) \propto \int I_1(t) I_2(t-\tau) dt \tag{74}$$

where τ is the delay time introduced by the delay line. If one of the fields is very short (for example an unshaped reference pulse), the cross-correlation signal gives the intensity profile of the other field. If the two fields are identical the signal is called the autocorrelation signal. By assuming a functional form for an unshaped pulse (for example gaussian) the actual pulse intensity profile can be deconvolved from the autocorrelation signal. This characterized unshaped pulse can then be used as the reference pulse in a cross-correlation measurement of a shaped pulse so that the deconvolved signal gives the intensity profile of the shaped waveform.

Characterization of the phase profiles of ultrashort waveforms are more complicated. Though we have not explicitly measured the temporal phase profiles of the waveforms shaped by our apparatus, the apparatus is capable of manipulating both spectral amplitude and phase. Since these combine to produce the desired temporal intensity profile, which is subsequently confirmed by the cross-correlation measurement, it is assumed that they combine correctly to produce the desired temporal phase profile. In addition to the cross-correlation measurement, we can also

measure the spectrum of the shaped waveform, this equivalent to rechecking the calibration of the LC device across its array for a particular pattern. Though simultaneous information about the temporal and spectral intensity profiles of waveform do not uniquely specify its complex amplitude in either domain (for example the sign of the quadratic spectral phase sweep in a chirped pulse remains ambiguous), it is assumed that the experimental waveform is close enough to the desired waveform that other waveforms with equivalent spectral and temporal intensity profiles can be ruled out. Therefore measurement of the anticipated cross-correlation profile along with an accurate calibration of the dual-LC-mask device should be sufficient in practice to confirm the generation of the desired waveform.

Nonetheless there has been emerging optical techniques that can unambiguously characterize the complex amplitude profile of optical waveforms [39-41]. One technique is termed frequency-resolved-optical-gating or FROG. In FROG, an auto-(or cross-)correlation measurement based on a higher-order non-linearity (usually a Kerr gate) is frequency resolved yielding a unique two dimensional data set. Algorithms have been developed to convert this data set to the complete electric field profile. FROG has been successfully used in characterizing higher-order phase distortions in temporally broadened pulses after chirped pulse amplification [42]. We tried to use FROG on shaped waveforms, however practical problems arise since very small temporal features need to be resolved over a large temporal range, unlike the case of temporally broadened (typically by a factor of less than 5) single pulses. The two dimensional data set becomes too large for algorithms to converge in a reasonable time. In practice FROG techniques are very good at aiding the recompression of

amplified pulses to their bandwidth-limited pulse duration, but are ackward for more complicated waveforms.

Complete characterization of the shaped waveform is also possible if a completely characterized reference pulse is available. Such a reference pulse could be characterized by FROG or simply by it spectrum if its pulse duration appears bandwidth-limited. In this case, spectral interferometry could be used, in which the shape waveform $e_S(t)$ and reference pulse $e_r(t)$ (which are derived from the same source) are recombined interferometrically with a controllable delay τ, and the combined spectrum is measured. The signal in this case is given by:

$$Signal(\tau,\omega) \propto \left|E_r(\omega)\right|^2 + \left|E_s(\omega)\right|^2 + 2\,\mathrm{Re}\left\{E_r^*(\omega)E_s(\omega)\exp(i\omega\tau)\right\} \tag{75}$$

where ω is angular frequency and $E_r(\omega)$ and $E_S(\omega)$ are the Fouler transforms of $e_S(t)$ and $e_r(t)$. Since $E_r(\omega)$ is known, the delay τ can be varied to given the complex amplitude of $E_S(\omega)$ thereby completely characterizing the shaped waveform.

Since the LC masks are programmable, the fidelity of the shaped waveform can be iteratively improved if its profile is characterized. To account for systematic limitations (e.g. gaps), misalignment, and imperfect calibration, the algorithm described in section 6.2 could be implemented, though rather than calculating the output waveform (which would require complete knowledge of all pulse shaping parameters) the output waveform would be measured experimentally. The mask filters would then be iteratively improved according to equation 67. Based on the impressive

results illustrated in section 8, such efforts are probably unnecessary for must practical situations.

APPENDIX 2A: GENERAL FORMALISM FOR SHAPED WAVEFORMS

Subject to a limited time window and temporal features no shorter than the bandwidth limited input pulse, the possible 'arbitrary' wave form envelopes that can be produced by the N pixel mask are given by:

$$e_{desired}(t) = e_{in}(t) \otimes \sum_{n=0}^{N-1} H_n \partial(t - T_n) \qquad (A1)$$

where $-N\tau/2 \le T_n < N\tau/2$.

The input pulse can be placed at various times T_n (within the time window) with a complex amplitude H_n, and the resulting superposition produces the output waveform. Placing more than N input pulses in the desired output waveform is redundant because of the limited time window and the temporal width of the input pulse.

To show the equivalence of the waveform described by equation A1 and the waveform described by equation 65 within the time window $-N\tau/2 \le t < N\tau/2$, we will fouler transform the two expressions:

$$E_{in}(\omega) \sum_{n=0}^{N-1} H_n \exp(i\omega T_n) = E_{in}(\omega) \sum_{n=-N/2}^{N/2-1} C_n \exp(i\omega n\tau) \qquad (A2)$$

Since the spectrum of the input pulse is assumed to on the mask, we can remove the term $E_{in}(\omega)$ from the above expression and require the equivalence only over the range given by $-\pi/\tau \le \omega \le \pi/\tau$. The

appropriate coefficients C_n can then be determined easily by multiplying both sides by $\exp(-i\omega\tau n')$ and integrating over ω in the range $-\pi/\tau \le \omega \le \pi/\tau$:

$$C_{n'} = \frac{\tau}{2\pi} \int_{-\pi/\tau}^{\pi/\tau} \left\{ \sum_{n=0}^{N} H_n \exp(i\omega T_n) \right\} \exp(-i\omega\tau n') d\omega \qquad \text{(A3)}$$

Thus the arbitrary wave form described by equation 65 is equivalent to equation A1.

APPENDIX 2B: CALIBRATION OF DUAL LIQUID CRYSTAL MASK

Recall from section 2, that the complex amplitude filter for pixel n on the dual-LC-mask device (including the polarizers) described in section 8, is given by:

$$B_n = \exp\left(i\left(\Delta\phi^{(1)} + \Delta\phi^{(2)}\right)/2\right)\cos\left(\left(\Delta\phi^{(1)} - \Delta\phi^{(2)}\right)/2\right) \qquad \text{(B1)}$$

where $\Delta\phi^{(i)}\left(V_n^{(i)}\right)$ is the voltage-(V)-dependent birefringence for pixel n on the ith mask. To perform a calibration of the masks, attenuation is measured as a uniform voltage is varied across each of the masks. In practice we have found that the response across each mask is uniform so that different pixels on the same mask do not need to be calibrated individually. If the voltage across the second mask is fixed at zero, while the voltage across the first mask is scanned, and then vice-versa, the following functions $f_1(V^{(1)})$ and $f_2(V^{(2)})$ can be determined:

$$f_1\left(V^{(1)}\right) = \Delta\phi^{(1)}\left(V^{(1)}\right) - \Delta\phi^{(2)}\left(V^{(2)} = 0\right) \quad \text{(B2)}$$

$$f_2\left(V^{(2)}\right) = \Delta\phi^{(1)}\left(V^{(1)} = 0\right) - \Delta\phi^{(2)}\left(V^{(2)}\right) \quad \text{(B3)}$$

Note that $f_1(0)=f_2(0)$ which we will define as the constant f_0. Based on these calibration files, one wants to determine the voltages required to produce the desired filter. In comparison with B1, the desired filter can be specified by ϕ_{phase} and $\phi_{amplitude}$ where:

$$B_{desired} = \exp(i\phi_{phase})\cos\left(\phi_{amplitude}\right) \quad \text{(B4)}$$

Since the expressions B2 and B3 can be inverted, the problem reduces to expressing f_1 and f_2 in terms of ϕ_{phase} and $\phi_{amplitude}$. This can be accomplished because we can add a voltage-independent constant to ϕ_{phase} without physically changing the spectral filter across the array. This is because it is only the relative differences in phase between pixels that contribute to the shape of the output waveform. Setting this constant equal to $-\Delta\phi^{(1)}\left(V^{(1)} = 0\right)$ we can write the following expressions:

$$f_1\left(V^{(1)}\right) = \phi_{phase} + \phi_{amplitude} + f_0 \quad \text{(B5)}$$

$$f_2\left(V^{(2)}\right) = -\phi_{phase} + \phi_{amplitude} \quad \text{(B6)}$$

Using the calibration curves for f_1 and f_2, the current voltages can be determined to produce the desired complex amplitude filter.

CHAPTER 2 REFERENCES

1. W. S. Warren, H. Rabitz, M. Dahleh, Science, **259**, 1581 (1993)
2. R. Kosloff, A. D. Hammerich, D. Tannor, Phys. Rev. Lett. **69**, 2172 (1992)
3. J. A. Cina, T. J. Smith, submitted to J. Chem. Phys. (1992)
4. S. Shi, A. Woody, H. Rabitz, J. Chem. Phys. **88**, 6870 (1988)
5. B. Kohler, J. L. Krause, F. Raksi, C. Rose-Petruck, A. M. Whitnell, K. R. Wilson, V. V. Vakolev, Y. Yan, S. Mukamel, J. Phys. Chem. **97**, 12602 (1993)
6. W. S. Warren, A. H. Zewail, J. Chem. Phys. **78**, 2279 (1983)
7. A. M. Weiner, D. E. Leaird, G. P. Wiederrecht, K. A. Nelson, Science **247**, 1317 (1990)
8. N. F. Scherer, R. J. Carlson, A. Mato, M. Du, A. J. Ruggiero, V. Romero-Rochin, J. A. Cina, G. R. Fleming, S.A. Rice, J. Chem. Phys. **95**, 1487 (1991)
9. A. M. Weiner, J. P. Heritage, J. A. Salehi, Opt. Lett. **13**, 300 (1988)
10. A. M. Weiner, Y. Silberberg, H. Fouckhardt, D. E. Leaird, M. A. Saifi, M. J. Andrejco, P.W. Smith, IEEE J. Quan. Elec. **25**, 2648 (1989)
11. A. M. Weiner, R. N. Thurston, W. J. Tomlinson, J. P. Heritage, D. E. Leaird, E. M. Kirschner, R. J. Hawkins, Opt. Lett. **14**, 868 (1989)
12. M. Haner, W. S. Warren, Opt. Lett. **12**, 398 (1987)
13. M. Haner, W. S. Warren, Appl. Phys. Lett. **52**, 1458 (1988)
14. K. B. Hill, D. J. Brady, Opt. Lett.**18**, 1739 (1993)
15. D. J. Brady, A. G. S. Chen, G. Rodriguez, Opt. Lett. **14**, 868 (1989)
16. A. M. Weiner, D. E. Leaird, D. H. Reitze, E. G. Paek, Opt. Lett. **17**, 224 (1992)
17. C. Froehly, B. Colmbeau, M. Vampouille, Progress in Optics E. Wolf, ed. (North-Holland, Amsterdam, 1983), vol. 20, pp.115-121
18. J. P. Heritage, A. M. Weiner, R. N. Thurston, Opt. Lett. **10**, 609 (1985)
19. A. M. Weiner, D. E. Leaird, Opt. Lett. **15**, 51 (1990)
20 A. M. Weiner, J. P. Heritage, E. M. Kirschner, J. Opt. Soc. Am. **B5**, 1563 (1988)
21. A. M. Weiner, D. E. Leaird, J. S. Patel, J. R. Wullert, Opt. Lett. **15**, 326 (1990)
22. A. M. Weiner, D. E. Leaird, J. S. Patel, J. R. Wullert, IEEE J. Quan. Elec. **QE-28**, 908 (1992)
23. M. M. Wefers, K. A. Nelson, Opt. Lett. **18**, 2032 (1993)
24. M. M. Wefers, K. A. Nelson, Science **262**, 1381 (1993)
25. M. M. Wefers, K. A. Nelson, Opt. Lett. **20**, 1047 (1995)
26. M. M. Wefers, H. Kawashima, K. A. Nelson, J. Chem. Phys. **102**, 9133 (1995)
27. C. W. Hillegas, J. X. Tull, D. Goswami, D. Strickland, W. S. Warren, Opt. Lett. **19**. 737 (1994)

28. M. M. Wefers, K. A. Nelson, Programmable femtosecond multiple pulse generation and spectroscopy, in Ultrafast Phenomena, Vol. 7, 1994 OSA Technical Digest Series (Optical Society of America, Washington, DC, 1994) pp 39-41
29. O. E. Martinez, J. Opt. Soc. Am. **B3**, 929 (1986)
30. O.E. Martinez, IEEE J. Quan. Elec. **QE-23**, 59 (1987)
31. R. N. Thurston, J. P. Heritage, A. M. Weiner, W. J. Tomlinson, IEEE J. Quan.Elec. **QE-22**, 682 (1986)
32. R. N. Bracewell, The Fourier Transform and its Applications, New York: McGraw-Hill 1986
33. M. B. Danailov, I. P. Christov, J. Mod. Opt. **36**, 725 (1989)
34. A. M .Weiner, S. Oudin, D. E. Leaird, D. H. Reitze, J. Opt. Soc. Am. A **10**, 1112 (1993)
35. W. H. Press, B. P. Flannery, S. A. Teukolsky, W. T. Vetterling, Numerical Recipes in C, The Art of Scientific Computing, (Cambridge University Press, Cambridge, 1988)
36. F. Salin, J. Squier, G. Mourou, G. Vaillancourt, Opt. Lett. **16**, 1964 (1991)
37. C. P. J. Barty, G. Korn, F. Raksi, C. Rose-Petruck, J. Squier, A.-C. Tien, K. R. Wilson, V. V. Yakolev, K. Yamakawa, *Opt. Lett.* **21**, 219 (1996)
38. J.-C. Diels, J. J. Fontaine, I. C. McMichael, F. Simoni, *Appl. Opt.* **24**, 1270 (1985)
39. D. J. Kane, R. Trebino, Opt. Lett. **18**, 823 (1993)
40. R. Trebino, D. J. Kane, J. Opt. Soc Am **A10**, 1101 (1993)
41. J. L. A. Chilla, O. E. Martinez, Opt. Lett. **16**, 39 (1991)
42. B. Kohler, V. V. Yakolev, K. R. Wilson, J. Squier, K. W. Delong, R. Trebino, *Opt. Lett.* **20**, 483 (1995)

Chapter 3
Space-Time Profiles of Shaped Ultrafast Optical Waveforms

The work in this chapter is published in:

M. M. Wefers, K. A. Nelson, J. Quan. Elec. 32, 161 (1996)

3.1 INTRODUCTION

In this chapter. a completely general derivation for the space-time profiles of ultrafast optical waveforms shaped by filtering of spatially separated frequency components is presented. Closed form expressions for the space-time impulse response functions are given for the cases of single and double passes through a pulse shaping apparatus. For a single pass and a short unshaped pulse, diffraction by the mask filter gives rise to a translational spatial shift in the desired electric field profile that varies linearly with time along the shaped waveform. The result was determined for some specific cases in the previous chapter but in fact is completely general, and applies to frequency-domain pulse shaping with either continuous or discrete mask filters. It is also shown that double passing the apparatus does not generally reverse this effect but rather introduces further space-time coupling such as a time-varying spotsize.

The generation of arbitrarily shaped optical waveforms is of great interest in a number fields including coherent control spectroscopy [1-4] and optical communications [5-6]. Though some pulse-shaping techniques have been developed for modulation of waveforms directly in the time domain [7], and other emerging techniques based on holography have been

introduced [8-10], the majority of pulses shaping efforts have involved the filtering of spatially separated frequency components [11-20].

In this frequency-domain technique a grating and lens (or focussing reflector [15]) is used to image the frequency spectrum of an ultrashort pulse onto a spatially varying mask. The mask filter can retard (vary the optical path length of) or attenuate different frequency components, i.e. a phase or amplitude mask can be used. The spectrally filtered frequency components are then recombined with a second lens and grating, yielding a 'shaped' waveform in the time domain. If the gratings, lenses, and mask are each separated by the focal length of the lenses, the apparatus is in a '4-f' arrangement and is dispersion free [21] so that the output pulse would be unchanged for a uniform mask. Prefabricated substrates were originally used as masks [12-15]. More recently liquid crystal (LC) spatial light modulators (SLM) [16-19] and acousto-optic (AO) modulators [20] have been used as programmable masks to permit computer-controlled generation of ultrafast waveforms.

The pulse shaping process depends on the spatial separation of different frequency components at the mask, where selective spectral manipulation takes place through the different absorption or retardance properties of the separate mask regions. However each individual frequency component has a finite spatial extent at the mask, and so the different spatial regions of a single component may encounter different optical properties. This results in spatial shaping of individual frequency components. For example, differences in retardation of nearby mask regions can produce variable deflection of nearby spatial regions of a single frequency component, and for impixellated masks such as LCD masks, diffraction will occur at the pixel edges. Thus the masking

procedure results in shaping of the both spectral and spatial profiles of the incident optical pulse. We will generally use the term "diffraction" to describe any spatial shaping arising from the spatially varying pattern of either continuous or discrete masks.

This effect has been noticed both experimentally and theoretically. In the pioneering pulse-shaping efforts of Weiner and co-workers [12-17,22], it was shown that the temporal extent of shaped waveforms depended not only on the spatial resolution of the mask filter but also on the spatial extent of the focussed frequency components incident on the mask. Under the assumption of a gaussian spatial profile for the input pulse, it was shown theoretically that the temporal profile of the gaussian spatial mode of the output waveform is modulated by a gaussian envelope that depends on the spot size of an individual frequency component at the mask [21]. Parts of the shaped waveform which fall outside this time window are diffracted into higher-order spatial modes which are presumably removed by spatial filtering. In the Bellcore experiments an aperture was used to perform this function. Nonetheless, it was observed that experimentally generated waveforms (THz-frequency sequences of evenly spaced ultrashort optical pulses) whose intensity profiles were expected to be symmetric in time according to the spectral filter of the mask were sometimes asymmetric [13-14]. The asymmetry seemed to depend on the distance of the mask from the focal plane of the lens pair and on the size of the aperture.

We have made similar observations. In particular, we noticed that the asymmetry in the intensity of a pulse train measured by non-collinear cross-correlation with an unshaped reference pulse varied systematically with the position of the mixing crystal which is used for the cross-

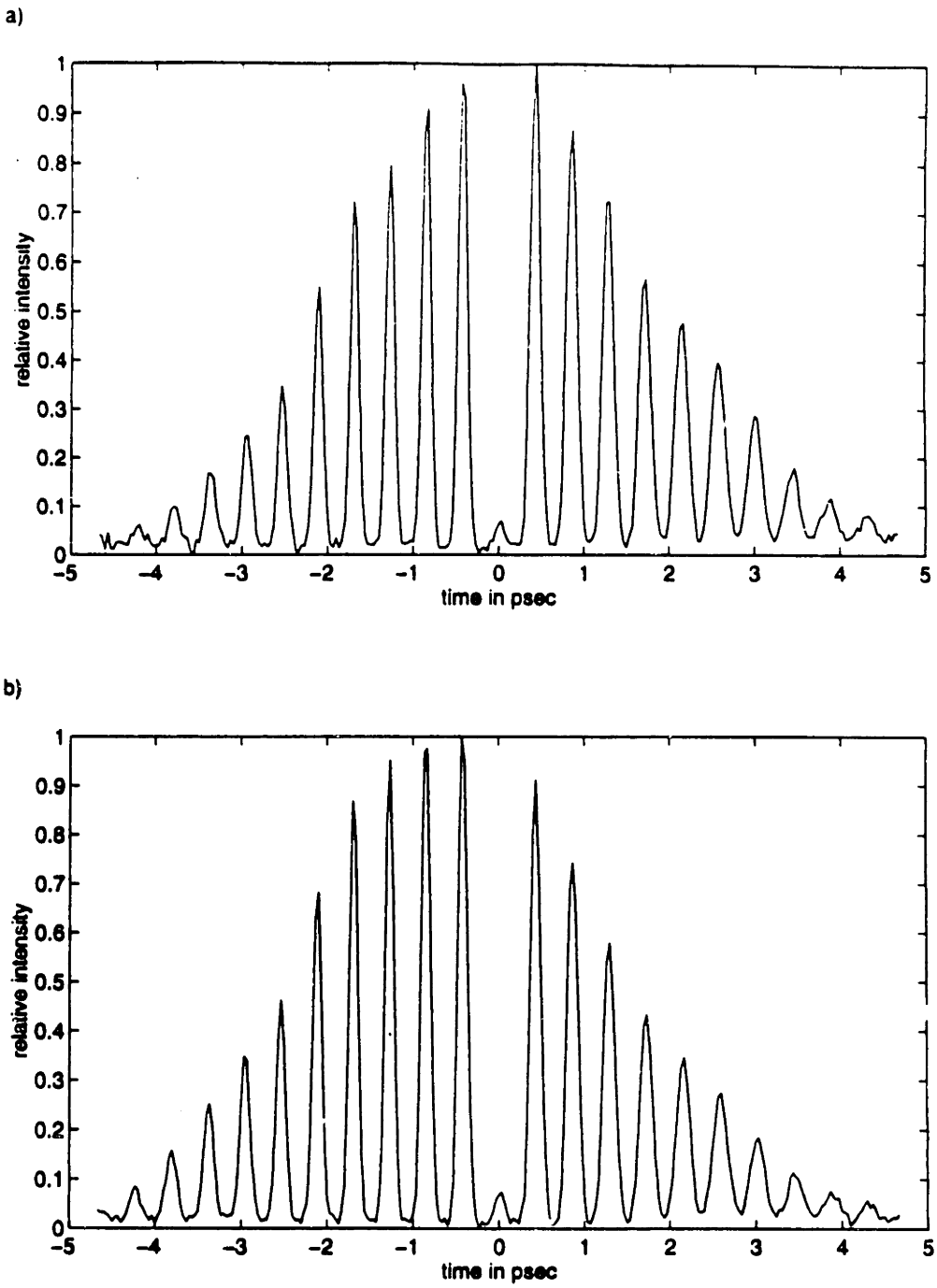

Figure 1: Experimental cross-correlation measurements of a pulse train produced by a single pass through the pulse shaping apparatus with a particular mask pattern. Figures 1a and 1b are measurements of the identical waveform, but with the doubling crystal used to perform the cross-correlation displaced along the direction of beam propagation by 300 μm. Note the higher cross-correlation intensity at early times in figure 1b.

correlation, as shown in figure 1. Figures 1a and 1b illustrate cross-correlation measurements of an identically prepared waveform under identical conditions except for the position of the doubling crystal along the propagation direction of the beams, which differed by 300 μm. The earlier or later parts of the cross-correlation signal are seen to be favored depending on the mixing crystal position. This observation is consistent with the hypothesis that the shaped waveform has a space-time dependence which in this case affects the spatial overlap and phase-matching with the reference pulse in the doubling crystal.

A theoretical expression for the space-time profile of a waveform produced by frequency domain pulse shaping has been presented by Danailov and Christov [23] for the case of an input pulse which separable and gaussian in space and time. However the result is not in closed form and it is difficult to interpret deviations from the desired waveform for arbitrary mask patterns. Recently Paye and Migus [24] have described space-time operations using generalized space-time Wigner functions and a pulse shaper as a specific example. The formalism can easily be extended to more complicated systems. However, results for the pulse shaper were only presented for a single mask pattern and general features for arbitrary mask patterns are once again difficult to interpret.

The results of this chapter show that for the usual case of an ultrashort unshaped input pulse, the shaped waveform has the temporal profile expected based on the spectral filtering of the mask, but its spatial profile also undergoes a time-varying translational shift. Rather than producing a shaped waveform described by:

$$e_{shaped}(x,t) = e_{shaped}(t)g_{input}(x) \qquad (1)$$

where x is the direction along which the mask is patterned and the spectral components of the pulse are dispersed, g(x) is the spatial profile of the input pulse and e(t) is the shaped waveform based on the frequency filter, the output waveform is described approximately by:

$$e_{shaped}(x,t) = e_{shaped}(t)g_{input}(x+vt) \qquad (2)$$

where v describes the time-dependent shift of the shaped waveform. It will be shown that the time-dependent shift parameter v depends only on the angular dispersion produced by the grating. We first identified this result in a general paper on pulse shaping using one or two liquid crystal spatial light modulators [25]. Among other results, it decribed this space-time shift for the case of a separable input pulse with a gaussian spatial profile and a mask pattern consisting of a linear array of pixels. In this chapter, results are derived in a simple manner that yields the space-time shaping for arbitrary mask patterns and arbitrary input pulses.

Results are also presented for the case in which the pulse shaping apparatus is double-passed. In analogy to double-passed pulse stretchers used for chirped pulse amplification [26], it might be anticipated that double passing the pulse shaper will make the shaped waveform separable in space and time. It will be shown that this is only true for very simple mask patterns (such as those that produce a linearly chirped pulse) and that in general double-passing the pulse shaper can introduce significant deviation from the desired waveform.

In section 2, we derive the impulse response function and the parameters that determine the space-time coupling for the single-passed

pulse shaper. In section 3, we illustrate this result for a practical pulse shaping set-up with a number of particular mask patterns including those that generate pulse trains and those that could be used for pulse recompression. In section 4, the impulse response function for the double-passed pulse shaper is presented along with results for particular mask patterns. In section 5, we discuss the practical impact of these results on the generation of shaped waveforms. The absolute lateral shifts for practical mask systems with nearly continuous or discrete patterns are estimated.

3.2. ANALYSIS FOR SINGLE PASS

3.2a. Impulse response derivation

The electric field is represented in either position or wavevector space (x,k) and either time or frequency space (t,ω), as distinguished by the notations $e(x,t)$, $E(x,\omega)$, $\bar{e}(k,t)$, and $\bar{E}(k,\omega)$. The following convention will be used for Fourier transforms:

$$F(k,\omega) = (2\pi)^{-1} \iint f(x,t) e^{i(kx-\omega t)} dx dt \qquad (3)$$
$$f(x,t) = (2\pi)^{-1} \iint F(k,\omega) e^{-i(kx-\omega t)} dk d\omega$$

The derivation follows a formalism similar to the treatment by Danailov and Christov [23], which exploits the Fourier transform relationship between the spatial electric field profiles in the object plane and image planes of a lens. For a lens of focal length f placed at z=0, the spatial electric field profiles in the two focal planes are related according to:

$$E(x, z=-f) = E(x) \Leftrightarrow E(x, z=f) = \sqrt{2\pi/\lambda f} \cdot \overline{E}(2\pi x/\lambda f) \tag{4}$$

where $E(x)$ and $\overline{E}(k)$ are a Fourier transform pair. To study cases in which the mask(s) are displaced from the focal plane [25], one could simply propagate the electric field away from the focal plane according to equation 5

$$\overline{E}(k,z) = \overline{E}(k,z_0)\exp\left(-i(z-z_0)\lambda k^2/4\pi\right) \tag{5}$$

The pulse shaping apparatus and reference frame are shown in figure 2. The apparatus consists of a 1:1 telescope sandwiched within a pair of anti-parallel gratings. The lenses and gratings are separated by distance f and the two lenses by 2f, where f is the focal length of the lenses. The mask is placed in the focal plane of the lens pair, where the grating and lens have optimally separated the different frequency components. The propagation direction of the beam is given by the **z**-axis and the transvere coordinate is given by the **x**-axis as labelled in figure 2. The apparatus is uniform along the **y** coordinate so we do not to consider this coordinate explicitly. The possibility of double passing the apparatus (illustrated within the dashed box) will be discussed in section 4.

The electric field incident upon the pulse shaping apparatus (immediately prior to the grating) is defined in the slowly varying envelope approximation as:

$$e_1(x,t) = e_{in}(x,t)\exp(i\varpi t) \tag{6}$$

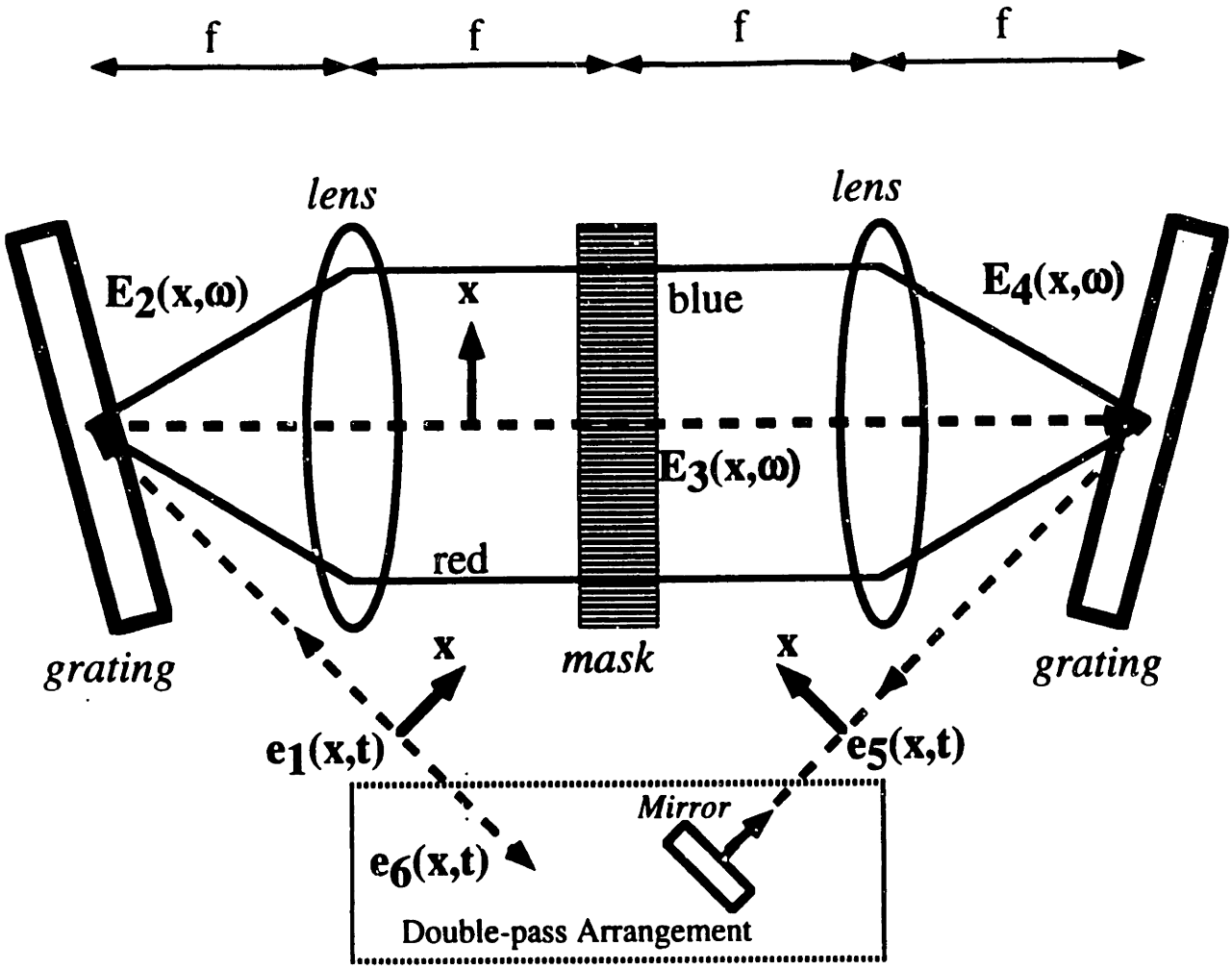

Figure 2: Schematic illustration of a pulse shaping apparatus based on the filtering of spatially separated frequency components. A grating and lens image the spectrum of an ultrashort pulse onto a spatially varying mask. A second lens and grating recombine the spectrally filtered pulse yielding a shaped waveform in the time domain. The x-axis specifies the transverse spatial profile of the electric field. The electric field profile $e_i(x,t)$ or $E_i(x,\omega)$ at different points in the apparatus is given by the expressions derived in section 2. The dashed box illustrates the case in which the apparatus is double-passed (with a vertical offset). The calculations in the text assume negligible separation between the mirror and the second grating.

where ϖ is the optical carrier frequency and $e_{in}(x,t)$ is the space-time envelope for the input optical pulse. In many cases $e_{in}(x,t)$ is separable in space and time.

Following the results of Martinez [27], the electric field immediately after the grating in frequency and position space is given by:

$$E_2(x,\omega)=\sqrt{\beta}\cdot E_{in}(\beta x,\Omega)\exp(i\gamma\Omega x) \qquad (7)$$

with $\beta=\cos(\theta_i)/\cos(\theta_d)$, $\gamma=2\pi/\varpi d\cos(\theta_d)$, and $\Omega=\omega-\varpi$, where $E_{in}(x,\omega)$ is the temporal Fourier transform of the input pulse envelope $e_{in}(x,t)$, θ_i and θ_d are the angles of incidence and diffraction respectively, and d is the grating line spacing.

The electric field profile in the focal plane of the lens is given by the spatial Fourier transform of equation 7 with the substitution $k=2\pi x/f\lambda$, where f is the focal length of the lens and λ is the center wavelength of the input field. The electric field is then multiplied by the mask filter $m(x)$ to give:

$$E_3(x,\omega)=\sqrt{2\pi/\beta\lambda f}\cdot\bar{E}_{in}(2\pi x/\beta\lambda f+\gamma\Omega/\beta,\Omega)m(x) \qquad (8)$$

where $\bar{E}_{in}(k,\omega)$ is the spatial Fourier transform of $E_{in}(x,\omega)$.

To determine the electric field profile immediately before the second grating, a spatial Fourier transform of equation 8 is taken, again with the substitution $k=2\pi x/f\lambda$, giving:

$$E_4(x,\omega)=\left(\sqrt{2\pi\beta}/\lambda f\right)\int E_{in}(-\beta x',\Omega)\exp(-i\gamma\Omega x') \cdot M(2\pi(x-x')/\lambda f)dx' \qquad (9)$$

where $M(k)$ is the spatial Fourier transform of the mask pattern $m(x)$.

Again following Martinez, the inverse transfer function of the second grating (which is anti-parallel to the first) gives the electric field profile after the grating as:

$$E_5(x,\omega)=\sqrt{1/\beta}\cdot E_4(x/\beta,\omega)\exp(i\gamma\Omega x/\beta) \tag{10}$$

Substituting equation 9 into 10 gives:

$$\begin{aligned} E_5(x,\omega)=&\left(\sqrt{2\pi}/\beta\lambda f\right)\int E_{in}(-x',\Omega) \\ &\cdot\exp\left(i\gamma\Omega(x-x')/\beta\right)M\left(2\pi(x-x')/\beta\lambda f\right)dx' \end{aligned} \tag{11}$$

Taking the inverse temporal Fourier transform of equation 11 yields the electric field profile of the output waveform in the position and time domains:

$$\begin{aligned} e_5(x,t)=&\left(1/\lambda f\sqrt{2\pi}\right)\exp(i\varpi t) \\ &\cdot\left[\begin{array}{l}\iint E_{in}(-x',\Omega)M\left(2\pi(x-x')/\beta\lambda f\right) \\ \quad\cdot\exp\left(i\Omega\left(t+\gamma(x-x')/\beta\right)\right)d\Omega dx'\end{array}\right] \end{aligned} \tag{12}$$

Performing the integration over Ω and using the convolution theorem for Fourier transforms in equation 12 gives the final expression for the shaped waveform:

$$e_5(x,t)=\exp(i\varpi t)\int e_{in}\left(-(x-x'),t-t'\right)g(x',t')dx'dt' \tag{13}$$

where $g(x,t)$ is the impulse response function for the single-pass pulse shaper (not including the image inversion imparted by the telescope which is given by the negative sign in the argument of $e_{in}(x,t)$) and can be expressed as:

$$g(x,t)=\left(\sqrt{2\pi}/\beta\lambda f\right)M\left(2\pi x/\beta\lambda f\right)\delta\left(t+\gamma x/\beta\right) \tag{14}$$

or equivalently as:

$$g(x,t)=\left(\sqrt{2\pi}/\gamma\lambda f\right)M\left(-2\pi t/\gamma\lambda f\right)\delta\left(x+\beta t/\gamma\right) . \tag{15}$$

where $\delta(x)$ is the Dirac delta function. Equation 13 can also be written in wavevector and frequency space by taking its Fourier transform:

$$E_5(k,\omega) = \overline{E}_{in}(-k,\Omega)\overline{G}(k,\Omega) \tag{16}$$

where $\overline{G}(k,\omega)$ is the impulse response function in wavevector and frequency space:

$$\overline{G}(k,\Omega)=m\left(-\lambda f\left(\gamma\omega+\beta k\right)/2\pi\right) \tag{17}$$

3.2b. Limiting cases

The important result in equations 13-15 is that the space-time coupling in the shaped output waveform is entirely given by the delta function in equations 14 and 15. The size of this coupling is given by the parameter γ/β which equals:

$$\gamma / \beta = \lambda / \left(cd \cos(\theta_i) \right) \tag{18}$$

where c is the speed of light, d is the grating line spacing, λ the center wavelength, and θ_i the angle of incidence onto the grating. Hence this parameter is entirely described by the angular dispersion imparted by the grating which subsequently produces the transverse dispersion in the masking plane.

In the limit that the grating behaves as a simple mirror (d very large), γ / β becomes zero and equations 13 and 14 simplify to give:

$$\begin{aligned} e_5(x,t) = & \left(\sqrt{2\pi} / \beta \lambda f \right) \exp(i\varpi t) \\ & \cdot \int e_{in}\left(-(x - x'), t \right) M\left(2\pi x / \beta \lambda f \right) dx' \end{aligned} \tag{19}$$

This corresponds to the case of spatial filtering [28], and for an input envelope whose spatial and temporal dependences are separable, i.e. $e_{in}(x,t) = f_{in}(x) h_{in}(t)$, only the spatial profile of the input waveform is shaped:

$$\begin{aligned} e_5(x,t) = & \left(\sqrt{2\pi} / \beta \lambda f \right) \exp(i\varpi t) h_{in}(t) \\ & \cdot \int f_{in}\left(-(x - x') \right) M\left(2\pi x / \beta \lambda f \right) dx' \end{aligned} \tag{20}$$

In the opposite limit of highly dispersive gratings γ / β becomes very large, and for a separable input envelope only the temporal profile of the input waveform is shaped:

$$e_5(x,t) = f_{in}(-x)\left(\sqrt{2\pi}/\gamma\lambda f\right)\exp(i\varpi t) \cdot \int h_{in}(t-t')M(-2\pi t'/\gamma\lambda f)dt' \tag{21}$$

For most practical cases γ/β is not so large that one can ignore the time argument in the delta function of equations 14 or 15. Thus combining equations 13 and 15 gives:

$$e_5(x,t)=\left(\sqrt{2\pi}/\gamma\lambda f\right)\exp(i\varpi t) \cdot \int e_{in}\left(-(x+\beta t'/\gamma),t-t'\right)M(-2\pi t'/\gamma\lambda f)dt' \tag{22}$$

If the temporal duration of the input envelope $e_{in}(x,t)$ is given by τ_{in}, and the spatial extent of the shortest spatial feature of $e_{in}(x,t)$ is given by χ_{in}, then under the condition:

$$\chi_{in} >> \tau_{in}\beta/\gamma \tag{23}$$

equation 20 can be simplified by replacing t' with t in the spatial argument of $e_{in}(x,t)$ giving:

$$e_5(x,t)=\left(\sqrt{2\pi}/\gamma\lambda f\right)\exp(i\varpi t) \cdot \int e_{in}\left(-(x+t\beta/\gamma),t-t'\right)M(-2\pi t'/\gamma\lambda f)dt' \tag{24}$$

Equation 24 shows that the effect of spatial diffraction on the temporal profile of the shaped waveform is to introduce a shift in the spatial profile that varies linearly with time with a slope given by $-\beta/\gamma$. For the case of a separable input envelope we have:

$$e_5(x,t)=f_{in}\left(-(x+t\beta/\gamma)\right)\left(\sqrt{2\pi}/\gamma\lambda f\right)\exp(i\varpi t) \cdot \int h_{in}(t-t')M(-2\pi t'/\gamma\lambda f)dt' \quad (25)$$

With the exception of the transverse spatial shift, equation 25 is identical to equation 21. Equation 21 corresponds to the case where the spectrum of the input pulse is perfectly resolved onto the mask filter m(x) and so the spatial profile of individual frequency components are not diffracted by the mask pattern. However because individual frequency components focussed onto the mask do have some finite spatial extent, diffraction modulates the space-time profile of the shaped waveform according to equation 25. The waveform is shaped not along the **z**-axis (i.e. in time) exclusively but rather in the **x-z** plane along an axis given by slope $\Delta z/\Delta x=-c\gamma/\beta$. The condition in equation 23 implies that this slope gives rise to negligible displacement along the x-axis for individual features of the shaped waveform that are comparable to the input pulse duration.

3.3. PRACTICAL EXAMPLES FOR THE SINGLE PASSED APPARATUS

Most current efforts of experimental ultrafast waveform generation involve input pulses of 20-100 fsec duration with the center wavelength in the visible to near-infrared spectral region. To consider an approximate value for $-\beta/\gamma$, we consider an apparatus consisting of 1800 lines/mm gratings aligned at Littrow angle $(\theta_i=\theta_d)$ for a center wavelength of 800 nm. Using equation 18 gives $-\beta/\gamma$ equal to -0.145 mm/psec. This slope is inversely proportional to the number of lines on the grating and

would be larger if less dispersive gratings are used accomodate the broad bandwidths of very short pulses (20 fs) on finite mask apertures. In practice the input pulses are also separable in space and time with spotsizes of about 2 mm. Under these circumstances the condition of equation 23 is easily satisfied and equation 25 is valid. In this limit (which is the usual case in practice), the effect of diffraction is completely summarized by a linear time dependence in the transverse spatial position of the temporally shaped electric field amplitude, regardless of the mask pattern.

Nonetheless we will now illustrate the space-time profile of the shaped waveform for some particular mask patterns. For simplicity we will assume that the input pulse envelope can be described as:

$$e_{in}(x,t) = \exp(-a^2 t^2) \cdot \exp\left(-x^2/A^2\right) \tag{26}$$

with a=2x 10^{13} s^{-1} (fwhm pulse duration of 59 fs) and A=1.5 mm (fwhm spotsize of 1.76 mm). In addition to the previously specified parameters we take f (focal length of the lenses) to be 15 cm.

First we consider a mask consisting of a slit of width w separated from the center of the mask by x_0, where the slit width is much smaller than the total width of the spectrum imaged onto the mask. This is equivalent to saying that the spectral amplitude is constant across the slit width. Solving equation 25 gives:

$$e_5(x,t) = \exp\left(-(x + t\beta/\gamma)^2/A^2\right)\exp\left(i(\varpi - 2\pi x_0/\gamma\lambda f)t\right) \cdot \sin(-\pi w t/\gamma\lambda f)/\pi t \tag{27}$$

This set-up is essentially a monochromator with the slit selecting a small portion of the spatially separated spectrum. Equation 27 shows that the temporal profile consists of a broad sinc envelope with a shift in optical carrier frequency. However in addition to this expected temporal profile there is a time varying shift in the spatial profile of the waveform. Figure 3 illustrates the space-time intensity profile of a waveform described by equation 27 for w=100 μm. The sinc envelope has a pulse width of about 8 psec and there is a spatial shift of about 1 mm over this duration. The pulse duration along a particular spatial coordinate is shorter than the pulse width of the sinc envelope because of the time-dependent spatial shaping. This reflects the fact that frequency components that were centered outside the slit width in the mask plane may still partially contribute to the output waveform because they have a non-infinitesmal spatial extent. This result may impact attempts to determine the local spectral phase profile of an ultrashort waveform by measuring the temporal shifts in cross correlation measurements of the waveform shaped as above with a short reference pulse [29]. The spatial shift illustrated in figure 2 can make these cross-correlation measurements somewhat ambiguous as illustrated in figure 1.

Now we consider a mask pattern in which the desired waveform consists of a multiple pulse sequence. In this case the mask pattern would be given by:

$$m(x) = \sum_n c_n \exp\left(i2\pi k_n x\right) \tag{28}$$

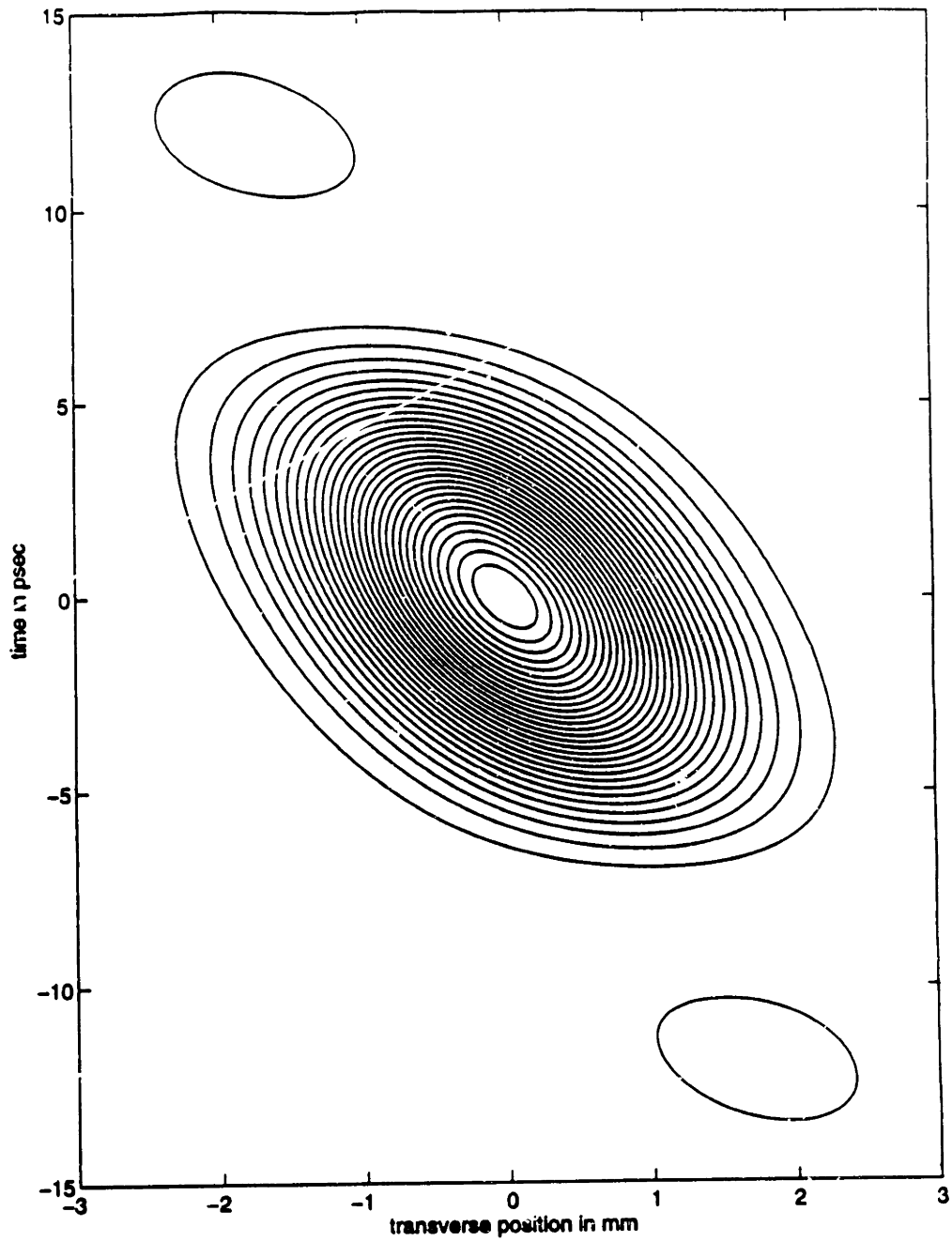

Figure 3: The theoretical space-time electric field intensity profile of a waveform shaped by a single pass through the pulse shaping apparatus. The mask consists of a single narrow slit and the input pulse is short and unshaped. The parameters for the simulation are described in the text. A time-dependent spatial shift in the shaped waveform is clearly evident.

For such a mask pattern, the solution to equation 22 is straightforward, and it is not necessary to use the approximate expression given in equation 25. Solving equation 22 for this mask pattern gives:

$$e_5(x,t) = \exp(i\varpi t)\sum_n c_n \exp\left(-a^2(t-\tau_n)^2\right) \cdot \exp\left(-(x+\chi_n)^2/A^2\right) \tag{29}$$

where $\tau_n = \gamma\lambda f k_n$ and $\chi_n = \beta\lambda f k_n$. Equation 29 shows that pulses are temporally displaced as desired but are accompanied by a corresponding shift in spatial position. These time-dependent shifts in the transverse positions of the respective pulses is identical to the slope described in equation 25. Had the shaped waveform been determined according to equation 25 rather than the exact expression of equation 22, there would be a linear time-dependent spatial shift across the individual profiles of the pulses in addition to the relative shifts in their central position. This spatial shift would be equal to $\beta/a\gamma$ (~7 μm) which is negligible compared to the spotsize (~2 mm), and thus the two results are essentially equivalent. The condition imposed by equation 23 holds, and implies that results determined according to equation 25 (or equation 24) accurately describe the spatial profile of the shaped waveform to within $\beta/a\gamma$. Figure 4 illustrates the space-time intensity profile for a multiple-pulse sequence described by equation 29 produced by a mask pattern consisting of evenly spaced slits of width w (100 μm) separated by distances L (800 μm) and an input pulse given by equation 26. The desired waveform in this case is a train of evenly spaced pulses separated by $\gamma\lambda f/L$ (1.03 psec) under a sinc

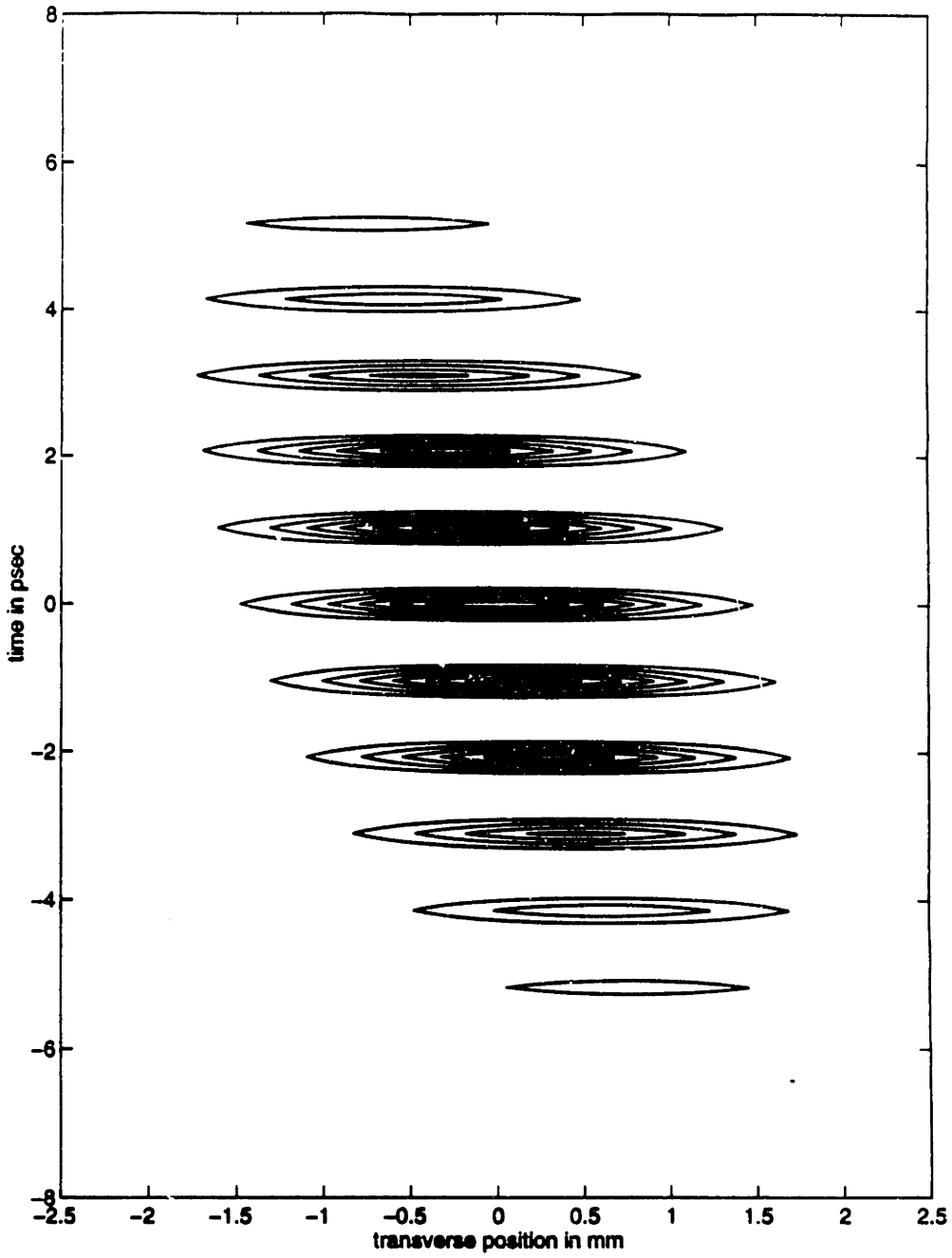

Figure 4: The theoretical space-time electric field intensity profile of a multiple-pulse waveform shaped by single-passing the pulse shaping apparatus. The parameters for the simulation are described in the text. A time-dependent spatial shift in the shaped waveform is clearly evident.

envelope given by $\sin(\pi wt/\gamma\lambda f)/(\pi Lt/\gamma\lambda f)$ [17,25]. The time-dependent transverse shifts in the central position of the pulses is clearly apparant.

We now consider a mask pattern consisting of a quadratic phase sweep:

$$m(x) = \exp\left(i\xi^2 x^2\right) \tag{30}$$

A quadratic spectral phase sweep produces a 'chirped' pulse in the time domain. This is a pulse with a temporally broadened (or 'stretched') envelope and an instantaneous carrier frequency that varies linearly with time under that envelope. We consider the case in which the input pulse is given by equation 26 and is short enough to satisfy equation 23, and also that the quadratic phase sweep stretches the pulse to a duration much longer than the bandwidth-limited pulse duration. This last assumption is equivalent to the condition $a >> d$ where $d = \pi/\gamma\lambda f\xi$. Solving equation 13 under these conditions gives:

$$\begin{aligned} e_5(x,t) \propto \exp\left(i\left(\varpi - d^2 t\right)t\right)\exp\left(-d^4 t^2/a^2\right) \\ \cdot \exp\left(-\left(x + t\beta/\gamma\right)^2/A^2\right) \end{aligned} \tag{31}$$

The anticipated 'chirped' temporal profile is present in equation 31, but again the spatial profile of the overall electric field amplitude has a transverse shift that varies linearly with time. Figure 5 illustrates the space-time intensity profile of a 59 fsec pulse that is stretched to about 6 psec ($d=2x10^{12}$ s^{-1}). Since the instantaneous carrier frequency of the chirped pulse varies linearly with time and the waveform undergoes a

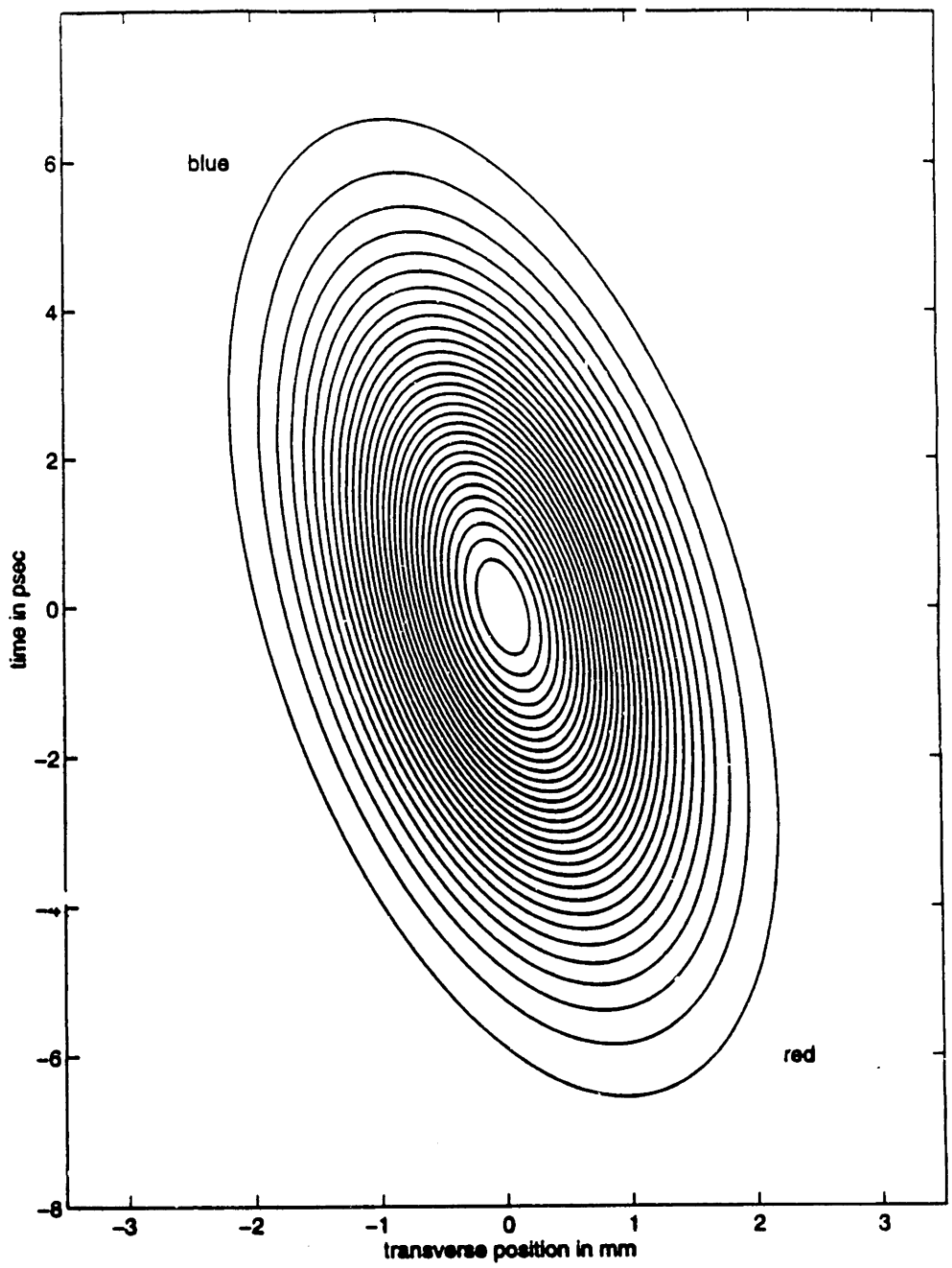

Figure 5: The theoretical space-time electric field intensity profile of a waveform shaped by single-passing the pulse shaping apparatus. The mask consists of a quadratic phase sweep and the input pulse is short and unshaped. The generated waveform is a temporally as well as spatially chirped pulse.

time-dependent spatial shift, the frequency content of the waveform (described by equation 31) has a linear dependence on both space and time. So in this example the red frequency components are shifted both to positive times and negative transverse positions by the pulse shaping apparatus. The effect of a mask consisting of a quadratic phase sweep is equivalent to displacing the position (while maintaining the angular alignment) of the second grating. This displacement means that the different frequency components are not exactly overlapped spatially when incident on the second grating. Instead their spatial centers are linearly dispersed along the grating. The second grating collimates the different frequency components and the displacement imparts a quadratic path length variation but because the different frequency components are not exactly overlapped the waveform has both a temporal and spatial chirp.

These three examples illustrate that the time-dependent electric field amplitude is shaped both in space and time by the pulse shaping apparatus. Since the temporal amplitude of the shaped electric field depends on the spatial coordinate, it follows that the spectral amplitude also depends on the spatial coordinate. This is clearly illustrated by the spatial chirp in the third example. Each example is a specific case of equation 25 and results physically from the spatial diffraction of individual frequency components by the mask pattern that occurs in addition to the spectral filtering.

In the examples studied above we have assumed that the input pulse is both short and bandwidth-limited. However, one of the applications of frequency-domain pulse shaping is recompression of ultrashort pulses [16-17]. In cases where the input pulse is not bandwidth-limited but still short enough to satisfy equation 23, the appropriate mask filter can still completely recompress the input pulse according to equation 25. The

explicit time-dependent spatial shift in equation 25 is negligible because of the short duration of the fully recompressed pulse. However, if the duration of the uncompressed input pulse is long enough that equation 23 is no longer satisfied, no mask pattern will completely recompress the input pulse. This is because spatial diffraction of individual frequency components by the mask pattern will be large enough that the frequency content of the input pulse cannot be perfectly overlapped in both space and time. In this limit equation 25 is not valid and we must use the more general expression given by equation 22. We now consider the case where the input pulse envelope is chirped to many times its bandwidth-limited pulse duration and is given by:

$$e_{in}(x,t) = \exp\left(-\left(a^2 - ib^2\right)t^2\right)\exp\left(-x^2/A^2\right) \qquad (32)$$

with $b >> a$. The expression for the optimally compressed pulse envelope in this case would be:

$$e_{compressed}(x,t) \propto \exp\left(-b^4 t^2/a^2\right)\exp\left(-x^2/A^2\right) \qquad (33)$$

The compressed pulse duration is assumed to be short enough to satisfy equation 23. We now solve equation 22 for the case where the pulse shaping apparatus is used to impart the appropriate quadratic spectral phase sweep to compress equation 32 to equation 33 (setting $\xi = \pi/\gamma\lambda fb$ in equation 30):

$$e_5(x,t) \propto \exp(i\varpi t)\exp\left(-b^4t^2/a^2\Gamma^2\right)\exp\left(-x^2/A^2\Gamma^2\right) \cdot \exp\left(i2xtb^2\gamma\left(\Gamma^2-1\right)/\beta\Gamma^2\right) \tag{34}$$

where $\Gamma = \left(1+\left(\beta/\gamma aA\right)^2\right)^{1/2}$. Note that satisfying equation 23 is equivalent to $\Gamma \approx 1$. Equation 34 shows that both the spotsize and pulse duration are larger by a factor of Γ than those of the optimally compressed pulse in equation 33. Furthermore there is a phase term that varies linearly with xt. This phase term corresponds to linear lateral dispersion (spatial chirp) in the frequency content of the shaped waveform, just as in the case of the bandwidth-limited input pulse considered previously. The slope of this dispersion with respect to transverse position is given by $2b^2\gamma\left(\Gamma^2-1\right)/\beta\Gamma^2$. This means that the quadratic spectral phase sweep produced by the mask to temporally recompress the pulse is necessarily accompanied by spatial diffraction which produces a spatial chirp. As in the previous example of the bandwidth limited input pulse, the mask pattern is equivalent to the displacement of the second grating. In this case the path length variation compensates for the temporal chirp in the input pulse but the accompanying spatial chirp produces imperfect recompression of the broad bandwidth pulse.

Pulse shaping by the displacement of the second grating (rather than use of a mask pattern) is quite common for stretching (chirping) and compression of ultrashort pulses. It is found that by double passing the apparatus the spatial chirp is removed and the quadratic spectral phase sweep is doubled. Hence in the particular case of a mask consisting of a quadratic phase sweep, double-passing the apparatus reverses the space-

time coupling resulting from diffraction. In the following section we will explore the impact of double passing the pulse shaping apparatus for more general mask patterns.

In appendix 1, the exact solutions to equation 22 are given for the two cases of a variably chirped input pulse and a mask consisting of a variable quadratic phase sweep. From the expressions, the limiting cases of equations 31 and 34 follow.

3.4. DOUBLE-PASSING THE PULSE SHAPER

To double-pass the pulse shaper a mirror is placed shortly after the second grating normal to the propagation direction of $e_5(x,t)$, so that the beam retraces its path through the pulse shaper. The double-passed output emerges before the first grating and propagates in a direction opposite to $e_1(x,t)$ (as illustrated within the dashed box in figure 2). We will define the electric field amplitude after double passing the pulse shaper as $e_6(x,t)$. For simplicity we ignore the effects of propagation between the second grating and the mirror. Following the same procedure as in section 2a, the electric field amplitude for $e_6(x,t)$ can be easily derived and is given as:

$$e_6(x,t) = \exp(i\varpi t)\int e_{in}(x-x',t-t')g^{double}(x',t')dx'dt' \quad (35)$$

where $g^{double}(x,t)$ is the impulse response function for the double-passed pulse shaper and is given by:

$$g^{double}(x,t)=\left(\pi/\gamma\beta(\lambda f)^2\right)M_1\left(-\pi(\beta t+\gamma x)/\lambda f\gamma\beta\right) \cdot M_2\left(-\pi(\beta t-\gamma x)/\lambda f\gamma\beta\right) \tag{36}$$

The subscripts on M(k) (the spatial Fourier transform of the mask pattern m(x)) denote the first and second passes respectively. Unless the mask pattern changes on a very fast (nanosecond) timescale, we usually have $m_1(x) = m_2(x) \equiv m(x)$. Note that for the special case of $m_2(x) = 1$ (uniform mask pattern) equations 35 and 36 reduce to equations 13 and 15 with the exception that $e_6(x,t) = e_5(-x,t)$ to account for the image inversion resulting from the second pass through the lens pair.

The impulse response function can also be written in wavevector and frequency space:

$$\overline{E}_6(k,\omega) = \overline{E}_{in}(k,\Omega)\overline{G}^{double}(k,\Omega) \tag{37}$$

and

$$\overline{G}^{double}(k,\omega)=m_1\left(-\lambda f(\gamma\Omega-\beta k)/2\pi\right) \cdot m_2\left(-\lambda f(\gamma\Omega+\beta k)/2\pi\right) \tag{38}$$

Equations 36 and 38 show that double passing the pulse shaping apparatus still generally couples the space-time dependence of the output electric field amplitude. The coupling also appears to be more complicated than that of the single pass. However if we consider the particular case of a mask pattern consisting of a quadratic phase sweep (Equation 30) we see

that the expressions for $\overline{G}^{double}(k,\omega)$ and $g^{double}(x,t)$ become uncoupled. Substituting equation 30 into equation 38 gives:

$$\overline{G}^{double}(k,\omega) = \exp\left(i2(\xi\lambda f\gamma/2\pi)^2\omega^2\right)\cdot\exp\left(i2(\xi\lambda f\beta/2\pi)^2 k^2\right) \quad (39)$$

Equation 39 shows that $\overline{G}^{double}(k,\omega)$ is separable, so that if the input pulse is separable in space and time the output pulse will also be separable. The frequency-dependent part of $\overline{G}^{double}(k,\omega)$ shows that the quadratic spectral phase sweep is simply doubled as a result of the double pass. The wavevector dependent part of $\overline{G}^{double}(k,\omega)$ corresponds to the spatial propagation of the input pulse by a distance $z = -2\lambda(\xi f\beta)^2/\pi$. For the parameters chosen in the example illustrated by figure 3 this distance is about 41 mm. Unless the input pulse were tightly focussed when incident on the first grating, the effect of this propagation distance on the spatial profile of the output waveform would be negligible. Thus with the double pass, only the temporal profile of the input waveform is shaped and pulses can be temporally stretched or compressed without spatial aberrations.

General inspection of equation 38 show that only simple masks consisting of exponential or gaussian patterns will uncouple the space-time coordinates in a similar manner when the apparatus is double-passed. For mask patterns other than these, the expression for $\overline{G}^{double}(k,\omega)$ or equivalently for $g^{double}(x,t)$ are not generally separable. However, both expressions are symmetric with respect to a change of sign in the wavevector or spatial coordinate. This means that for any mask pattern if the spatial profile of the input waveform is symmetric about x=0, then the

spatial profile of the shaped waveform when double-passed through the apparatus is also symmetric about the x=0 plane.

Reconsidering the mask pattern consisting of a single open slit of width w displaced from the center of the mask by a distance x_0, the impulse response function $g^{double}(x,t)$ when the apparatus is double passed is:

$$g^{double}(x,t) = (2\gamma\beta/\pi)\sin(\pi w(\beta t+\gamma x)/2\beta\gamma\lambda f)/(\beta t+\gamma x) \cdot \sin(\pi w(\beta t-\gamma x)/2\beta\gamma\lambda f)/(\beta t-\gamma x) \quad (40)$$

Note that taking x=0 in equation 40 shows that the impulse response function is now proportional to the square of a temporal sinc function (though with an argument that is half the value as that in equation 27). If diffraction is ignored, double passing the mask should leave the spectral filter unchanged for the case of a slit and the temporal impulse response should be linearly rather than quadratically proportional to a sinc function. Figure 6a illustrates the space-time electric field intensity profile for the input waveform described by equation 26 which is double-passed through a mask with a slit of width 100 μm. The waveform is now symmetric about x=0, but has a pulse duration that is broader than one would expect if diffraction were ignored or even if the apparatus were only single-passed for an identical mask (figure 3). Figure 6b illustrates the total time-dependent intensity profile (integrated over transverse position) for the waveform generated by double-passing (dashed curve) and single-passing (solid curve) the pulse shaping apparatus. For this mask pattern, the waveform shaped by a single pass gives rise to a time-dependent transverse shift but otherwise leaves the time-dependent intensity profile unchanged,

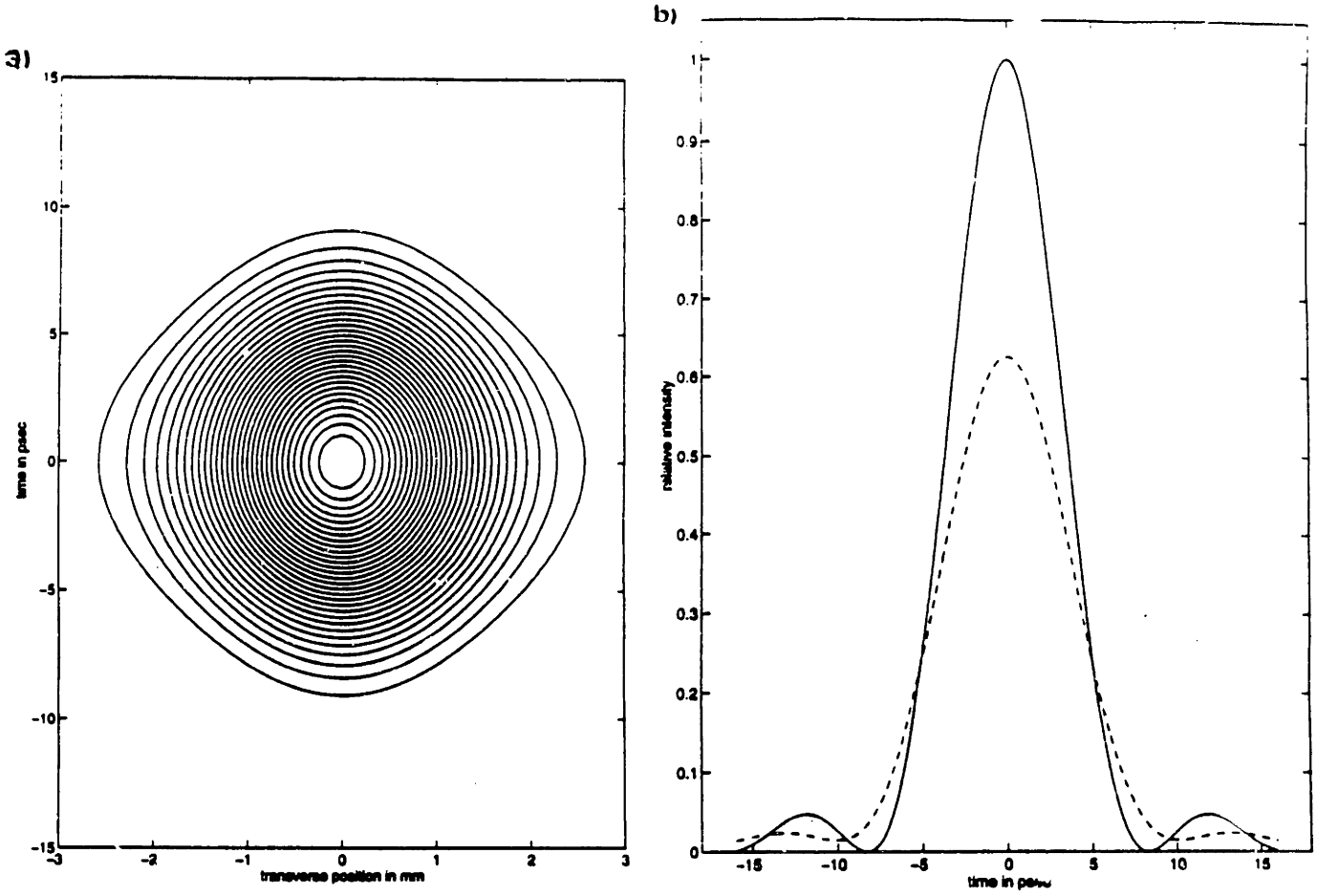

Figure 6: a) The theoretical space-time electric field intensity profile of a waveform produced by double-passing the pulse shaping apparatus. The mask consists of a single narrow slit which is identical to that illustrated in figure 3, and the input pulse is short and unshaped. b) The total time-dependent intensity profile for the double-passed waveform illustrated in a) (dashed curve) and the single-passed waveform illustrated in figure 3 (solid curve). The diffraction effects from the second pass change the total time-dependent intensity profile.

so the solid curve in figure 6b also describes the intensity profile in the limit of no diffraction. In addition to illustrating the different temporal profiles, figure 6b shows that the total energy in the waveform that is produced by double-passing the apparatus is reduced. Since the waveform is spatially shaped upon the first pass through the mask, additional energy is removed upon the second pass through the mask.

If we return to mask patterns that produce multiple-pulse sequences, similar space-time aberrations become apparant. For a mask pattern described by equation 28, the shaped electric field amplitude when the apparatus is double-passed is given by:

$$e_6(x,t) = \exp(i\varpi t) \cdot \sum_n \sum_{n'} c_n c_{n'} e_{in}\left(x-(\chi_n-\chi_{n'}), t-(\tau_n+\tau_{n'})\right) \quad (41)$$

where as before $\tau_n = \gamma\lambda f k_n$ and $\chi_n = \beta\lambda f k_n$. Thus the overall amplitude profile is given by the superposition of many pulses that are displaced both temporally and spatially. We return to the example in section 3 of a mask pattern consisting of evenly spaced slits of width w (100 μm) separated by distances L (800 μm) and an input pulse given by equation 26. Ignoring diffraction, such a mask, when single-passed, will produce a sequence of evenly spaced pulses under a sinc envelope as described by:

$$e_6(x,t) = \exp(i\varpi t)\sum_n c_n e_{in}\left(x, t-\tau_n\right) \quad (42)$$

with $\tau_n = n\gamma\lambda f/L$ and $c_n = \sin(\pi n w/L)/(\pi n)$ [17,25]. As in the case of a mask consisting of a single slit, double-passing this mask should leave the shaped waveform unchanged if diffraction effects are ignored for both passes. In section 3, it was shown that when diffraction is taken into account and the apparatus is single-passed, the pulses undergo a spatial shift that varies linearly with time, so that the 'x' in the spatial argument of the input pulse in equation 42 is replaced with $x + \chi_n$ where $\chi_n = n\beta\lambda f/L$. For the double-passed apparatus the output waveform is correctly given by equation 41 with the definitions for c_n, χ_n, and τ_n just specified. Figure 7a gives the calculated space-time electric field intensity profile for such a waveform. The pulse train is now symmetric about x=0 but the time-dependent amplitudes for the pulses are no longer given by c_n.

To compare the relative intensities of the pulses, we integrate over the transverse coordinate to get the total time-dependent intensity profile of the waveform and then consider the envelope function that weights the total intensities of the pulses in the pulse train (for example, the envelope function would be a constant for a train of pulses with equal intensities). Figure 7b illustrates the envelope function for the pulse train produced by single-passing (solid curve) and double-passing (dashed curve) the apparatus with the mask pattern described previously. As in the case of the single-slit mask pattern, the solid curve also gives the total intensity profile for the waveform in the limit of no diffraction since the time-dependent spatial shift resulting from the single pass does not change the total time-dependent intensity profile. The envelope functions for the single and double-pass cases are different and as in the case of the single slit mask pattern, the total energy in the waveform produced by double-passing the apparatus is reduced. The dashed-dotted curve in figure 7b illustrates the

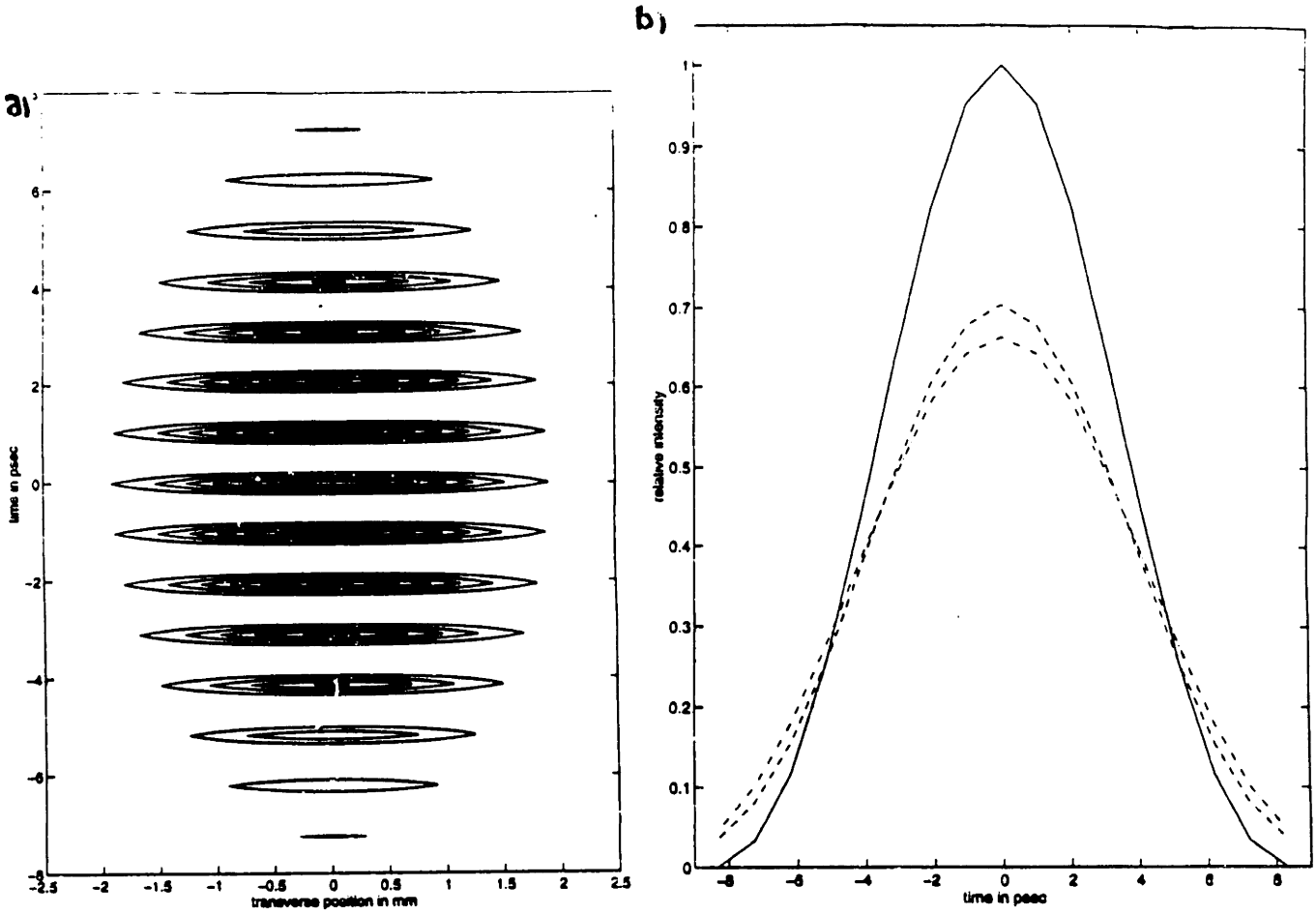

Figure 7: a) The theoretical space-time electric field intensity profile of a waveform produced by double-passing the pulse shaping apparatus. The mask consists of a series of evenly spaced slits and the input pulse is short and unshaped. The waveform produced by single-passing this mask pattern was illustrated in figure 4. In the limit of no diffraction the waveforms produced by single or double-passing the apparatus with this particular mask are pulse trains with identical amplitude envelopes. b) The total time-dependent intensity envelope functions that weight the intensities of the pulses in the waveform produced by double-passing (dashed curve) and single-passing (solid curve) the apparatus. The dash-dotted curve gives the intensity envelope (normalized to the magnitude of the dashed curve) along the x=0 coordinate of the waveform illustrated in a).

normalized intensity envelope function along the x=0 spatial coordinate of the waveform produced by double-passing the apparatus (figure 7a). Figure 7b shows that the pulses in figure 7a have a time-dependent spotsize (which is larger near t=0 and smaller away from t=0) since the dashed-dotted curve is smaller than the dashed curve at t=0 but larger at times away from t=0. The amplitudes of the different pulses can no longer be meaningfully specified since their spotsizes are varying.

If the spatial shifts are ignored in equation 41, then the interferences in the double summation will generate the temporal profile anticipated by simply squaring the perfectly resolved spectral filter. However because of the spatial shifts in the sum, the interferences in the double sum are not fully realized. For example consider the case where the desired waveform consists of four pulses at times $(-2\tau, -\tau, \tau, 2\tau)$ with complex amplitudes $(-\sqrt{2}, 4i, 4i, -\sqrt{2})$, and the waveform is to be produced by double-passing the apparatus. The mask pattern is determined by ignoring diffraction effects and taking the square root (since the mask will be double passed) of the appropriate spectral filter. Figure 8 illustrates the space-time intensity profile of the shaped waveform for such a mask pattern. The input waveform is given by equation 26 and $\tau = 4$ ps. The value beneath each pulse gives its relative intensity along with its relative intensity in the desired waveform (which would be produced in the limit of no diffraction) in parenthesis. Figure 8 shows that the intensities of the pulses differ from those of the desired waveform, including a non-zero intensity at zero time. This reflects the fact that the spatial shifts produced by diffraction in equation 41 produce imperfect cancellation of the electric field amplitude at zero time. Note that figure 8 shows only the intensity effects of double-

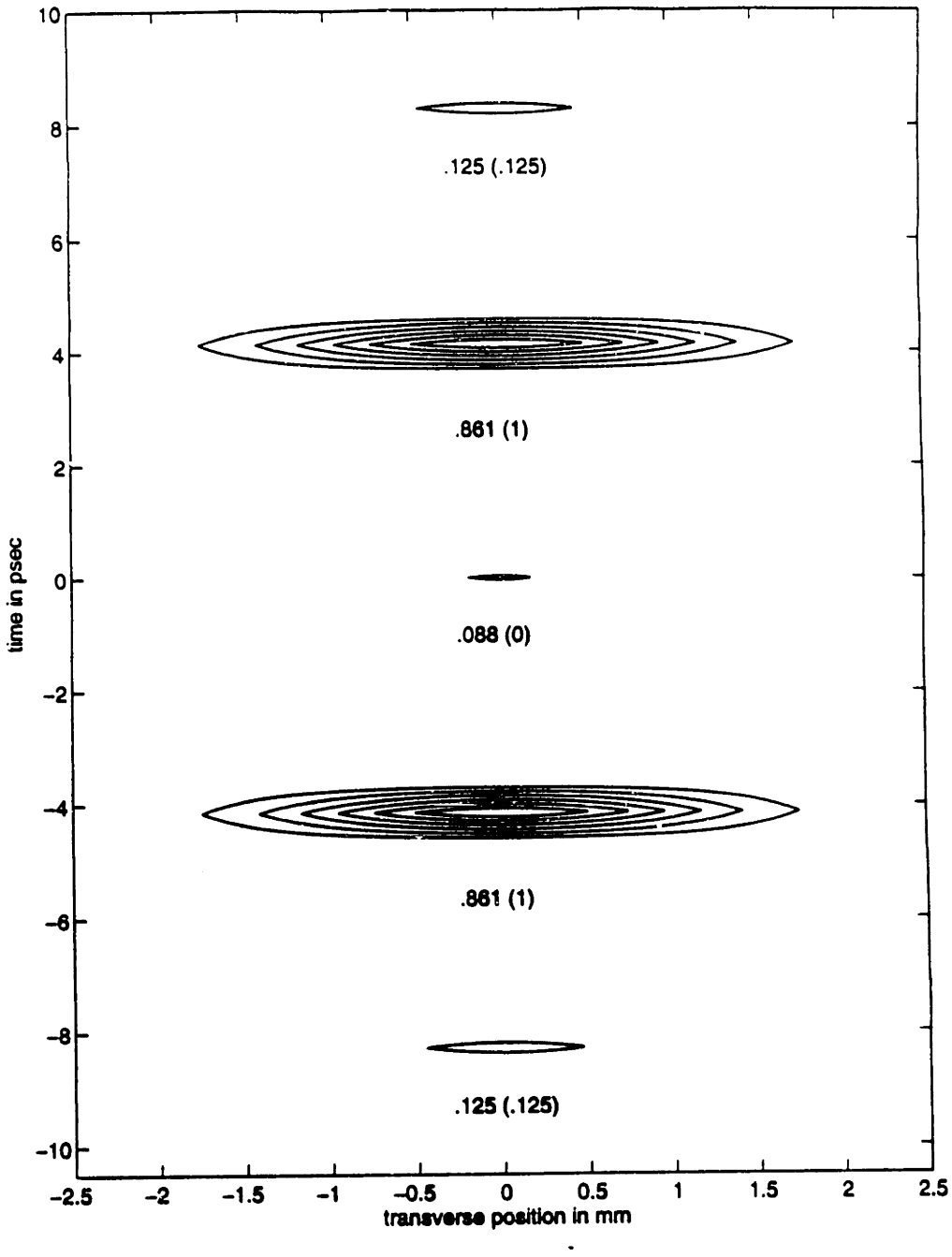

Figure 8: a) The theoretical space-time electric field intensity profile of a waveform produced by double-passing the pulse shaping apparatus. The desired waveform consists of pulses with complex amplitudes $\left(-\sqrt{2}, 4i, 4i, -\sqrt{2}\right)$ at times $\left(-2\tau, -\tau, \tau, 2\tau\right)$ with τ=4 psec. The mask pattern is determined by ignoring diffraction effects, and as a result the relative intensities of the peaks (listed on the contour plot) differ from the desired values (listed in parenthesis on the contour plot).

passing. The temporal phase profile of the generated waveform will also be affected.

These examples show that double-passing the pulse shaping apparatus does not generally reverse space-time coupling in the shaped waveform and can produce complicated space-time profiles.

3.5. PRACTICAL IMPACT AND PROSPECTS

The derived impulse response functions (equations 15 and 36) for both the single and double passed apparatus clearly show that pulse shaping operations generally shape and couple the temporal and spatial profiles of the output waveform. As mentioned in the first section, this follows from the fact that spatially separated frequency components incident on the mask have a finite spatial extent across the mask pattern. The mask therefore filters both the spectral and wavevector components of the input pulse. It follows that the temporal and spatial extents of the impulse response functions vary inversely with the size of individual mask features. The relative mapping of the mask pattern onto the spectral and wavevector profiles of the input pulse is given by the parameter γ/β, which as shown in equation 18 is proportional to the angular dispersion produced by the grating. The resulting frequency and wavevector-dependent filter is imparted onto the input pulse. Clearly if the filter is relatively constant over either the wavevector or frequency content of the input pulse then there is no shaping in the respective coordinate (nor its conjugate variable). Hence the limiting case of purely temporal shaping occurs when the wavevector content of the input pulse is small (equivalent to a large input spot size) and the angular dispersion produced by the grating is large.

As pointed out in section 2c, in most practical cases γ/β is not large enough to completely ignore the effects of spatial shaping. In most cases (single pass, short input pulse) equation 25 is a reliable expression for the space-time profile of the shaped waveform. Also, in practice the length of the mask filter is fixed such that after angular dispersion and focussing, the entire spectrum fits onto the mask. Since the temporal extent of the shaped waveform is limited by the spatial resolution of the mask features [13,17,25], we can estimate the maximum lateral displacement χ in the center of the waveform over this temporal extent. If the spatial resolution of the mask is given by σ, the temporal range T of the shaped waveform is given by $T = \gamma\lambda f/\sigma$ (derived in appendix 2). Hence the maximum lateral displacement χ is given by

$$\chi = T|-\beta/\gamma| = \frac{\beta\lambda f}{\sigma}. \tag{43}$$

Equation 43 gives a simple measure of the lateral shift resulting from single-pass space-time shaping in terms of practical parameters. To exploit the spatial resolution of a given mask (and to produce temporally extended waveforms) and to minimize the effect of diffraction, the spotsize of the input pulse should be large compared to χ. This is true for both the single and double passed apparati.

Many masks used in practice (etched substrates, LC SLMs) are impixellated devices that discretely approximate a desired spectral filter function. The discreteness produces a response function that includes the desired response function as well as temporally displaced replicas of it (at multiples of T for a pixel size σ) under a sinc modulation envelope [25,30].

It has been argued that the replicas arising from the discreteness of a mask can be largely ignored since the finite spot sizes of frequency components imaged onto the mask "blurs" the physically discrete mask, producing a smooth frequency filter. The results of section 2 tell us that for a single pass apparatus, the low-intensity replicas produced at long times by discrete sampling are present but undergo larger spatial shifts than those of the desired waveform. In practice the replicas are undesirable and can be largely removed by spatial filtering if the spatial separations between the replicas and the desired waveform are large compared to the input spotsize. This imposes an additional constraint on the temporal range of desired waveforms, since the spotsize should be large compared to the spatial shifts within the temporal extent of the desired waveform but small compared to the spatial shifts of the replicas.

Section 4 showed that double passing the pulse shaping apparatus does not generally reverse the space-time coupling in the output waveform. For example we can consider the overall time-dependent intensity profile of a short separable waveform I(t) shaped by a single passing the apparatus. Using equation 25 and integrating $|e_5(x,t)|^2$ over x gives:

$$I(t) = \int |e_5(x,t)|^2 dx \propto \left| \int h_{in}(t-t') M(-2\pi t'/\gamma\lambda f) dt' \right|^2 \qquad (44)$$

This result is identical to the one obtained in the limit of no diffraction, it gives the overall intensity profile of the desired waveform. However this result does not generally hold true for a waveform shaped by double passing the apparatus because the spatial shaping now yields a more complicated result than a linear time-dependent spatial shift. The total

time-dependent intensity profile can be different than the desired one as clearly illustrated in the examples of section 4. Furthermore if a discrete mask is used in a double-pass apparatus, the replica waveforms that are produced at long times and with large transverse displacements after a single pass will be spatially translated back toward x=0 and can interfere with the spectral filtering used to produce the desired waveform near t=0 during the second pass. Hence the replicas at long times cannot be removed by spatial filtering and the desired waveform near t=0 is perturbed. This makes double-passing a discrete mask an extremely unattractive option for most high-fidelity pulse shaping.

In general the shaped waveform produced by either single or double passing the pulse shaping apparatus can be expanded into Hermite-Gaussian modes with time-dependent amplitudes. If some spatial filter operation could retain only a single one of these spatial modes (e.g. the gaussian spatial mode), the resulting waveform would be separable in space and time. The mask pattern could be chosen to compensate for this filtering so that the desired temporal amplitude is produced within the selected spatial mode [25]. Unfortunately spatial filtering with a simple aperture does not produce a gaussian spatial mode. However this may be possible by propagating the shaped waveform through a single-mode fiber which can only support a gaussian mode [6,31]. Similarly, regenerative amplification of the shaped waveform in a cavity which only supports a gaussian mode should also make this possible [32]. Note that for some applications, such as repetitive excitation of propagating phonon-polaritons modes [33], it might be possible to exploit the coupled space-time shaping produced by the pulse shaping apparatus.

In conclusion, we have derived the impulse response functions for single and double passed pulse shaping apparati based on the filtering of spatially separated frequency components to properly examine the role of diffraction on the spatial shaping of the output waveform. For the practical case of a short input pulse, the waveform produced by the pulse shaping apparatus has the desired temporal profile except that the spatial profile of the waveform undergoes a spatial shift that varies linearly with time. This space-time coupling is not generally reversed by double-passing the apparatus.

APPENDIX 1

Here we present the exact solution to equation 22 for a variably chirped input pulse given by equation 32 and a quadratic phase mask given by equation 30. The result is:

$$e_5(x,t) \propto \exp(i\varpi t)\exp\left(-\left(\Theta_R - i\Theta_I\right)/\Delta\right) \tag{A1}$$

where

$$\begin{aligned}\Theta_R = {} & (c/v)^2\left(a^2\left(a^2+c^2\right)+b^2\left(b^2-d^2\right)\right)(x-vt)^2 \\ & +d^2\left(a^2d^2-b^2c^2\right)t^2-(c/v)^2d^2\left(b^2-d^2\right)x^2\end{aligned} \tag{A2}$$

$$\begin{aligned}\Theta_I = {} & (c/v)^2\left(b^2\left(a^2+c^2\right)-a^2\left(b^2-d^2\right)\right)(x-vt)^2 \\ & -d^2\left(a^2\left(a^2+c^2\right)+b^2\left(b^2-d^2\right)\right)t^2 \\ & -(c/v)^2d^2\left(a^2+c^2\right)x^2\end{aligned} \tag{A3}$$

$$\Delta = \left(a^2 + c^2\right)^2 + \left(b^2 - d^2\right)^2 \qquad \text{(A4)}$$

and $v = -\beta/\gamma$, $d = \pi/\gamma\lambda f\xi$, $c = v/A$, with a, b, and A describing the duration, chirp, and spotsize of the input puise respectively as described in equation 32 for the input pulse.

Equation 31 is derived from A1 for the case b=0 and a>>c,d. Equation 34 is derived from A1 for the case b=d and a<<b.

APPENDIX 2

Here we show the relationship between the spatial resolution of the mask and the temporal range over which a waveform can be shaped. From Fourier analysis [29], if $m(x)$ has features as short as σ, the range in wavevector space Δk of $M(k)$ is given by:

$$\Delta k = 2\pi/\sigma \qquad \text{(A5)}$$

From equation 15, we see that the temporal impulse response function for the mask is given by $M(-2\pi t/\gamma\lambda f)$. Combining this result with equation A5 gives the temporal range T of the effective spectral mask filter as:

$$T = \gamma\lambda f/\sigma \qquad \text{(A6)}$$

CHAPTER 3: REFERENCES

1. W. S. Warren, H. Rabitz, M. Dahleh, 'Coherent Control of Quantum Dynamics: The Dream is Alive', *Science* **259**, 1581-1589 (1993)

2. P. Brumer and M. Shapiro, 'Laser Control of Molecular Processes', *Annu. Rev. Phys. Chem.* **43**, 257-282 (1992)

3. H. Kawashima, M. M. Wefers, K. A. Nelson, 'Femtosecond pulse shaping, multiple-pulse spectroscopy, and optical control', *Annu. Rev. Phys. Chem.* (in press) 1995

4. J. L. Krause, R. M. Whitnell, K. R. Wilson, Y. Yan, S. Mukamel, 'Optical Control of molecular dynamics: Molecular Cannons, reflectrons, and wave-packet focusers', *J. Chem. Phys.* **99**, 6562-6578 (1993)

5. A. M .Weiner, J. P. Heritage, J. A . Salehi, 'Encoding and decoding of femtosecond pulses', *Opt. Lett.* **13**, 300-302 (1988)

6. A. M. Weiner, Y. Silberberg, H. Fouckhardt, D. E. Leaird, M. A. Saifi, M. J. Andrejco, P. W. Smith, 'Use of Femtosecond Square Pulses to Avoid Pulse Breakup in All-Optical Switching', *IEEE J. Quan. Elec.* **25**, 2648-2655 (1989)

7. M. Haner, W. S. Warren, 'Generation of programmable, picosecond-resolution shaped laser pulses by fiber-grating pulse compression', *Opt. Lett.* **12**, 398-400 (1987)

8. K. B. Hill, D. J. Brady, 'Pulse shaping in volume reflection holograms', *Opt. Lett.* **18**, 1739-1741 (1993)

9. D. J. Brady, A. G. S. Chen, G. Rodriguez, 'Volume holographic pulse shaping', *Opt. Lett.* **17**, 610-612 (1989)

10. A. M .Weiner, D. E. Leaird, D. H. Reitze, E. G. Paek, 'Spectral holography of shaped pulses', *Opt. Lett.* **17**, 224-226 (1992)

11 C. Froehly, B. Colombeau, M. Vampouille, *Progress in Optics* E. Wolf, ed. (North-Holland, Amsterdam, 1983), vol. 20, pp. 115-121

12 J. P. Heritage, A. M. Weiner, R. N. Thurston, 'Picosecond pulse shaping by spectral phase and amplitude manipulation', *Opt. Lett.* **10**, 609-611 (1985)

13. A. M .Weiner, J. P. Heritage, E. M. Kirschner, 'High-resolution femto-second pulse-shaping', *J. Opt. Soc. Am.* **B5**, 1563-1572 (1988)

14 A. M. Weiner, D. E. Leaird, 'Generation of terahertz-rate trains of femtosecond pulses by phase-only filtering', *Opt. Lett.* **15**, 51-53 (1990)

15. D. H. Reitze, A. M. Weiner, D. E. Leaird, 'Shaping of wide bandwidth 20 femtosecond optical pulses', *Appl. Phys. Lett.* **61**, 1260-1262, (1992)

16. A. M. Weiner, D. E. Leaird, J. S. Patel, J. R. Wullert, 'Programmable femtosecond pulse shaping by use of a multielement liquid-crystal phase modulator', *Opt. Lett.* **15**, 326-328 (1990)

17. A. M. Weiner, D. E. Leaird, J. S. Patel, J. R. Wullert, 'Programmable Shaping of Femtosecond Optical Pulses by Use of 128-element Liquid Crystal Phase Modulator', *IEEE J. Quan. Elec.* **28**, 908-920 (1992)
18. M. M. Wefers, K. A. Nelson, 'Programmable phase and amplitude femtosecond pulse shaping', *Opt. Lett.* **18**, 2032-2034 (1993)
19. M. M .Wefers, K. A, Nelson, 'Generation of high-fidelity programmable shaped ultrafast optical waveforms', *Opt. Lett.* **20**, 1047-1049 (1995)
20. C. W. Hillegas, J. X. Tull, D. Goswami, D. Strickland, W. S. Warren, 'Femtosecond laser pulse shaping by use of microsecond radio-frequency pulses' *Opt. Lett.* **19**, 737-739 (1994)
21. O. E. Martinez, '3000 Times Grating Compressor with Positive Group Velocity Dispersion: Application to Fiber Compensation in 1.3-1.6 μm Region', *IEEE J. Quan. Elec.* **23**, 59-64 (1987)
22. R. N. Thurston, J. P. Heritage, A. M. Weiner, W. J. Tomlinson, 'Analysis of Picosecond Pulse Shape Synthesis by Spectral Masking in a Grating Pulse Compressor', *IEEE J. Quan. Elec.* **22**, 682-696 (1986)
23. M. B. Danailov, I. P. Christov, 'Time-space shaping of light pulses by Fourier optical processing', *J. Mod. Opt.* **36**, 725-731 (1989)
24. J. Paye, A Migus, 'Space-Time Wigner Functions.and their Application to the Analysis of a Pulse Shaper', *J. Opt. Soc. Am. B.* to be published (1995)
25. M. M. Wefers, K. A. Nelson, 'Analysis of programmable ultrashort waveform generation using liquid crystal spatial light modulators', *J. Opt. Soc. Am. B.* **12**, 1343-1362 (1995)
26. J. Squier, F. Salin, G. Mourou, D. Harter, '100-fs pulse generation and amplification in Ti:Al_2O_3', *Opt. Lett.* **16**, 324-326 (1991)
27. O. E. Martinez, 'Grating and prism compressors in the case of finite beam size', *J. Opt. Soc. Am.* **B3**, 929-934 (1986)
28. G. R. Fowles, *Modern Optics*, p139-141, (Dover Publications Inc., New York, NY 1975)
29. J. L. A. Chilla, O. E. Martinez, 'Direct determination of amplitude and phase of femtosecond light pulses', *Opt. Lett.* **16**, 39-41 (1991)
30. R. N. Bracewell, *The Fourier Transform and its Applications,* (McGraw-Hill, New York, NY, 1986)
31. A. M. Weiner, J. P. Heritage, R. J. Hawkins, R. N. Thurston, E. M. Kirschner, D. E. Leaird, W. J. Tomlinson, 'Experimental Observation of the Dark Soliton in Optical Fibers', *Phys. Rev. Lett.* **61**, 2445-2448 (1988)

32 M. M. Wefers, H. Kawashima, K. A. Nelson, 'Programmable femtosecond pulse shaping and spectroscopy' in *Ultrafast Phemonena IX*, G. A. Mourou, A. H. Zewail, P. F. Barbara, W. H. Knox, Eds. (Springer-Verlag, Berlin, 1994)
33. K. A. Nelson, 'Coherent Control: Optics, Molecules, and Materials', in *Ultrafast Phemonena IX*, G. A. Mourou, A. H. Zewail, P. F. Barbara, W. H. Knox, Eds. (Springer-Verlag, Berlin, 1994)
34. A. E. Siegman, *Lasers*, p658-661, (University Science Books, Mill Valley, CA 1986)

Chapter 4
Automated Multi-Dimensional Optical Spectroscopy: Control over Electronic Coherences in Atomic Potassium Vapor

The work is this chapter is published in:

1. M. M. Wefers, H. Kawashima, K. A. Nelson, J. Chem. Phys. ***102****, 1995*

2. H. Kawashima, M. M. Wefers, K. A. Nelson, Annu. Rev. Phys. Chem. ***46****, 627, 1995*

4.1 INTRODUCTION

In this chapter the automated generation of ultrafast optical waveforms, described in the chapter 2, will be demonstrated by using two- and three- pulse sequences to control electronic coherences in atomic potassium vapor. These electronic coherences will be sensitive to the inter-pulse delays and phase relationships and give rise to a macroscopic observable, frequency-resolved fluorescence. Waveform parameters such as number of pulses, inter-pulse delay, and inter-pulse phase relationships, are scanned in an automated fashion as fluorescence is monitored. From an operational point of view, the experiment demonstrates that optical pulse shaping techniques approach the level of multiple-pulse multidimensional NMR: a spectroscopic observable is monitored while (RF or optical) waveform parameters are varied, following the computer-guided instructions of a user who need not be intimately familiar with the technology of waveform generation.

There are a number of differences between this experiment and the multiple-pulse experiments on molecular and ionic crystals [1,2] described

in the first chapter which also utilized pulse shaping techniques. First, prefabricated masks were used so that the apparatus was not automated and the desired waveforms needed to be known prior to the experiment and changing of the shaped waveform required manual changing of the masks. Second, phase-only masks were used so that the phase-relationships between adjacent pulses in the sequence could not be specified. This was unimportant in those experiments since the optical carrier frequency of the waveform was not resonant with any transitions. Rather, ground-state vibrational motion was induced through non-resonant impulsive stimulated Raman scattering which depends only on the intensity profile of the shaped waveform. In this experiment on potassium vapor, the optical carrier frequency of the shaped waveform is near resonance creating electronic coherences whose form will depend on both intensity and phase profiles of the shaped waveform. Arbitrary excited-state preparations can be specified demonstrating a simple example of quantum control. With the current versatility of the pulse shaping apparatus, experiments on more complicated systems are possible in which both electronic and vibrational coherences are simultaneously controlled. Specific schemes and examples are described in the end of the chapter.

Other researchers have used ultrashort phase-locked pulse-pairs to manipulate electronic coherences in atoms [3], molecules [4], and quantum well heterostructures [5]. Phase-locked pulse-pairs have also been used to separate real and imaginary contributions to time-resolved photon-echo responses [6,7]. In all of these experiments, phase-locked pulse-pairs were produced by recombining identical pulses with interferometric accuracy (the temporal delay is stabilized to much less than an optical period). Hence for a particular phase relationship, the pulse delay can only be

varied in steps that are integral numbers of optical periods. In contrast, our pulse shaping apparatus is capable of continuously scanning both the optical phases and delays between pulses. This distinction becomes important when the number of optical cycles within the individual pulses becomes small. Furthermore, our pulse shaping apparatus easily allows for the generation of more than two phase-related pulses or more generally an arbitrary optical waveform.

4.2 THEORETICAL DESCRIPTION

The 4s to 4p transition in atomic potassium vapor is split by spin-orbit coupling to yield $4^2P_{1/2}$ at 769 nm and $4^2P_{3/2}$ at 766.5 nm. This splitting is well within the 12-nm bandwidth of a 70-fsec pulse (the duration of pulses from our oscillator) centered between the two resonances. The shaped waveform hence interacts with a three-level system whose two excited levels are optically coupled with the ground state $4^2S_{1/2}$. The dipole moment for the transition to $4^2P_{1/2}$ is larger than that to $4^2P_{3/2}$ by a factor of $\sqrt{2}$. Note that Doppler broadening and hyperfine splittings are manifested only on slower time scales than those of this experiment.

The electric field of a multiple-pulse sequence produced by the pulse-shaper can be described as follows:

$$e_{shaped}(t) = e^{i\omega_0 t} \sum_n A_n e^{i\phi_n} g(t - \tau_n) \qquad (1)$$

where ω_0 is the optical carrier frequency, $g(t)$ is the amplitude envelope for the unshaped pulse, and A_n, τ_n, and ϕ_n are the amplitude, temporal

position, and optical phase respectively of the n^{th} pulse in the sequence. The overall phase is not specified uniquely.

Assuming that the bandwidth associated with the unshaped pulse equally covers both resonances and in that we are in the weak-field regime (so that first order perturbation theory applies), the amplitude for excited state j is

$$c_j \propto \mu_j \sum_n A_n \, e^{i(\Delta_j \tau_n + \phi_n)} \tag{2}$$

where suffices j = 1, 2 represent $4^2P_{1/2}$, $4^2P_{3/2}$, respectively, Δj the detuning of the carrier frequency ω_0 from the resonance.

The total fluorescence intensity emitted from the system following excitation by a sequence of pulses specified by the set of delays and phases (τ_i, ϕ_i) is

$$I(\tau_i, \phi_i) \propto \left|c_1(\tau_i, \phi_i)\right|^2 + \left|c_2(\tau_i, \phi_i)\right|^2 \tag{3}$$

In our experiments, the total fluorescence (or frequency-resolved fluorescence from either one of the levels) is measured as the excitation waveform characteristics (τ_i, ϕ_i) are varied continuously, under computer control. The total fluorescence can be compared to the prediction given by equation 3.

As a an example of a simple control objective, a two-pulse sequence may be devised that exclusively populates only one of the two excited state levels. The first pulse excites coherences between the ground and both of the excited state levels. After a time $t = T_{21} / 2$, where

$T_{21} \equiv 2\pi / (\omega_2 - \omega_1)$ is the beat period given by the difference between the resonance frequencies ω_1 and ω_2, the two coherences are exactly out of phase with one and other. Hence if the optical phase of the second pulse is chosen to constructively interfere with one coherence its interference with the other coherence is necessarily destructive.

If instead two phase-related pulses are separated by T_{21} , the full period associated with the excited-state splitting, the coherences excited by the first pulse are back in phase with each other at the time of the second pulse. In this case, if the second pulse interferes constructively with one coherence it also does so with the other coherence and similarly for destructive interference.

Other control objectives may be to produce a pair of coherences whose relative amplitudes and phases can be specified arbitrarily, or to produce selected coherent states at particular times. Such objectives would be difficult to achieve using combinations of narrowband excitation frequencies tuned to the resonances. Three or more pulses may be required in the waveform depending on the type and number of intermediate states involved.

4.3 EXPERIMENTAL APPARATUS AND RESULTS

70-fsec, 767.4-nm pulses from a titanium:sapphire laser operating at 76 MHz were shaped by the liquid crystal pulse-shaping apparatus described in chapter 2 section 8. The shaped waveforms have a total energy of approximately 0.5 nJ. The total energy was kept constant as relative delays and phases were scanned during spectroscopy measurements. The shaped pulse sequences were then directed through a spectroscopic quartz cell containing atomic potassium. The temperature of the cell was

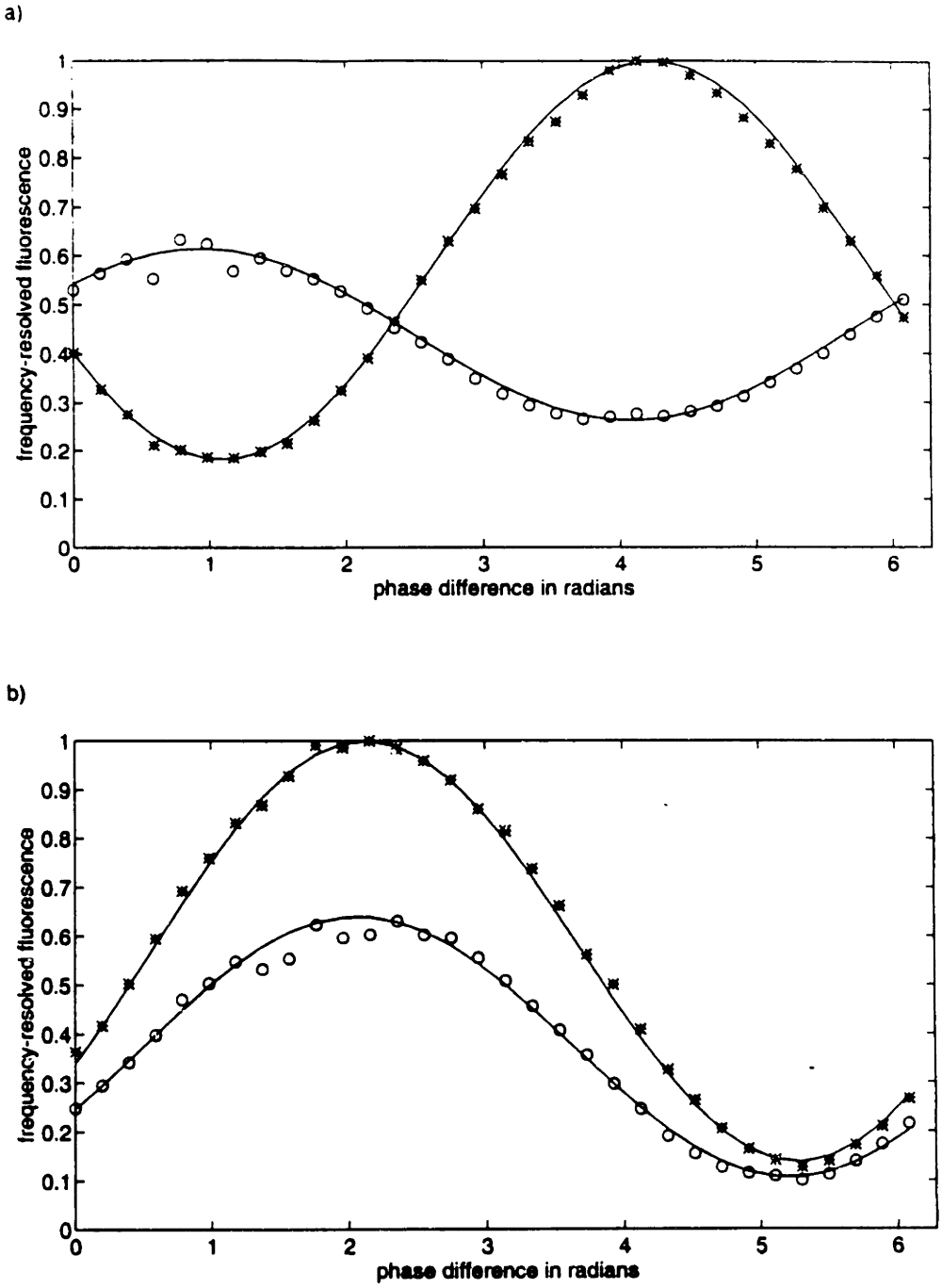

figure 1: Frequency-resolved potassium fluorescence intensity measured as a function of optical phase difference between two pulses separated by 288 fsec (figure 1a) and 576 fsec (figure 1b). The stars (circles) correspond data points with the monochromater set at 766.5 nm (769 nm). The solid curves correspond to the best sinusoidal fits through the data.

maintained at 590 K. The amount of potassium in the cell was so small that optical density effects were negligible. The emitted fluorescence was collected at a 90-degree angle from the excitation beam path by a photomultiplier tube, and a low-resolution monochromater was used to help eliminate scattered light and resolve the two resonances.

Figure 1 shows the frequency-resolved fluorescence from the potassium cell when excited by two pulses separated by 288 fsec (figure 1a) and 576 fsec (figure 1b), as a function of the phase difference between the two pulses. These separations correspond to T_{21} / 2, T_{21}(the beat period) respectively. The stars (circles) correspond to the fluorescence measured with the monochromater set to 766.5 nm (769 nm) and the solid lines are best sinusoidal fits to the data. As anticipated, the data show a sinusoidal dependence on the optical phase difference between the pair of pulses. The signal of the 766.5 nm resonance is approximately twice that of the 769 nm resonance which follows from their respective dipole moments. The two sinusoids are out of phase with one another in figure 1a, demonstrating that pulses separated by T_{21} / 2 with the correct optical phase difference can selectively populate one of the excited-state levels. This is in contrast to pulses separated by T_{21} (figure 1b) which maximize (or minimize) population in both excited state levels simultaneously when the optical phase difference between the pulses is chosen appropriately. More generally, depending on the delay time and phase difference chosen, any choice of relative phases and amplitudes of the two coherences can be realized.

Figure 1 shows raw data that are not corrected for background signal from scattered light or the imperfect resolution between the two resonant frequencies by the monochromater. To make a more quantitative

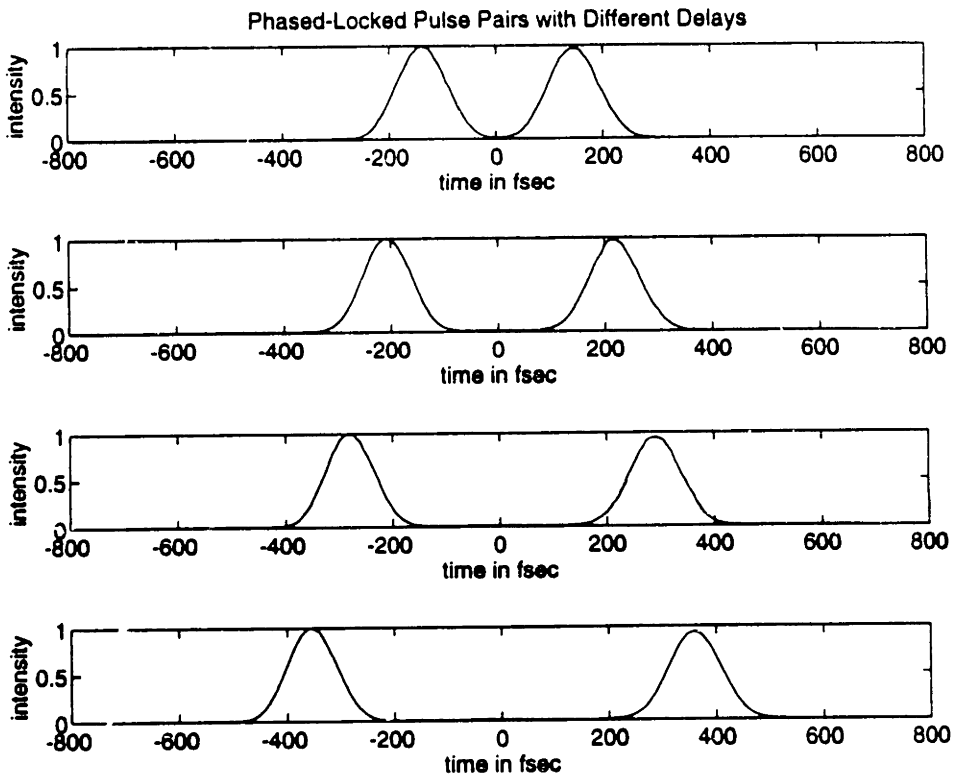

figure 2: Cross-correlation measurements of some of the phase-related two pulse sequences generated in an automated fashion and used to excite the potassium sample.

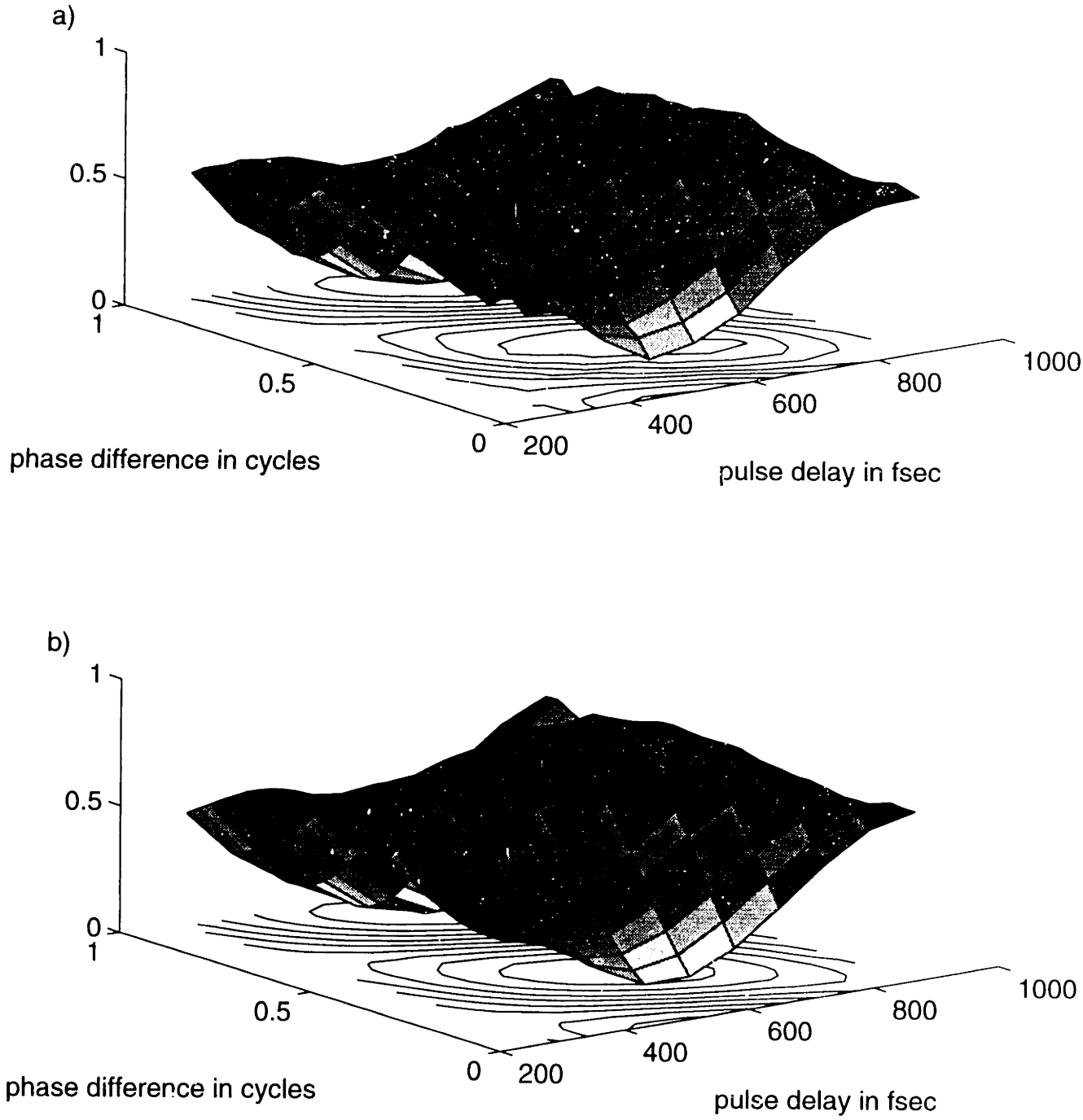

figure 3: Total potassium fluorescence intensity measured experimentally (a) and predicted theoretically (b) as a function of the relative delay (288-864 fsec) and optical phase (0-2pi radians) of a two-pulse sequence. The experiment and theory agree with a standard deviation of 0.6% across the two-dimensional manifold.

comparison to the theoretical predictions described in the previous section, the experiment was repeated but instead the total fluorescence was measured over a two-dimensional manifold of pulse sequences whose relative delay and phase were scanned. Figure 2 shows cross-correlation measurements of some of these excitation waveforms. A small constant background term was subtracted from the two-dimensional data set which was then compared to the theoretical predictions without any free parameters. Figure 3 shows the experimental results and the results predicted by eqs. 2-4. The agreement between the two is excellent, with a standard deviation of 0.6% across the manifold.

Experiments with three phase-related pulses were also carried out. In this case, up to four parameters (two relative delays and phases) could be scanned by the pulse-shaping apparatus. For purposes of tractable display, we chose to fix the delays and vary the phases. Figure 4 shows cross-correlation measurements of some of these excitation waveforms with the pulse arrival times fixed at -450 fsec, 0 fsec, and 300 fsec and the optical phase differences varied between 0 and 2p radians. Since only the phase relationships are varied, the cross-correlation measurements appear to be almost identical. However the coherent excitation produced by these waveforms is very different despite their similar intensity profiles. Figure 5 shows the total measured and predicted fluorescence intensities as the two sets of phase-relationships are varied. Again the agreement between the two results is excellent, with a standard deviation of 1.9% across the two-dimensional manifold.

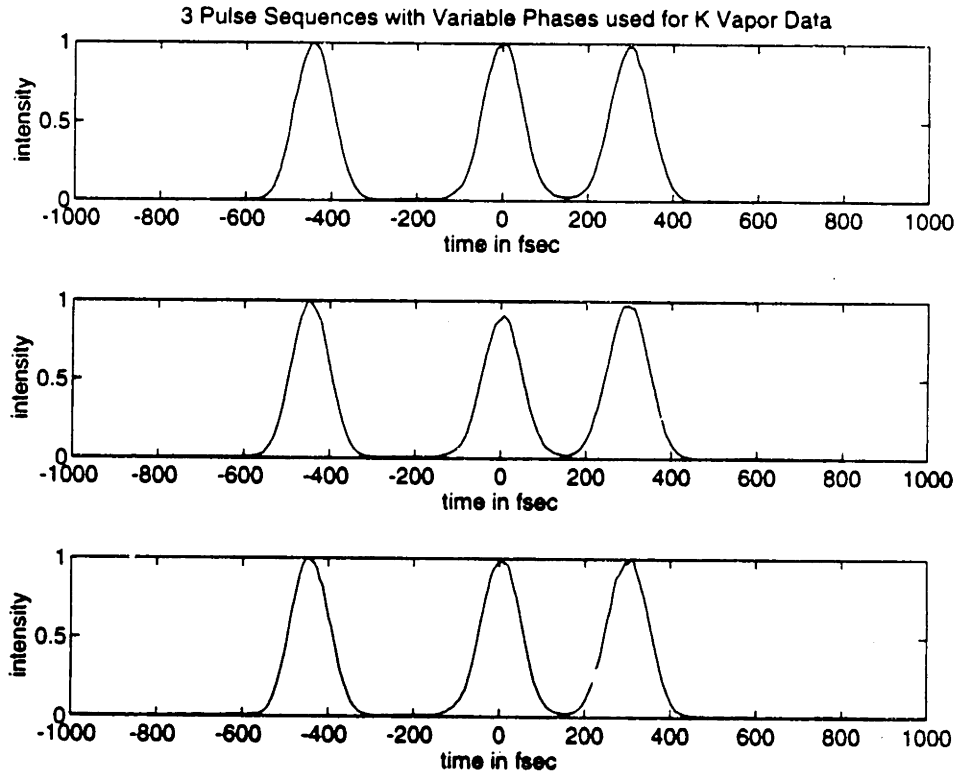

figure 4: Cross-correlation measurements of some of the three-pulse phase-related pulse sequences generated in an automated fashion by the pulse shaper and used to excite the potassium sample. In this case the delays of the pulses were fixed, so the amplitude profile of the different waveforms are the same and therefore their cross-correlation measurements are identical. The waveforms are different however, because the phase relationships between adjacent pulses is being varied.

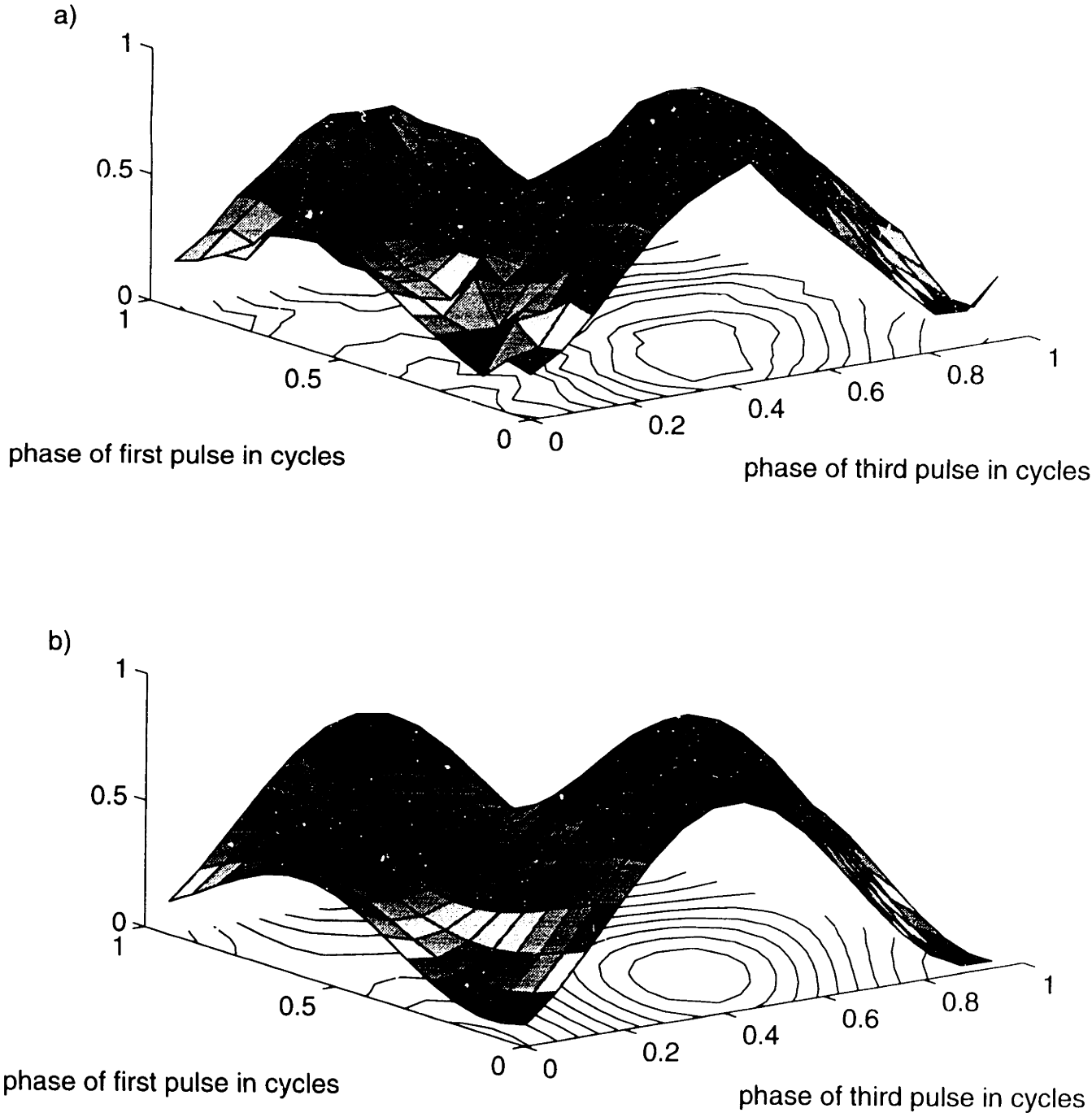

figure 5: Total potassium fluorescence intensity measured experimentally (a) and predicted theoretically (b) as a function of the optical phase differences (0-2pi radians) between the first and second pulses and the second and thrid pulses of a three-pulse sequence. The arrival times of the three pulses are -450 fsec, 0 fsec, and 300 fsec. Experiment and theory agree with a standard deviation of 1.9% across the two-dimensional manifold.

4.4 DISCUSSION

The results of the previous section demonstrate the fidelity and versatility of our pulse shaping apparatus. In particular, the results confirm that the phase-relationships between adjacent pulses are indeed being specified as desired. Recall from chapter 2 that characterization by cross-correlation did not explicitly measure the temporal phase of the shaped waveforms. The results also demonstrate a simple example of quantum control. Each point on the two-dimensional plots in figures 5 and 7 correspond to the coherent preparation of a specified quantum state by the shaped excitation waveform. Since there are only two excited-state levels only two excitation pulses are necessary to produce an arbitrary coherent state. However if the bandwidth of the shaped waveform overlapped with more than two levels, additional pulses could be employed to specify a desired coherent state. The quantum states produce in this manner may be part of an extended scheme involving subsequent excitation to different quantum levels. We have only considered excitation in the weak field limit in which coherent amplitude in the ground state is nearly unity and the relative (but small) complex amplitudes in the two excited states are arbitrarily specified after excitation. However our pulse shaping apparatus can also manipulate the amplitudes of successive pulses, therefore in the strong field limit, where population inversion is possible, one can arbitrarily specify the complete three-level quantum system following excitation.

The experiments on this simple system can also be understood in the frequency domain. From first order perturbation theory, the amplitude for excited state j can also be expressed as $c_j \propto E\left(\varepsilon_j/\hbar\right)$ where $E(\omega)$ is the Fourier transform of the shaped waveform and ε_j is the energy of the

state j relative to the ground state energy. In practice this meant that only two frequency components in the shaped waveform interacted (to first order) with the potassium sample. Changing the delays and temporal phase relationships between adjacent pulses in the excitation pulse sequences results in changing the complex spectral amplitude at these two frequency components thereby affected the observed fluorescence. While the majority of the bandwidth in the shaped excitation waveform does not interact with the sample, the large bandwidth allows the interaction to occur over a short period of time.

It is also worth noting that the 'path' over which the system evolved during excitation might be part of the coherent control objective. For example, in recent experiments on three-level quantum-well heterostructures [5], terahertz radiation is produced since the two excited state levels are optically coupled. The total intensity of this terahertz radiation will be proportional to the induced coherence between the two excited state levels following excitation which equals

$$\left|c_1 c_2^*\right|^2 = \left|E(\varepsilon_1/\hbar)\right|^2 \left|E(\varepsilon_2/\hbar)\right|^2 \qquad (4)$$

In a recent article [8], Weiner addressed whether pulse shaping techniques could enhance terahertz emmision from engineered quantum well systems. It was pointed out that pulse shaping techniques cannot enhance terahertz emmision relative to a single pulse excitation since the technique only filters existing frequency components and thus the product in equation 4 can only be reduced and not enhanced by pulse shaping. However, though the total intensity of the terahertz radiation can not be increased, the time-dependent form of the emitted radiation can clearly be

manipulated by a shaped excitation waveform. In particular, it was shown (by computation) that the peak intensity in the emitted terahertz radiation can be made larger by using a shaped waveform for excitation rather than an unshaped single pulse. This can be understood by realizing that the amplitude of some frequency components of the shaped waveform can be increased if the shaped waveform is temporally truncated, thereby increasing the magnitude of $\left|c_1 c_2^*\right|^2$ during the excitation. This example shows that the evolution prescribed by a shaped waveform during excitation can also be important.

4.5 FUTURE PROSPECTS

4.5.1 Resonance-Enhanced Ground-State Vibrational Motion

One of the motivations behind previous multiple-pulse experiments [1] was the amplification of ground-state vibrational motion through impulsive stimulated Raman scattering (ISRS). Considerable enhancement is possible in ISRS if pulses resonant with an electronic excited state surface are used [9]. However, in this case, enhanced ground-state vibrational motion is accompanied by excited electronic-state vibrational motion. This excited state population can lead to optical damage in solid state samples. A number of theorists have considered using resonant excitation to enhance ground-state vibrational motion while shaping the excitation waveform to minimize excited-state population. Kosloff and co-workers [10] developed a scheme in which a small coherent electronic polarization is produced through resonant excitation with a weak pulse, and then a waveform whose phase is adjusted to always remain locked-in-phase with this polarization is used for resonance-enhanced ISRS with suppression of further electronic excitation. One drawback with this scheme is that there must be now

electronic dephasing during the excitation waveform. In another scheme, Cina and co-workers proposed using sequences of out-of-phase resonant pulse pairs [11]. If the pulse pair separation is short compared electronic dephasing and excited-state vibrational motion, minimal excited state population results while ground-state vibrational motion is imparted. Sequences of these pulse-pairs could be matched to the vibrational period of the ground-state motion, as in previous non-resonant experiments, thus amplifying coherent displacements. In more recent work, Cina has shown that sequences of nearly resonant pulses are also sufficient to enhance ground-state vibrational motion while minimizing excited-state population [12]. Pulse sequences were also suggested for minimization of wavepacket spreading in either position or momentum.

Resonant interaction with an excited electronic-state surface might also facilitate optical switching between multiple wells in a ground-state surface, such as different ferroelectric domains [13]. For a ground state with a symmetric double-well potential energy surface, excitation from one potential well into an excited-state potential energy surface with higher symmetry should lead to excited-state wavepacket propagation. Using a second pulse, this wavepacket can be projected back down to the other potential well of the ground state.

4.5.2 Molecular Wavepacket Shaping

The analysis for the excitation of excited-state electronic levels in section 2 is equally valid for vibrational levels on an excited-state potential energy surface in the weak field limit. All transitions that are within the bandwidth of the input pulse and have non-zero matrix elements can be excited. Since the excitation waveform can be shaped, the relative

amplitudes and phases of these excited state coherences can specified producing a 'shaped' molecular wavepacket on the excited-state surface. with ground. In some sense, the allowed transitions that are within the bandwidth of the input pulse may be considered 'building blocks' through which an arbitrary superposition may be created. The resulting excited-state superposition, following excitation, will not be an eigenstate, and therefore will evolve in time. But this evolution will be prescribed by the initial superposition produced by the shaped waveform.

Experiments of this type have been demonstrated on molecular iodine [14]. Excitation pulses were 'chirped' so that the excited-state molecular wavepacket evolved into a minimum-uncertainty wavepacket at some specified later time as it propagated along the excited-state potential energy surface. In contrast, excitation with a short unshaped pulse results in an excited-state wavepacket that is initially focused (a minimum-uncertainty wavepacket) and then spreads as it propagates on a excited-state surface that has a curvature that differs from the that of the ground-state potential. The chirped excitation pulse is equivalent to a waveform in which the different frequency components undergo a quadratic spectral phase sweep. The variation in spectral phase precompensates for the wavepacket spreading so that the wavepacket becomes focused at some later time. This might be the first step in an extended coherent control scheme, in which one requires maximal Franck-Condon overlap (and hence a minimum uncertainty wavepacket) for a subsequent transition to a different electronic state manifold.

A related molecular wavepacket scenario involves using a sequence of many variably chirped pulses to produce a series of focused wavepackets on the excited-state potential energy surface. Thus one could produce a

transient periodic structure of probability density in position space on the order of nano- to picometers [15]. This could be used as a ultrafast programmable gate to diffract additional beams (e.g. X-rays or electron beams). We showed in chapter 2 that our state-of-the art pulse shaping techniques can already generate complicated shaped waveforms such as a sequences of variably chirped pulses.

4.5.3 Real-Time Feedback in Quantum Control

Our simple experiments on potassium vapor demonstrate the automated and programmable nature of our pulse shaping apparatus. These capabilities are essential for reaching more complicated control objectives in which the Hamiltonian of the system, and therefore the optimal excitation waveform, is not known precisely. In such cases iterative improvement of the excitation waveform, based on measured sample responses to earlier trial waveforms, can be carried out. Computer simulations of real-time feedback in quantum control experiments in the presence of uncertainties have been performed with modest success [16].

CHAPTER 4: REFERENCES

1. A. M. Weiner, D. E. Leaird, G. P. Wiederrecht, K. A. Nelson, Science **247**, 1317 (1990)
2. G. P. Wiederrecht, T. P. Dougherty, L. Dhar, K. A.Nelson, D. E. Leaird, A. M. Weiner, *Phys. Rev. B.* **51**, 916 (1995)
3. J. T. Fourkas, W. L. Wilson, G. Wackerle, A. E. Frost, M. D. Fayer, *J. Opt. Soc. Am. B.* **6**, 1905 (1989)
4. N. F. Scherer, A. J. Ruggiero, M. Du, G. R. Fleming, *J. Chem. Phys.* **93**, 856 (1990)
5. P. C. M. Planken, I. Brener, M. C. Nuss, M. S. C. Luo, S. L. Chuang, *Phys. Rev. B* **48**, 4903 (1993)
6. W. P. de Boeij, M. S. Pshenichnikov, D. A. Wiersma, *Chem. Phys. Lett.* **238**, 1 (1995)
7. W. P. de Boeij, M. S. Pshenichnikov, D. A. Wiersma, *Chem. Phys. Lett.* **247**, 264 (1995)
8. A. M. Weiner, *J. Opt. Soc. Am. B.* **11**, 2480 (1994)
9. L. Dhar, J. A. Rogers, K. A. Nelson, *Chem. Reviews* **94**, 157 (1994)
10. R. Kosloff, A. D. Hammerich, D. J. Tannor, *Phys. Rev. Lett.* **69**, 2172 (1992)
11. J. A. Cina, T. J. Smith, *J. Chem. Phys.* **98**, 9211 (1993)
12. T. J. Smith, J. A. Cina, *J. Chem. Phys.* **104**, 1272 (1996)
13. S. Fahy, R. Merlin, *Phys. Rev. Lett.* **73**, 1122 (1994)
14. B. Kohler, V. V. Yakovlev, J. Che, J. L. Krause, M. Messina, K. R. Wilson, N. Schwentner, R. M. Whitnell, Y.-J. Yan, *Phys. Rev. Lett.* **74**, 3360 (1995)
15. B. Kohler, J. L. Krause, F. Raksi, K. R. Wilson, V. V. Yakolev, R. M. Whitnell, Y. Yan, *Acc. Chem. Res.* **28**, 133 (1995)
16. G. J. Toth, A. Lorincz, and H. Rabitz, *J. Chem. Phys.* **101**, 3715 (1994)

Chapter 5:
Psuedorotation in Crystalline Quartz

The work in this chapter is in preparation for publication in:

1. M. M. Wefers, H. Kawashima, K. A. Nelson, Chem. Phys. Lett. (in preparation)

2. M. M. Wefers, H. Kawashima, K. A. Nelson, J. Phys. Chem. Sol. (in press) (1996)

5.1 INTRODUCTION

In this chapter we demonstrate control over vibrational motion in two dimensions. This is made possible by using pairs of pulses with different polarizations to impart momentum impulsively and selectively to orthogonal modes in an E-symmetry degenerate vibration. Control over the amplitude and phase of the orthogonal modes govern the trajectory of the vibrational motion in two dimensions. In particular, if there is a difference in phase between the two orthogonal modes, the degenerate vibration will exhibit psuedorotational motion, meaning that the atoms involved in the degenerate vibration will travel in an elliptical orbit around their equilibrium positions. The experiment is based on theoretical work showing that controlled ground state psuedorotation can be initiated by properly polarized pairs of non-resonant ultrashort pulses in systems with Jahn-Teller like electronic excited states [1]. As we shall see however, the underlying idea is applicable to a broad class of degenerate vibrational modes.

This experiment is similar to the one described previously on atomic potassium vapor in that multiple pulses are used to control the phase and

amplitude of multiple coherences and produce a desired superposition. In this case however, it is the amplitude, optical delay, and *polarization* of the respective pulses rather than their amplitude, optical delay and *optical phases*, which provides the means for control. Consideration of these control parameters partially motivated the pulse shaping results described previously which demonstrate the generation of ultrafast waveforms with tailored time-dependent polarization profiles.

The excitation mechanism which will be exploited is impulsive stimulated Raman scattering (ISRS), through which an ultrashort optical pulse exerts a sudden ("impulsive") driving force on Raman-active vibrational modes [2]. The pulse duration must be short relative to the vibrational period for the impulsive force to be exerted. For pulse durations on the order of 50 femtoseconds, vibrational modes of energies up to about 300 cm^{-1}, i.e. of frequencies up to about 5 THz, can be driven through ISRS. The Raman excitation is governed by a component of the polarizability tensor which will have a specific form depending on the symmetry of the crystal and the vibrational mode in question. Hence the orientation of the crystal relative to the polarization(s) of the excitation beam(s) also determines whether a particular mode is impulsively excited. For a doubly degenerate (E-symmetry) Raman-active vibrational mode, a femtosecond pulse may exert a driving force on one or both of these modes through ISRS, depending on its polarization. If two femtosecond pulses with different optical polarizations and a controllable delay time between them are incident on the sample, they can initiate motions along the two modes with controllable amplitudes and initial displacement times, i.e. controllable vibrational amplitudes and phases. This is the requirement to induce and control pseudorotational motion.

Excitation of pseudorotational motion will be demonstrated on the 128 cm^{-1} E-symmetry optic phonon in the α-phase (room temperature) of crystalline quartz. Two nearly collinear sub-100 fsec pulses are used to excite the psuedorotation, and the trajectory of the degenerate vibration will be inferred from the induced birefringence detected by a third nearly collinear sub-100 fsec pulse. Before proceeding with the experimental results, a more formal description of the excitation and detection mechanisms will be outlined in the next section.

5.2 EXCITATION AND DETECTION OF PSUEDOROTATION

To illustrate the excitation mechanism, we envision a system with a C_3 axis of symmetry such as a hypothetical triatomic with atoms on the corners of an equilateral triangle. The normal vibrational modes for such a system are illustrated in figure 1. They consist of the symmetric A_1 breathing mode and two degenerate E-symmetry vibrations which we will denote as Q_1 and Q_2. Any orthonormal pair of vibrations Q_1' and Q_2', where Q_1' and Q_2' are superpositions of Q_1 and Q_2, is an equally valid representation of the non-symmetric degenerate vibration. Consideration of the complex superpositions Q_1+iQ_2 and Q_1-iQ_2, illustrate examples of psuedorotation as shown in figure 2.

The Hamiltonian for the degenerate mode system can be written (in mass-weighted units) as:

$$H_0 = \tfrac{1}{2}\left(P_1^2 + P_2^2\right) + \omega^2 \tfrac{}{2}\left(Q_1^2 + Q_2^2\right) \qquad (1)$$

where ω is the angular frequency of the degenerate mode and P_1 and P_2 are the conjugate momenta. Optical pulses that are non-resonant with any

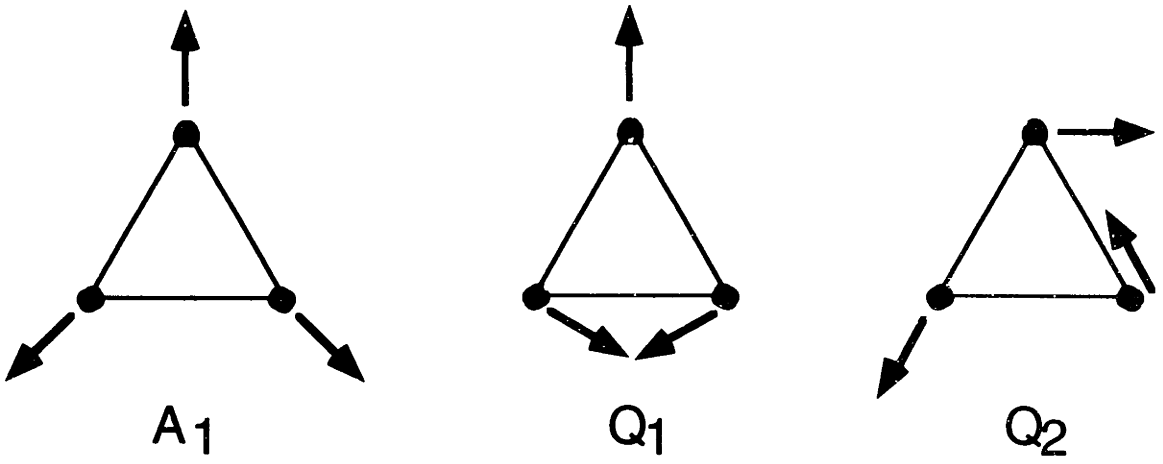

Figure 1: Normal mode vibrations for hypothetical system with C_3 symmetry. There is a symmetric A_1 'breathing ' vibration and a doubly-degenerate E-symmetry vibration with orthogonal modes that we desiginate Q_1 and Q_2.

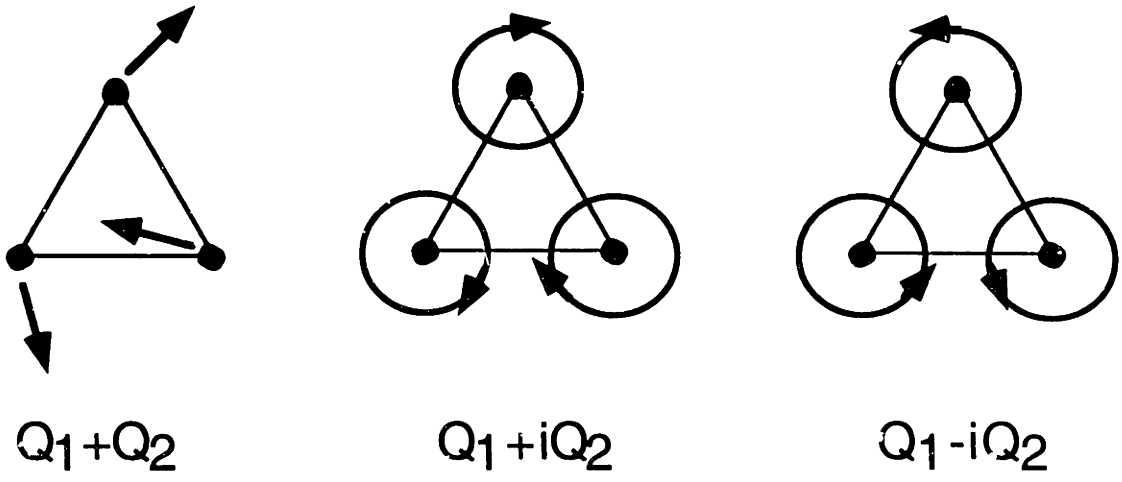

Figure 2: Superpositions of the degenerate E-symmetry normal modes Q_1 and Q_2. Complex superpositions produce examples of psuedorotational motion.

electronic transition are assumed, so that the lowest order term in the interaction Hamiltonian is:

$$H_1(t) = -\tfrac{1}{2}\,\mathbf{E}(t)\cdot\underline{\underline{\alpha}}(t)\cdot\mathbf{E}(t) \tag{2}$$

where **E**(t) is the electric field vector and α(t) the polarizability tensor. Based on symmetry considerations and group theory calculations [3], the form of the component of the polarizability tensor that depends to first order on Q_1 and Q_2, $\underline{\underline{\delta\alpha}}(t)$, is determined to be:

$$\underline{\underline{\delta\alpha}}(t) = \begin{bmatrix} 0 & c & d \\ c & 0 & 0 \\ d & 0 & 0 \end{bmatrix} Q_1(t) + \begin{bmatrix} c & 0 & 0 \\ 0 & -c & d \\ 0 & d & 0 \end{bmatrix} Q_2(t) \tag{3}$$

where the **z**-axis in the Cartesian reference frame is along the C_3 axis.

Assuming that the system is excited with optical pulses whose duration is short compared to the vibrational period, the imparted momenta $(\delta P_1, \delta P_2)$, following impulsive excitation can be determined from equations 2 and 3 as:

$$\delta P_1 \propto 2cE_xE_y + 2dE_zE_x \tag{4a}$$

$$\delta P_2 \propto c\left(E_x^2 - E_y^2\right) + 2dE_yE_x \tag{4b}$$

where E_i is the electric field amplitude along the ith Cartesian coordinate. For the case of light propagating along the **z**-axis, one can see from equations 4a and 4b that light linearly polarized along either the **x**- or **y**-

axes will selectively excite mode Q_2, whereas light polarized linearly along either the **x**+**y**- or **x**-**y**-axes will selectively excite Q_1.

In what follows ,we will assume pulses that propagate along the principle axis (**z**-axis) of the crystal. Excitation with a single linearly polarized pulse will initiate motion which oscillates with angular frequency ω, along a coordinate that is some real linear combination of Q_1 and Q_2 (which looks similar to the motion illustrated in figures 1b and 1c). Excitation with two time-coincident linearly polarized pulses will produce a similar result since the field is identical to a single pulse whose polarization is given by the vector sum of the two pulses. If however the two pulses are temporally separated from one another, psuedorotational motion can be induced. For example, a first **y**-polarized pulse will initiate motion along Q_2, followed by a second temporally-delayed $(\mathbf{x}+\mathbf{y})/\sqrt{2}$-polarized pulse which will initiate motion along Q_1. Though both of these motions will oscillate with angular frequency ω, the difference in phase between the two motions will result in an elliptical motion. The phase difference φ is given by:

$$\phi = \omega\tau \tag{5}$$

where τ is the separation between the two excitation pulses. Figure 3 illustrates trajectories in the phase space of (Q_1,Q_2) for phase differences or 0, $\pi/2$, π, and $3\pi/2$. These trajectories correspond respectively to the vibrational superpositions previously illustrated in figure 2. The ellipticity and directionality of the vibrational trajectory is controlled by temporal delay between the two excitation pulses. This psuedorotational motion implies a vibrational angular momentum L, which is quantified as:

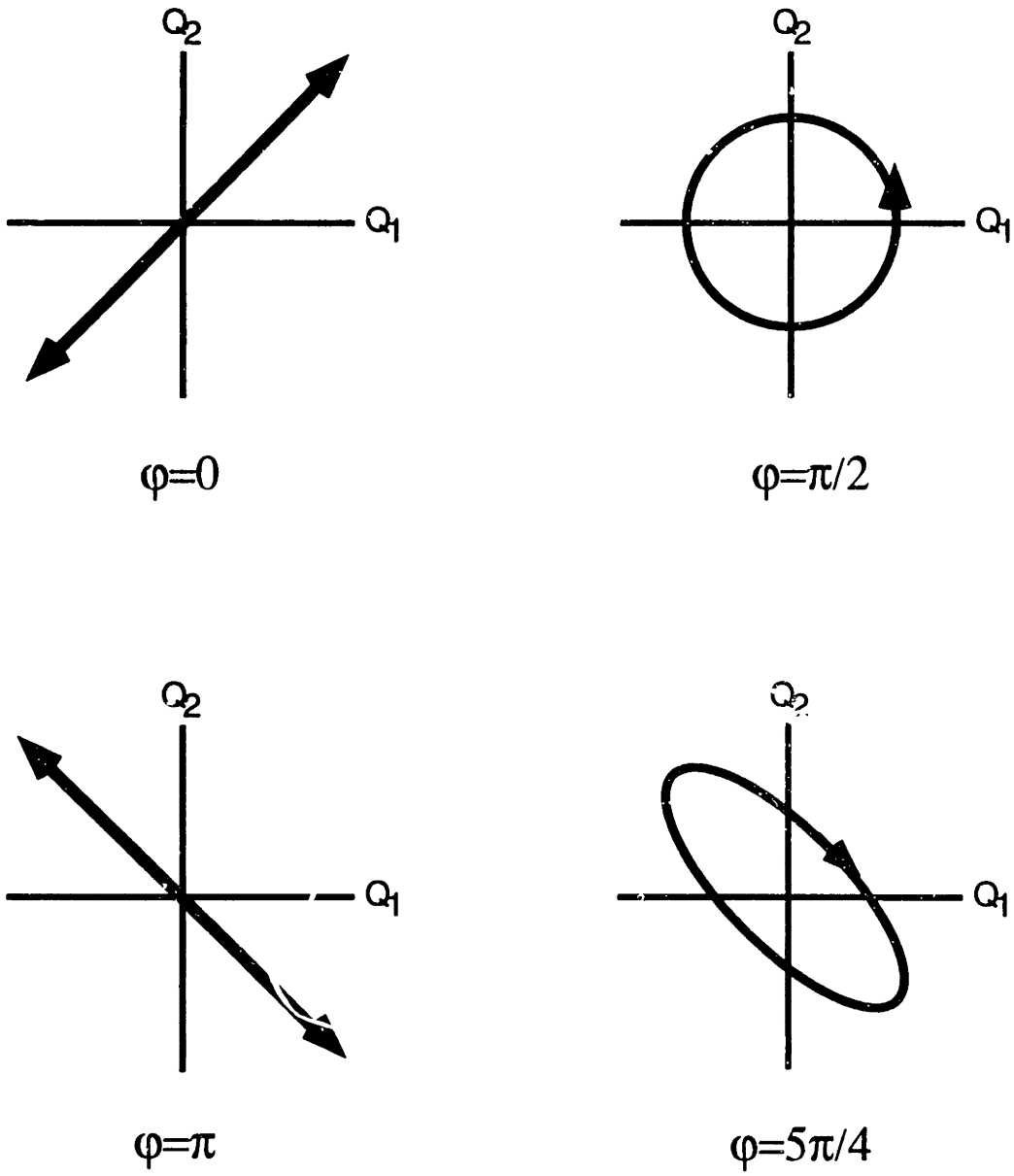

Figure 3: Trajectories of the degenerate vibrational motion in the phase space (Q_1,Q_2) for different delays between the excitation pulses. The excitation delay produces a phase shift between the two orthogonal modes that constitute the degenerate vibration.

$$L = Q_1 P_2 - Q_2 P_1 \propto \sin\phi \tag{6}$$

Though we have assumed that the two excitation pulses are respectively **y**- and (**x**+**y**)/$\sqrt{2}$-polarized, any two pulses propagating along the **z**-axis with linear polarizations that differ by 45 degrees will excite orthogonal modes of the degenerate vibration selectively. The induced vibrational angular momentum (which is equivalent to the ellipticity and directionality of the vibrational trajectory) will be independent of the absolute polarizations and depend only on the time delay between pulses. Hence rotating the polarizations but keeping their difference fixed simply rotates the coordinate axes but not the trajectories illustrated in figure 3.

The vibrational motion initiated by the excitation pulses give rise to a transient birefringence in the sample which can be probed by subsequent time-delayed pulses. The perturbation to the dielectric tensor will have the same form as equation 3, which following excitation is:

$$\underline{\underline{\delta\varepsilon}}(t) = \begin{bmatrix} \Delta\varepsilon_2 & \Delta\varepsilon_1 \\ \Delta\varepsilon_1 & -\Delta\varepsilon_2 \end{bmatrix} \propto \begin{bmatrix} u(t)I_1 \sin(\omega t) & u(t-\tau)I_2 \sin(\omega t - \phi) \\ u(t-\tau)I_2 \sin(\omega t - \phi) & -u(t)I_1 \sin(\omega t) \end{bmatrix} \tag{7}$$

where the **z**-coordinate has been omitted, u(t) is defined for causality (u(t)=1 for t>0, u(t)=0 for t<0), I_1 is the intensity of the **y**-polarized pulse and I_2 is the intensity of the (**x**+**y**)/$\sqrt{2}$-polarized pulse. Following excitation, equation 7 can be diagonalized and written in the form below:

$$\underline{\underline{\delta\varepsilon}}(t) = \sqrt{\Delta\varepsilon_1^2 + \Delta\varepsilon_2^2}\,\underline{\underline{R^{-1}}}(\Theta)\cdot\begin{bmatrix}1 & 0\\ 0 & -1\end{bmatrix}\cdot\underline{\underline{R}}(\Theta) \qquad (8)$$

where $R(\Theta)$ describes a rotation by an angle of $\Theta = \pi/4 - \theta/2$ about the z-axis, with q defined so that $\cos\theta = \Delta\varepsilon_1 / \sqrt{\Delta\varepsilon_1^2 + \Delta\varepsilon_2^2}$ and $\sin\theta = \Delta\varepsilon_2 / \sqrt{\Delta\varepsilon_1^2 + \Delta\varepsilon_2^2}$.

For small vibrational displacements, $\Delta\varepsilon_1$ and $\Delta\varepsilon_2$ are small compared to ε_0, so that equation 8 is equivalent to describing the sample as a waveplate with a principle axis at an angle Θ in the x-y plane and a retardance δ:

$$\delta \approx 2\pi L\sqrt{\Delta\varepsilon_1^2 + \Delta\varepsilon_2^2}\,/n\lambda \qquad (9)$$

where L is the thickness of the sample, λ the wavelength of the probe pulse, and n the index of refraction at equilibrium. For equal intensity excitation pulses, a temporal separation that gives a phase difference in equation 5 that equals multiples of π, produces an orientation Θ that is constant in time and equal to $\pi/8$ with a retardance undergoes oscillations in time $\delta \propto \sin\omega t$. If instead, the temporal separation between equal intensity excitation pulses gives a phase difference of $\pi/2$ plus multiples of π, it is the orientation Θ which rotates in time as $\Theta \approx \omega t/2$, while the retardance is constant. In the former case, the oscillators are locked in phase (or out of phase), with zero angular momentum following a linear trajectory given by Q1+Q2 (Q1-Q2). In the later case, the oscillators are locked in quadrature, with maximal angular momentum following a circular trajectory given by Q1±iQ2. The dielectric ellipsoid illustrates the

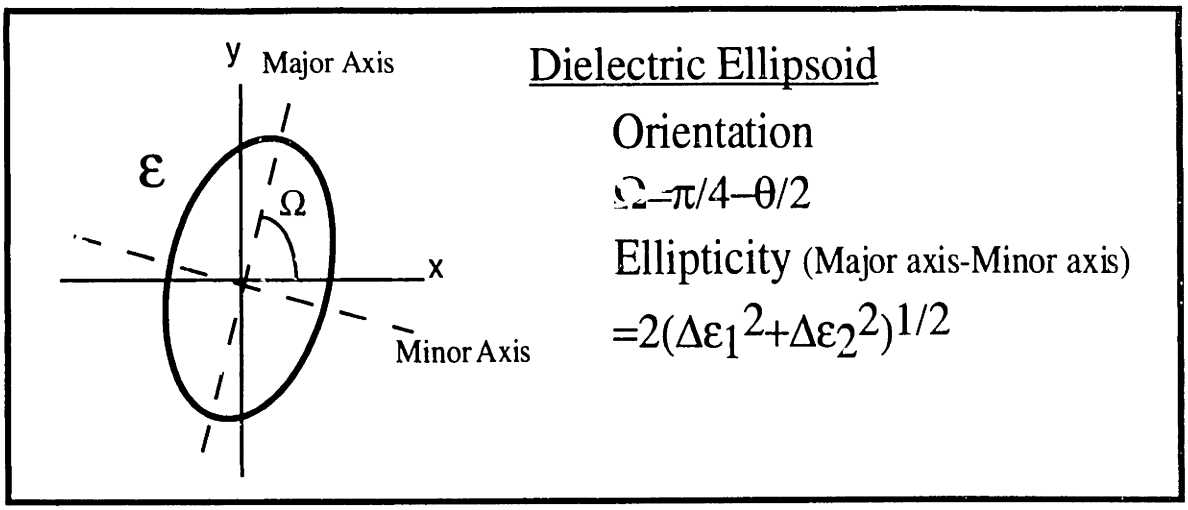

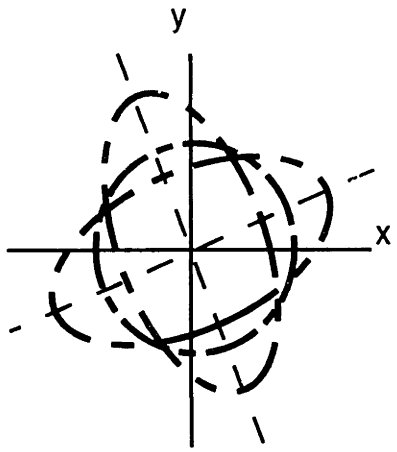

In-phase-lock
Orientation is time-independent
Ω=π/8
Ellipticity is time-dependent
$=2^{1/2}C\sin(\omega t)$

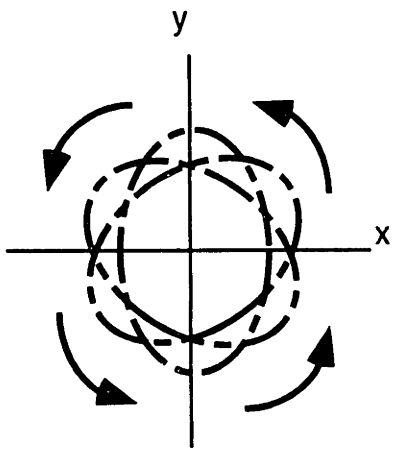

In-quadrature-lock
Orientation is time-dependent
Ω=ωt
Ellipiticity is time-independent
=C

Figure 4: Dielectric ellipsoid for in-phase and in-quadrature excitation. The pump pulse delay controls the form of the induced dielectric tensor.

orientation and amplitudes of the principle axes for the dielectric tensor. They are shown in figure 4 for the cases of in-phase and in quadrature excitation. One can thus see that control over the delay and polarizations of the excitation pulse pairs produces a controlled microscopic vibrational trajectory as well as a controlled macroscopic response, the form of the induced dielectric tensor.

To characterize the induced dielectric tensor, one measures the transmission of a probe pulse with an initial linear polarization $\begin{bmatrix} e_x \\ e_y \end{bmatrix}$ after passing through sample and a subsequent polarizer that is oriented perpendicular to the initial polarization. Treating the sample as a waveplate, the resulting probe field amplitude (signal) S is given by equations 8 and 9 as:

$$S = \begin{bmatrix} -e_y & e_x \end{bmatrix} \cdot \delta \begin{bmatrix} \cos 2\Theta & \sin 2\Theta \\ \sin 2\Theta & -\cos 2\Theta \end{bmatrix} \cdot \begin{bmatrix} e_x \\ e_y \end{bmatrix} \qquad (10)$$

Characterization of both Θ and δ requires measurement of the transmitted probe field amplitude for two initial polarizations, for example (**x**+**y**)/$\sqrt{2}$- and **y**-polarized light. Note that the use of orthogonal initial polarizations will yield two redundant equations. With regard to the microscopic motion, a particular choice of initial polarization produces a signal amplitude that is proportional to the displacement along a coordinate that is a real superposition of Q1 and Q2 and equal to $\left(e_x^2 - e_y^2\right)Q_1 - 2e_x e_y Q_2$. For example, probe pulses polarized linearly along axes that respectively make angles with the **x**-axis of $\pi/8$ and $3\pi/8$ (22.5 and 67.5 degrees), respectively monitor the vibrational motion along coordinates Q1+Q2 and

Q_1-Q_2. In this way, the vibrational trajectories illustrated in figure 3 can be mapped out using two sets of data in which the polarization of the variably-delayed probe pulse is rotated (along with the subsequent polarizer preceding the detector) by 45 degrees.

5.3 EXPERIMENTAL SET-UP

Experiments were conducted at room temperature on the uniaxial crystal α-quartz (SiO_2). Quartz undergoes a phase transition at 575°C and the low and high temperature phases are respectively designated α- and β-quartz [4]. α-Quartz has a trigonal crystal structure with D_3 symmetry and 9 atoms per unit cell. The silicon ions are tetragonally coordinated with oxygen ions, which in turn are linearly coordinated with silicon atoms. Group theory calculations [5] show that the 3N=27 degrees of freedom are divided into two acoustic vibrations of A_2+E symmetry and sixteen optical vibrations of $4A_1+4A_2+8E$ symmetry. The A_1 modes are Raman active, the A_2 modes are infrared active for the extraordinary ray, and the doubly degenerate E vibrations are both infrared active for the ordinary ray and Raman active.

Ultrashort pulses were derived from a commercial (Coherent) mode-locked Ti:Sapphire laser producing 80-fsec pulse at 800 nm with about 6-7 nJ per pulse at a 76 MHz repetition rate. The quartz sample (from CVI) was 1-mm thick and cut so that the front and rear faces were normal to the **c**-axis (the principle axis of the C_3 symmetry). The lowest frequency optical mode in α-quartz is an E-symmetry mode at 128 cm^{-1} (267 fs vibrational period) which exhibits intense Raman scattering [4]. This mode is excited impulsively by the sub-100-fsec pulse in a manner described by equations 6.1-6.4. The next lowest frequency mode has a much weaker

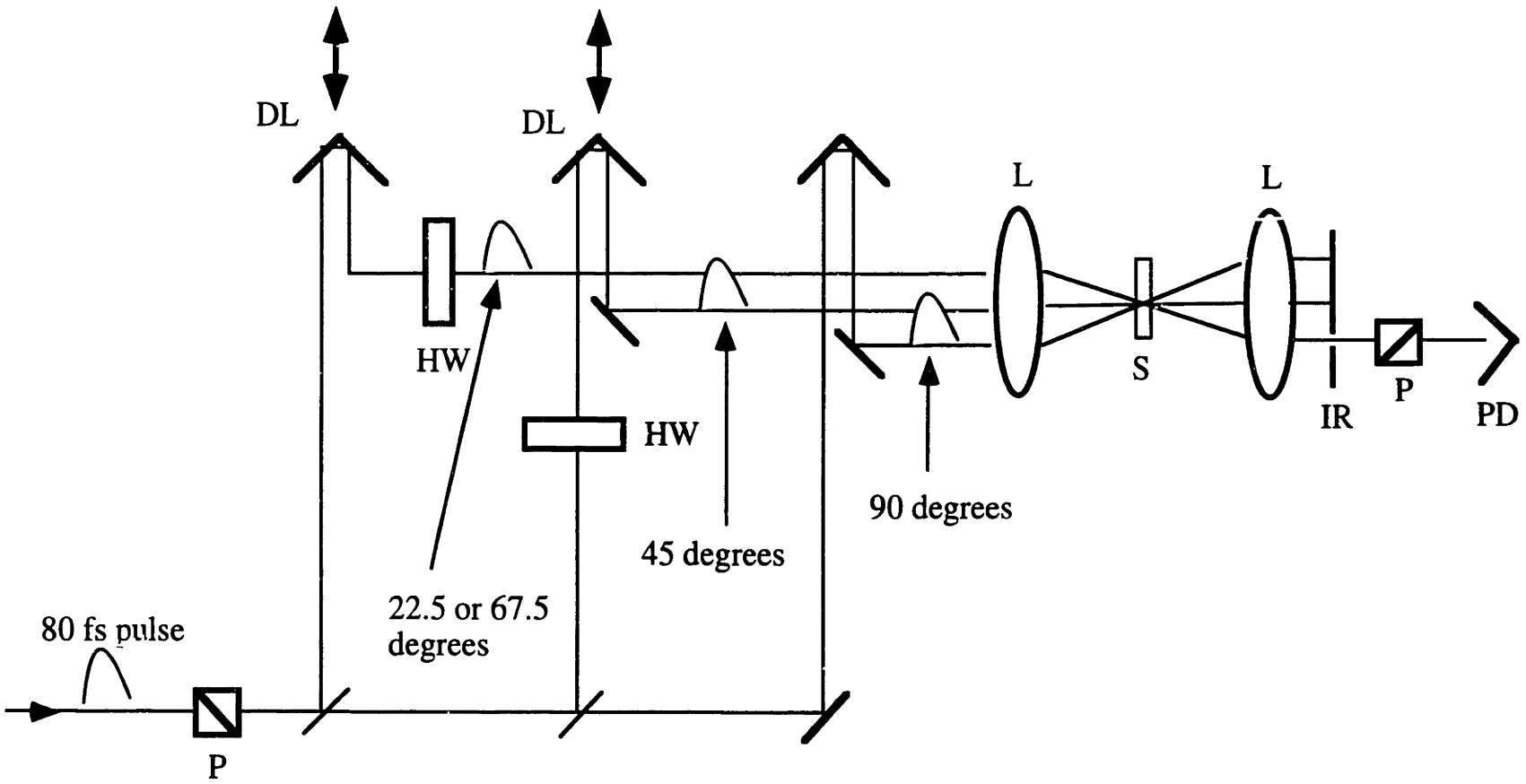

Figure 5: Schematic of experimental apparatus. (P polarizer, HW half-wave plate, DL delay line, L spherical lense, S quartz sample, IR iris, PD photodiode detector)

Raman cross-section and at 265 cm^{-1} its vibrational period is too short to be excited effectively by the 80-fsec pulses.

Two equal intensity (3nJ) excitation pulses and a weaker (0.5 nJ) probe pulse, derived from the mode-locked laser, are made nearly collinear (along the z-axis) and focused on the sample with a 20-cm lens to a spot size of about 100 microns. The respective delays and polarizations of the three pulses were controlled using standard methods employing beamsplitters, delay lines, and polarization optics. Though the pulse shaping methods described in the previous chapters could be employed to generate the excitation pulse pair, they are difficult by comparison and more appropriate for complicated waveforms that could not be produced otherwise. The probe pulse is separated from the pump pulses by an aperture following the sample and then passed through a polarizer that is perpendicular to its initial polarization prior to the sample. Due to some static birefringence in the sample, a portion of the light leaks through the polarizer even in the absence of the pump beams. This light acts as a local oscillator, to which light passing through the polarizer as a result of the induced vibrational motion may add or subtract. In our case, the leakage due to the static birefringence is much larger than the signal resulting from the vibrational motion and so the total signal intensity at the detector looks like:

$$S_{tot}^2 = (S_{LO} + S_{vib})^2 \approx S_{LO}^2 + 2S_{LO}S_{vib} \qquad (11)$$

where S_{LO} is the field amplitude associated with the local oscillator and S_{vib} is the field amplitude given by equation 10. A mechanical chopper is used to chop the pump beams so that lock-in detection will give the second

term in 11 which is linearly proportional to vibrational displacement. A schematic of the experimental set-up is shown in figure 5.

It should also be noted that α-quartz is optically active for light propagating along its principle axis. For the 1-mm thick sample, linearly polarized light is rotated by about 20 degrees. Hence the polarization of the pump, probe, and signal beams are rotated as they propagate through the sample. However, since this is a static effect the polarization differences between these respective beams remain constant, and so our formalism remains valid though the designation of Q_1 and Q_2 is implicitly understood to rotate through the thickness of the sample. Because of the optical activity, the polarizer following the sample is not oriented at 90 degrees to the initial probe polarization (as stated above), but rather it is oriented to minimize the transmission of the probe beam (in the absence of pump beams) and account for the polarization rotation.

5.4 RESULTS AND DISCUSSION

First we monitor the response of the quartz sample following excitation with only a single pulse, as shown in figure 6. The polarizations of the excitation and probe beams are respectively at 90 and 45 degrees to the **x**-axis (which is parallel to the optical table), and the probe pulse is variably-delayed to map out the response of the sample. While the excitation pulse is in the sample there is an instantaneous electronic response which produces strong signal at zero time delay. Thereafter vibrational oscillations corresponding to the 128 cm^{-1} mode are observed. The single pulse excites linear vibrational motion along what we have designated the Q_2 coordinate. If the probe polarization is oriented at 0 or

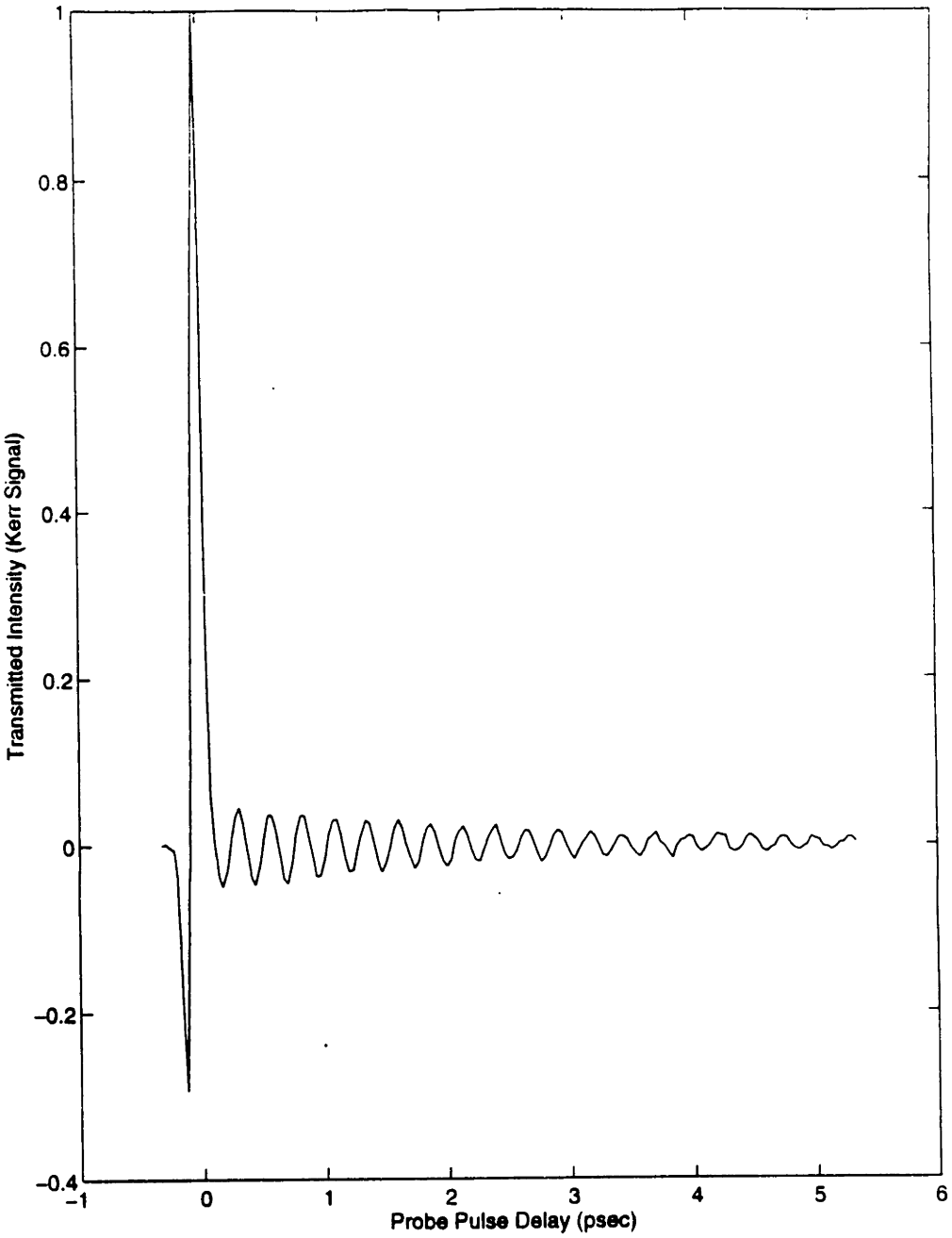

Figure 6: Kerr signal from quartz following excitation with a single pulse polarized at 90 degrees and probed with a pulse polarized at 45 degrees. The 267 fsec oscillation corresponds to the 128 cm^{-1} E-symmetry vibration.

90 degrees to the **x**-axis no vibrational oscillations are observed and accordingly no coherent motion is excited along the Q_1 mode.

To excite psuedorotational motion, two pump beams are used with polarizations respectively aligned at 45 and 90 degrees to the **x**-axis. Figure 7 shows data that illustrate the responses of the system for a variety of temporal delays between the two pump beams with the probe polarization set to 67.5 degrees to the **x**-axis. As with single-pulse excitation, the electronic contributions complicates the response while either pump beam is present in the sample. The amplitude and phase of the vibrational response exhibit a clear dependence on pump delay. For example at zero pump delay, no vibrational response is observed. This by itself could simply indicate that there is no vibrational response, or that the vibrational response is orthogonal to the displacement direction monitored by the pulse. Figure 8 shows data from an identical experiment except that the response is monitored with probe pulse polarized at 112.5 degrees to the **x**-axis. The amplitude and phase of the vibrational response once again depends strongly on the pump delay. In particular, there is a vibrational response at zero pump delay. Recall from section 5.2 that collinear probe pulses with polarizations that differ by 45 degrees will monitor the degenerate vibrational motion along orthogonal coordinates. In figures 7 and 8, motion along the orthogonal coordinates Q_1-Q_2 and Q_1+Q_2 are respectively monitored. Therefore for time coincident pump pulses, we only have motion along Q_1-Q_2. This is only reasonable since the two pulse are equivalent to a single pulse and therefore will be unable excite psuedorotational motion. In contrast, inspection of figures 7 and 8 for a pump delay of 60 fsec show that there is motion of similar amplitude

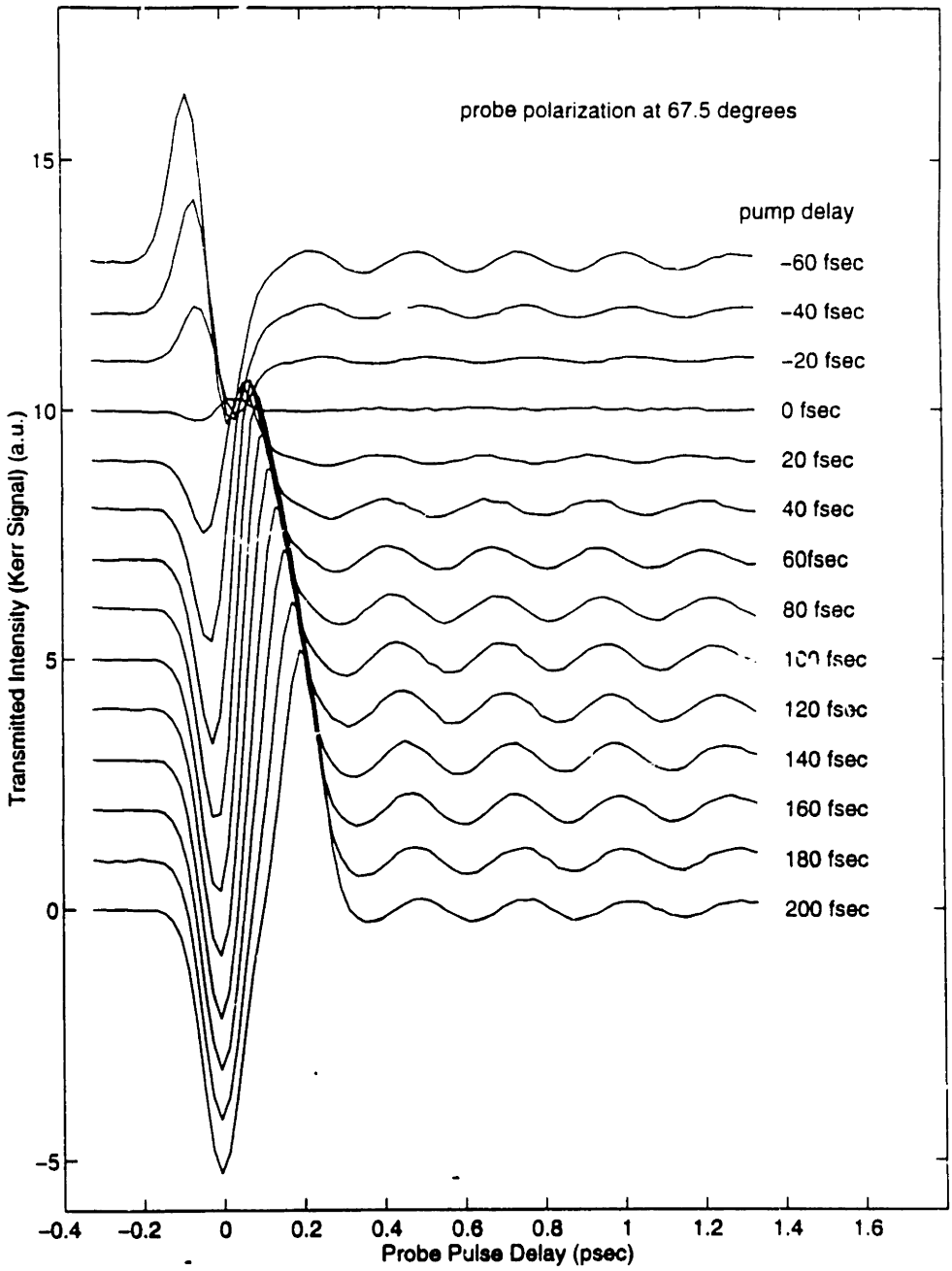

Figure 7: Kerr response from quartz following excitation with two variably-delayed pump pulses with polarizations of 45 and 90 degrees respectively. The probe beam polarization is 67.5 degrees thereby monitoring motion along the coordinate Q_1-Q_1. The results show that the pump delay controls the amplitude and phase of the vibrational motion along this coordinate.

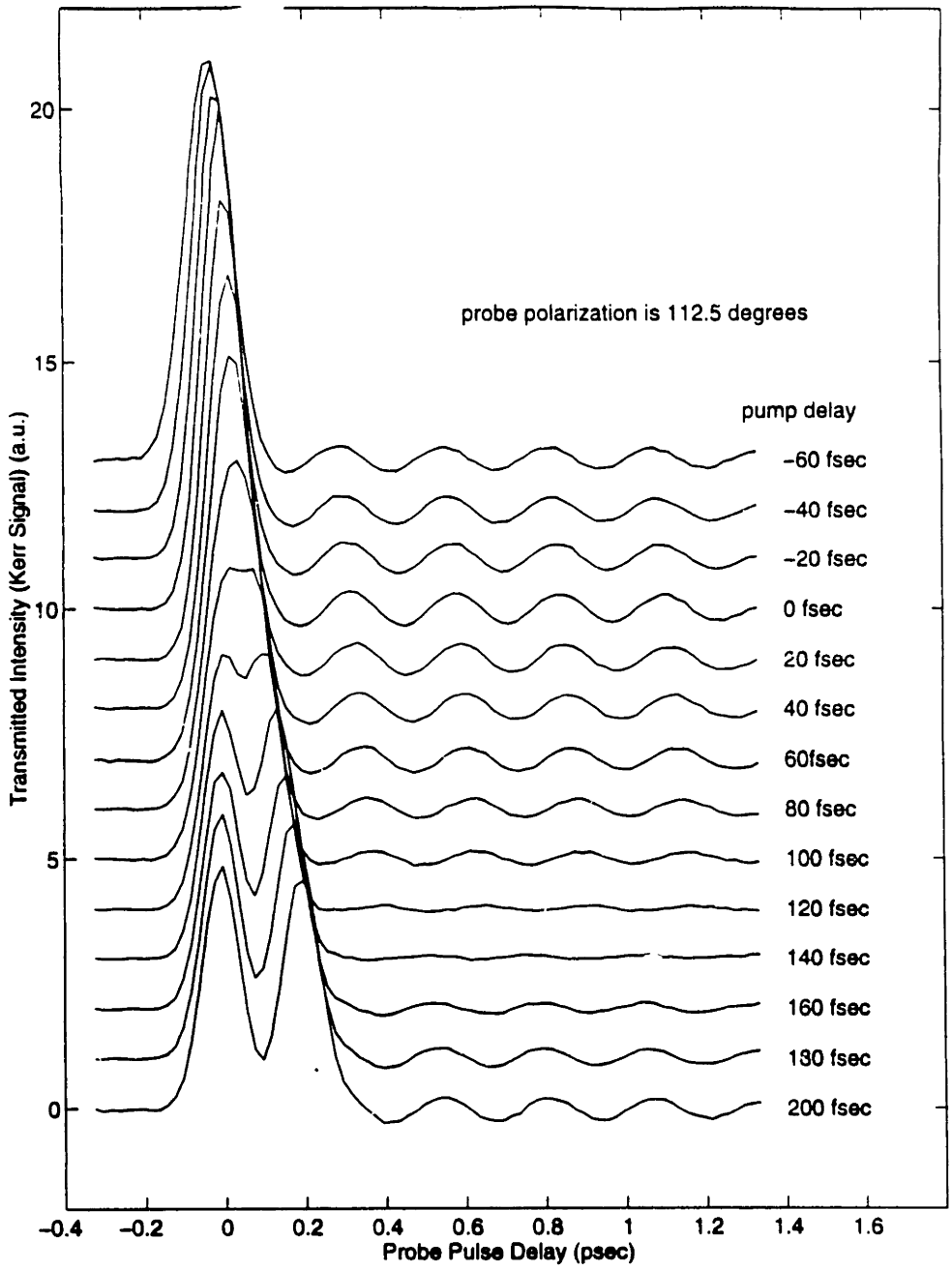

Figure 8: Kerr response from quartz following excitation with two excitation pulses with polarizations of 45 and 90 degrees. In contrast to figure 7, the probe polarization is 112.5 degrees, thereby monitoring motion along the coordinate Q_1+Q_2. As in figure 7, the pump delay controls the amplitude and phase of the vibrational motion along this coordinate. Note the diffrences howver, for example, the vibrational motion along Q_1+Q_2 has maximal amplitude for zero delay between pump pulses, while figure 7 shows that vibrational motion along Q_1-Q_2 is minimized this pump pulse delay.

along the orthogonal coordinates and that the respective motions are in quadrature indicating circular psuedorotation.

The data from figures 7 and 8 can be combined to construct the phase space trajectory of the degenerate vibration for the different excitation parameters. Since the signal following the electronic response is proportional to the displacement along the two orthogonal vibrational coordinates, time-coincident points from figure 7 and 8 correspond to a time-dependent point in the (Q_1+Q_2,Q_1-Q_2) phase space of the vibrational motion. Successive points can therefore map out the trajectory of the vibrational motion and illustrate the psuedorotational motion as was done theoretically in figure 4. Figure 9 shows such a construction for a number of pump delays. Only probe delay points that follow the electronic response are included and the points are separated by 20 fsec. Temporally adjacent points are connected by lines so that the motion in phase space is illustrated. The ellipticity and direction of the psuedorotational motion has the dependence on pump delay anticipated in section 6.2. For pump delays that are 1/4 or -1/4 of the vibrational period (+/- 67 fsec), circular trajectories with either clockwise or counter-clockwise directions are observed. Pump delays that are full or half multiples of the vibrational period yield linear trajectories consisting of either Q_1+Q_2 or Q_1-Q_2 motions. Intermediate pump delays yield the full range of elliptical orbits.

The trajectories in the figure also show a gradual decay toward the origin indicating vibrational relaxation. To determine whether the relaxation time depends on the ellipticity of the vibrational motion, longtime scans of Q_1-Q_2 (probe polarization at 22.5 degrees to the **x**-axis) were taken for circular (pump delay is 67 fsec) and linear (pump delay of 133 fsec) motions. Figure 10 shows these results. The vibrational

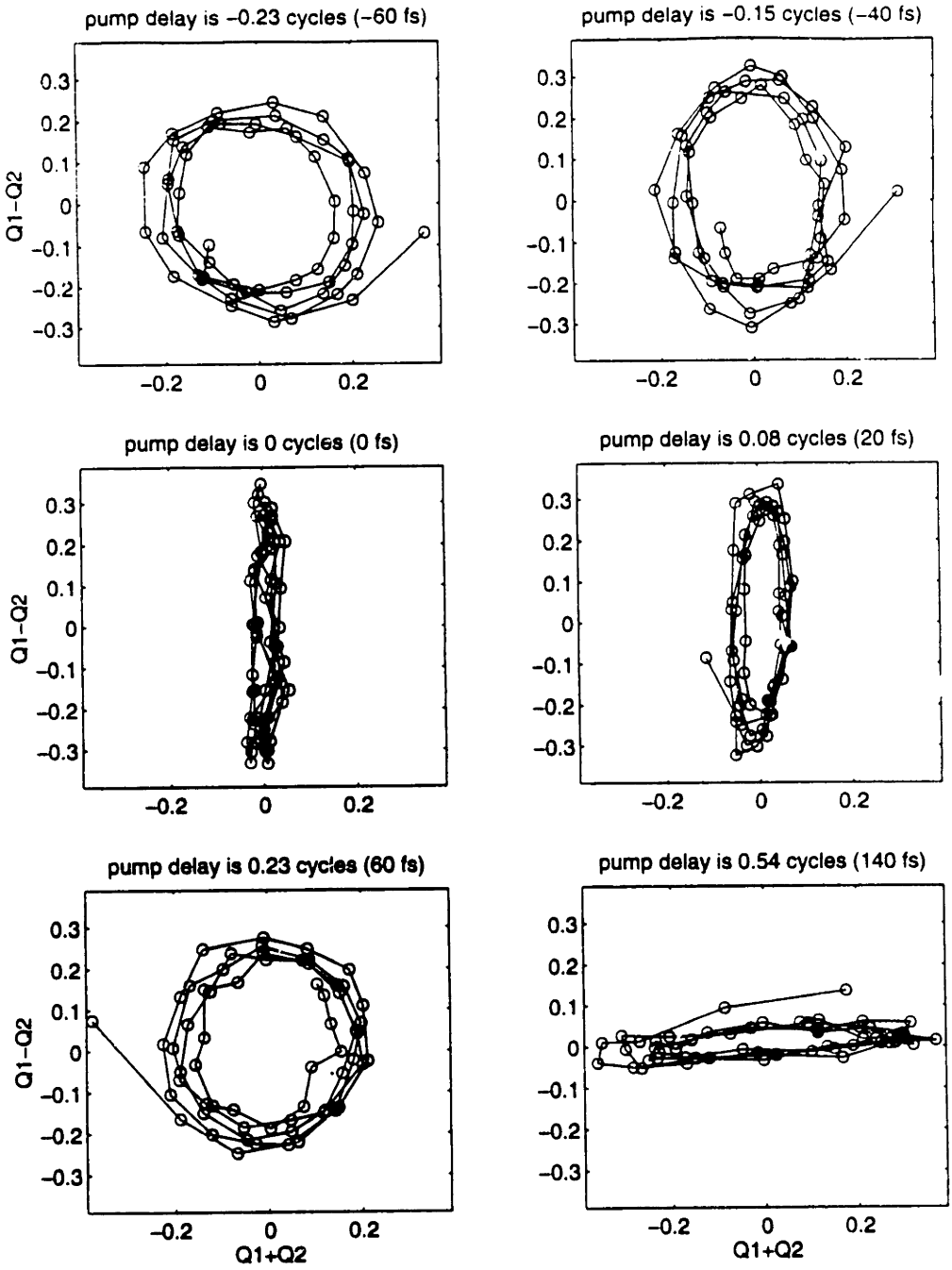

Figure 9: Trajectories of the degenerate vibrational motion in the phase space (Q1,Q2) constructed from the data in figures 7 and 8. Only the data points following the instantaneous are included and the displacements are in arbitrary units. The figure shows that the pump pulse delay controls the ellipticity of the psuedorotational motion.

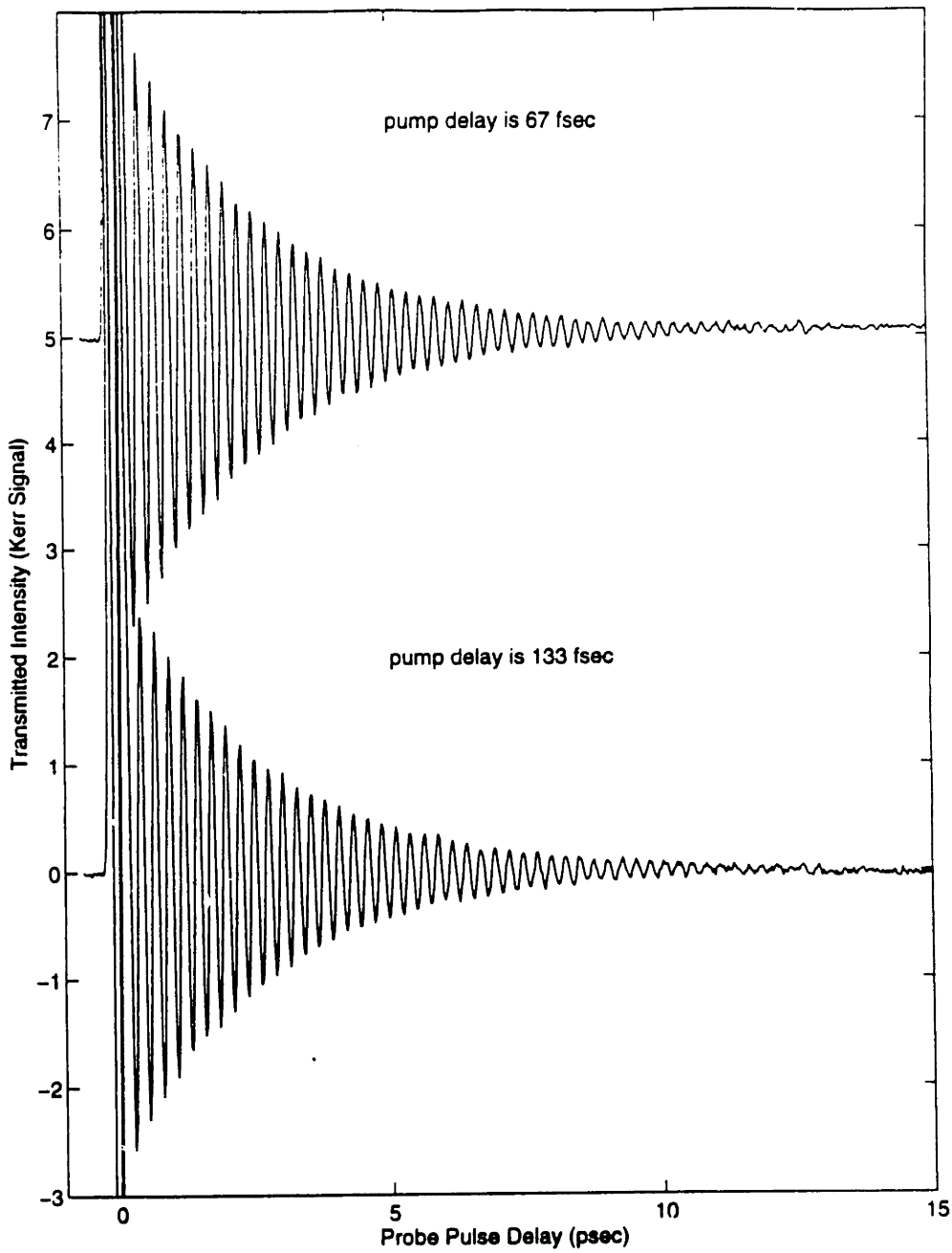

Figure 10: Long time Kerr responses from quartz following excitation with two pump pulses with polarizations of 45 and 90 degrees. The probe pulse is polarized at 67.5 degrees. The two pump delays correspond to excitation of circular psuedorotation (67 fsec delay) and linear motion (133 fsec). The data show that vibrational relaxation is comparable for the two types of motion.

response for the linear motion has an amplitude that is twice that of the circular orbit since our choice of probe polarization monitors displacement along the coordinate that exactly matches the linear motion. The two responses are otherwise identical, indicating equivalent relaxation times. This is reasonable. If the two modes Q1 and Q2 are truly orthogonal, they will couple to relaxational channels separately, and so the phase differences which produce the elliptical orbits will not alter their relaxation mechanisms.

More interesting results can be anticipated when the vibrational displacements become large enough that they sample higher order terms in the potential energy in which Q1 and Q2 are coupled. The form of the lowest order anharmonic correction to the potential energy can be determined by making sure that it remains invariant under any symmetry operation, and is given by:

$$V_{anh} \propto Q_1^3 - 3Q_1Q_2^2 \tag{12}$$

for a particular choice of Q_1 and Q_2. These terms would introduce sinusoidal terms to Q_1 and Q_2 that are harmonics of the fundamental vibrational frequency ω_0, resulting in the deformation of the orbital trajectories illustrated in figure 9.

It is worthwhile to compare the results above in which the polarizations of the two pump pulse differ by 45 degrees with the case in which the pump polarizations differ by 90 degrees. For example if the pump beams were polarized at 0 and 90 degrees from the x-axis, then according to section 2, they both drive the same component of the degenerate vibration (Q2 in this case) but impart momentum in opposite

directions. Since only Q_2 is driven, there is no pseudorotation regardless of the pump delay. The vibrational response along Q_2 however, depends strongly on the delay between the two pump pulses. The second pulse may add to the momentum constructively or destructively. For example for a pump delay of half a vibrational period, the momentum is imparted in the same direction by the two pulses and so the amplitude of the vibrational displacement is increased. Similarly, for a delay equal to a full vibrational period, the two pump pulses impart momentum in opposite directions resulting in no net vibrational motion. Data shown in figure 11, with the probe polarization at 45 and 90 degrees to the **x**-axis (monitoring the motion of Q_2), illustrates these results for a number of pump pulse delays. The results with the probe polarization at 90 degrees to the **x**-axis (monitoring motion along Q_1), confirms that there is no vibrational response for a number of pump delays and hence no pseudorotation.

This last set of result is similar to the case of multiple-pulse excitation described in the first chapter where a sequence of appropriately timed pulses repetitively excite and amplify vibrational lattice motion [6]. That experiment provided an example of how a shaped excitation waveform could modify vibrational motion along a single vibrational coordinate. The results of this chapter show that it is possible to manipulate vibrational motion along the two dimensions of an E-symmetry vibration using a pair of pulses with different polarizations. Using shaped waveforms along two polarizations, more complicated two-dimensional trajectories can be induced, and a series of specified steps could be carried out. In experiments with larger phonon amplitudes, multiple steps could facilitate access to interesting regions of anharmonic potential energy

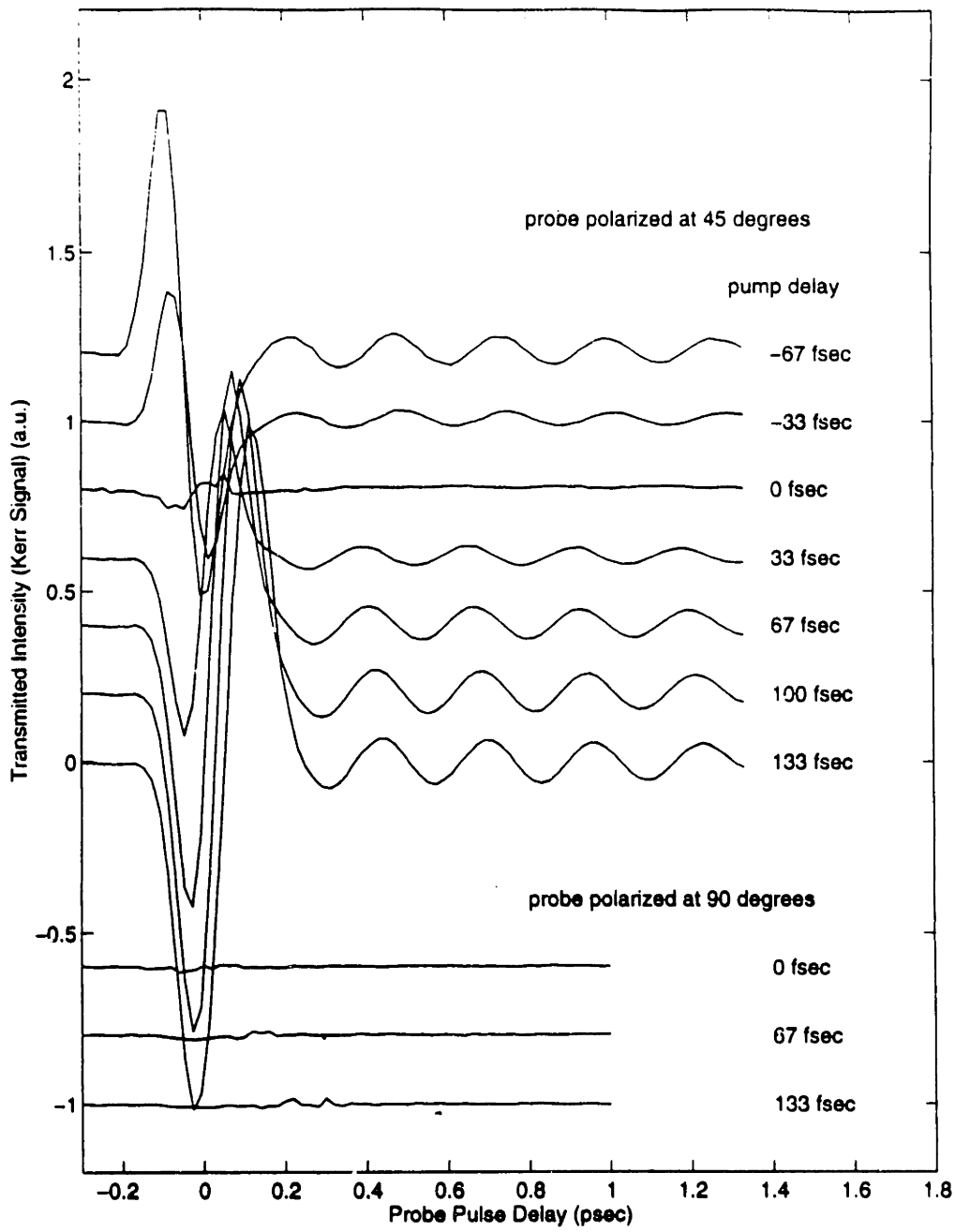

Figure 11: Kerr response following excitation with two variably-delayed pump pulses with polarizations of 0 and 90 degrees. This combination should only excite motion along Q2. Scans are shown for different pump pulse delays, and probe polarizations of 45 degrees (monitors motion along Q2) and 90 degrees (monitor motion along Q1). The results show that no vibrational motion is excited along Q1 and that the amplitude and phase of motion along Q2 is controlled by the pump pulse delay.

surfaces such as saddle points or other relatively low-energy pathways into new structures.

It is also worth noting that in systems without inversion symmetry (such as α-quartz), the Raman-active phonon modes excited through ISRS can also be polar. If two degenerate, orthogonal modes are polar, then their distortions induce electric polarizations along orthogonal directions in a plane. In this case, the vibrational trajectories illustrated in figures 3 and 9 also correspond to the time-dependent direction of an induced electric polarization, say along the **x**- and **y**-axes. (Note: by electric polarization we refer to the macroscopic response of a crystal or a collection of molecules, not a light polarization. We do not distinguish between electronic and ionic contributions to this term.) Any in-plane electric polarization can be written in terms of a linear combination of distortions of the two polar modes. Using the methods described in this chapter, it should therefore be possible to control and produce complicated time-dependent macroscopic electric polarizations. The polar modes will in turn emit far-IR radiation which will be modified according to its vibrational trajectory. For the particular case of the 128 cm^{-1} E-symmetry mode in quartz, there is no observable frequency splitting between the transverse optic and longitudinal optic modes [4], indicating that the displacements are only weakly polar.

Finally, we will discuss the systems in which the excitation of psuedorotational motion described in this chapter are possible. The necessary criterion is a degenerate Raman-active mode for which light of selected polarizations can excite orthogonal modes with equal amplitude. Inspection of the character tables for crystal structures of different symmetry give the form of the polarizability tensor for different vibrations

[5]. Adding the condition that the variably-polarized excitation light be collinear, we can list the following set of systems: E-symmetry vibrations in C_3, C_{3v}, D_{3i}, D_{3d}, and D_3 trigonal crystal structures, E_2-symmetry vibrations in C_6, C_{6v}, and D_6 hexagonal crystal structures, and E'-symmetry vibrations in C_{3h}, C_{6h}, D_{3h}, and D_{6h} hexagonal crystal structures. In all of these systems there is at least a C_3 axis of symmetry (the principle axis), and for light propagating along the principle axis, linear polarizations that differ by 45 degrees will excite degenerate orthogonal modes with equal amplitude. In T, T_h, T_d, O, and O_h cubic crystal structure, excitation of degenerate orthogonal modes is also possible for the E-symmetry mode but only with comparable and not equal amplitude. For example, (again defining the **z**-axis as the principle (C_4) axis) light polarized at 45 degrees to **x**-axis will only excite Q_1, while light polarized at -45 degrees to the **x**-axis will only excite Q_2 but do so three times more efficiently (with respect to energy). For excitation beams that propagate perpendicular to one another, polarization combinations exist that will excite selectively, orthogonal modes of the E-symmetry vibrations in tetragonal crystal structures, the remaining E-symmetry vibrations in trigonal crystal structures, and the triply-degenerate F (T and T_h) or F_2 (T_d, O, and O_h) vibrations in cubic crystal structures. As an example, the 98 cm^{-1} E_2 vibration in the hexagonal crystal $LiIO_3$ [7] is another system in which psuedorotation might be induced through ISRS.

5.5 CONCLUSIONS

Using pairs of short excitation pulses with different polarizations, orthogonal modes of a degenerate vibrational mode can be selectively excited. The delay between the two excitation pulses governs the phase

difference in the oscillations of these modes thereby controlling the ellipticity of the two-dimensional vibrational motion. Control over this 'psuedorotational' motion was demonstrated on the 128 cm^{-1} E-symmetry mode in α-quartz. The results suggest prospects for more detailed control over multi-dimensional vibrational motion using variably-polarized shaped waveforms. Possibilities include modification of far-IR radiation emitted from impulsively driven polar vibrations that travel along a specified trajectory.

CHAPTER 5 REFERENCES

1. J. A. Cina, V. Romero-Rochin, J. Chem. Phys. **93**, 3844 (1990)
2. L. Dhar, J. A. Rogers, K. A. Nelson, Chem. Rev. **94**, 157 (1994)
3. E. B. Wilson, J. C. Decius, P. C. Cross, Molecular Vibrations: The Theory of Infrared and Raman Vibrational Spectra, (McGraw-Hill Book Co., New York 1955)
4. J. F. Scott, S. P. S. Porto, Phys. Rev. **161**, 903 (1967)
5. J. C. Decius, R. M. Hexter, Molecular Vibrations in Crystals, (McGraw-Hill Inc.,New York, 1977)
6. A. M. Weiner, D. E. Leaird, G. P. Wiederrecht, K. A. Nelson, Science **247**, 1317 (1990)
7. W. Otaguro, E. Wiener-Avnear, C. A. Arguello, S. P. S. Porto, Phys. Rev. B. **4**, 4542 (1971)

Chapter 6:
Multi-Dimensional Shaping of Ultrafast Optical Waveforms and Control Over Propagating Responses

Some of the work in this chapter is published:

M. M. Wefers, K. A. Nelson, A. M. Weiner, Opt. Lett. ***21****, 746 (1996)*

6.1 INTRODUCTION

In this chapter, combined temporal and spatial shaping of ultrashort optical pulses based on the linear spectral filtering of spatially-separated frequency components [1-2] is demonstrated. This permits generation of coherent high-fidelity ultrashort optical waveforms with tailored profiles along both the propagation direction, i.e. the temporal coordinate, and one perpendicular direction, i.e. one spatial coordinate. As an example, a single input pulse is transformed into 11 spatially separated output beams, each with an independent temporal profile. Multidimensional pulse shaping is a logical extension to our earlier work on high-fidelity temporal pulse shaping [3] (described in chapter 2), and profoundly expands the possible complexity of the waveforms produced.

Shaped ultrafast optical waveforms that have tailored profiles along two dimensions permit a large multiplex advantage in terahertz-bandwidth optical signal processing and could play an important role in ultrafast optical communications. Interconversion of temporally shaped waveforms to and from spatial images in one and two dimensions by means of spectral holography have been reported [4-5], as has the generation of ultrafast time-varying two-dimensional spatial images using volume holographic

techniques [6]. The technique for multidimensional shaping described in this chapter, however, allows for high-fidelity shaping in the time domain and is therefore more suitable to optical control schemes.

Temporal and spatial pulse shaping offer novel possibilities for manipulation of propagating excitations and other non-local material responses [7]. As discussed throughout this work, a particular control objective of interest to our group is the excitation of large-amplitude lattice displacements that could give rise to optically-induced structural rearrangements or novel non-linear lattice dynamics [8]. The usual limitation is that the optical excitation intensities required to generate such responses also excite competing reaction channels, such as multiphoton processes, that produce sample damage. One of the objectives of pulse shaping is to shape an excitation waveform in such a way as to circumvent sample damage (for example by minimizing peak intensity) while amplifying the desired response, such as a vibrational displacement. Excitation with a temporally as well as spatially shaped waveform allows the possibility of amplifying propagating responses by spreading out optical excitation intensity over a large area, thereby minimizing peak optical intensity, but shaping the field so that it continuously drives the propagating response which at any time is confined to a small area.

In section 6.2, multidimensional pulse shaping will be described and demonstrated. In section 6.3, application of spatially shaped waveforms to the amplification of propagating phonon-polaritons will be discussed. In section 6.4, a particular scenario is outlined in which a spatially shaped waveform is used to compress a phonon-polariton wavepacket at some later time. In section 6.5, some additional prospects involving non-linear

mixing experiments and terahertz signal processing will be briefly discussed.

6.2 MULTI-DIMENSIONAL PULSE SHAPING

6.2.1 Experimental demonstration

Temporal and spatial pulse shaping is made possible by using both spatial dimensions of a mask placed in the focal plane of a zero-dispersion 4-f grating and lens apparatus as shown in Figure 1. This set-up is identical to those described previously in chapter 2 [1-3] except that, following the first grating which disperses the frequency components of the incident pulse along the horizontal or x-axis, a cylindrical lens with curvature along the x-axis rather than a spherical lens is used. With a spherical lens, the spatially separated frequency components are focused to different regions of a horizontal line across the mask, and a horizontally oriented mask pattern is used for phase and/or amplitude filtering of selected frequency components. With a cylindrical lens, each of the horizontally separated frequency components is spread out along the y-axis so that a large two-dimensional area of the mask is irradiated. Many horizontally oriented mask patterns, separated in the vertical direction, can be used for temporal shaping of vertically separated "strips" of dispersed light. More generally, the mask patterns in the vertical direction are used for spatial (or wavevector) shaping of the filtered light. As in earlier pulse shaping setups, a subsequent spherical lens and anti-parallel grating are used to recombine the spectrally filtered frequency components.

A second spherical lens, following the pulse shaping apparatus, is used to image the spatial pattern (along the y-axis) imparted by the mask onto the sample while focusing the beam along the horizontal direction.

The sample in this case is a KTP doubling crystal within which the shaped output and a variably delayed, unshaped pulse that is cylindrically focused to a vertical strip are overlapped spatially. The frequency-doubled light arising when different spatial regions of the beams are time-coincident provides a spatially varying cross-correlation pattern that is imaged onto a CCD camera, producing temporally resolved spatial images of the shaped waveform. An 80-fsec, 10-μJ pulse at 788 nm from a 1-kHz titanium:sapphire regenerative amplifier was used to generate both the input pulse (8 μJ) and the unshaped reference pulse (2 μJ).

As a demonstration, we used a prefabricated phase mask consisting of about 28 separate horizontal patterns on a 9-mm by 7-mm area of a fused silica substrate. The patterns are designed to generate pulse sequences with slightly different terahertz-frequency repetition rates. In the original use [9-10], a single mask pattern was inserted into the beam path within a pulse shaper to produce a single pulse sequence of selected repetition rate, and a different mask was inserted to change the repetition rate. In the present experiment, the incoming beam is not focused along the y direction and so different horizontal strips of the spectrally dispersed light in the focal plane are incident onto many (about eleven) different patterns rather than on a single pattern as in previous experiments. Light in between these strips is blocked by reflecting regions between the adjacent patterns on the mask. Following shaping, the beam consists of eleven spatially separated 175-micron spots. The temporal profile of each spot is a pulse train with its own distinct repetition rate. In this particular case, it may seem appropriate to describe the procedure as multiplexed or "parallel" pulse shaping in which one beam enters and eleven beams, each with an independently controlled temporal profile, emerge. However, it is

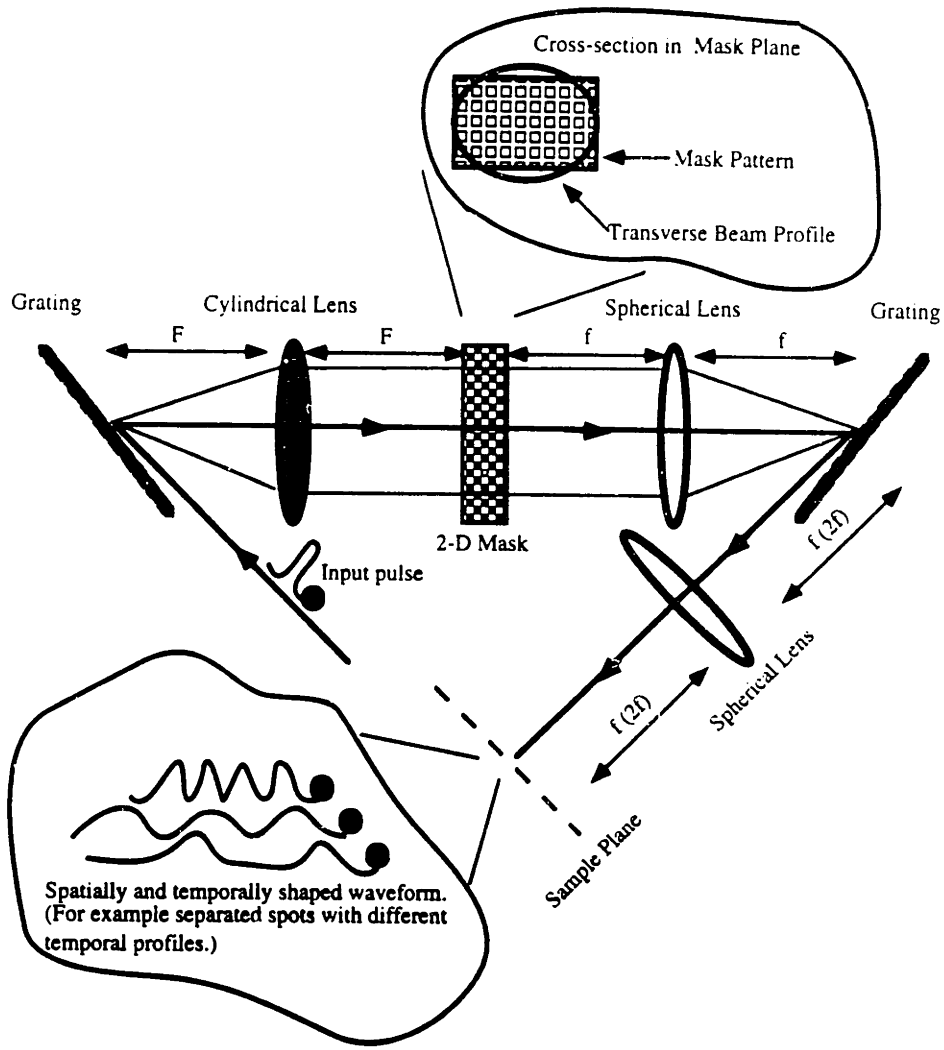

Figure 1: Apparatus used for generation of multidimensional ultrafast optical waveforms. The first grating disperses the frequency components of the incident pulse along the **x** (horizontal) axis. The cylindrical lens focuses the separated components onto different, horizontally separated regions of the mask, but leaves them unfocused along the vertical (**y**-axis) direction. The mask filters different frequency components along the **x** axis and different spatial or wavevector components along the **y** axis. The subsequent spherical lens and anti-parallel grating recombine the spectrally filtered frequency components. A second spherical lens SL is positioned to either form a one-to-one telescope with the spherical lens following the mask to image the spatial shaping from the mask onto the sample. To filter vertical wavevector instead of spatial components, the second spherical lens could be positioned a distance 2f (rather than f) from both the sample and the second grating, thereby imaging onto the sample the spatial profile of the beam immediately after the grating.

important to realize that for an arbitrary two-dimensional mask (including the one used here), the shaped waveform is both temporally and spatially coherent.

The pulse shaper consists of the mask, two 1200-line/mm gratings, a first 20-cm focal-length cylindrical lens (with curvature along the x-axis), and a second 15-cm focal-length spherical lens. The elements are placed in the usual 4-F arrangement (each element separated by the focal length of the lens nearest to them). Ideally the cylindrical and spherical lens should be of the same focal length, otherwise a pair of anti-parallel gratings will not be able to properly recombine the spatially-separated frequency components and there will be angular dispersion in the outgoing beam. In this example, the orientation of the second grating was adjusted to best compensate for this angular dispersion so that the pulse shaper approximately dispersion-free for the unshaped 70-fsec input pulse. To characterize the waveform, a second 15-cm focal-length spherical lens was placed a distance of one focal-length after the second grating and the doubling crystal was placed two focal-lengths from the second grating. With respect to the **y**-axis, the two spherical lenses form a telescope that images the mask pattern along the vertical dimension onto the doubling crystal. Along the **x**-axis, the second spherical lens focuses the collimated exit beam onto the doubling crystal. Cross-correlation is performed with a variably-delayed unshaped reference pulse that is focused to a line and is spatially overlapped with the shaped beam on the doubling crystal. The reference pulse is focused to a vertical line by passing it through the second spherical lens following the pulse shaper and a prior cylindrical lens with curvature along the **y**-axis. The frequency-doubled light arising from the simultaneous temporal and spatial overlap of

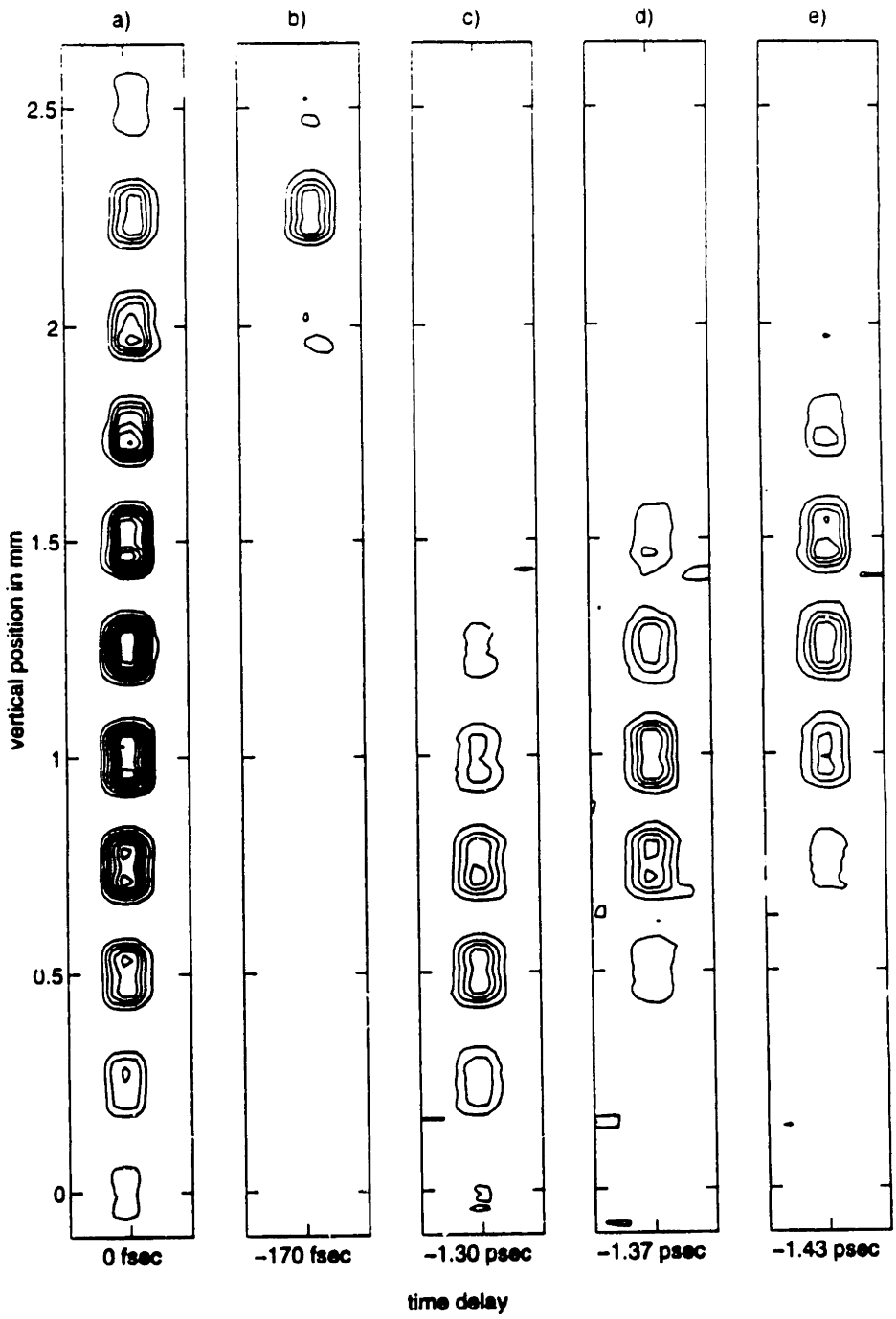

Figure 2: Cross-correlation images of the shaped waveform at different times. The images show that different spots appear and disappear on femtosecond time scales.

the two beams is imaged onto a CCD camera by a another spherical lens.

Figure 2a-e shows CCD camera images of the frequency-doubled light from the KTP cross-correlation crystal with various delay times between the shaped waveform and the reference pulse. At zero time delay (fig. 2a) eleven separate spots are visible. Ten of the spots consist of pulse trains with repetition rates ranging from 2.00 to 2.41 THz, all of which include a pulse at zero time delay. The second spot from the top consists of only a single pulse which is time-delayed but somewhat lengthened and of sufficient intensity to produce signal at zero time delay. At a 30-fs time delay (fig. 2b) only the spot associated with the single pulse produces signal. At longer time delays, the pulses in the different pulse trains are no longer temporally coincident. Figures 2c-2e show that different produce signal as the time delay is varied, as expected for pulse trains of varying repetition rates.

Figure 3 shows cross-correlation measurements of each of the eleven separated spots in the shaped waveform, recorded separately by using a 100-micron pinhole to isolate the frequency-doubled light from each spot. The central pulse is more intense than the other pulses in each of the pulse trains because the etch depth of the phase mask was optimized for 620 nm rather than the 788-nm wavelength used presently. The figure shows well defined pulse trains of varying repetition rates, as well as the single time-delayed pulse (second from top). A dotted line is placed along time delay -1.37 psec (corresponding to figure 2d) to emphasize the varying repetition rates. The signal levels in the top and bottom cross-correlations are relatively weak because the shaped and reference beam intensities were relatively low near their top and bottom edges.

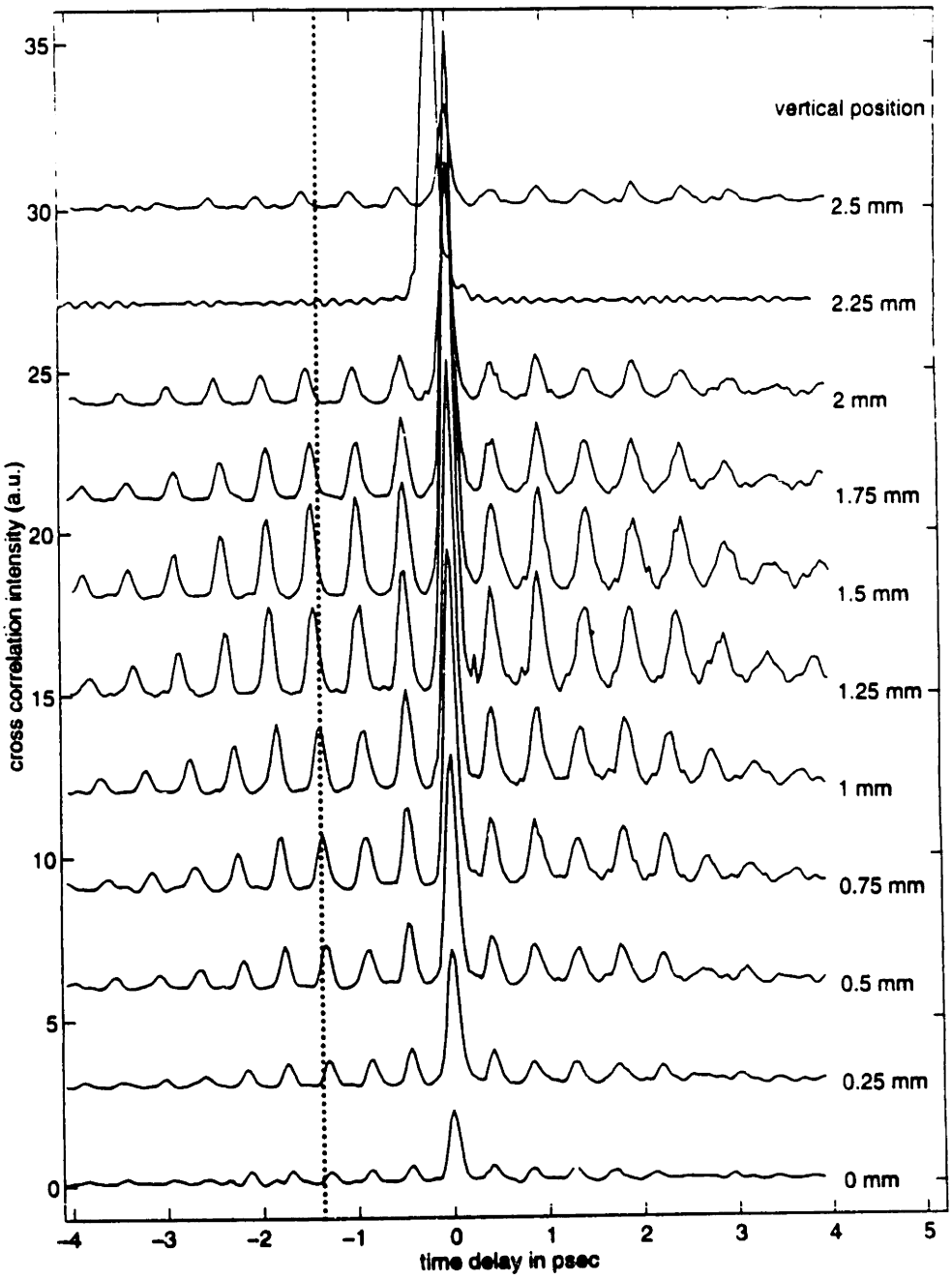

Figure 3: Spatially resolved cross-correlation measurements of the shaped waveform. The waveform consists of eleven spots separated by 250 microns. The cross-correlation of each spot shows a sequence of equally-spaced femtosecond pulses. A dotted line is placed along time-delay -1.37 psec to illustrate the varying repetition rate between adjacent spots and to provide a comparison with figure 2d which shows the spatial profile at this delay time.

6.2.2 Mathematical description and wavevector shaping

In the previous example, the spatial image associated with the vertical dimension of the mask is directly imparted to the shaped waveform in the plane of the doubling crystal. We refer to this type of pulse shaping as 'spatial' shaping since the spatial profile of the desired waveform is filtered directly by the mask. As we will describe subsequently, it is also possible for the wavevector components of the desired waveform to be filtered directly by the mask. Spatial shaping can be described mathematically as follows, if the mask filter pattern is given by m(x,y) and the input electric field $e_{in}(t,y)$, the shaped electric field $e_{out}(t,y)$ (ignoring inversions resulting from various telescopes) is given by:

$$e_{out}(t,y) = \int d\omega \exp(i\omega t) E_{in}(\omega, y) m(\alpha(\omega - \varpi), y) \qquad (1)$$

where $E_{in}(\omega, y) \propto \int dt \exp(-i\omega t) e_{in}(t, y)$, ϖ is the angular frequency component imaged onto the center of the mask, and α describes the lateral dispersion in the masking plane resulting from the first lens and grating [2]. Equations 1 ignores any shaping along the x coordinate and assumes perfect frequency resolution in the masking plane. The pulse shaping described in equation 1 can be thought of as shaping in parallel since the horizontal mask patterns produce a series of one-dimensional pulse shapers and imaging is used to keep their outputs spatially-separated.

One problem with 'spatial' shaping is that the spatial resolution of the shaped waveform is directly proportional to the spatial resolution of the mask. Thus it is difficult to produce shaped waveforms with small spatial features using modulators consisting 100-micron pixels. Instead, one can

image taking a shaped waveform produced by 'spatial' shaping and focusing it onto the sample with a spherical lens. This operation produces the Fourier transform of the spatial profile of the shaped waveform. However since the spatial profile of the shaped waveform is time-dependent, both the temporal and spatial profiles are changed by taking the Fourier transform operation. Furthermore, the new shaped waveform can have spatial features as small as the inverse of the spatial extent of the waveform prior to focusing. The spatial extent of the waveform prior to focusing is proportional to the total aperture of the mask pattern that produced it and can be relatively large in practice (typically 1-2 cm), so that the new waveform produced by focusing can indeed have very small spatial features (less than 10 microns).

Generating a desired multidimensional waveform by focusing the shaped waveform produced by 'spatial' shaping is equivalent to filtering spatial-wavevector components with the vertical dimension of the mask, and we therefore refer to it as 'wavevector' shaping. Wavevector filtering requires no change whatsoever in the pulse shaping setup, but only a change in the subsequent imaging of the shaped waveform. Rather than the mask pattern, it is the shaped waveform immediately after the second grating, which should be imaged onto the autocorrelation crystal (or in general, onto a detector or a sample). Filtering of the vertical wavevector components in the masking plane is coupled with filtering of the (horizontally) dispersed frequency components, so that $e_{out}(t,y)$ is now given by:

$$e_{out}(t,y) = \iint dy' d\omega \exp\left(i(\omega t - 2\pi y y'/\lambda f)\right) E_{in}(\omega, y') m(\alpha(\omega - \varpi), y') \tag{2}$$

where λ is the center wavelength and f is the focal length of the spherical lens before the second grating. In this configuration, the mask used in our experiment would no longer produce pulse trains since we can no longer consider the various horizontal frequency filters as separate. Nonetheless equation 2 can be inverted readily to describe the appropriate mask pattern m(x,y) for a desired shaped waveform. This situation is entirely analogous to two-dimensional spatial Fourier filtering of wavefronts [11] with the exception that the horizontal dimension of the mask is used to filter spatially separated frequency components rather than horizontal-wavevector components. Depending on the desired spatial profile of the shaped waveform along the **y**-axis, direct spatial filtering or wavevector filtering along this axis can be performed. We note that in general there is a small degree of spatial shaping of the waveforms along the **x** axis, due to diffraction effects arising from imperfect spectral resolution along this axis as was described in chapter 4 [12].

Wavevector shaping offers some advantages for the case in which there are large dead spaces or cases in which the mask filter is not arbitrary (for example phase filtering only). In wavevector shaping, field amplitude incident on each pixel on the mask contributes to field amplitude across the entire spatial extent of the output waveform. Therefore a hard aperture can be used on the output waveform to remove amplitude outside a given region. For example, light which is not controlled because it is incident on gap regions produces light intensity over a large spatial region in the output waveform. This light is inconsequential if it can be removed by a hard aperture and the desired waveform is contained within the aperture. For the case of a limited mask filter, the hard aperture adds

additional degrees of freedom, by providing partial filtering in the conjugate domain. In contrast, spatial shaping directly imparts the mask pattern, along with any imperfections, onto the output waveform. The hard aperture would therefore be redundant.

6.2.3 Different configurations

The essential feature of multidimensional pulse shaping is that both dimensions of the mask pattern impart information onto the incident light field. One dimension is used to filter frequency components and one must be careful to properly recombine these spatially-separated frequency components into a collimated beam (along the transverse direction perpendicular to the spatial shaping). This requires that along the direction of frequency dispersion (usually the **x**-axis) the pulse shaper is identical to that of a one-dimensional pulse shaper (a 4-f arrangement consisting of a one-to-one telescope sandwiched between anti-parallel gratings). This could be accomplished with a pair of cylindrical lenses rather than the cylindrical/spherical combination used in our demonstration. In this case, the spatial pattern imparted by the mask along the other transverse coordinate will begin 'blur' (diffract) as the beam propagates. Separate cylindrical lenses with curvature along this direction can be used to image (spatial shaping), or focus (wavevector shaping) this pattern onto the desired sample. Many configurations are possible and the particular choice of using separate cylindrical lenses or cylindrical lenses in combination with spherical lenses depends on whether the desired waveform is focused along the transverse dimension perpendicular to the spatial shaping and on the choice of spatial or wavevector shaping. One must also insure that the

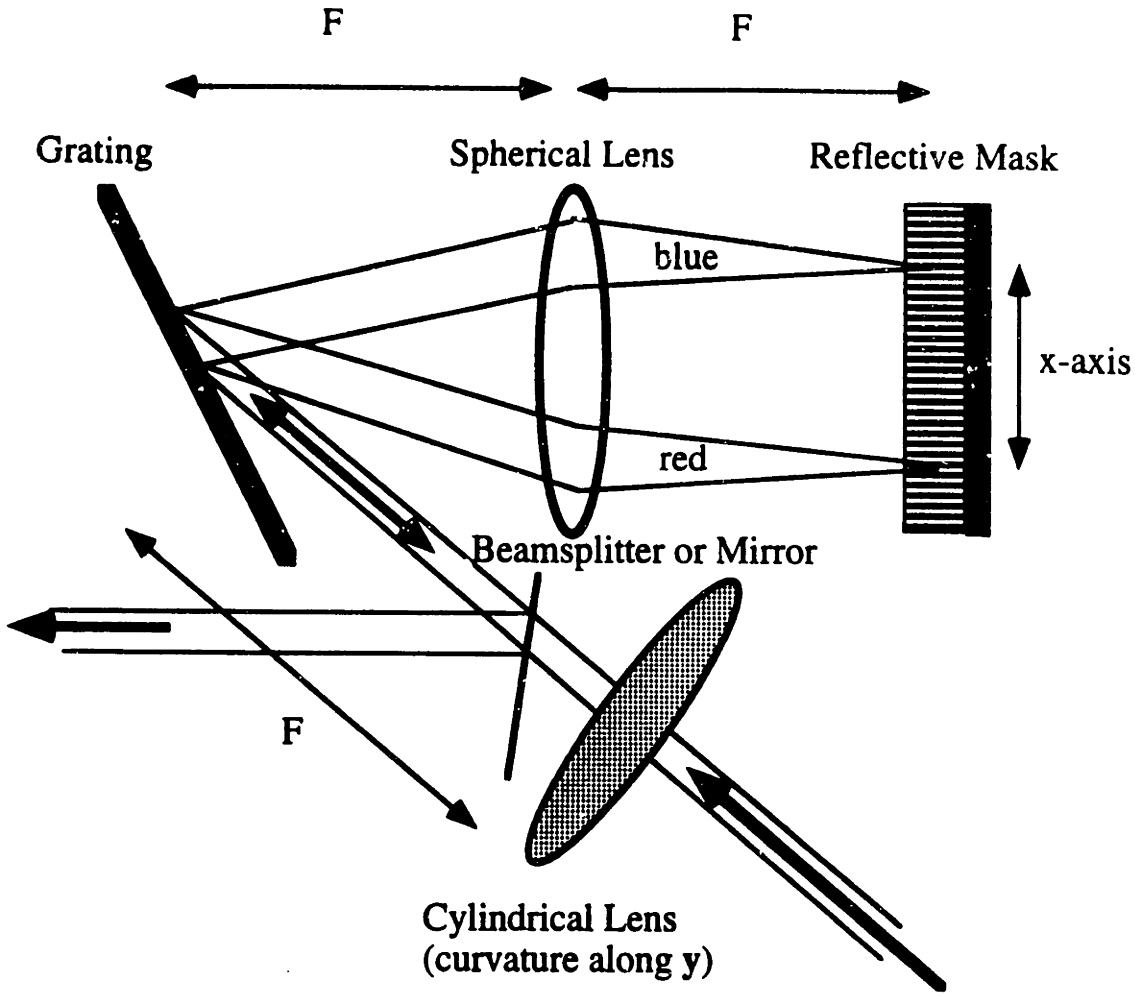

Figure 4: Schematic of a two-dimensional pulse shaping apparatus using a reflective mask.

different lenses have numerical aperture large enough to image the desired waveform onto the sample with sufficient resolution.

In practice programmable transmissive two-dimensional masks will have large interpixel 'dead' spaces which accommodate circuitry for driving electronics. Figure 4 shows a possible schematic of a 2-D pulse shaper using a reflective mask. In this case, the pulse shaper consists of a single grating, a single spherical lens, and the reflective mask, each spaced one focal-length apart. In addition, the input pulse is passed through a cylindrical lens with curvature along the y-axis which forms a one-to-one telescope (along this coordinate) with the spherical lens in the pulse shaper. Each frequency component incident on the mask will therefore be spatially extended along the y-axis, as desired. Upon reflection back through the lens and grating, the beam is picked off by a beamsplitter (or a mirror if a small tilt is introduced by the mask) before the cylindrical lens. Optics after the beamsplitter can image the beam onto the sample as was done with a transmissive mask (described previously).

6.3 APPLICATION TO PROPAGATING PHONON-POLARITONS

Using the methods described in the previous section, waveforms can be generated that manipulate and follow propagating responses. Of particular interest to this group has been the study of dispersive phonon-polaritons [13-15]. A phonon-polariton is a coupled response that is part electromagnetic (EM) field and part polar lattice vibration [16]. They occur in the low wavevector regime where the EM frequency is comparable to the frequency of a polar transverse lattice vibration. Because the polar vibration couples to EM radiation, the lattice vibration is dispersive in this wavevector regime and gives rise to propagating

responses. Figure 5 illustrates a typical dispersion curve for the frequency of a transverse polar lattice vibration in the polariton region. The frequency of the lower branch approaches the transverse optic phonon frequency (in the absence of EM coupling) at large k (wavevector) while the frequency of the higher branch approaches the longitudinal optic phonon frequency at low k (wavevector). Frequencies between the transverse and longitudinal phonon frequencies are forbidden.

Polar lattice vibrations in ferroelectric crystals in the polariton regime have been studied by this group by impulsive stimulated Raman scattering (ISRS) [13]. This is possible in non-centrosymmetric systems where polar modes can also be Raman active. In these experiments two ultrashort (<100 fsec) excitation pulses of wavevectors $\mathbf{k_1}$and $\mathbf{k_2}$, with $\mathbf{q_0} = \mathbf{k_1} - \mathbf{k_2}$, are crossed at a small angle on the sample producing a sinusoidal intensity pattern. In regions of optical intensity, the excitation pulses impulsively impart momentum to the Raman-active modes in that region (provided the vibrational period of these modes is long compared to the optical pulse duration). The central wavevectors ($\mathbf{q_0}$and -$\mathbf{q_0}$) of the lattice excitation are therefore specified by the crossing angle of the two excitation pulses. Since the spotsizes of the two excitation beams are finite, a range of wavevectors is excited and the polariton dispersion produces two counter-propagating wavepackets following excitation. Typically the response is monitored by the diffraction of a variably-delayed probe pulse off the long-lived vibrational grating. To avoid ambiguities in the characterization of these polaritons modes arising from propagation effects, excitation pulses with very large spotsizes along the direction of propagation are used. Dispersion curves, as illustrated in figure 5, can

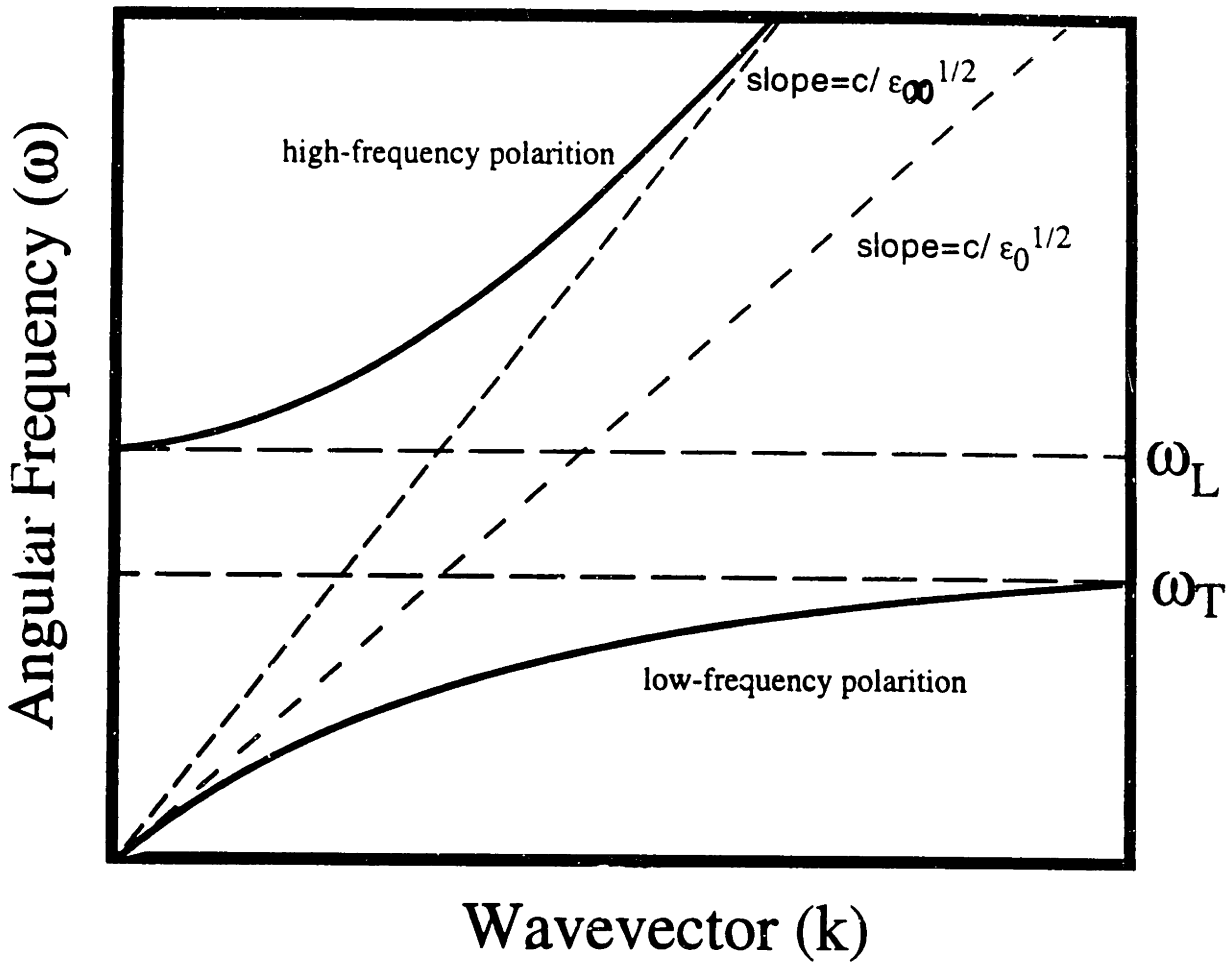

Figure 5: Typical dispersion curves for a polar optic phonon-polariton in the low wavevector region. ω_T and ω_L denote the natural (uncoupled to the EM field) transverse and longitudinal phonon angular frequencies, while ε_0 and ε_∞ denote the low and high frequency dielectric constants.

therefore be mapped out experimentally by using a range of excitation angles.

In other experiments, a single excitation pulse has been used to launch propagating phonon-polaritons [17-18]. Here rectification of the optical excitation pulse impulsively drives the polar vibration via the electro-optic effect. Furthermore, in this case a single beam is used for excitation, and only very low frequency wavevector components are excited, with a range inversely proportional to spotsize of the excitation beam. In this region, the frequency of the lower branch polariton varies linearly with wavevector and the polariton excitation radiates outward from the beam at the low frequency speed of light. Since the excitation pulse travels through the sample at the high frequency speed of light (exciting polaritons throughout the thickness of the sample), the overall polariton response propagates at an angle from the excitation beam that is given by the ratio of the high and low frequency speeds of light [19]. This response, including evidence of propagation, is characterized by the polarization rotation induced on a variably-delayed probe pulse. The probe pulse propagates parallel to the excitation pulse but is spatially translated to map out the propagating response. Complete temporally-resolved images of the propagating response should be possible with spatially-extended reference pulses imaged onto a CCD camera.

Spatially and temporally shaped waveforms could be used to manipulate and shape these propagating responses. For example a series of spatially and temporally separated pulses which are matched to the polariton propagation could be used to repetitively amplify the lattice displacement. This has the advantage of spreading optical intensity over a large region, thereby circumventing damage associated with peak intensity,

while still maximizing and localizing the vibrational response. Computer simulations for $LiTaO_3$ show that vibrational amplitudes can be increased by a factor 10 using this method [20]. The factor limiting amplification in this system is vibrational relaxation which by no means excludes much more impressive vibrational displacements in other systems. In addition to amplification, shaped waveforms could be used to compensate for wavepacket spreading due to group-velocity dispersion or other factors. Furthermore, these responses are polar and produce terahertz radiation whose form can now be manipulated by the shaped optical waveforms used to initially excite the polariton.

6.4 SPATIAL SHAPING FOR POLARITON COMPRESSION

In this section we will provide a mathematical description for excitation of phonon-polaritons with a spatially shaped waveform, within certain approximations. Extension to excitation with both temporally and spatially shaped waveforms is straightforward. It is then demonstrated that wavepacket spreading from group-velocity dispersion can be compensated by an appropriately shaped waveform. This particular example also shows that for highly dispersive systems, optical excitation intensity can be spread over a large region and used to excite a polariton wavepacket that becomes compressed at some later time producing a large peak vibrational displacement. There has also been some preliminary experimental work that demonstrates some of these ideas [21].

6.4.1 Description of polariton dispersion

In the polariton regime, the transverse optic phonon can be modeled as a damped harmonic oscillator that is coupled to the electric field [16]:

$$\ddot{Q} = b_{11}Q - \Gamma\dot{Q} + b_{12}E + f \tag{3}$$

$$P = b_{21}Q + b_{22}E \tag{4}$$

where Q is the phonon displacement, E is the electric field, P is the polarization, f is a time dependent driving force, and Γ is a phenomenological damping constant. Mass-weighted units are used (Q and F are divided by the square root of the reduced mass) and the dots above Q indicate temporal derivatives. The coupling constant are defined as follows:

$$b_{11} = -\omega_T^2 \tag{5}$$

$$b_{12} = b_{21} = \omega_T \left(\frac{\varepsilon_0 - \varepsilon_\infty}{4\pi} \right)^{1/2} \tag{6}$$

$$b_{22} = \frac{\varepsilon_\infty - 1}{4\pi} \tag{7}$$

where ω_T is the natural frequency for the transverse optic mode, ε_0 is the low frequency permittivity, and ε_∞ is the high frequency permittivity.

Though E, Q, and P are in general vector quantities, we will treat these quantities as scalars and consider only the case where they are all parallel to the polar axis of the crystal and the polariton propagates in a plane normal to this axis. Given equation 4 and Maxwell's equation, the wave equation in a polarizable medium can be derived as:

$$\nabla^2 E = \frac{1}{c^2}\left(\varepsilon_\infty \ddot{E} + 4\pi b_{21}\ddot{Q}\right) \tag{8}$$

The pair of coupled differential equations, equations 3 and 8, govern the polariton propagation. Using traveling-wave solutions $\exp\left(i\left(kx-\omega(k)t\right)\right)$ as trial solutions for Q and E in equations 3 and 8 in the absence of a driving force F, one can derive the following expression for the dispersion equation:

$$\omega^4 + i\Gamma\omega^3 - \frac{ck^2 + \omega_T^2\varepsilon_0}{\varepsilon_\infty}\omega^2 - \frac{i\Gamma c^2k^2}{\varepsilon_\infty}\omega + \frac{\omega_T^2 c^2 k^2}{\varepsilon_\infty} = 0 \qquad (9)$$

Equation 9 gives two sets of solutions for $\omega(k)$, representing the higher and lower polariton branches illustrated previously in figure 6. Expressions for Q and E can subsequently be expressed as:

$$Q(x,t) = \int dk \sum_j A_j(k)\exp\left(i\left(kx-\omega_j(k)t\right)\right) \qquad (10)$$

$$E(x,t) = \int dk \sum_j B_j(k)\exp\left(i\left(kx-\omega_j(k)t\right)\right) \qquad (11)$$

where

$$B_j(k) = -\left(\omega_j^2(k) + i\omega_j^2(k)\Gamma + b_{11}\right)A_j(k)/b_{12} \qquad (12)$$

and the subscripts denote the different solutions for $\omega(k)$, and $A^j(k)$ is specified by the conditions immediately after excitation with the driving force f.

6.4.2 Polariton Excitation with ISRS

To solve for the coefficients in the integrands of equations 10 and 11, a delta function excitation is assumed for the time dependence of f.

Since this will give the impulse response function for an arbitrary spatial excitation profile, responses to more complicated time-dependence in f (produced by shaping, for example) can be determined by convolution. The force (via the ISRS mechanism) is given by:

$$f(x,t) = -\left(\partial\alpha/\partial Q\right) I(x)\delta(t)/2 \equiv f_o(x)\delta(t) \equiv \delta(t)\int dkF(k)\exp(ikx) \tag{13}$$

where α is the polarizabiility and I(x) is the spatial intensity profile of the excitation pulse.

Assuming that Q and E are both zero at t=0, integration of equations 3 and 4 about t=0 gives the additional initial conditions:

$$\dot{Q}(x,t=0) = f_0(x) \text{ and } \dot{E}(x,t=0) = -4\pi b_{21} f_0(x)/\varepsilon_\infty \tag{14}$$

this along with equations 10-12, give the following set of equations for $A_j(k)$:

$$\sum_j A_j(k) = 0 \tag{15}$$

$$\sum_j A_j(k)\left(\omega_j^2(k) + i\omega_j^2(k)\Gamma + b_{11}\right)/b_{12} = 0 \tag{16}$$

$$\sum_j \left(-i\omega_j(k)\right)A_j(k) = F(k) \tag{17}$$

$$\sum_j A_j(k)\left(-i\omega_j(k)\right)\left(\omega_j^2(k) + i\omega_j^2(k)\Gamma + b_{11}\right)/b_{12} = 4\pi b_{21}F(k)/\varepsilon_\infty \tag{18}$$

The solution to this set of equations can be very cumbersome but shows that the relative partitioning between the high frequency and low frequency branches of the polariton is wavevector dependent. At very low wavevectors, the lower branch is predominantly light-like and while the higher branch is predominantly lattice-vibration, and therefore the ISRS excitation drives the higher-branch polariton more effectively. At larger wavevectors, the character of the two polariton branches is reversed as is the effectiveness of ISRS excitation.

In the limit where damping is negligible, i.e. $\Gamma << \omega_T$, the solutions to the dispersion equation are $\pm\omega_1$ and $\pm\omega_2$ for the high and low frequency branches, with:

$$\omega_{1,2}^2 = \frac{c^2k^2 + \omega_T^2\varepsilon_0 \mp \sqrt{\left(c^2k^2 + \omega_T^2\varepsilon_0\right) - 4\varepsilon_\infty\omega_T^2c^2k^2}}{2\varepsilon_\infty} \tag{19}$$

The solution to equations 15-18, in this case, is:

$$A_{1+}(k) = \frac{iF(k)\left(c^2k^2 - \varepsilon_\infty\omega_1^2(k)\right)}{2\varepsilon_0\omega_1(k)\left(\omega_2^2(k) - \omega_1^2(k)\right)} \tag{20}$$

$$A_{2+}(k) = \frac{-iF(k)\left(c^2k^2 - \varepsilon_\infty\omega_2^2(k)\right)}{2\varepsilon_0\omega_2(k)\left(\omega_2^2(k) - \omega_1^2(k)\right)} \tag{21}$$

and $A_{j-}(k) = -A_{j+}(k)$ for the other two coefficients.

Pulse durations used in most ISRS experiments are only sufficient to impulsively excite the lower branch of the polariton, in which case only the

low frequency amplitude coefficients $A_{1\pm}(k)$ should be retained in equation 10, and we can write (for underdamped responses):

$$Q(x,t) = \int dk\left(A(k)\exp\left(i\left(kx - \omega(k)t\right)\right) + c.c.\right) \tag{22}$$

where c.c. denotes complex conjugate and the 1+ subscript in A(k) has been dropped. Though the solution to equations 15-18 is cumbersome, we can generally write:

$$A(k) = iF(k)\chi(k) \tag{23}$$

where $\chi(k)$ gives the wavevector-dependent partitioning of excitation amplitude to the lower frequency polariton. Equation 20 shows that $A_{1\pm}(k) = 0$, but this is true even for non-zero damping and therefore very low wavevector frequency spatial excitations (such as the non-sinusoidal constant component in a grating excitation) do not produce any response in ISRS experiments (though they could produce a response via the electro-optic effect).

The results in equations 22 and 23 show that the spatial profile of the excitation waveform prescribes not only the initial polariton wavepacket but also its time-dependent evolution. This situation is similar to what was described in chapter 4 regarding molecular wavepacket shaping. In both cases, a range of basis wavefunctions can be selectively excited to produce a desired superposition state. However, in this case, the form of $\tilde{F}(k)$ is not arbitrary, since f(x) is real and either positive or negative depending on the sign of $\left(\partial\alpha/\partial Q\right)$ (since the intensity is always positive), and therefore

completely arbitrary polariton wavepackets cannot be specified. If combined temporal and spatial shaping is used, this problem can be overcome. For example, if the central wavevector of the wavepacket is $\pm q_0$ and $\omega(\pm q_0) = \omega_0$ and propagation during the first temporal period is ignored, four separate ultrashort spatially-shaped excitation waveforms could be used at quarter-cycle intervals to generate an arbitrary set of initial conditions following excitation. Each waveform would respectively specify the positive and negative initial values of Q and $\dot{Q}$. The evolution of Q can therefore be prescribed in an arbitrary manner though specification for long times is ultimately limited by non-zero relaxation rates.

6.4.3 Polariton compression

We will now consider the case in which a spatially shaped excitation waveform precompensates for group-velocity dispersion so that counter-propagating polariton wavepackets become compressed during propagation. This is an example in which optical excitation intensity can be spread over a large region but produces a large peak-amplitude displacement at a later time.

We will assume that the excitation waveform takes the form:

$$I(x,t) = I_0\delta(t)\exp\left(-x^2w^2/\left(w^4+16\gamma^2\right)\right) \cdot\left\{1+\cos\left[q_0x-\left(4\gamma/\left(w^4+16\gamma^2\right)\right)x^2\right]\right\} \tag{24}$$

For the case of γ=0, this excitation waveform is identical to the usual case of two focused beams (with spotsizes w) crossed at an angle θ such that:

$$q_0 = 4\pi \sin(\theta/2)/\lambda \tag{25}$$

For cases in which γ is non-zero the fringe spacing given by equation 24 increases linearly along the beam profile. Such a waveform could be produced by wavevector filtering with a one-dimensional dual-LC-mask described in chapter 2, as could more complicated spatially shaped waveforms. The excitation pattern can also be produced quite easily by using lenses to overlap two crossed beams with wavefronts of opposite curvature. For example the beams could be overlapped such that the sample is before the focus of the first beam and after the focus of the second beam.

We will assume that the excitation waveform temporal features are short enough in duration to only drive the lower branch polariton impulsively so only wavevectors near $k = \pm q_0$ will be excited. Furthermore we will assume that the polariton in this region is only weakly damped and that both the damping Γ_0 and susceptibility $\chi(k)$ are wavevector independent over the range wavevectors in the excitation waveform. Finally we assume that the real part of ω in the exponential terms can be expanded to second order about $k = \pm q_0$:

$$\omega_{real}(k \text{ near } \pm q_0) \approx \omega_0 + \omega_1(\pm k - q_0) + \omega_2(\pm k - q_0)^2 \tag{26}$$

Note, from equation 9, that $\omega_{real}(k) = \omega_{real}(-k)$.

Taking the Fourier transform of equation 24 gives:

$$F(k) \propto \exp\left(-(k-q_0)^2\left(w^2/4 - i\gamma\right)\right) + \exp\left(-(k+q_0)^2\left(w^2/4 + i\gamma\right)\right)$$

(27)

Combining equations 27,26, 23, and 22 gives the following response for Q:

$$Q(x,t>0) \propto i\exp(-\Gamma_0 t)/2\omega_0$$
$$\cdot\left\{\begin{array}{l}\exp(\mathrm{i}(\mathrm{q}_0 x-\omega_0 t))\\ \cdot\int dk\exp\left(i(x-\omega_1 t)(k-q_o)-\left(w^2/4+i(\omega_2 t-\gamma)\right)(k-q_0)^2\right)\\ +\exp(\text{-}\mathrm{i}(\mathrm{q}_0 x+\omega_0 t))\\ \cdot\int dk\exp\left(i(x+\omega_1 t)(k+q_o)-\left(w^2/4+i(\omega_2 t+\gamma)\right)(k+q_0)^2\right)\\ -c.c.\end{array}\right\}$$

(28)

Integration of equation 28 gives:

$$Q(x,t>0) \propto \frac{\exp(-\Gamma_0 t)}{\omega_0\sqrt{w^2+16(\omega_2 t-\gamma)^2/w^2}}\exp\left(-\frac{w^2(x-\omega_1 t)^2}{w^4+16(\omega_2 t-\gamma)^2}\right)$$
$$\cdot\sin\left(\mathrm{q}_0 x-\omega_0 t+\frac{4(\omega_2 t-\gamma)(x-\omega_1 t)^2}{w^4+16(\omega_2 t-\gamma)^2}\right)$$
$$-\frac{\exp(-\Gamma_0 t)}{\omega_0\sqrt{w^2+16(\omega_2 t+\gamma)^2/w^2}}\exp\left(-\frac{w^2(x+\omega_1 t)^2}{w^4+16(\omega_2 t+\gamma)^2}\right)$$
$$\cdot\sin\left(\mathrm{q}_0 x+\omega_0 t+\frac{4(\omega_2 t+\gamma)(x+\omega_1 t)^2}{w^4+16(\omega_2 t+\gamma)^2}\right)$$

(29)

Equation 29 shows that the response from the crossed excitation beams is indeed composed of counterpropagating wavepackets with widths initially equal to the spotsize of the excitation beams. The two wavepackets are both 'chirped' with a central phase velocity given by ω_0/q_0 and group velocities given by $\pm\omega_1$, which is the slope of the dispersion curve for the lower polariton branch at $\pm q_0$. The chirp evolves as the wavepacket propagates due to group velocity dispersion given by ω_2. Since the shaped excitation pulse introduced an initial spread (or chirp) of polariton wavefronts of different wavevectors, the group-velocity dispersion during propagation results in the compression of one of the wavepackets and the further spreading of the other wavepacket.

For example, if γ is chosen so that $\omega_2\tau - \gamma = 0$, the right propagating wavepacket will be fully compressed at time τ and centered at $x = \omega_1\tau$, after which it will begin to spread. The ratio of the peak intensity of this wavepacket when fully compressed to its peak intensity immediately after excitation is given by (after the two wavepackets have separated):

$$\text{amplification factor} = \exp(-2\Gamma_0\tau)\left(\frac{w^4 + 16(\omega_2\tau)^2}{2w^4}\right) \qquad (30)$$

The ratio of the widths of the intensity distribution of the wavepacket at these two times is given by:

$$\text{compression factor} = \frac{w^4}{w^4 + 16(\omega_2\tau)^2} \qquad (31)$$

The assumption in equation 30 and 31 is that γ can be made arbitrarily large, which in practice is true. Recall that w is the diffraction limited spotsize of the excitation beams, but since γ is non-zero, the actual spot size is much larger.

Equation 30 and 31 show that excitation optical intensity can be spread over a large area (spot size equal to $w\sqrt{1+16\gamma^2/w^4}$) with peak intensity less than the damage threshold for the material, but can produce a lattice displacement that is compressed to a large peak amplitude at a later time. This peak amplitude could be made arbitrarily large if not for the relaxation term in equation 30. For modest relaxation rates, equation 30 is approximately maximized at $\tau = 1/\Gamma_0$ giving an amplification factor of approximately $\exp(-2)8\omega_2^2/\Gamma^2 w^4$. Therefore amplification can be made largest for systems that exhibit large quadratic dispersion and have long relaxation lifetimes, and with excitation beams that have very small diffraction-limited spotsizes. However, if this last factor is made too small, equation 26 will not remain valid over the range of excited wavevectors, and more versatile spatial shaping will be necessary to compensate for dispersion to higher orders.

As an example, inspection of the dispersion curve for the lower branch polariton of $LiTaO_3$ [22] gives a value for ω_2 of about -2e6 cm^2/s near k=5000 cm^{-1} and a vibrational time constant of about 3 psec. These factors combine to give a compression factor of only about 1/2, indicating the importance of long vibrational lifetimes in producing large amplification factors.

In more complicated schemes, combined temporal and spatial shaping could be used to excite only a single wavepacket or to compress

both wavepackets simultaneously. Furthermore, beams with very small diffraction-limited spot sizes could be shaped to precompensate for non-linear dispersion over a very large wavevector range (rather than just to second order as in the previous example), enhancing the potential for amplification and compression. Time-resolved imaging and characterization of the polariton propagation could also be interfaced with the waveform generation.

6.5 ADDITIONAL PROSPECTS

A wide range of spectroscopy experiments, especially ultrafast high-order nonlinear spectroscopy, could be conducted in a novel way through the use of temporal and spatial (or wavevector) shaping. For example, time-delayed degenerate four-wave or higher-order mixing experiments could be conducted, with phase-sensitive heterodyning [23] and temporal gating if desired, without beamsplitters or delay lines. A single incident pulse could be transformed into three or more beams separated by appropriate amounts such that, when focused by a lens into a single spot, they cross with the wavevectors needed to satisfy phase-matching conditions. Each beam could consist of a single pulse or a complex waveform, and could play the role of excitation, probe, or heterodyne-gate pulse when those roles are distinct. All the delays, wavevectors and phases, and ultimately the polarizations, could be controlled through temporal and spatial pulse shaping.

Combined spatial and temporal pulse shaping has interesting implications for optical signal generation and information processing. The pulse shaping operation can be thought of as highly multiplexed terabit signal generation, with the different signals directed under operator control

toward different addresses on a receiving device. The four-wave and higher-order mixing measurements described above can be thought of as logic or arithmetic operations, permitting optical processing of the terabit signals so that the outcome, at somewhat lower bandwidth, could be compatible with high-speed (but sub-THz bandwidth) electronics. Finally, control over propagating polarizations associated with mixed excitations such as phonon-polaritons or exciton-polaritons can be thought of in terms of guidance as well as manipulation (filtering, etc.) of high-bandwidth signals as they propagate from one address to another. As a simple example, an ultrashort phonon-polariton or exciton-polariton wavepacket ordinarily broadens as it propagates since the host medium is not a zero-dispersion propagation line but rather exhibits dispersion among the many frequency components of the ultrashort, ultrawide-bandwidth excitation. Through spatial and temporal pulse shaping, light could be made to interfere destructively with the leading and trailing edges of the wavepacket and constructively with the center, continuously maintaining the short duration and high bandwidth until a target address is reached. More complex manipulation of the signal, such as filtering or partial reflection, could also be achieved.

CHAPTER 6 REFERENCES

1. A. M .Weiner, J. P. Heritage, E. M. Kirschner, *J. Opt. Soc. Am.* **B5**, 1563 (1988)
2. C. Froehly, B. Colombeau,M. Vampouille, *Progress in Optics* E. Wolf, ed. (North-Holland, Amsterdam, 1983), vol. 20, pp. 115-121
2. A. M. Weiner, D. E. Leaird, J. S. Patel, J. R. Wullert, *IEEE J. Quan. Elec.* **28**, 908 (1992)
3. M. M. Wefers, K. A. Nelson, *Opt. Lett.* **20**, 1047 (1995)
4. M. C. Nuss, M. Li, T. H. Chiu, A. M. Weiner, A. Partovi, *Opt. Lett.* **19**, 664 (1994)
5. M. C. Nuss, R. L. Morrison, *Opt. Lett.* **20**, 740 (1995)
6. K. B. Hill, K. G. P. Purchase, D. J. Brady, *Opt. Lett.* **20**, 1201 (1995)
7. K. A. Nelson, 'Coherent Control: Optics, Molecules, and Materials', pp.47-49 in *Ultrafast Phemonena IX*, G. A. Mourou, A. H. Zewail, P. F. Barbara, W. H. Knox, Eds. (Springer-Verlag, Berlin, 1994)
8. T. Rossler, J. B. Page, 'Intrinsic Localized Modes in Driven Anharmonic Lattices with Realistic Potentials', *Phys. Lett. A.* (in press) (1996)
9 A. M. Weiner, D. E. Leaird,*Opt. Lett.* **15**, 51-53 (1990)
10. A. M .Weiner, D. E. Leaird, G. P. Wiederrecht, K. A. Nelson, *Science* **247**, 1317 (1990)
11. E. G. Steward, 'Fourier Optcs: An Introduction' (Ellis Horwood Limited, Chicester, 1987)
12. M. M. Wefers, K. A. Nelson, *IEEE J. Quan. Elec.* **32**, 161 (1996)
13. T. P. Dougherty, G. P. Wiederrecht, K. A.Nelson, *J. Opt. Soc. Am. B.* **9**, 2179 (1992)
14. G. P. Wiederrecht, T. P. Dougherty, L. Dhar, K. A. Nelson, D. E. Leaird, A. M. Weiner, *Phys. Rev. B.* **51**, 916 (1995)
15. T. P. Dougherty, G. P. Wiederrecht, K. A. Nelson, *Science* **258**, 770 (1992)
16. A. S. Barker, R. Loudon, Rev. Mod. Phys. **44**, 18 (1972)
17. D. H. Auston, *Appl. Phys. Lett.* **43**, 713 (1983)
18. D. H. Auston, M. C.Nuss, *IEEE J. Quan. Elec.* **24**, 184 (1988)
19. D. A. Kleinman, D. H. Auston, *IEEE J. Quan. Elec.* **20**, 964 (1984)
20. L. Dhar, B. Berfeindt, K. A. Nelson, *Ferroelectrics* **164**, 1 (1995)
21. H. Kawashima, F. Sasaki, S. Kobayashi, T. Tani, 'Transient grating with asymmetric arms for electro-optic generation of THz radiation' *Opt. Lett.* (in press) (1996)
22. G. P. Wiederrecht, T. P. Dougherty, L. Dhar, K. A. Nelson, A. M. Weiner, D. E. Leaird, *Ferroelectrics* **144**, 1 (1993)

23. W. P. de Boeij, M. S. Pshenichnikov, D. A. Wiersma, *Chem. Phys. Lett.* **238**, 1 (1995)

Chapter 7:
Anharmonic Responses in Transient Grating Experiments

7.1 INTRODUCTION

A principle objective of this group, and one that motivates the development of pulse shaping techniques, is optically-induced large-amplitude lattice displacements in condensed-phase systems. Such displacements could lead to optically-controlled structural rearrangement, such as ferroelectric domain switching, and could permit probing of anharmonic regions of lattice potential energy surfaces. Recent theoretical models suggest that anharmonic potentials can give rise to interesting non-linear lattice dynamics, such as soliton propagation [1-2].

In this chapter, we describe the nuclear response produced by ISRS grating excitation in model systems with anharmonic terms in their potential energy. This theoretical description is part of an experimental effort to observe anharmonic lattice responses from condensed-phase systems in the time domain using increased optical intensity. Clearly this is the first step to the more exciting possibilities involving shaped excitation waveforms and non-linear lattice dynamics.

In typical ISRS experiments [3-4], two short excitation beams are crossed in a sample, forming a sinusoidal intensity pattern which in turn impulsively excites a sinusoidal material response in the sample. This response can be probed by the diffraction of a time-delayed reference pulse. In most cases, the grating fringe spacing is small compared to the optical thickness of the sample and so the incident reference pulse and diffracted beam must satisfy the Bragg condition [5]. This implies that a

particular angle of incidence must be used for the probe pulse in order for the diffracted light to be phase-matched throughout the thickness of the sample. We will show that anharmonic terms generate additional sinusoidal material responses at spatial harmonics of the optical excitation grating. The presence of these higher-order spatial gratings can be probed by an incident pulse satisfying a different Bragg condition, isolating the anharmonic response from the overwhelming harmonic response produced by the fundamental excitation grating. My colleague, Ciaran Brennan, has termed this experimental technique to observe lattice anharmonicity *time-resolved wavevector overtone spectroscopy,* and is performing computational simulations in concert with these analytical results [6].

Responses are determined for both non-dispersive optic phonons (section 7.2) and dispersive phonon-polaritons (section 7.3) using perturbation theory. The analytical results are therefore only valid as lowest-order corrections to the response that is linear with intensity. One particularly interesting result is that for the case of dispersive polaritons, the anharmonic response does not contribute to diffraction by the fundamental grating. In previous experiments it was hoped that increased optical excitation intensity would facilitate observation of anharmonicity, but we will show that this is not possible. In section 7.4, we will discuss additional factors that could contribute to the signal when the probe beam is phase-matched for diffraction from higher-order gratings produced by the anharmonic lattice contribution. Higher-order diffraction from the fundamental grating and the quadratic term in the polarizability when it is expanded in terms of nuclear displacement will be considered.

7.2 NON-LINEAR RESPONSE FOR OPTIC PHONONS

The mass-weighted displacement amplitude Q (absolute displacement amplitude divided by the square root of the reduced mass) of a non-dispersive mode, such as an optic phonon, can be described by the differential equation:

$$\ddot{Q} + 2\gamma\dot{Q} + \omega_0^2 Q\left(1 + aQ + bQ^2\right) = f \tag{1}$$

where a and b are coefficients for the anharmonic terms, and f is the time-dependent excitation force. The zeroth order homogeneous solution ($a = b = 0$) is the usual harmonic response:

$$Q = A_+ \exp(i\omega_+ t) + A_- \exp(i\omega_- t) \tag{2}$$

$$\omega_\pm = i\gamma \pm \omega_0\sqrt{1 - \gamma^2/\omega_0^2} \tag{3}$$

For the anharmonic case we consider a homogeneous solution of the form:

$$Q = \sum_{n=1} A_+^{(n)} \exp(in\omega_+ t) + A_-^{(n)} \exp(in\omega_- t) \tag{4}$$

$A_\pm^{(n>1)}$ can be solved iteratively in terms of $A_\pm^{(1)}$ by collecting terms in $\exp(in\omega_\pm t)$ when equation 4 is subsituted into equation 1 (for f=0), while the initial conditions following the excitation force f specify $A_\pm^{(1)}$.

We consider only the first order perturbation to the harmonic solution $a^2Q^2, b^2Q^4, abQ^3 << 1$, and so we will only keep terms that are up to first order in either a or b. For simplicity, we will also only consider the case of weak damping, i.e. $\gamma^2/\omega_0^2 << 1$. These

considerations give the following expression for Q where we have also included the fact that Q must be real (which would have been determined subsequently by the initial conditions):

$$Q = \left\{ \begin{array}{c} A\exp(-\gamma t + i\omega_0 t) + \dfrac{a(3 - i4\gamma/\omega_0)A^2}{9}\exp(-2\gamma t + 2i\omega_0 t) \\ + \dfrac{b(2 - i3\gamma/\omega_0)A^3}{16}\exp(-3\gamma t + 3i\omega_0 t) \end{array} \right\} + c.c. \tag{5}$$

The excitation mechanism for ISRS has been described in chapter 5 section 2 and we will assume a delta function excitation pulse giving:

$$f(x,t) = -(\partial\alpha/\partial Q)I(x)\delta(t)/2 \tag{6}$$

where I is the excitation intensity profile and α is the polarizability. Integration of equation 1 about t=0 using equation 6 gives:

$$\dot{Q}(x,t=0) = -(\partial\alpha/\partial Q)I(x)/2 \tag{7}$$

where we also assume that $Q(x,t=0) = 0$. These conditions specify A in equation 5. The resulting expression for Q, giving the first order correction to the harmonic solution (including terms only up to first order in a or b.), is:

$$
\begin{aligned}
Q(x,t>0) = &\left(A_0 + \frac{5\gamma}{18\omega_0} aA_0^2 + \frac{3}{32} bA_0^3 \right) \exp(-\gamma t)\sin(\omega_0 t) \\
&+ \left(\frac{1}{6} aA_0^2 - \frac{3\gamma}{64\omega_0} bA_0^3 \right) \exp(-\gamma t)\cos(\omega_0 t) \\
&- \frac{1}{6} aA_0^2 \exp(-2\gamma t)\left(\cos(2\omega_0 t) + \frac{4\gamma}{3\omega_0} \sin(2\omega_0 t) \right) \\
&+ \frac{1}{32} bA_0^3 \exp(-3\gamma t)\left(\frac{3\gamma}{2\omega_0} \cos(3\omega_0 t) - \sin(3\omega_0 t) \right)
\end{aligned} \tag{8}
$$

where $A_0(x) \equiv -I(x)(\partial\alpha/\partial Q)/2\omega_0$

Equation 8 shows that the impulse response to the anharmonic potential includes harmonics of the fundamental frequency ω_0. At first this might seem unintuitive, since one expects that the frequency of oscillation would gradually change as the oscillator relaxes from the anharmonic regions of potential energy to the harmonic regions. In fact equation 8 exactly describes this situation since the different harmonics are phase shifted and have different relaxation rates. In the limit of no damping the solution becomes periodic, but this is what one would expect from a classical anharmonic oscillator with no losses.

The term $A_0(x)$ is proportional to the optical excitation intensity profile which for a grating excitation looks like:

$$
I(x) = I_0\left(1 + \cos(qx)\right) \tag{9}
$$

The quadratic and cubic terms in $A_0(x)$ therefore produce sinusoidal material gratings at spatial harmonics of the fundamental excitation wavevector q. Using equation 9 along with:

$$I^2(x) = I_0^2\left(\frac{3}{2} + 2\cos(qx) + \frac{1}{2}\cos(2qx)\right) \tag{10}$$

$$I^3(x) = I_0^3\left(\frac{5}{2} + \frac{15}{4}\cos(qx) + \frac{3}{2}\cos(2qx) + \frac{1}{4}\cos(3qx)\right) \tag{11}$$

one can express equation 8 as:

$$Q(x, t > 0) = \sum_{n=0} R_n(t)\cos(nqx) \tag{12}$$

where the functions $R_n(t)$ can be determined from equations 8-11.

$R_n(t)$ gives the temporal response for the material excitation with wavevector nq, which can be probed by its diffraction of a properly phase-matched reference beam. Inspection shows that the cubic potential energy terms produces temporal responses with frequencies $\omega_0, 2\omega_0$ and contributes to the gratings at wavevectors $\pm nq$ with n<3, while the quartic potential energy term produces temporal responses with frequencies $\omega_0, 3\omega_0$ and contributes to the material grating at wavevectors $\pm nq$ with n<4. Material excitation at spatial harmonics of the fundamental optical excitation wavevector is evidence of anharmonic terms in the potential energy, and though equations 8-12 show that the response can be complicated, the higher order frequency responses can be used to separate the contributions from the cubic and quartic potential energy terms.

7.3 NON-LINEAR RESPONSE FOR PHONON-POLARITONS

Since phonon-polaritons are dispersive, as discussed in sections 3 and 4 in chapter 6, the spatial degree of freedom must be included explicitly in the derivation of the non-linear response unlike the example in previous section. A mathematical description of the impulse response for phonon-polaritons with a harmonic potential has already been worked out in section 4.1 and 4.2 of chapter 6. The differential equations to be solved in this case are:

$$\ddot{Q} = b_{11}\left(1 + aQ + bQ^2\right)Q - \Gamma\dot{Q} + b_{12}E + f \tag{13}$$

$$\nabla^2 E = \left(\varepsilon_\infty \ddot{E} + 4\pi b_{21}\ddot{Q}\right)/c^2 \tag{14}$$

where Q is the lattice displacement (in mass-weighted units), E is electric field, and f is the time-dependent ISRS excitation. The coupling constant are defined as follows:

$$b_{11} = -\omega_T^2 \tag{15}$$

$$b_{12} = b_{21} = \omega_T\left(\frac{\varepsilon_0 - \varepsilon_\infty}{4\pi}\right)^{1/2} \tag{16}$$

$$b_{22} = \frac{\varepsilon_\infty - 1}{4\pi} \tag{17}$$

where ω_T is the natural frequency for the transverse optic mode, ε_0 is the low frequency permittivity, and ε_∞ is the high frequency permittivity.

The zeroth order solution (harmonic potential only) gives the following dispersion equation:

$$\omega^4 + i\Gamma\omega^3 - \frac{ck^2 + \omega_T^2\varepsilon_0}{\varepsilon_\infty}\omega^2 - \frac{i\Gamma c^2k^2}{\varepsilon_\infty}\omega + \frac{\omega_T^2 c^2 k^2}{\varepsilon_\infty} = 0 \qquad (18)$$

For the anharmonic case we will use the following trial solutions:

$$Q_j(k,t) = \sum_{n=1} A_j^{(n)}(k)\exp\left(in\left(kx - \omega_j(k)t\right)\right) \qquad (19)$$

$$E_j(k,t) = \sum_{n=1} B_j^{(n)}(k)\exp\left(in\left(kx - \omega_j(k)t\right)\right) \qquad (20)$$

where ω_j are the solutions to the dispersion equation. Using equation 18 and substituting equations 19,20 into equation 14 give:

$$B_j^{(n)} = -A_j^{(n)}\left(\omega_j^2 + i\omega_j\Gamma + b_{11}\right)/b_{12} \qquad (21)$$

As in the previous example, $A_j^{(n)}$ can be solved iteratively in terms of $\exp\left(in\left(kx - \omega_j t\right)\right)$ by substituting equations 19-21 into equation 13. Again we consider only the first order perturbation to the harmonic solution, i.e. $a^2Q^2, b^2Q^4, abQ^3 << 1$, and so we will only keep terms that are up to first order in either a or b. This gives:

$$Q_j(k,t) = A_j(k)\exp\left(i\left(kx - \omega_j t\right)\right) + \frac{a\omega_T^2 A_j^2(k)}{3\omega_j^2 + i\omega\Gamma}\exp\left(i2\left(kx - \omega_j t\right)\right) + \frac{b\omega_T^2 A_j^3(k)}{8\omega_j^2 + 2i\omega\Gamma}\exp\left(i3\left(kx - \omega_j t\right)\right) \qquad (22)$$

$$E_j(k,t) = -Q_j(k,t)\left(\omega_j^2 + i\omega_j\Gamma - \omega_T^2\right)\Big/\left[\omega_T^2(\varepsilon_0 - \varepsilon_\infty)/4\pi\right]^{1/2} \tag{23}$$

General solutions are then given by:

$$Q(x,t) = \int dk \sum_j Q_j(k,t) \tag{24}$$

$$E(x,t) = \int dk \sum_j E_j(k,t) \tag{25}$$

Initial conditions following ISRS excitation are given:

$$Q(x,t=0) = 0 \text{ and } E(x,t=0) = 0 \tag{26}$$

$$\dot{Q}(x,t=0) = f_0(x) \text{ and } \dot{E}(x,t=0) = -4\pi b_{21} f_0(x)/\varepsilon_\infty \tag{27}$$

$$f(x,t) = -\left(\partial\alpha/\partial Q\right) I(x)\delta(t)/2 \equiv f_o(x)\delta(t) \equiv \delta(t)\int dk F(k)\exp(ikx) \tag{28}$$

where f(x,t) describes the ISRS excitation.

Equations 22-28 can be used to determine $A_j(k)$ in terms of F(k) where only terms up to first order in either a or b are kept. In this calculation, it is easiest to expand $A_j(k)$ in a power series in a and b, and use the zeroth order solution (no anharmonicity) to solve for the first order solutions. In the calculation that follows we will assume no damping, i.e. $\Gamma = 0$ and that the excitation pulse duration impulsively drives only the low frequency polariton branch (and its harmonics). The frequencies of the excited polariton response are then given by $\pm n\omega_1$, where the solutions to the dispersion equation are now given by:

$$\omega_{1,2}^2(k) = \frac{c^2k^2 + \omega_T^2\varepsilon_0 \mp \sqrt{\left(c^2k^2 + \omega_T^2\varepsilon_0\right) - 4\varepsilon_\infty\omega_T^2c^2k^2}}{2\varepsilon_\infty} \tag{29}$$

where the fundamental polariton frequencies for the lower and upper branches are respectively given by ω_1 and ω_2. The optical intensity for grating excitation is given by:

$$I(x) = I_0\left(1 + \cos(qx)\right). \tag{30}$$

The constant term only drives the high frequency branch of the polariton, while the grating term will drive both polariton branches. After some algebra, equations 22-30 yield the following response for Q(x,t):

$$\begin{aligned} Q(x,t>0) = {} & A_0(q)\chi_1^{(1)}(q)\cos(qx)\sin\left(\omega_1(q)t\right) \\ & - \frac{a\omega_T^2A_0^2(q)}{12\omega_1^2(q)}\cos(2qx) \\ & \cdot\left[\left(\chi_1^{(1)}(q)\right)^2\cos\left(2\omega_1(q)t\right) - \chi_1^{(2)}(q)\cos\left(\omega_1(2q)t\right)\right] \\ & - \frac{b\omega_T^2A_0^3(q)}{128\omega_1^2(q)}\cos(3qx) \\ & \cdot\left[\left(\chi_1^{(1)}(q)\right)^3\sin\left(3\omega_1(q)t\right) - \chi_1^{(3)}(q)\sin\left(\omega_1(3q)t\right)\right] \end{aligned} \tag{31}$$

with

$$A_0(q) = \frac{-(\partial\alpha/\partial Q)I_0}{2\omega_1(q)} \tag{32}$$

The $\chi_j^{(n)}(k)$ terms are wavevector-dependent functions that partition the ISRS excitation between the lower (j=1) and upper (j=2) polariton branches for the nth order of excitation intensity:

$$\chi_1^{(1)}(k) = \frac{\left(c^2k^2 - \varepsilon_\infty\omega_1^2(k)\right)}{2\varepsilon_0\omega_1(k)\left(\omega_2^2(k) - \omega_1^2(k)\right)} \tag{33}$$

$$\chi_2^{(1)}(k) = \frac{\left(c^2k^2 - \varepsilon_\infty\omega_2^2(k)\right)}{2\varepsilon_0\omega_2(k)\left(\omega_1^2(k) - \omega_2^2(k)\right)} \tag{34}$$

$$\chi_1^{(2)}(k) = \frac{\left(\chi_1^{(1)}(k)\right)^2\left(\omega_1^2(k) - \omega_2^2(2k)\right)}{\omega_1^2(2k) - \omega_2^2(2k)} + \frac{\left(\chi_2^{(1)}(k)\right)^2\left(\omega_2^2(k) - \omega_2^2(2k)\right)}{\omega_1^2(2k) - \omega_2^2(2k)} \tag{35}$$

$$\chi_1^{(3)}(k) = \frac{\left(\chi_1^{(1)}(k)\right)^3 3\omega_1(k)\left(\omega_1^2(k) - \omega_2^2(3k)\right)}{\omega(3k)\left(\omega_1^2(3k) - \omega_2^2(3k)\right)} + \frac{\left(\chi_2^{(1)}(k)\right)^2 3\omega_2(3k)\left(\omega_2^2(k) - \omega_2^2(3k)\right)}{\omega(3k)\left(\omega_1^2(3k) - \omega_2^2(3k)\right)} \tag{36}$$

In analogy with the previous example of a non-dispersive optic phonon, equation 31 can be expressed as:

$$Q(x,t>0)=\sum_n R_n(t)\cos(nqx) \tag{37}$$

where the $R_n(t)$ are given by inspection.

Equation 31 shows that once again the anharmonic potential energy terms produce sinusoidal material responses at harmonics of the optical intensity grating. In contrast to the example of a non-dispersive mode in the previous section, the cubic and quartic potential energy terms only contribute to the material response at a single wavevector. The cubic term only contributes to the grating at $2q$ and generates temporal frequencies $2\omega(q),\omega(2q)$, while the quartic term only contributes to the grating at $3q$ and generates temporal frequencies $3\omega(q),\omega(3q)$. In particular neither term contributes to the response at the fundamental grating and so the results from ISRS grating experiments performed in the usual way are completely insensitive to lattice anharmonicities for the case of polaritons.

At first, it may seem surprising that these results are so different from the case of optic phonons, especially in the limit of large excitation wavevector q when the polar mode becomes uncoupled with the electric field. In this limit $\omega(q)\approx\omega_T$ so that the polariton is no longer dispersive, and the two cases should become physically similar. The difference lies in the constant term in the spatial excitation profile. This term cannot drive a response from the lower branch of the polariton but it can for the non-polar optic phonon. If only the highest spatial frequency components of the $I^n(x)$ intensity terms (equations 9-11) are retained in equation 8 (the non-polar optic phonon response), the results are identical to equation 31 (the response for the polariton) in the limit of large q.

The temporal response for the higher-order spatial gratings can also be expressed to include a product of sinusoids with frequencies $(2\omega(q) \pm \omega(2q))/2$ and $(3\omega(q) \pm \omega(3q))/2$, which will produce a high frequency oscillation (which might not be resolved by the finite duration of the probe pulse) riding on a low frequency oscillation. In preliminary computational simulations low frequency oscillations are observed in the signal [6].

7.4 ADDITIONAL CONTRIBUTIONS TO THE OBSERVED RESPONSE

7.4.1 Detection of a Material Excitation Grating

Transient grating and four-wave-mixing experiments have been treated extensively [5]. Here we provide only a basic description. The displacement of the lattice mode described in the previous sections modifies the optical properties of the sample. For the case of non-resonant Raman excitation (no optical absorption), the oscillating material grating results in a small time-dependent change in the real part of the index of refraction n:

$$n(x,t) = n_0 + \delta n(x,t) \tag{38}$$

$$\delta n(x,t) \approx (\partial\alpha/\partial Q)Q(x,t)/2n_0 \tag{39}$$

This material excitation is probed with a beam propagating along the wavevector $\mathbf{k_p} = k_{px}\hat{\mathbf{x}} + k_{pz}\hat{\mathbf{z}}$, where z is the direction through the thickness of the sample. For the case of a thin sample, this probe beam sees a transmittance function t(x) that looks like:

$$t(x) = \exp(i2\pi d\delta n(x,t)/\lambda) \tag{40}$$

where d is the sample thickness and λ is the wavelength of the probe beam. The electric field immediately following the sample is given by a superposition of waves with wavevectors $\mathbf{k_d}$ such that $|\mathbf{k_d}| = |\mathbf{k_p}|$, and such that the superposition matches the boundary condition given by the product of the transmittance function and the incident beam.

For a sinusoidal material grating of wavevector q and amplitude $R_q(t)$, the expansion of the exponential term in equation 40 will result in a series of terms $\cos(mqx)$ producing a superposition of diffracted waves such that:

$$k_{dx} = k_{px} \pm mq \tag{41}$$

$$k_{dz} = \sqrt{|\mathbf{k_p}|^2 - k_{dx}^2} \tag{42}$$

If δn is small, as is usually the case, the expansion in equation 40 gives the amplitude of the mth order diffracted beam to be proportional to $R_q^m(t)$.

For a thick grating, one can consider the superposition of waves that result from a series of thin gratings. However, beams diffracted from different gratings will be phase shifted from one another resulting in destructive interference. This is physical basis for the well-known Bragg condition for thick gratings which requires:

$$\mathbf{k_d} = \mathbf{k_p} \pm mq\hat{\mathbf{x}} \tag{43}$$

Since the absolute value of the wavevectors for the diffracted and incident beams must be the same, equation 43 demands that:

$$k_{px} = \mp mq/2 \tag{44}$$

This equation implies that the probe beam be incident at a specific angle to produce diffraction in a thick sample. In addition, when this condition is satisfied only the selected order of diffraction is observed. This condition also implies that the plane of the sample bisects the incident and diffracted beams.

A correctly aligned probe beam should therefore allow observation of the higher order material gratings arising from anharmonicity by detecting the intensity of diffracted probe light that is phase-matched to a selected material grating. The signal intensity would be given by $S(\tau) \propto |R_n(\tau)|^2$, where τ is the delay of the of the reference pulse relative to the excitation beams, thereby characterizing the lattice anharmonicity. Unfortunately, as we will discuss in the next two sections, there may be additional terms of comparable order that contribute to this signal.

7.4.2 Higher-Order Contributions from the Polarizability

Anharmonic terms in the potential energy produce a non-linear restoring force (with respect to the lattice displacement amplitude). Non-linear terms can also exist in the expansion of the polarizability. Since we assume that the lattice displacement amplitude is initially zero, these higher order terms will not contribute to the ISRS excitation, but they will modify the diffraction of the subsequent probe beam. Instead of equation 39 we have:

$$\delta n(x,t) \approx (\partial\alpha/\partial Q)Q(x,t)/2n_0 + \left(\partial^2\alpha/\partial Q^2\right)Q^2(x,t)/4n_0 + \left(\partial^3\alpha/\partial Q^3\right)Q^3(x,t)/24n_0 \quad (45)$$

Equation 45 shows that these higher order terms also generate material excitations at harmonics of the optical excitation grating, even in the absence of lattice anharmonicity. Assuming both terms are present, the signal at the second and third spatial harmonics would be:

$$S(\tau;2q) \propto \left|R_2(\tau) + R_1^2(\tau)\left(\partial^2\alpha/\partial Q^2\right)/4\right|^2 \quad (46)$$

$$S(\tau,3q) \propto \left|R_3(\tau) + R_1^3(\tau)\left(\partial^3\alpha/\partial Q^3\right)/48\right|^2 \quad (47)$$

Both terms in either expression depend on excitation intensity to the same power. Therefore the observation of diffraction intensity from higher order material gratings cannot be interpreted as a definitive signature of lattice anharmonicity since it is not clear whether a should be larger than $\left(\partial^2\alpha/\partial Q^2\right)$ or that b should be larger than $\left(\partial^3\alpha/\partial Q^3\right)$. These terms produce slightly different time-dependent responses, however, and this might be used to distinguish between them.

7.4.3 Contributions from Higher-Order Diffraction

In section 7.4.1, it was shown that for a single sinusoidal material grating in a thick sample, a properly phase-matched probe pulse produces a single diffracted beam. Usually the Bragg condition (equations 43 and 44) is met for first-order diffraction (m=1) producing the largest signal since it depends on intensity to the lowest order. In the presence of multiple

material gratings, the Bragg condition can be met for both gratings but at different orders. For example, if the probe beam is phase-matched for first order diffraction from a material grating at $2q$, it is also phase-matched for second-order diffraction from a material grating at q. The diffracted beams from these two gratings are collinear.

Unfortunately this is our situation. Non-linear terms in the restoring force and polarizability with respect to Q, generate material gratings at spatial harmonics of the optical excitation intensity grating. Therefore, if the probe beam is phase-matched to observe the response from the grating with wavevector mq, it is also phase-matched for m^{th} order diffraction from the fundamental grating. The signal intensity in these cases is given by:

$$S(\tau;mq) \propto \left| R_m(\tau) + \frac{2R_1^m(\tau)}{m!}\left(\frac{(\partial\alpha/\partial Q)\pi d}{2n_0\lambda}\right)^m \right|^2 \qquad (48)$$

The terms in equation 48 depend on the excitation intensity to the same order. Therefore the presence of signal when the probe beam is phase-matched for first order diffraction from a higher-order grating can occur even in the absence of lattice anharmonicity, or non-linearity in the polarizability, or both.

One must look at the temporal form of the signal in order to ascertain its physical origin. For example, if we consider probing first order diffraction from the second harmonic of the fundamental excitation grating, the cubic anharmonic term in the potential generates terms in $R_2(t)$ that include oscillations at the frequency ω_0 (or $\omega(2q)$ for the

case of a polariton), while the oscillating term in $R_1^2(t)$ is at higher frequency $2\omega_0$ (or $2\omega(q)$ for the polariton). Therefore low frequency oscillations can be an indication of cubic anharmonicity in the potential.

It might be possible to circumvent contributions from higher-order diffraction through the use of multiple pairs of excitation beams. For example, if four beams were crossed on the sample rather than only two, multiple intensity gratings would be formed with wavevectors $q_1, q_2, \frac{q_1 \pm q_2}{2}$. The non-linear terms would generate material gratings at the sums or differences of these wavevectors, for example at $3q_1 - q_2$. Since this is not a harmonic of any of the fundamental gratings, no higher-order diffraction would be produced and the presence of signal would be unambiguously indicative of non-linearity.

7.5 SUMMARY

This technique has great potential for observing non-linearities in lattice dynamics. What is particularly exciting is that the experiments (at least with only two excitation beams) should not be much more difficult than standard ISRS grating experiments. While there might be additional contributions that obscure characterization of the non-linearities, the form of the temporal response should indicate whether the signal is simply due to higher-order diffraction. Depending on these results, more challenging experiments using multiple excitation beams could be tried.

CHAPTER 7 REFERENCES

1. D. P. Kien, J. C. Loulergue, J. Etchepare, *Opt. Commun.* **101**, 53 (1993)

2. T. Rossler, J. B. Page, 'Intrinsic Localized Modes in Driven Anharmonic Lattices with Realistic Potentials', *Phys. Lett. A* (in press) (1996)

3. Y. Yan, K. A. Nelson, *J. Chem. Phys.* **87**, 6240 (1987)

4. L. Dhar, J. A. Rogers, K. A. Nelson, *Chem. Rev.* **94**, 157 (1994)

5. H. J. Eichler, P. Gunter, D. W. Pohl, Laser-Induced Dynamic Gratings (Springer-Verlag, Berlin, 1986)

6. C. J. Brennan, K. A. Nelson, 'Simulation of time-resolved wavevector overtone spectroscopy anharmonic phonon-polaritons in ferroelectrics' (in preparation)